

# Characterization and modeling of fiber reinforced concrete for structural applications in beams and plates

**Paegle, Ieva**

*Publication date:*
2015

*Document Version*
Publisher's PDF, also known as Version of record

# Characterization and modeling of fiber reinforced concrete for structural applications in beams and plates

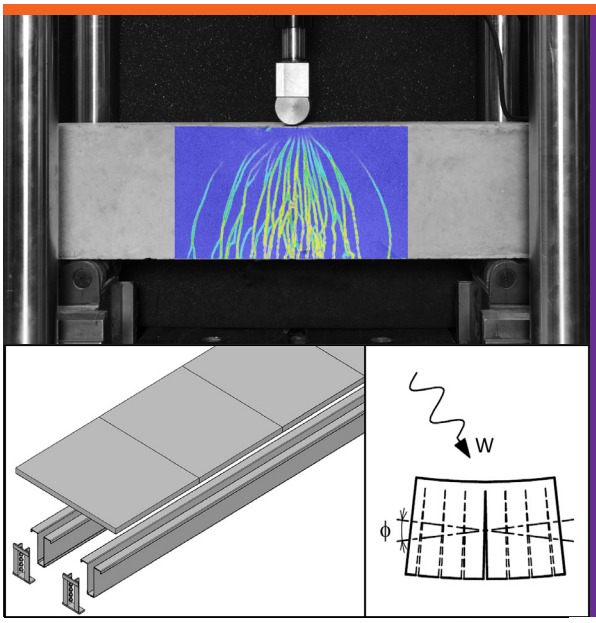


Ieva Paegle

PhD Thesis

Department of Civil Engineering
2015

DTU Civil Engineering Report R-327
November 2015

DTU Civil Engineering
Department of Civil Engineering

# Characterization and modeling of fiber reinforced concrete for structural applications in beams and plates

Ieva Paegle

Ph.D. Thesis

Department of Civil Engineering
Technical University of Denmark

2015

Characterization and modeling of fiber reinforced concrete for structural applications in beams and plates



Department of Civil Engineering

Technical University of Denmark

ISBN: 9788778774170

Report: Byg R-327

# Preface

This thesis is submitted as a partial fulfilment of the requirements for the Danish Ph.D. degree. The thesis is based on experimental and analytical investigations carried out as part of the Ph.D. project "Structural Design of Lightweight Composite Floor and Roof Panels," completed at the Department of Civil Engineering at the Technical University of Denmark (DTU Byg), Kgs. Lyngby, Denmark between September 2009 and June 2015.

The principal supervisor of the Ph.D. project was Associate Professor Gregor Fischer from DTU Byg with co-supervisor, Jeppe Jönsson, also from DTU Byg.

Kgs. Lyngby the 16th of November 2015

Ieva Paegle

# Acknowledgments

I would like to express my deepest gratitude to my main supervisor, Associate Professor Gregor Fischer from Technical University of Denmark for his advice and support during my Ph.D. study. I have enjoyed our discussions and working with him. The years during my Ph.D. have been filled with many professional and personal highlights, with a few obstacles; Gregor has given me the support and encouragement not only to develop my professional career but also given friendly advices in personal situations. The support of my co-supervisor, Professor Jeppe Jönsson, was also highly appreciated.

I would like to thank Assistant Professor Fausto Minelli from university of Brescia for the guidance and support through my external stay in Italy. Also, I would like to thank Professor Leonīds Pakrastiņš and Andīna Sprince from Riga Technical University in Latvia for their assistance on experimental works carried out in Riga. Furthermore, I appreciate the support and assistance of all the laboratory technicians at DTU BYG where the majority of experimental works were completed.

I would also like to acknowledge the financial support of Aase and Ejnar Danielsens Fond and Knud Højgaards Fond for funding this Ph.D. project. Financial contributions from the Otto Mønsteds Fond for travel and conference fees were also highly appreciated.

I would like to thank my colleagues, especially Larus Larusson and Eduardo Nuno Borges Pereira for their close collaboration, support, and countless discussions during our studies. Further, I would like to thank my colleagues and fellow Ph.D. students at the Technical University of Denmark for the fantastic times over the past years. Special thanks to Anders, Christian, Alex, Jacob, Evangelos, Henning, Sebastian, Jesper, Celeste, Jan, Giulia, Anna, Nina and Chiara. Also I would like to acknowledge the work from masters and bachelor students with whom I worked on parts of the experimental program, with special thanks to Silvia, Daniela, Carlo, Marco, Francesco, Francesco and Giovanni. The friendly conversations and laughter with my colleagues and friends in DTU while working, having lunch or other type of gatherings, made the time in Denmark and DTU more special for me.

I would also like to acknowledge the continuous support and the help with babysitting while I was working on my PhD of my family and friends, including my dad Dainis, my brothers Aldis and Jānis, my aunts Vija and Baiba and friends Mareike, André, Anja, Ismael and Anna. Thanks to my family for encouraging me to take the opportunity to do the PhD in DTU. Special thanks to my husband, Brad and daughter, Evita who have always given me their love, care and continuous encouragement.

# Abstract

Fiber reinforced concrete (FRC) with discrete, short and randomly distributed fibers can be specified and designed for structural applications in flexural members. In certain cases, fibers are used as the only reinforcement, while in other cases fibers are used in combination with a reduced amount of conventional reinforcement. While practical applications for FRC have been developed, shortcomings in test methods for determining mechanical properties and overly conservative design approaches limit the economic viability of FRC.

The measured mechanical properties of FRC, determined through standard test methods, vary widely depending on the prescribed test method. These variations in mechanical properties impact the structural design, typically resulting in increased dimensions of the FRC structural element. To address these shortcomings in evaluation methods and how measured mechanical properties are considered in structural design, the work presented in this thesis analyzes in detail many commonly used test methods on three types of FRC, including Polypropylene Fiber Reinforced Concrete (PP-FRC), Polyvinyl Alcohol Fiber Reinforced Concrete called Engineered Cementitious Composite (ECC) and Steel Fiber Reinforced Concrete (SFRC). These materials are representative for the two main types of tension-softening and strain-hardening FRC.

The direct tension tests most realistically describe the tensile properties and result in a cohesive relationship between model parameters that can be used in the design of FRC structures. However, direct tension tests may be difficult to conduct in standard testing laboratories and may not be best suited for quality control purposes. For this reason, alternative test methods are needed to obtain the most relevant properties of FRC. The assessment of the mechanical properties through flexural testing is generally easier to perform than direct tension tests in conventional testing laboratories. Various standardized test methods, based on beams and plates in flexure, are typically used to characterize FRC. However, the suitability of these methods for FRC materials with tension softening and hardening responses is not fully understood, and therefore investigated in this thesis. Advantages, disadvantages and specific features of various test methods are evaluated in detail and recommendations for modifications in standardized test methods are given to characterize FRC either with softening or hardening post cracking responses in the most efficient way.

Based on the findings in the characterization of FRC, a modeling approach to predict the flexural behavior of FRC elements is developed. The model predicts the flexural behavior of FRC by assuming a loaded structure consisting of a multitude of interconnected cracked segments, called Representative Flexural Segments (RFS), combined with rigid segments representing uncracked regions. The behavior of the RFS is characterized by the energy needed to deform a segment by a given rotational

angle which can be derived either from material properties in direct tension and compression or from flexural beam tests. The model considers the balance between work done on the deformed structure and the energy required to induce the corresponding rotational deformations in the RFS. The flexural response in terms of load-deflection of a structural element can be accurately predicted for a FRC with either softening or hardening post cracking behavior in direct tension or bending. The model is verified through experimental results of four-point bending beams and round determinate panels. Additionally, potential applications of SFRC representing a tension-softening FRC and ECC representing a strain-hardening FRC are investigated and used for model verification. This universally applicable model has been found to predict the flexural behavior of a structure in good agreement with experimentally obtained results.

Additional possible applications of FRC are investigated, including full or partial replacement of traditional shear reinforcement (i.e., stirrups) with fibers; and prefabricated lightweight composite roof and floor panels with an ECC slab.

Specifically, an example application of FRC as an alternative to traditional shear reinforcement (i.e., stirrups) is investigated in detail using digital image correlation (DIC) measurement technique. The use of steel fibers to replace traditional shear reinforcement is not without precedent in current reinforced concrete design codes. However, more detailed information is provided in this thesis on the formation of shear cracks and fiber bridging mechanisms to utilize the capacity of FRC. Based on the shear stress-strain responses and DIC measurements of the specimen deformations, a conceptual description of the shear crack opening, crack sliding and subsequent failure of reinforced concrete and reinforced FRC with a strain hardening behavior in tension are proposed. For reinforced concrete, forces are transferred over the shear crack only by stirrups, aggregate interlock and dowel effect of longitudinal reinforcement. The crack development mechanism for reinforced FRC with strain hardening behavior in tension is more complex due to the fiber bridging mechanisms, which induces multiple cracking resulting in smaller crack openings at a given shear stress as well as higher ultimate shear stress.

A new prefabricated lightweight composite roof and floor panel with ECC slabs has been developed as one of the main objectives in this PhD project. The lightweight prefabricated modular system consists of thin ECC plates connected to lightweight steel joists. The modular concept introduced aims at ease of manufacturing and storage processes of the panels by casting the ECC slab in relatively small elements and subsequently joining them with the lightweight steel profiles. The proposed design of prefabricated lightweight composite panel with an ECC slab is investigated experimentally to inspect the structural behavior of the panel under service and at ultimate conditions.

In summary, the work presented in this thesis offers new insights into application of FRC in structural elements, presents findings on experimental evaluation (tension, bending, shear, creep) and characterization of FRC and suggests a universally applicable model to predict the flexural response of both strain-hardening and tension-softening FRC.

# Resumé

Fiberarmeret beton (FRC) med små diskrete tilfældigt fordelte fibre, kan specificeres og designes til konstruktions anvendelse i bøjningspåvirkede elementer. I nogle tilfælde kan fibrene anvendes som den eneste tilstedeværende armering, mens de i andre tilfælde kan anvendes med en reduceret konventionel armering. Der er allerede fundet praktiske anvendelsesområder for FRC, men på grund af mangler i testmetoder for de mekaniske egenskaber og konservative designmetoder, begrænses den økonomiske bæredygtighed af FRC.

De målte mekaniske egenskaber af FRC bestemt gennem diverse standardiserede prøvemetoder, varierer meget afhængig af den enkelte metode. Disse variationer i de mekaniske egenskaber har indflydelse på design, og resulterer ofte i en forøget størrelse af FRC konstruktionselementet. For at imødekomme disse mangler i evaluering af test resultater og hvordan de målte mekaniske egenskaber anvendes i forbindelse med design, vil mange af de normalt anvendte testmetoder på tre forskellige FRC materialer, Polypropylene-Fiberarmeret beton (PP-FRC), Polyvinyl-Alcohol-Fiberarmeret beton eller Engineered Cementitious Composite (ECC) og Stålfiberarmeret beton (SFRC) blive grundigt analyseret. Disse materialer er repræsentative for tøjningssvækkende og tøjningshærdende FRC.

Rene trækforsøg beskriver mest realistisk trækegenskaberne, og resulterer i et kohæsivt forhold mellem modelparametre, der kan anvendes i design af FRC-konstruktioner. Det bør dog bemærkes at rene trækforsøg kan være svære at udføre med standard forsøgsudstyr, og er muligvis ikke det bedst egnede forsøg med hensyn til kvalitetskontrol. Der er derfor behov for alternative testmetoder for at fremskaffe de mest relevante materialeegenskaber for FRC. Måling af materialeegenskaberne gennem et bøjningsforsøg er overordnet set lettere at udføre end rene trækforsøg i almindelige materialelaboratorier. Diverse standardiserede forsøgsopstillinger baseret på bøjning af bjælker og plader er da også brugt til at karakterisere FRC. Dog er egnetheden af disse forsøgsmetoder for FRC materialer med tøjningssvækning og tøjningshærdning endnu ikke fuldt forstået, og de er derfor undersøgt i denne afhandling. Fordele og ulemper ved de forskellige forsøgsmetoder undersøges til bunds, og anbefalinger til modifikationer af standardiserede forsøgsmetoder præsenteres, med det formål at karakterisere tøjningssvækkende eller tæjningshærdende FRC så effektivt som muligt.

Baseret på resultaterne fundet under karakteriseringen af FRC, er en procedure for forudsigelsen af FRC konstruktionselementer udsat for bøjning udviklet. Modellen forudsiger bøjningsopførslen af FRC ved at antage en belastet konstruktion bestående af en række sammensatte revnede elementer kaldet repræsentative bøjningselementer (RFS), kombineret med stive elementer, der repræsenterer urevnede dele. Responset fra RFS elementet beskrives ved den energi det kræves for at give et segment en vis

vinkeldrejning, som kan udledes fra materialeegenskaber, der kan komme fra rene træk og trykforsøg eller bøjningsforsøg. Modellen tager hensyn til energibalancen mellem arbejdet udført i den deformerede konstruktion og energien der er nødvendig for at opnå de nødvendige rotationsdeformationer i RFS. Last-deformationskurver kan forudsiges præcist for konstruktioner af FRC med tøjningssvækning eller tøjningshærdning. Modellen er verificeret gennem resultater fra fire-punkts bøjning og runde statisk bestemte pladeforsøg. Derudover er potentielle anvendelsesmuligheder af SFRC, der repræsenterer tøjningssvækkende FRC, og ECC, der repræsenterer tøjningshærdende FRC, er blevet undersøgt og anvendt til modelverifikation. Denne universelt anvendelige model er fundet i god overensstemmelse med forsøgsresultater.

Yderligere anvendelser af FRC er undersøgt, hvor traditionelle armeringsbøjler helt eller delvist er erstattet af fibre; og præfabrikerede letvægts kompositttag og etagedæk med ECC plader.

Specielt er eksemplet, hvor FRC er anvendt i stedet for konventionel forskydningsarmering, undersøgt detaljeret ved brug af digitale billedekorrelationsteknikker (DIC). Brugen af stålfibre som erstatning for forskydningsarmering er set før i diverse normer og standarder¬¬. Der bliver dog i denne afhandling præsenteret detaljerede oplysninger om forskydningsrevnedannelse og fibrenes kraftoverførsel i revnerne, der kan tillade bedre udnyttelse af FRC. Baseret på forskydningsarbejdslinier for revner og DIC-målinger af forsøgsemnets deformationer, beskrives konceptuelt forskydningsrevneåbningen, revneglidningen og efterfølgende brud af armeret beton og af armeret FRC med tøjningshærdende egenskaber. For den armerede betons tilfælde er kraften langs forskydningsrevnen kun båret af bøjlearmeringen, revnens ruhed og dybeleffekt i længdearmeringen. Revneudviklingen er mere kompleks i armeret FRC med tøjningshærdende egenskaber på grund af fibrenes kraftoverførsel kraftoverførslen i revnerne, der giver flere revner og mindre revnevidder ved en given forskydningsspænding samt en højere forskydningsbæreevne.

Et nyt præfabrikeret letvægts kompositagplade og etagedæksplade med ECC-plader er blevet udviklet som en del af det overordnede mål med dette PhD-projekt. Dette letvægts præfabrikerede modulære system består af tynde ECC-plader sammensat med letvægts stålbjælker. Det viste koncept sigter efter at have en nem fremstilling og opbevaring af ECC-pladerne ved at støbe dem i små længder, for derefter at forbinde dem til letvægtsstålbjælkerne. Det i afhandlingen præsenterede design undersøges eksperimentelt for at klarlægge konstruktionselementets opførsel under anvendelseslaster og brudlast.

Kort sagt giver arbejdet præsenteret i denne afhandling ny indsigt indenfor brugen af FRC i bærende konstruktioner, præsenterer resultater fra eksperimentelle undersøgelser (træk, bøjning, forskydning og krybning) og karakterisering af FRC, og

præsenterer en universelt brugbar model til modellering af bøjning i tøjningssvækkende og tøjningshærdende FRC.

# Table of Contents

# List of abbreviations

| | |
|---|---|
| CCD | charged couple device |
| CMOD | crack mouth opening displacement |
| CTT | compact tension test |
| DH-FRC | deflection hardening fiber reinforced concrete |
| DIC | digital image correlation |
| DS-FRC | deflection softening fiber reinforced concrete |
| DTU | Technical University of Denmark |
| ECC | engineered cementitious composite |
| FRC | fiber reinforced concrete |
| ICP | integrally cast panel |
| LVDT | linear variable differential transducer |
| MP | modular panel |
| PP | polypropylene |
| PP-FRC | polypropylene fiber reinforced concrete |
| RC | reinforced concrete |
| RDP | round determinate panel |
| RECC | reinforced engineered cementitious composite |
| RFS | representative flexural segment |
| RTU | Riga's Technical University |
| SFRC | steel fiber reinforced concrete |
| SLS | service limit state |
| SMP | semi-modular panel |
| ULS | ultimate limit state |

# Chapter 1

# Introduction

## 1.1 Background

The addition of fibers to concrete, a quasi-brittle material, enhances the post-cracking properties by increasing ductility. Fibers transfer tensile forces across cracks, reducing the width of cracks compared to unreinforced concrete and improving the post-cracking performance of the concrete. The performance of fiber reinforced concrete (FRC) depends on the physical and mechanical properties of the fibers, the fiber distribution and content, the fiber-concrete bond properties and the properties of the concrete.

In recent years, FRC with discrete, short, and randomly distributed fibers are being specified for structural applications with significant flexural loads, including ground- and pile-supported slabs, tunnel linings, various precast elements, raft foundations, and other applications (Oslejs 2008; Winkler et al. 2014). In certain cases, fibers provide the only reinforcement, while in other cases fibers are used in combination with a reduced amount of traditional reinforcement. While practical applications for FRC have been developed, shortcomings in test methods for determining mechanical properties and overly conservative design approaches limit the economic viability of FRC. As discussed in Chapters 2 and 3, the mechanical properties of FRC, determined through standard test methods, vary widely depending on the applied test method. Variations in mechanical properties impact the designed dimensions for FRC structural element.

To address these shortcomings in test methods and how the determined mechanical properties are considered in structural design, this Ph.D. thesis analyzes in detail the

most commonly used test methods on various types of FRC, evaluates advantages, disadvantages and specific features of them. Additionally, a novel model, capable of predicting the load capacity and deformations of flexural elements regardless of whether the FRC has a tension softening or a strain hardening post-cracking response, is developed and verified.

The following sections describe the historical development of FRC, a general classification system for FRC, current experimental characterization and design methods and provide initial details on three FRC materials, including Polypropylene Fiber Reinforced Concrete (PP-FRC), Polyvinyl Alcohol Fiber Reinforced Concrete called Engineered Cementitious Composite (ECC) and Steel Fiber Reinforced Concrete (SFRC), that are the main focus of the presented Ph.D. study.

### 1.1.1 Historical development of FRC

A US patent, granted in 1874 (Berard 1874), appears to be the starting point of what is known now as fiber reinforced concrete. The patent calls for the addition of waste granular iron to as an improvement to 'artificial stone.' During the following 40 years more patents were filed in USA, France and Germany, however, until the 1960's the field stagnated (Maidl 1995). The stagnation in development of FRC was likely due to high material costs, missing theoretical knowledge and a simultaneous focus of the civil engineering society on the steadily developing fields of traditional reinforced concrete and prestressed concrete.

The early 1960's marked the beginning of an era of increased focus on research and development on FRC (Naaman 2007). More rapid modern advances were paralleled by an increasing number of applications and introduction of new fiber types. The first of these "modern era" studies dated from 1960's, were conducted by Romauldi and Mandel (Romualdi & Mandel 1964). They demonstrated that the addition of short steel fibers to concrete reduced the brittleness, which is a limitation of the material. During the 1970s numerous research investigations were undertaken on FRC, including important works by (Aveston & Kelly 1973; Hannant 1978; Naaman & Shah 1979; Shah 1971; Swamy et al. 1974). The studies continued the expansion in fiber types to introduce new materials including glass, carbon, synthetics, various natural fibers and combinations of different fiber types and lengths.

At the end of 1970's researchers developed an FRC material with significantly enhanced ductility. Until then the toughness of the material was increased through insertion of fibers but ductility improvements were limited as a single crack typically led to failure. Fibers bridged the crack, but were unable to develop additional cracks, therefore limiting the impact on ductility. At the end of the 1970's, the first works reporting multiple cracking in tension and bending were published, with one of the first publications being by Naaman and Shah (Naaman & Shah 1979).

Since 1979, FRC has been a topic of continued research and development. Researched areas include short- and long-term mechanical properties (with an emphasis on post-cracking response), developments in mixture designs, the workability of the fresh material, the durability of FRC, structural applications of FRC, among other topics. Many of these more recent research efforts have been considered and are referred to and discussed throughout the following chapters of this thesis.

### 1.1.2 Development of classification for FRC

The most distinctive feature of FRC, in contrast to conventional concrete, is its ability to locally reinforce the cracked matrix by transferring stresses across the fractured surface. While conventional concrete accomplishes a very limited stress transfer across cracks by aggregate interlock, the presence of fibers enables significant transfer of tensile loads across cracks until the fiber either pulls out or ruptures.

The transfer of stress across cracks influences the crack opening process and may result in various load-deformation responses under direct tensile or flexural loading. Figure 1. illustrates the possible load-deformation responses for FRC, which include softening and hardening post-cracking responses.

The nature (i.e., softening or hardening) of the post-cracking response is dependent on the type, geometry, volume and properties of the fibers; the properties of the cementitious matrix; and the interface properties (Lim et al. 1987; Stang & Shah 1986; Naaman & Shah 1979 etc.).

If the maximum load carrying capacity corresponds to the first crack strength, the composite is considered to be softening. Figure 1.(a and b) provides examples of softening responses. The softening response is typically accompanied by a concentration of deformation, or localization, in a single crack.

If a higher load carrying capacity occurs subsequent to the first crack strength, the fiber bridging strength governs and the composite is considered to be hardening. Figure 1.(c and d)) provides examples of hardening responses. The hardening post-cracking response is typically accompanied by the formation of multiple cracks with controlled width (Victor C Li and Wu 1992; V C Li and Leung 1992; Wu and Li 1994; Naaman and Shah 1979; Naaman and Reinhardt 2004). As shown in Figure 1., the softening and hardening responses can be used to classify both tensile and bending load responses.

Figure 1. presents the possible connections between the tensile and bending post-cracking responses. An FRC with a hardening response in tension (referred to as strain hardening throughout this thesis) always results in a hardening response in bending (referred to as deflection hardening throughout this thesis). An FRC material with a softening response in tension (referred to as tension softening throughout this thesis) may lead to either a deflection softening or a deflection hardening response. In

cases where the maximum fiber bridging stress is equal to or slightly less than the first crack strength, tensile testing will indicate the FRC is tension softening. The altered stress field of a flexural element may results in a deflection hardening response for FRC with similar fiber bridging and first crack strengths in tension. The polypropylene fiber reinforced concrete (PP-FRC) material discussed in this thesis is an example of an FRC that has a softening response in tension and a hardening response in flexure.

Additional details on one typical tension softening FRC, steel fiber reinforced concrete (SFRC), is provided in Section 1.1.5, while Section 1.1.6 discusses a strain hardening FRC, Engineered Cementitious Composite (ECC).

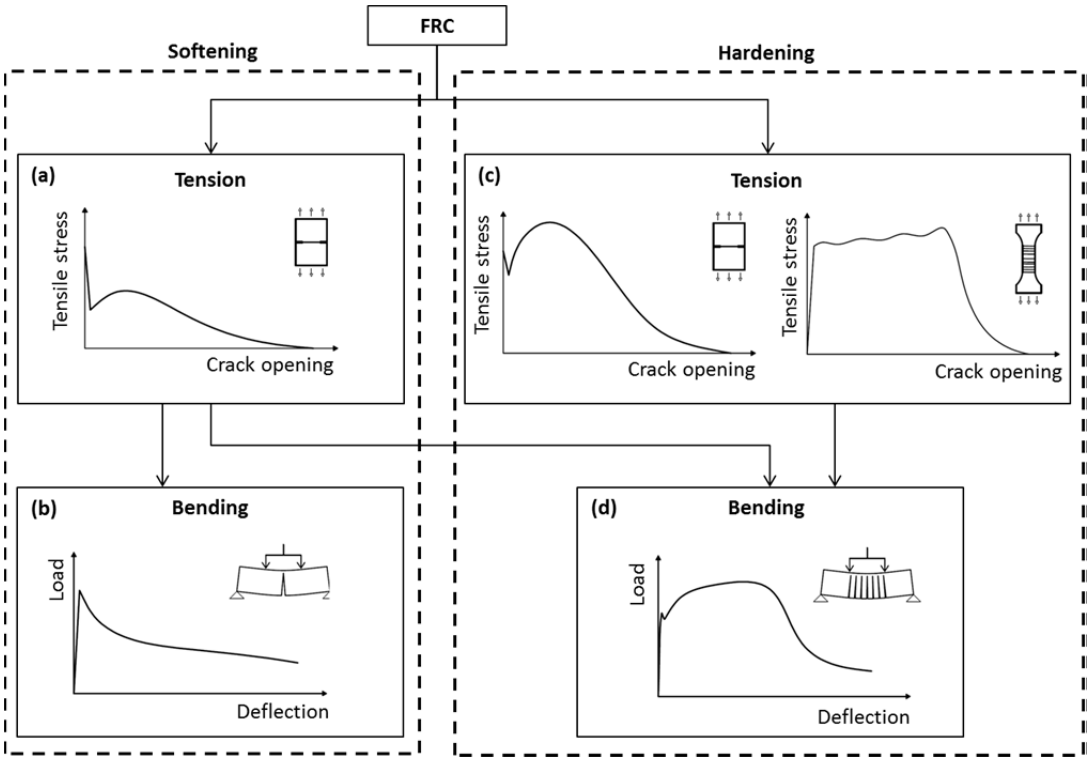


***Figure 1.1*** *Classification of FRC: (a) tension softening; (b) deflection softening; (c) strain hardening; and (d) deflection hardening*

## 1.1.3 Characterization of FRC through testing

To classify an FRC in the system illustrated in Figure 1. and ultimately to design with FRC (as discussed in Section 1.1.4), standard test methods are needed to measure and verify material parameters comply with design assumptions. The descriptions of testing and mechanical characterization of FRC provided in *fib* Model Code 2010 (fib 2012) emphasizes the significance of defining suitable material parameters, including post-peak tensile behavior, for structural design. Dimensioning and verifying the load capacity of any structural element made with randomly distributed fibers, with or without additional traditional reinforcement, requires the determination of equivalent elastic post-cracking strengths of the FRC material.

Three main categories of tests, characterized by setups and generated stress fields, may be used to evaluate the post-cracking response:

- Uni-axial tension tests, with a prescribed single crack or possible multiple cracking;
- Flexural beam tests, performed on notched or un-notched prisms, under three or four-point loading;
- Flexural plate tests (square panel with continuous support or round panel with 3 point supports).

Typically, for concrete the tensile strength is given as a percentage of compressive strength or as measured through split cylinder testing (e.g., ASTM C496, EN 12390-6). The split cylinder test provides sufficient information for brittle materials in tension, where post-cracking tensile strength and deformations are negligible compared to cracking strength. However, as significant post-cracking strength and deformations are evident in FRC, new test methods are needed to assess tensile properties.

The most common standard tests to characterize FRC are three- and four-point bending beam tests, with and without notches (ASTM-C1609 2012; CNR-DT204 2007; DAfStb 2010; DBV 2007; EN14651 2007; JCI-S-002 2003; JCI-S-003 2007). Some standards allow the use of various sized beams, which should be selected as a function of fiber length; other standards allow using particular specimen geometry, but set limits to fiber type and properties used in the FRC

Flexural plate tests are also a commonly specified test method, especially for sprayed FRC. The two most commonly used plate tests are ASTM C1550 (ASTM-C1550 2012) which is a round panel with 3 point supports and EN 14488-5 (EN14488-5 2006) which has a geometry of square panel with continuous support.

Chapters 2 and 3 provide detailed information on testing of FRC and recommendations for the selection of appropriate test methods for FRC materials with tensile softening and hardening responses.

### 1.1.4 Design of FRC

Various design codes, guidelines and suggested methods of design procedure of FRC flexural member are available in the literature (DAfStb 2010; fib 2012; SS812310 2014; TR63 2007). Most design codes, guidelines and other methods proposed utilizing experimental results from three- or four-point bending tests to estimate tensile properties based on simplified assumptions and analysis of the obtained results (e.g.., load-deformation (strain), load-deflection, or load-crack mouth opening displacement (CMOD) curves). In most cases, simplified strain compatibility and stress block analysis of a layered cross section (i.e., an assumed stress profile) is

required to compute the design ultimate moment capacity of a structural element. Therefore, two simplified assumptions are made, one for deriving the tensile properties from the flexural test, and a second in the design model for calculating the plastic moment capacity.

The flexural capacity of FRC members can also be designed based on a moment curvature analysis (Soranakom & Mobasher 2009) using simplified and normalized moment-curvature properties of FRC derived from a three-point bending (162-TDF 2002). The model by Soranakom and Mobasher is developed mainly for slab applications where the internal moment is relatively low, compared to cracking moment, and shear is not critical. While this approach can be used to design both for the ultimate strength and for serviceability, it is not intended for strain hardening FRC.

Chapter 5 of this thesis describes a novel modeling approach that links the energy required to induce rotational deformations in a representative flexural segment (RFS) to the load-deformation response of FRC structural members governed by flexure. The model marks a significant improvement over currently available design models for FRC, as softening and hardening response are both accurately modeled.

### 1.1.5 SFRC

Steel fiber reinforced concrete (SFRC) exhibits higher ductility compared to unreinforced mortar or concrete, which fail in tension and bending immediately after the formation of a single crack. This section provides details on the various types of steel fibers commonly used along with several example applications of SFRC.

The oldest and most basic steel fiber type is a straight fiber, cut from smooth cold-drawn wire. Unfortunately, such fibers do not ensure the full utilization of the strength of steel because of a lack of appropriate bond (anchorage) to the matrix. It was realized that the anchorage of fibers can be drastically improved by modifying the fiber shape, resulting in a wide range of steel fiber types, some of which are illustrated in Figure 1.2. Throughout the last 40-50 years steel fibers have been produced with twists; crimps; flattened-, spaded-, coned-, and hooked-ends; varying surface textures, and through melt-casting. These steel fibers had circular, square, rectangular, or irregular cross-sections. Each of the types was additionally varied by diameters and length (Katzer 2006; Maidl 1995).

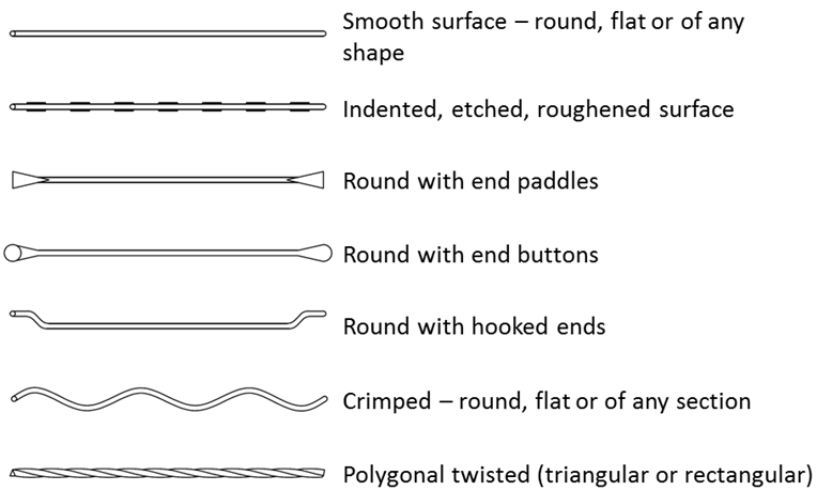


***Figure 1.2*** *Example of different shapes of steel fibers used in SFRC* (Naaman 2008)

The commonly used steel fibers are defined as short, discrete lengths of steel having an aspect ratio (ratio of length-to-diameter) from about 20 to 100, with various cross sections, with lengths between 25 and 60 mm and diameters between 0.4 and 1.3 mm. They are small enough to be randomly dispersed in a concrete mixture using usual mixing procedures.

Performances of SFRC depend on many factors, including the fiber material properties (fiber strength, stiffness and Poisson's ratio), fiber geometry (smooth, end-hooked, crimped and twisted fibers), fiber volume content, matrix properties (matrix strength, stiffness, Poisson's ratio), and interface properties (adhesion, frictional and mechanical bond). Clearly, for every matrix, type and quantity of fibers are key parameters that influence the performance of SFRC and its cost. Typical SFRC mix proportions provide tension and deflection softening responses (Figure 1.); however, the performance of SFRC can be improved to the point where it exhibits a deflection hardening response in bending. Very important is also the fact that the equipment for mixing, placing and finishing of conventional concrete can be interchangeably for SFRC with limited need for adjustments.

Example structural applications of SFRC, illustrated in Figure 1.3, include ground- and pile-supported slabs, tunnel linings, various precast elements, raft foundations, and others (Oslejs 2008; Winkler et al. 2014). The use of deformed steel fibers as an alternative to minimum transverse shear reinforcement was proposed (Parra-Montesinos 2006) and included in ACI 318-08 (ACI-318 2008).

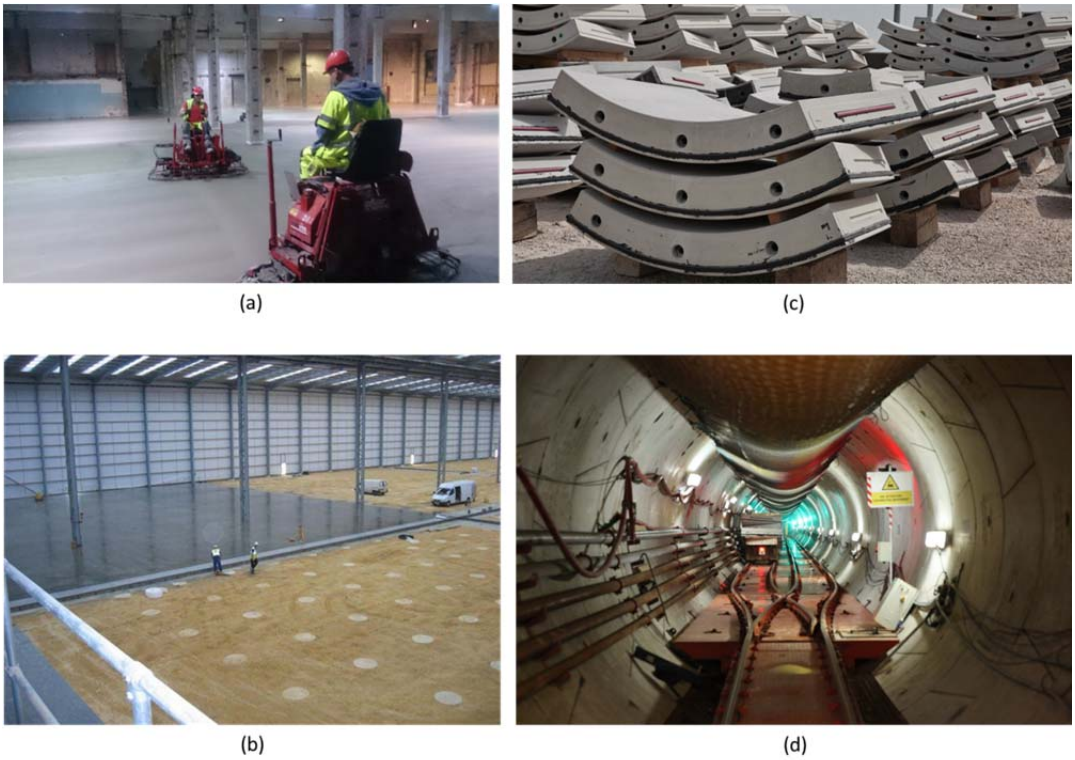


***Figure 1.3*** *Application of SFRC: (a) joint-less industrial floor slab on grade (www.twintec.co.uk); (b) SFRC floor slab suspended on piles (www.primekss.com); (c) precast tunnel elements and (d) steel and polypropylene fiber reinforced segments*

The use of steel fibers as reinforcement can be profitable over traditional reinforcement as a result of shorter construction time and ease of placement. Self-consolidating SFRC mix designs have also been developed, further reducing the need for workers on the jobsite. For some structural applications steel fibers are used in a supplementary role, either to inhibit cracking, improve resistance to material deterioration (as a result of fatigue, impact, shrinkage and thermal stresses), or as an alternative to traditional shear reinforcement. Critical members, significant to the structural system, commonly rely on traditional reinforcing bars to support the tensile loads. This conservative approach is justifiable by the variability of fiber distribution and flexural properties of FRC. The use of traditional reinforcement to carry the tensile loads increases the reliability of the critical member.

### 1.1.6 Engineered Cementitious Composite (ECC)

ECC is a type of fiber reinforced cementitious material characterized by a multiple cracking and strain hardening response under uni-axial tension. Usually, this behavior is achieved by reinforcing a cementitious matrix with a moderate volume fraction of short, randomly distributed synthetic fibers on the order of 2% by volume. Depending on the particular composition ECC typically has an ultimate tensile strength between 4 and 6 MPa, a first crack strength of 3 to 5 MPa, a tensile strain capacity of 2 to 5%,

a compression strength of 20 to 90 MPa, and Young's modulus of 18 to 34 GPa (Li & Fischer 2002; Li 1998). The cracking behavior of ECC is achieved by micromechanically influencing the interaction between fibers, matrix and their mutual interface. The bridging of cracks and subsequent deformation hardening lead to the formation of multiple cracks with the typical crack size between than 60 - 200 μm prior to localization of deformations (Larusson et al. 2010; Li & Fischer 2002) depending on the particular composition of ECC. The crack width control provided by ECC is desirable from a structural and durability viewpoint as it minimizes ingress of water and contained substances which can lead to depassivation and corrosion initiation of steel reinforcement (Hiraishi et al. 2003; Miyazato & Hiraishi 2005).

The improved tensile ductility and strength of ECC significantly alters the composite actions of ECC and steel reinforcement compared to traditional reinforced concrete (RC) (Fischer & Li 2002; Lárusson et al. 2011; Li & Fischer 2002; Paegle & Fischer 2011). The respective deformation mechanisms in tension can be explained by distinctly different post-cracking stress distributions in the reinforced ECC (RECC) composite due to formation of multiple cracking instead of localized cracking in the RC. The studies (Fischer & Li 2002; Lárusson et al. 2011; Li & Fischer 2002) present that the combination of reinforcement and ECC materials resulted in a composite with compatible inelastic deformations of the reinforcement and the ECC. Consequently, the damage induced by local slip and excessive interfacial bond stress between reinforcement and normal concrete is prevented. As the ECC matrix stiffens the composite at both cracked and uncracked sections, the load-deformation response of the composite is significantly improved.

In recent years, ECC has been used for specific structural applications, usually in combination with reinforcing bars. Figure 1.4(a) shows an example of a steel reinforced ECC link slab that integrally connects two adjacent bridge deck spans. The substructure girders is un-coupled from the reinforced ECC link slab, allowing the deformability and small crack widths of the ECC to create a continuous expansion joint construction, significantly reducing maintenance demands during the service life of the structure (Azizinamini et al. 2013; Lepech & Li 2009). Another application of ECC is in the Mitaka Dam in Japan, which was retrofitted in 2003 with a 30 mm layer of ECC, to minimize water penetration. The ECC was sprayed on top of the deteriorated existing concrete surface on the upstream side of the dam (Kunieda & Rokugo 2006).

An application of steel rebar reinforced ECC is shown in Figure 1.4(b). Steel reinforced ECC coupling beams are used in high-rise buildings in Japan as seismic dampers. The precast ECC beams were used as connection elements between main frames of reinforced concrete high-rise buildings in Tokyo and Yokohama. The dampers were designed to facilitate large deformations under earthquake actions by

utilizing the considerably high energy dissipation of the ECC member and to minimize repair work after an earthquake (Kunieda & Rokugo 2006).

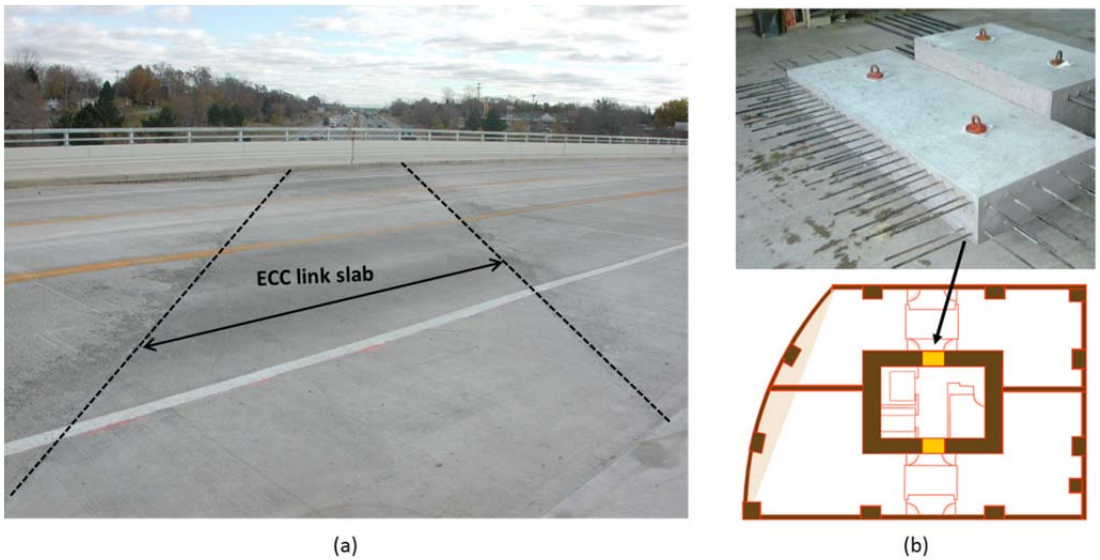


***Figure 1.4*** *Application of reinforced ECC in structural elements: (a) a continuous steel reinforced ECC slab in Michigan in 2005* (Lepech 2009)*; (b) steel reinforced ECC dampers in high-rise concrete buildings in Japan in 2004 and 2005* (Kunieda & Rokugo 2006)

## 1.2 Objectives

The main objectives of this Ph.D. study were to:

- Evaluate test methods for the characterization of FRC with strain hardening and tension softening responses in uniaxial tension. Evaluations consider the usefulness of the provided results and ease of implementation of the test method as a performance indicator.
- Develop analysis tools to relate various test methods, including:
    - The direct tension stress-crack opening response to the direct tension stress-strain response for strain hardening FRC and
    - Direct tension/compression responses to standard flexural test specimen.
- Develop a model to estimate the flexural response of structural elements using input parameters from either direct tension/compression test methods or flexural beam test methods.
- Highlight potential applications and facilitate the development of further structural applications of FRC with a hardening post-cracking response.
- To investigate the application of ECC in a prefabricated lightweight composite roof and floor panels.

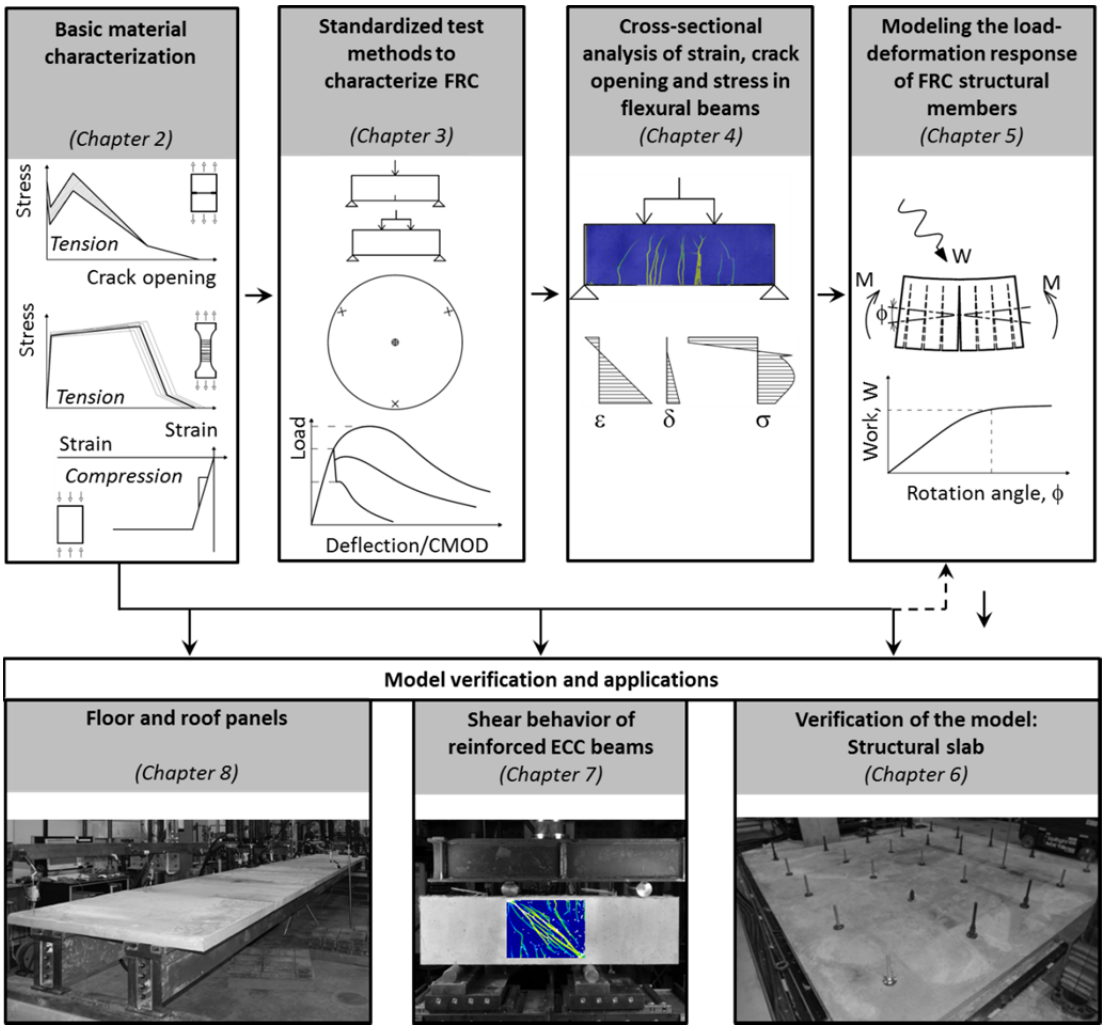


***Figure 1.5*** *Schematic overview of Ph.D. thesis*

## 1.3 Overview of the thesis

This thesis is divided in 9 Chapters. Chapter 1 gives a general background and motivation of the presented work and the objective and overview of the thesis. Chapters 2 to 8 include detailed information on the theoretical and experimental work completed through the Ph.D. study. The general overview and interconnection of the topics covered in Chapters 2 to 8 is provided in Figure 1.5.

The study involved three types of FRC:

1. Steel fiber reinforced concrete (SFRC). This material had a softening post-cracking response in tension and bending (tension softening and deflection softening);
2. Polypropylene fiber reinforced concrete (PP-FRC). This material had a softening post-cracking response in tension but hardening response in bending (tension softening and deflection hardening); and

3. Engineered Cementitious Composite (ECC). This material had a hardening post-cracking response in tension and bending (tension and deflection hardening)

Chapter 2 presents the constituent materials and mixture proportions of SFRC, ECC and PP-FRC used throughout the Ph.D. study. Basic fresh and hardened properties of each material are obtained and compared. Results presented in Chapter 2 show that the various FRC materials investigated in this study provided examples of both softening and hardening post-cracking responses.

Chapter 3 investigates the use of various standardized flexural tests to indirectly assess the tensile behavior of FRC, as an alternative to the direct measurement procedures described in Chapter 2. The flexural tests are generally easier to perform in typical concrete laboratories. However, the suitability of these standard methods for FRC materials with tension softening and hardening responses is not fully documented, and therefore investigated in this thesis. Recommendations are provided for the selection of appropriate test methods for FRC materials with tensile softening and hardening responses. Additionally, modifications to current standard flexural beam tests (sizes and notch configurations) are suggested.

Chapter 4 provides a more detailed analysis of compressive strain and tensile crack width profiles measured by digital image correlation (DIC) from four-point bending beams. Using the basic material responses provided in Chapter 2 and DIC measured strain/crack width profiles, the stress profile in the beam is derived. Bending moments, calculated from the derived stress profiles, accurately predict the applied flexural load at given strain/crack width profiles and the ultimate capacity. This chapter's findings indicate a potential for predicting the full flexural behavior (i.e., load-deflection) of FRC materials based on the basic compressive and tensile single crack responses.

Based on the conclusions of Chapter 2-4, a modeling approach is described in Chapter 5 to predict the load-deformation response of FRC flexural elements. The model assumes a flexural element consisting of a cracked rotationally deformable segment, referred to as representative flexural segment (RFS), and connected rigid segments. The properties of the RFS (i.e., work required to induce rotational deformation) are derived from either standard flexural beam test data or from tension and compression material properties. The model accurately predicts the load-deflection response for FRC materials with both tension softening and strain hardening post-cracking characteristics.

Chapters 6, 7 and 8 provide examples of structural applications of ECC.

Chapter 6 presents large-scale testing of FRC structural slabs. The results provide both a means for verification of the model presented in Chapter 5 and highlight a potential application of ECC and SFRC.

Chapter 7 presents the use of ECC as an alternative to traditional shear reinforcement (i.e., stirrups). As previously introduced in Section 1.1.5, the use of steel fibers to replace traditional shear reinforcement is not without precedent. However, this study investigates and quantifies the effects of ECC's strain hardening and multiple cracking behaviors on the shear capacity of reinforced beams with varying stirrup spacing. DIC results indicate an additional mechanism (fiber bridging) contributes to the transfer of stresses across shear cracks. Results conclude that ECC provide increased shear capacity regardless of the stirrup spacing compared to RC with similar compressive strength.

Chapter 8 presents an experimental investigation of a structural behavior of a prefabricated modular roof and floor panels. The prefabricated modular panel consists of a thin-walled ECC plates on top and lightweight steel substructure. The features of this composite structure include lightweight, the modular manufacturing process and a use of the various materials in the most efficient way. The modular concept introduced aims at ease on manufacturing and storage processes of the panels by casting the ECC slab in relatively small elements and subsequently joining them with the lightweight steel profiles.

Chapter 9 summarizes the main findings of the Ph.D. work and provides a final discussion and conclusions from the entire body of work that was performed during the Ph.D. study and is presented in this thesis.

# Chapter 2

# Basic material characterization

This chapter presents the constituent materials and mixture proportions of the SFRC, ECC and PP-FRC used throughout the Ph.D. study. Test methods for the basic characterization of each material are described, obtained results are provided and the basic performance of each material is compared. Table 2.1 provides an overview of the test methods used for the basic characterizations of the fresh and hardened properties of each FRC material. As explained in Section 1.3, the overall experimental program required FRC materials with two different post-cracking responses, softening and hardening. Results presented in the following section indicate the SFRC and PP-FRC exhibited a tension softening response, while ECC provided a strain hardening response in tension.

It is noted that in Chapter 7, an additional mixture proportion for traditional concrete is introduced. The traditional concrete used in Chapter 7 is for comparison purposes in the investigation of using ECC as an alternative to traditional shear reinforcement (i.e., stirrups).

***Table 2.1*** *Overview of the test methods used for the basic characterizations of the fresh and hardened properties of each FRC material*

| | ECC | PP-FRC | SFRC |
|---|---|---|---|
| ***Fresh properties*** | | | |
| Slump test | - | - | x |
| Flowability test | x | x | - |
| ***Hardened properties*** | | | |
| Compression | x | x | x |
| Compact tension (CT) | x | - | - |
| Tensile stress-crack opening | x | x | x |
| Tensile stress-strain | x | - | - |
| Creep | x | - | - |
| Shrinkage | x | - | - |

## 2.1 Constituents materials and mixture proportions

The experimental program consisted of tests on specimens made of three types of fiber reinforced concretes (FRC) including two tension softening materials and a strain hardening material. The strain hardening ECC was reinforced with 2% by volume polyvinyl alcohol (PVA) fibers, equivalent to 26 kg/m$^3$. Throughout this study two types of tension softening FRC were tested: steel fiber reinforced concrete (SFRC) and polypropylene fiber reinforced concrete (PP-FRC). The SFRC was reinforced with 55 kg/m$^3$ steel fibers (Dramix 3D 45/50) (0.7% by volume) and PP-FRC was reinforced with 1.5% by volume of polypropylene (PP) fibers. The properties of fibers are listed in Table 2.2 and the mixture proportions are given in Table 2.3.

***Table 2.2*** *Properties of fibers*

| Fiber type | ∅ | L | L/∅ | $f_t$ | E | Tensile strain capacity |
|---|---|---|---|---|---|---|
| | μm | mm | | MPa | GPa | % |
| PVA | 40 | 8 | 200 | 1560 | 40 | 6.5 |
| Steel, Hooked-end | 1050 | 50 | 45 | 1115 | 210 | - |
| PP | 13 | 12.7 | 975 | 550 | 13.4 | 8 |

***Table 2.3*** *Mixture proportions of FRCs*

| | SFRC |
|---|---|
| | $kg/m^3$ |
| Cement | 300 |
| Sand | 792 |
| Aggregate 4-8 mm | 308 |
| Aggregate 8-16mm | 703 |
| Water | 145 |
| Steel fibers | 55 (0.7 %) |
| Superplasticizer | 2 |

| | PP-FRC | ECC |
|---|---|---|
| | $kg/m^3$ | $kg/m^3$ |
| Cement | 546 | 428 |
| Fly ash | 546 | 856 |
| Sand (≤0.18 mm) | 239 | 150 |
| Quartz powder | 143 | 150 |
| Water | 382 | 321 |
| Fibers | 13.7 (1.5 %) | 26 (2.0 %) |
| Superplasticizer | 8.5 | 4.3 |
| Cellulose | 1.0 | 0.5 |

## 2.2 Fresh material properties

### 2.2.1 Flowability test of ECC and PP-FRC

The flowability test was used to determine the consistency of fresh concrete. The objective of this test is to compare the workability of the ECC and PP-FRC mixtures with and without fibers. The flowability test was performed using a plastic cone mold with a dimensions in accordance with ASTM C1437 for measuring a flow of hydraulic cement mortar (ASTM-C1437 2013).

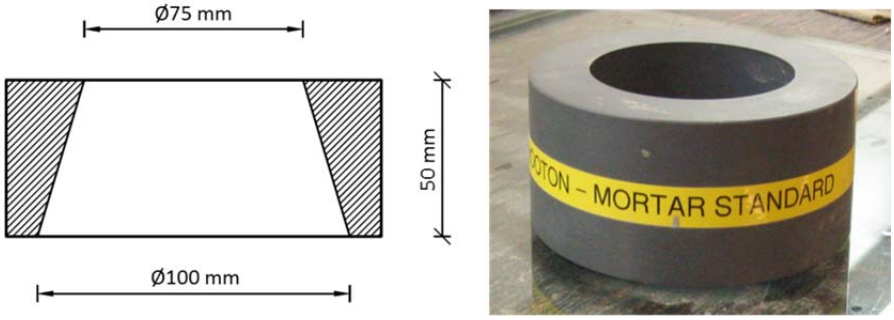


***Figure 2.1*** *Geometry of cone mold for flowability test*

The test procedure involved the following steps:

- Situate the cone mold on a center of a horizontal glass plate;
- Fill the cone by pouring in the material without external vibration or other means of consolidation;
- Lift the cone up allowing the mortar to flow freely by gravity; and
- Measure the diameter of a spread.

After measuring the spread of the material without fibers, the fibers were added to the mixture and the test was repeated. The average spread diameter measured for ECC was 31 cm without fibers and 21 cm with fibers, while for PP-FRC 31 cm was measured without fibers and 12-13 cm with fibers.

### 2.2.2 Slump test of SFRC

The slump of the SFRC was measured, in accordance with ASTM C 1437 (ASTM-C1437 2013), both before and after the addition of fibers to the concrete. The initial slump, prior to the addition of steel fibers, was 18 cm. This reduced to 12 cm with the addition of steel fibers.

## 2.3 Hardened mechanical material properties

As shown in Table 2.1, the basic hardened properties investigated for the materials included compressive properties, tensile properties, creep and shrinkage. Specimens in these investigations were demolded 24 to 48 hours after casting and were wet cured at 18± 2ºC until testing. For wet curing, the specimens were covered with wet burlap and plastic sheets during curing for 28 days. In some cases the impact of curing conditions was investigated. Additional information is provided in the following sections in those cases.

### 2.3.1 Compression and density

Compressive strength and modulus of elasticity were obtained using EN 12390-3 and ISO 1920-10 methods, respectively. Cylinders, with a 100 mm diameter and 200 mm height, were used for each material type and for each test method. The average density, measured from compression cylinders, was 1940 $kg/m^3$ for ECC, 1880 $kg/m^3$ for PP-FRC and 2420 $kg/m^3$ for SFRC.

The compressive properties of all three types of FRCs are presented in Figure 2.2 and Table 2.4.

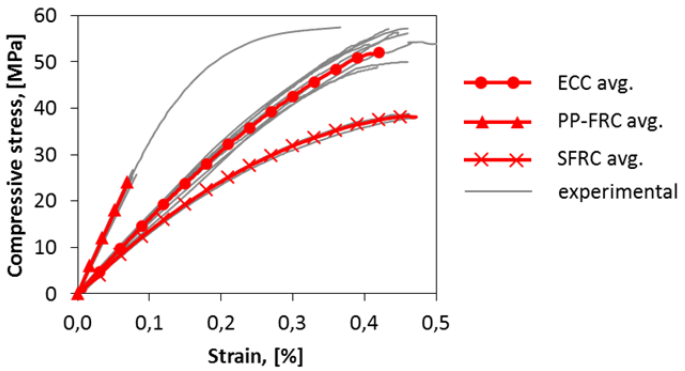


***Figure 2.2*** *Compressive properties of FRC*

***Table 2.4*** *Compressive properties of FRCs*

| Material | Number of samples | Avg. compressive strength | Avg. elastic modulus | Ultimate strain |
|---|---|---|---|---|
| | | MPa | GPa | % |
| ECC | 12 | 52.0 | 16.0 | 0.45 |
| SFRC | 6 | 57.1 | 34.5 | 0.35 |
| PP-FRC | 4 | 38.6 | 14.0 | 0.47 |

## 2.3.2 Tension

### 2.3.2.1 Tensile cracking strength

The mode I critical stress intensity factor, $K_{Ic}$ and the tensile cracking strength of the ECC matrix (i.e., ECC without fibers) was determined using the compact tension test (CTT). The test setup is shown in Figure 2.3. The thickness of the specimen was B = 12 mm.

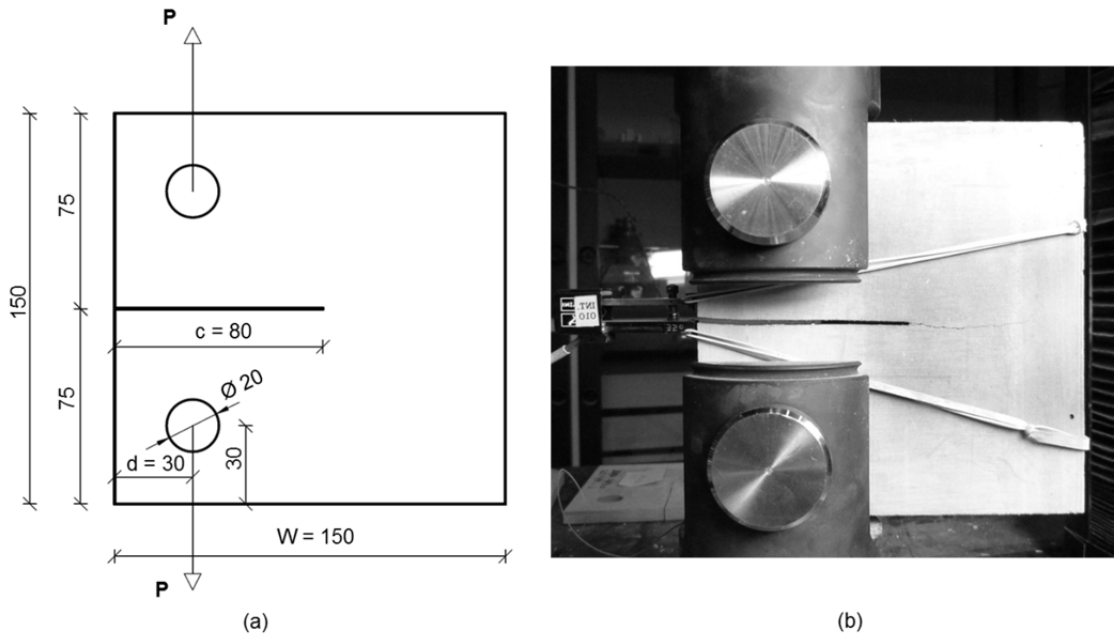


***Figure 2.3*** *Compact tension test: (a) geometry of the specimen; (b) test setup*

The testing procedure consisted of applying a tensile load to the notched CTT specimen. The notch, intended to maximize the stress intensity at its tip, was introduced using a 0.5 mm thick diamond cutting disc. The dimensions of the CTT specimens are presented in Figure 2.3(a). The testing sequence consisted of subjecting the specimens to a tensile load with a constant displacement rate. Tensile load was applied through two 20 mm diameter steel dowels (Figure 2.3(b)). The rods allowed

the transfer of the tensile load while allowing the specimen to rotate with respect to the dowels. The applied displacement rate was 1 μm/s.

The crack mouth opening displacement (CMOD) was measured using an extensometer with measuring range of ±2.5 mm. Additional details on the CTT setup can be found elsewhere (Sprince et al. 2014).

***Results – Stress intensity factor and tensile cracking strength***

The maximum load the 3 CTT specimens of ECC matrix resisted varied from 193 to 218 N, leading to a critical stress intensity factor, $K_{Ic}$ of 0.32 to 0.36 MPa$\sqrt{m}$. Stress intensity factor was calculated as proposed by Piascik and Newman (Piascik & Newman 1996):

$$K_I = \frac{P}{B\sqrt{W}} \cdot \frac{2+\lambda}{\sqrt{1-\lambda}\cdot\left(1-\frac{d}{W}\right)^{3/2}}(1.15 + 0.94\lambda - 2.48\lambda^2 + 2.95\lambda^3 - 1.24\lambda^4) \quad (2.1)$$

Where:

P – load;

B – thickness;

W – width of the specimen

$$\lambda = \frac{c-d}{W-d}$$

c – length of the notch

d – distance from specimen edge to load line (Figure 2.3)

The critical stress intensity, $K_{Ic}$ corresponds to the stress intensity at the cracking load.

#### 2.3.2.2 Tensile stress-crack opening

To obtain the tensile stress-crack opening relationship, or cohesive relationship, a single crack notched coupon test specimen was loaded under direct tension. The specimen geometry, shown in Figure 2.4, is intended to create a weak plan where a single crack forms. The test method, developed by Pereira et al. (Pereira et al. 2012), is intended for strain hardening FRC. Pereira et al. verified and confirmed the setup causes the formation of a single, localized crack and provides the relationship between the applied tensile load and single crack opening.

The cohesive relationship of the ECC and PP-FRC was determined using notched coupon specimens with a representative cross section of 8 mm × 30 mm. The size of the notched coupon specimen and the test setup are shown in Figure 2.4 and Table 2.5. The notch reduced the tested area of specimen by 60% to generate a single tensile crack in the specimen even for a strain hardening material. Deformation controlled tensile tests (0.3 mm/min loading rate) were conducted using clip gauges to measure

the opening displacement across the notch. Deformation was applied to the specimen through hydraulic grips, which provided a fixed support at both ends of the specimen (Fischer et al. 2007; Pereira et al. 2012). The specimen geometry used in these investigations was specifically designed for materials with small maximum aggregate size (0.18 mm) and 'flexible' fibers (i.e., PVA, polypropylene and polyacrylnitrile).

The cohesive relationship of the SFRC was determined using notched cube specimen with a representative cross section of 100 mm × 100 mm (Table 2.5, Figure 2.5). The notch reduced the tested area of specimen by 55% to generate a single tensile crack in the specimen. Cross-head displacement controlled tensile tests were performed with a loading rate of 0.05 mm/min up to cross-head displacement of 2 mm; subsequently the loading speed was raised to 0.5 mm/min. The crack opening was measured across the notch using two clip gauges affixed on opposite sides of the specimen. The test setup and specimen configuration were designed to apply the deformations to the specimen near the notch using a rigid steel frame (Figure 2.5). The size of the specimen is comparable to standard compression cube size and standard flexural beams (150mm x 150mm). The specimen is significantly larger than the specimen utilized for the ECC and PP-FRC as the maximum aggregate size and fiber dimensions were larger.

***Table 2.5*** *Properties of tensile specimens*

| Material | Test type | No. of samples | H | B | T | b | t | f | h | Weight |
|---|---|---|---|---|---|---|---|---|---|---|
| | | | mm | mm | mm | mm | mm | mm | mm | kg |
| ECC | Single crack | 10 | 100 - 120 | 50 | 12-16 | 30 | 8 | 0.25 | - | ≤0.2 |
| PP-FRC | Single crack | 6 | 100 - 120 | 50 | 12 | 30 | 8 | 0.25 | - | ≤0.2 |
| SFRC | Single crack | 7 | 150 | 150 | 150 | 100 | 100 | 2.0 | - | 8.2 |
| ECC | Dog-bone | 4 | 510 | 75 | 22 | 50 | 22 | - | 200 | 1.3 |

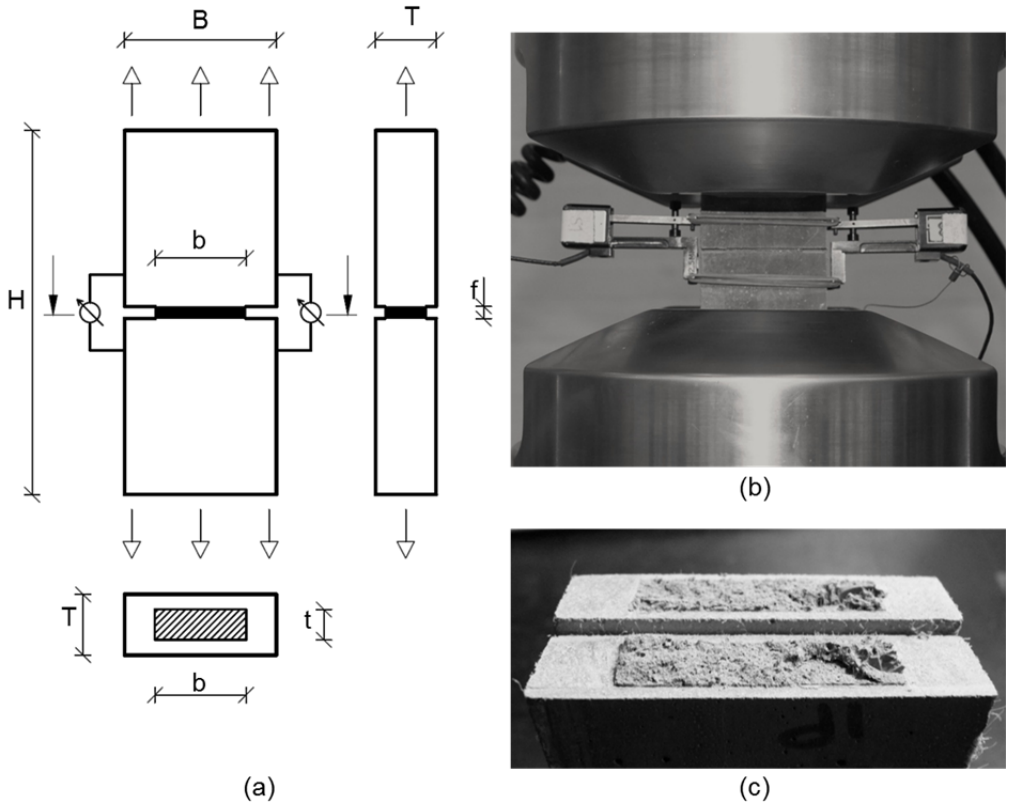


***Figure 2.4*** *Single crack notched coupon test of ECC and PP-FRC: (a) specimen geometry; (b) test setup; (c) specimen after testing*

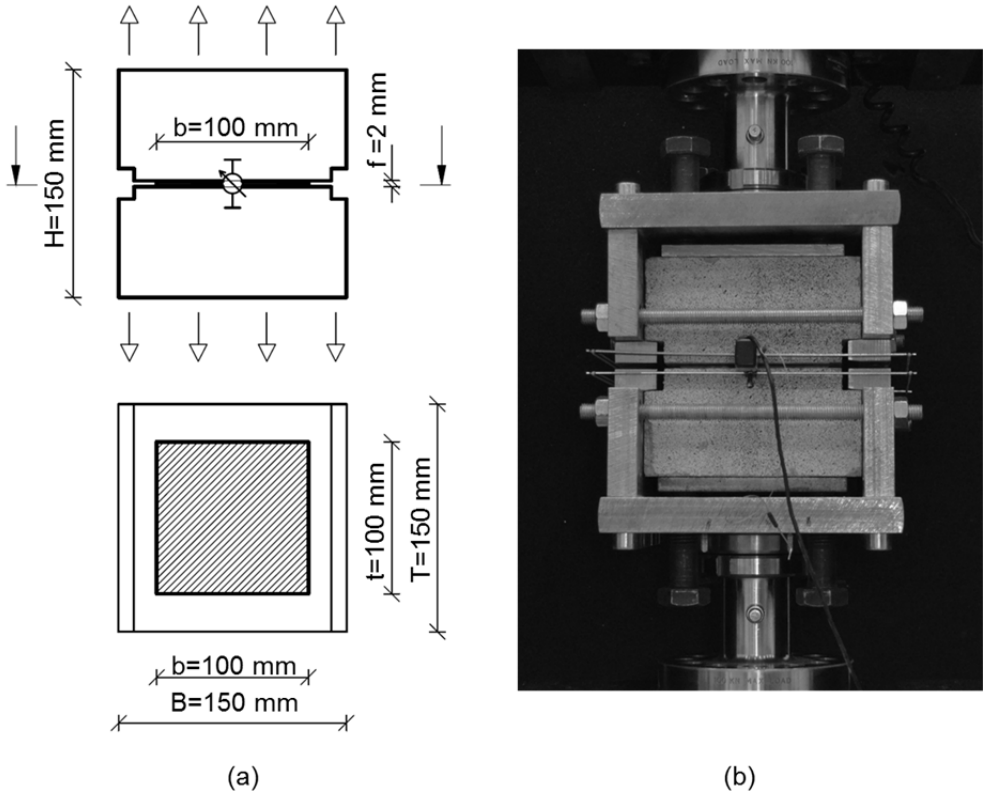


***Figure 2.5*** *Single crack notched coupon test of SFRC: (a) specimen geometry; (b) test setup*

***Results – Tensile stress-crack opening***

Figure 2.6 provides the determined cohesive relationships for (a) ECC (a), (b) PP-FRC, and (c) SFRC. As indicated in Figure 2.6(b), the cohesive relationship for all materials consisted of a first crack strength, a fiber bridging peak stress, and a softening branch. For PP-FRC and SFRC, the first cracking strength was easily determined through the direct tension tests. However, for ECC the first cracking strength was commonly undetectable in the single crack notched coupon test results. Rather than having an initial peak, the cohesive relationship gradually increased to the peak fiber bridging strength. It is possible the preparation of the ECC single crack notched coupon specimens, which involves cutting a notch on all sides of the specimen and clamping in the testing machine, introduced some minor damage into the ECC matrix.

The CTT testing, described in Section 2.3.2.1, was therefore performed to determine the first cracking strength for ECC. The cracking strength was calculated using the measured stress intensity factor, $K_I$ with the following equations (Broek 1991):

$$\sigma_{cr} = \frac{K_I}{Y\sqrt{a}} \tag{2.2}$$

Where the geometric function Y is calculated as:

$$Y = 1.99 + 0.76\frac{a}{W} - 8.48\left(\frac{a}{W}\right)^2 + 27.36\left(\frac{a}{W}\right)^3 \tag{2.3}$$

Where:

a – depth of the notch a = 2 mm;

W – width of the specimen, W = 12 mm;

$K_I$ – stress intensity factor

Using the critical stress intensity factor from Section 2.3.2.1, the cracking strength of the ECC matrix was computed to be between 3.6 and 4.0 MPa for the geometry of the single crack notched coupon.

Combining the first cracking strength from the CTT test and the results of the single crack notched provides the cohesive relationship for ECC, plotted in Figure 2.6(a). The first cracking strength of ECC (3.6 – 4.0 MPa) is smaller than the maximum fiber bridging stress (3.75 – 4.5 MPa). As the first cracking strength is lower than the ultimate stress of the fibers, multiple cracking and strain hardening behaviors under uni-axial tension in un-notched geometries can occur (Li & Kanda 1998; Pereira et al. 2012).

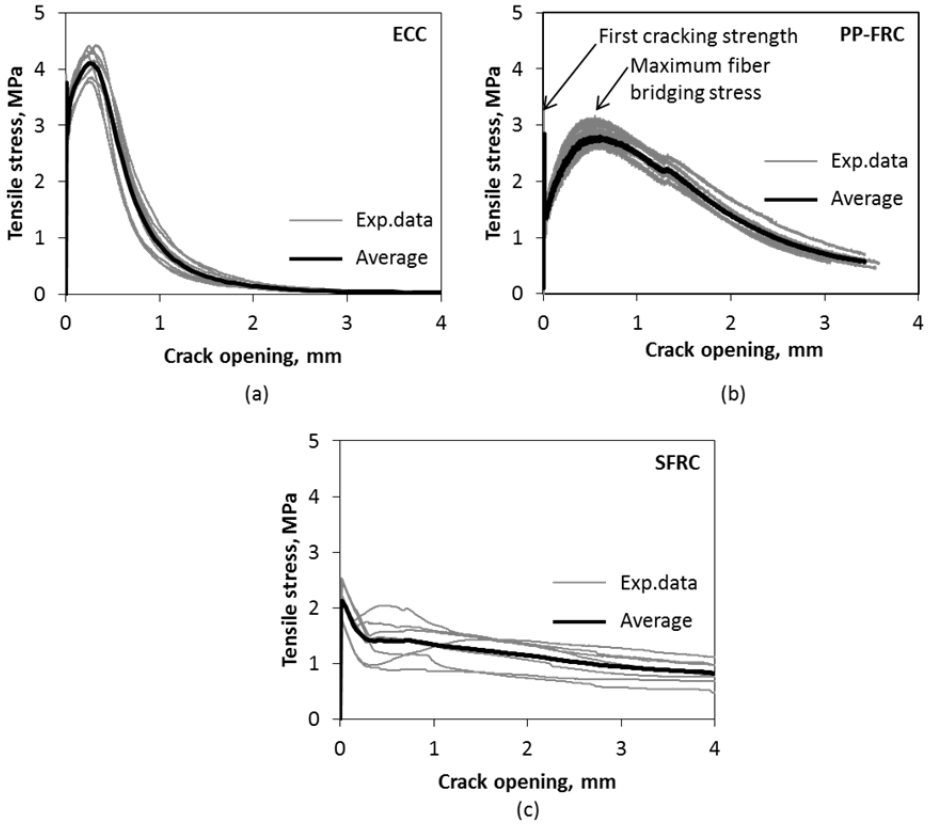


***Figure 2.6*** *Cohesive relationships of (a) ECC, (b) PP-FRC and (c) SFRC*

The obtained cohesive relationship for PP-FRC is plotted in Figure 2.6(b). The average first cracking strength of PP-FRC was 3.1 MPa (2.9 – 3.4 MPa) and the average maximum fiber bridging stress was 2.85 MPa (2.7 – 3.1 MPa). As the average first cracking strength is higher than the peak fiber bridging strength, a softening response for PP-FRC is expected under uni-axial tension.

The first cracking strength of SFRC (Figure 2.6(c)) was between 1.8 and 2.5 MPa, with no distinct second peak observed. The maximum fiber bridging stress varied widely from 0.9 to 2.0 MPa, likely due to the variation in number of fibers bridging the failure plane (23 to 42 fibers). The immediate crack opening was approximately 0.2 mm for all SFRC specimens.

#### 2.3.2.3 Tensile stress-strain

As indicated in Section 2.3.2.2, ECC may undergo multiple cracking. Therefore, the single crack behavior does not provide a complete characterization of the material response in uniaxial tension. It is also necessary to determine the strain capacity, crack spacing, and the average, minimum and maximum crack widths at increasing strain levels.

To experimentally determine the tensile stress-strain responses of ECC, the dogbone specimens, shown in Figure 2.7, with a representative cross section of 22 mm (t) × 50

mm (b) and with a representative length of 210 mm (h) were used. Similar to the single crack notched coupon test, deformations were applied to the specimen through hydraulic grips that provided fixed support to both specimen ends. Deformation controlled tensile tests (0.5 mm/min loading rate) were conducted with linear variable differential transducers (LVDTs) physically measuring the tensile deformations in the specimen. A digital image correlation (DIC) system was also adopted for measuring crack formations. The DIC equipment captured images of the representative section of the specimen at one second intervals (i.e., 1 hertz). Additional details on the DIC measurement technique are provided in Section 2.4.

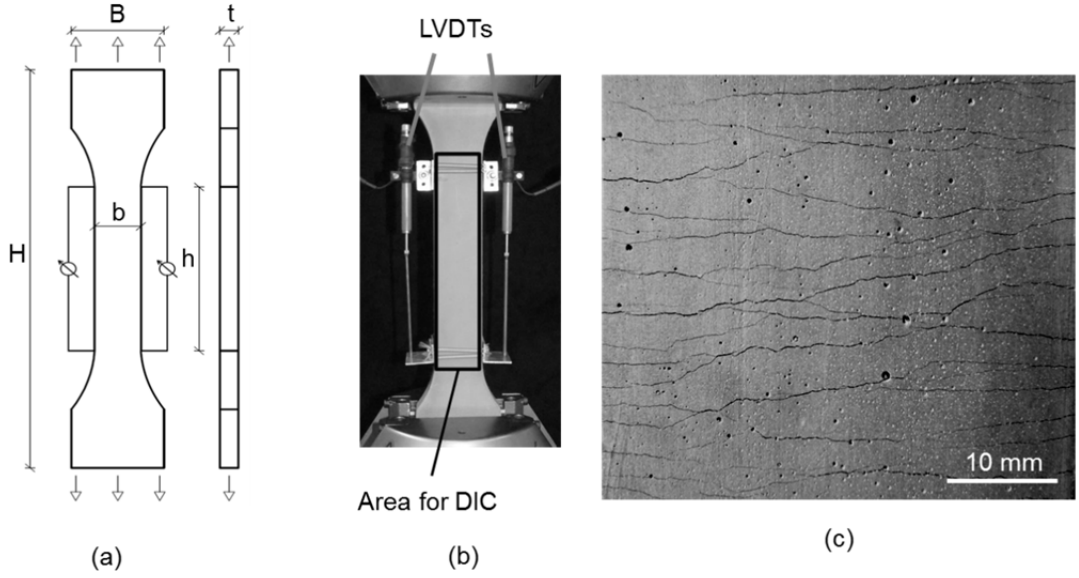


***Figure 2.7*** *Tensile dogbone test: (a) specimen geometry; (b) test setup; (c) multiple cracking of ECC*

***Results – Tensile stress-strain***

Typical tensile stress-strain relationships for ECC are plotted in Figure 2.8. The average first cracking strength taken from the six test specimens was 3.3 MPa, with an average ultimate tensile stress of 4.1 MPa at corresponding strains of 2-3%. Failure of the ECC dogbone specimens is considered to occur once the tensile stress drops continuously with increased tensile deformations.

The second vertical axis in Figure 2.8 provides statistics on crack widths (maximum, minimum and average), measured using DIC from a selected specimen in the series. During the strain hardening stage, additional applied tensile deformations result in both the growth of existing crack widths and the formation of new cracks. At a strain level of 2.8%, crack saturation was obtained in the selected. Once crack saturation occurs, no additional cracks form and all further applied tensile deformation result in the widening of existing cracks. Crack localization and subsequent failure occurred when the stress in the specimen reached the maximum bridging stress at the weakest cracked section.

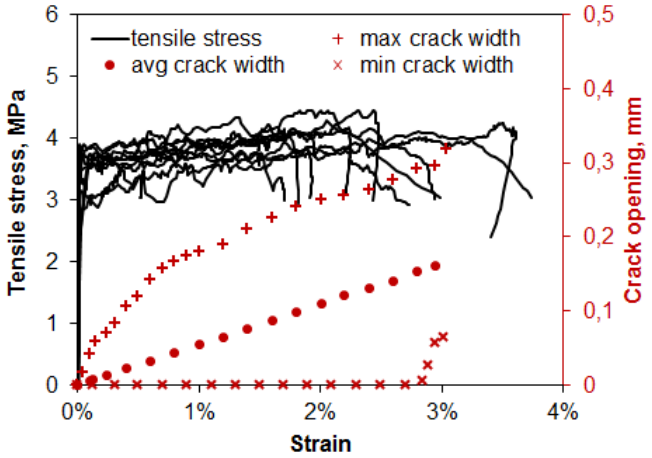


***Figure 2.8*** *Tensile properties of ECC*

Both tensile test methods provide significant insight for the characterization of ECC. The single crack notched coupon test provides qualitative basic information about the cohesive relationship. The single crack notched coupon test also provides an indication of whether the material is strain hardening or softening in tension. If the first cracking strength is lower than the maximum fiber bridging stress, the material is likely to have a strain hardening behavior in uni-axial tension, while materials with maximum fiber bridging stress less than the first cracking strength are likely to have a softening response. The dogbone test characterizes the overall strain capacity, crack distribution and ductility of ECC. For tension softening materials, the single crack coupon and dogbone tests show similar information as failure in tension softening materials by definition occurs at a single crack location.

### 2.3.3 Creep and Shrinkage

The long-term deformation characteristics of cementitious materials are important to structural design as these can significantly contribute to the overall capacity of the structural element. Two time-dependent deformations play a major role in successful and continuous use of structures, creep and shrinkage (Chern & Young 1989; Sprince et al. 2013). Long-term loading of a structural element causes viscoelastic creep deformations to occur, while changes in the moisture content of concrete causes various forms of shrinkage. If appropriate attention is not devoted to these effects, structural reliability in terms of serviceability and, in some cases, of ultimate safety may be unfavorably affected. Therefore, it is necessary to understand the creep and shrinkage properties of cementitious materials.

The extent of viscoelastic creep in cementitious materials is affected most prominently by the composition of cementitious material, i.e. on a type (mostly E-modulus) and grading of aggregates, type of cement, and water-to-cement ratio (w/c) (Bywalski & Kaminski 2013).

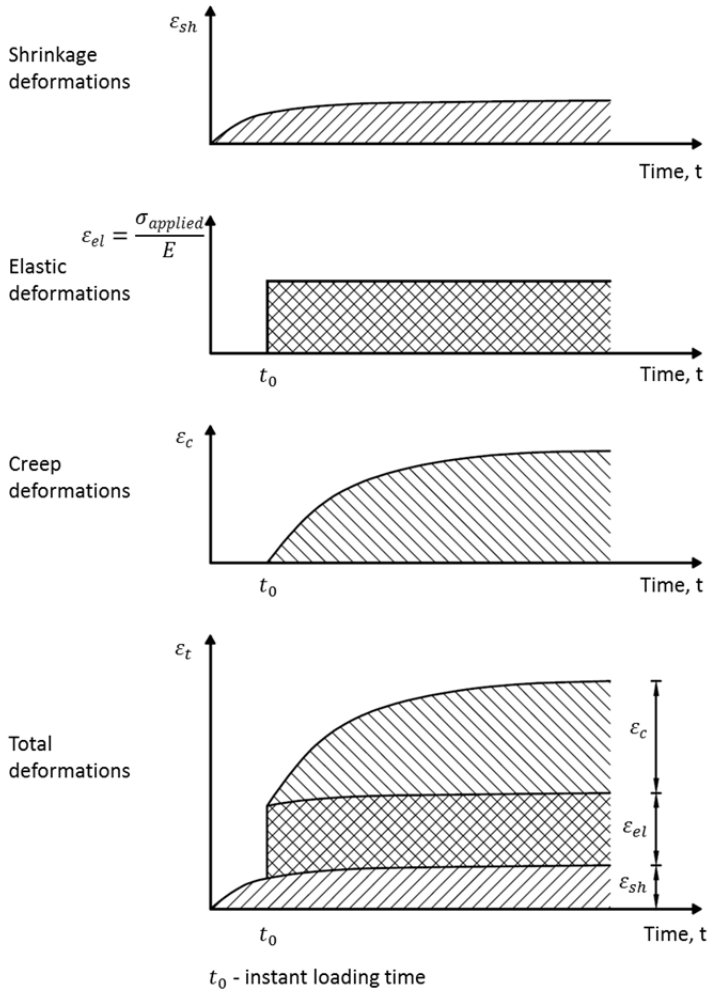


***Figure 2.9*** *Illustration of elastic and time dependent deformations*

Figure 2.9 illustrates the time-dependent deformations that develop in cementitious materials under long-term compressive loading. These deformations generally can be divided in three sources:

- Shrinkage, $\varepsilon_{sh}$ – deformations caused by changing moisture conditions (i.e., drying) within the pores of the cementitious material;
- Immediate elastic deformation, $\varepsilon_{el}$ – caused by application of load; and
- Creep, $\varepsilon_c$ – viscoelastic deformations caused by sustained permanent loading.

There is currently no broad consensus on the effect addition of steel fibers to concrete has on creep. Some studies (Chern & Young 1989; Mangat & Azari 1985) show reduced creep in SFRC with 1-3% volume fraction of fibers compared to the same material without fibers. Other studies (Balaguru & Ramakrishnan 1988; Velasco et al. 2009) indicate the addition of up to 2% volume fraction of steel fibers increases the creep. Other studies show the addition of up to 1% volume fraction of steel fiber has no significant impact on creep (Bywalski & Kaminski 2013). Due to the importance of creep and shrinkage on long-term structural performance and a lack of a general

conclusion on the impact fibers have on creep and shrinkage, testing of the ECC has been conducted as described in the following sections.

***Experimental program***

Experiments were conducted to measure creep deformations of ECC specimens, cured at varying conditions and exposed to various load levels.

In one study, conducted at Riga's Technical University (RTU), ECC specimens were placed in creep lever test stands (Figure 2.10(a)) and subjected to a constant 45 kN compressive load for 1060 days. Two cylinders sizes were tested (50 mm diameter x 100 mm height and 60 mm diameter x 120 mm height), resulting in two load levels; 30% and 45% of the average ultimate compressive strength. Creep deformations were measured across the middle 50 mm of the samples as the average of 3 individual on each specimen. Four specimens of each diameter were prepared according to description in Section 2.1 and cured in water for 25 days. After 25 days, four of specimens with diameter of each size were taken out of water and dried in and oven in 60±5°C for 3 days. When all specimens were 28 days old, they were wrapped in aluminum tape and subjected to load. The test program and properties of specimens are listed in Table 2.6. The relative humidity in the testing facility was 42±5% and temperature 22±2°C.

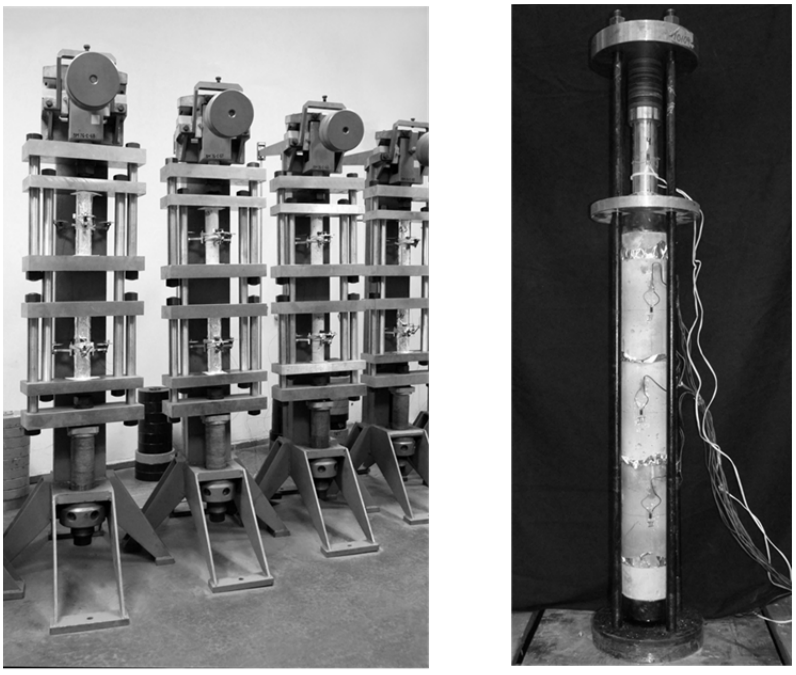

(a) (b)

***Figure 2.10*** *Creep test setup: (a) in creep lever test stand (RTU setup) and (b) spring loaded creep frame (DTU setup)*

***Table 2.6*** *Properties of creep specimens, Series I were the samples tested at Riga's Technical University, while Series II were the samples tested at DTU.*

| | Curing | # | Size | | Pre-dried | Sealed during creep testing | Loading | | Length of testing |
|---|---|---|---|---|---|---|---|---|---|
| | | | Ø | H | | | | | |
| | | | mm | mm | | | MPa | % | Days |
| I-Dry-30 | Water | 2 | 50 | 100 | Yes | Yes | 15.5 | 30 | 1060 |
| I-Wet-30 | Water | 2 | 50 | 100 | No | Yes | 15.5 | 30 | 1060 |
| I-Dry-45 | Water | 2 | 60 | 120 | Yes | Yes | 24.0 | 45 | 1060 |
| I-Wet-45 | Water | 2 | 60 | 120 | No | Yes | 24.0 | 45 | 1060 (815) |
| II-25-Water | Water | 3 | 100 | 200 | No | No | 12.5 | 23 | 420 |
| II-25-Air | Air | 3 | 100 | 200 | Yes | No | 12.5 | 23 | 400 |
| II-50-Water | Water | 3 | 100 | 200 | No | No | 27.0 | 50 | 420 |
| II-50-Air | Air | 3 | 100 | 200 | Yes | No | 27.0 | 50 | 400 |
| II-45-Water | Water | 2 | 100 | 200 | No | No | 34.0 | 60 | 420 |
| II-60-Air | Air | 3 | 100 | 200 | Yes | No | 24.0 | 45 | 400 |

A second creep study, completed at Technical University of Denmark (DTU), investigated the impact of curing conditions on creep deformations of ECC. The test setup consisted of six spring loaded creep frames (Figure 2.10(b)). More information of spring loaded creep fames are available elsewhere (Elgaard Jensen 1992). Three ECC cylinders with a diameter of 100 mm and height of 200 mm were tested in each frame. The deformations were measured with four strain gauges symmetrically glued on each specimen. The strain gauges were measuring the deformations over 8 mm of the middle section in the length direction of the cylinder. One-half of the specimens were air cured in laboratory with a temperature 22±2°C and relative humidity 50±5% for 40 days (dry cured). The other half were cured submerged in the water for 40 days. After 40 days the specimens were removed from the various curing conditions, were prepared for testing, by attaching strain gauges, and load was applied at a sample age of 55±5 days. The frames were loaded to various compressive stress levels in the cylinders of 20%, 50% and 60% of an average compressive strength. The test frame with wet cured samples intended to be loaded to 60% of the compressive strength was only loaded to 45% due to a technical problem with the test frame. Details on the test program and properties of the specimens are listed in Table 2.6. Creep stands were situated in a testing hall with a temperature of 21±4°C and varying humidity conditions. Thus, the results from the DTU tests series were intended to assess the impact of the curing conditions, but are not intended for comparison with the RTU test series or other tests.

The length change of the ECC was also investigated. The standard specimen geometry and measurements procedures, described in ASTM C 157 (ASTM-C157 2008), were used for this testing. The ECC samples were cast in standard molds, demolded after 24 hours, initial length and weight measurements recorded, and the samples were cured submerged in lime-saturated water for 7 days. After 7 days of wet curing, the samples were exposed to a 50% ±3% RH and 18° ±1° C environment. Length measurements were taken, initially daily, and then with reduced frequency for up to 80 days.

***Results – Creep and Shrinkage***

*RTU Test Series*

The total deformations of all specimens, $\varepsilon_t$, under continuous compressive loading for three years are illustrated in Figure 2.11 (a). The resulting creep deformations, $\varepsilon_c = \varepsilon_t - \varepsilon_{el}$, are illustrated in Figure 2.11 (b). The highest creep deformations were observed in specimens that were not pre-dried and that were exposed to a higher load level. The lowest creep strains were observed in the pre-dried specimens. The specific creep ($\varepsilon_c/\sigma_{applied}$) and creep coefficient ($\varepsilon_c/\varepsilon_{el}$), shown in Figure 2.11(c) and (d), are significantly affected by the initial moisture condition of the samples. However, the applied load level appears to have a negligible impact on the specific creep and creep coefficient.

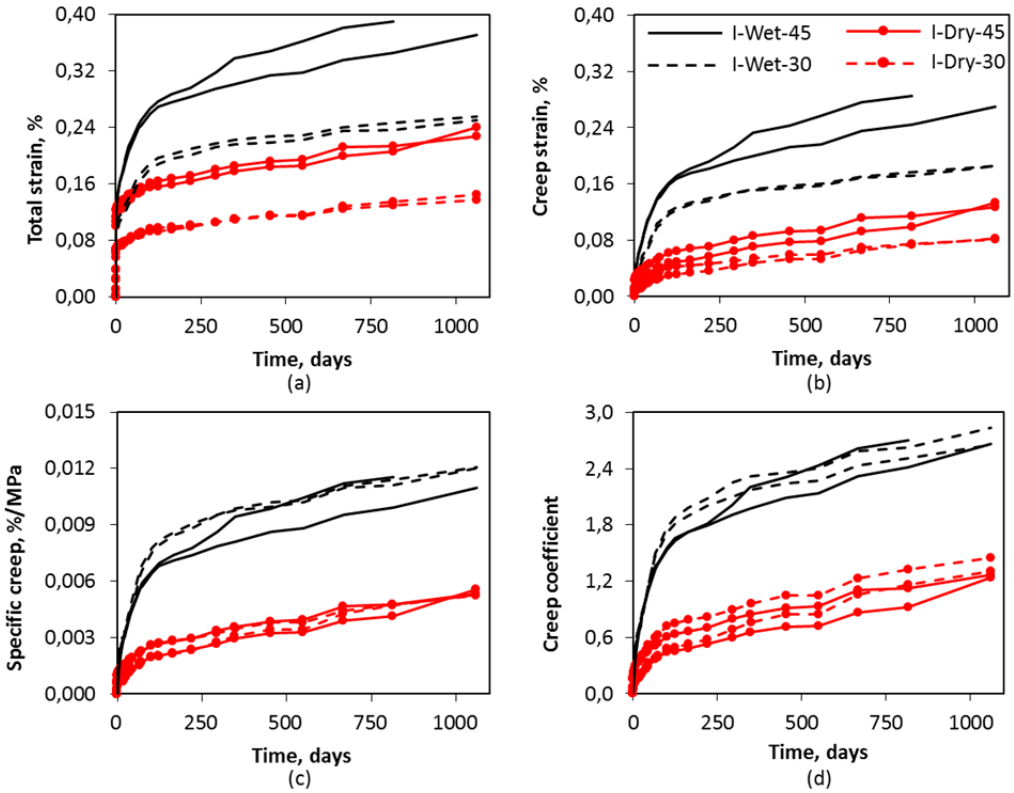


***Figure 2.11*** *Deformations under long term loading of first set of tests: (a) total deformations, (b) creep deformations, (c) specific creep and (b) creep coefficient*

The creep coefficient ($\varepsilon_c/\varepsilon_{el}$) is a significant parameter for structural design, especially for prestressed concrete elements. The creep coefficient of the wet ECC samples was 1.6 at 90 days (3 month) and 2.7 at 1060 days (3 years), while for the pre-dried ECC the creep coefficient was 0.5 and 1.2, respectively. For comparison, calculated creep coefficient for a concrete with similar strength class would be 1.5 at 90 days and 2.2 at 1060 days according to EC2 (EN1992-1-1 2010). It should be noted that shrinkage deformations were not measured, thus the creep deformations measured here may include some limited shrinkage contributions. Weight measurements before and after creep testing concluded the pre-dried samples lost on average 0.45% weight during creep testing, while the wet samples lost 1.0% on average in spite of the aluminum tape used to seal the samples.

*DTU Test Series*

The total deformations of all specimens, $\varepsilon_t$, under continuous compressive loading for three years are illustrated in Figure 2.12(a). The resulting creep deformations, $\varepsilon_c = \varepsilon_t - \varepsilon_{el}$, are illustrated in Figure 2.12(b). As expected, the highest creep deformations were observed in specimens that were subjected to higher load levels. No clear trends can be extracted from the specific creep and creep coefficient data shown in Figure 2.12(c) and (d) based on the applied load level or curing conditions. It is noted that the specific creep (Figure 2.12(c)) is slightly higher for the air cured samples.

The creep coefficients derived from the DTU test series were significantly lower than the creep coefficients observed in the RTU test series. This may be a result of different humidity and temperature conditions during testing and due to the different specimen sizes used in each tests series. An important parameter affecting creep is the ratio between the specimen volume and the surface area exposed to atmosphere (notional size, $h_0$, according to EC2, (EN1992-1-1 2010)):

$$h_0 = \frac{2A_c}{u} \tag{2-4}$$

Where, $A_c$ is the cross-sectional area and $u$ is a parameter of a member in contact with the atmosphere. The notional size of the specimens tested in the RTU test series were 25 and 30 mm while the DTU test series had a notional size of 50 mm.

Figure 2.13 provides the length change measurements for the ECC samples. During the first 7 days (i.e., when the samples were wet cured), limited shrinkage occurred. Upon exposure to the drying environment shrinkage occurred rapidly to -1096 με after 22 days (or 15 days of drying). Between 22 and 85 days, an additional 364 με of shrinkage occurred, for a total of 1460 με shrinkage at 85 days.

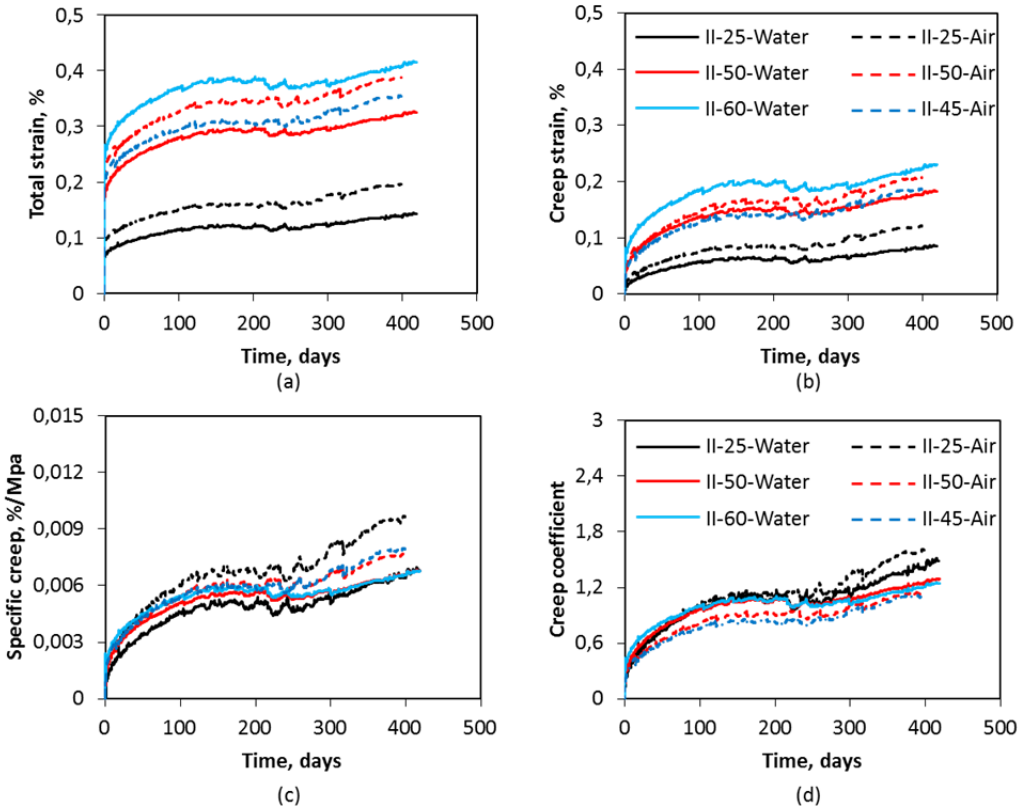


***Figure 2.12*** *Deformations under long term loading of second set of tests: (a) total deformations, (b) creep deformations, (c) specific creep and (b) creep coefficient*

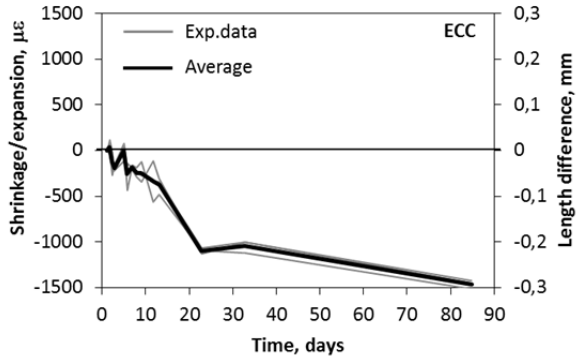


***Figure 2.13*** *Length change measurements of ECC*

## 2.4 Digital image correlation (DIC)

Digital image correlation (DIC) measurements were used extensively throughout the work presented in this thesis. The DIC system was used to measure surface deformations in a particular region of interest in various specimens. Deformations of selected specimens were verified by LVDTs, positioned on an opposite surface of the specimen.

A digital single-lens reflex camera (24 and 36 megapixel) with a macro lens (24, 60 or 105 mm) for two dimensional measurements were utilized to provide quantitative and qualitative information on the surface deformations of the specimen. Details of the measurement regions are illustrated in the figures below for each test separately. Digital images were recorded at specific time intervals, as described below for individual test methods. A commercially available DIC software called Aramis (GOM 2005) was used to process the images taken during the loading procedure, providing full field deformation measurements of the surface of the specimen, as shown in Figure 2.14.

The load state for each image is correlated by synchronizing time stamps from the load machine and the image file. To achieve adequate contrast in the gray-scale of individual objects, black and white spray paint was used to apply a stochastic pattern on the specimen surface.

The DIC system tracks movements of small areas (called facets) of the specimen surface corresponding to 15 by 15 pixel square areas; the step of the facets defined in the testing program was 13 pixels. For the most precise measurements, the optimal size of the gray-scale dots should be around 1/3 to 1/2 of a facets size. Additional details on the DIC technique and equipment are available elsewhere (GOM 2005; Pease et al. 2006).

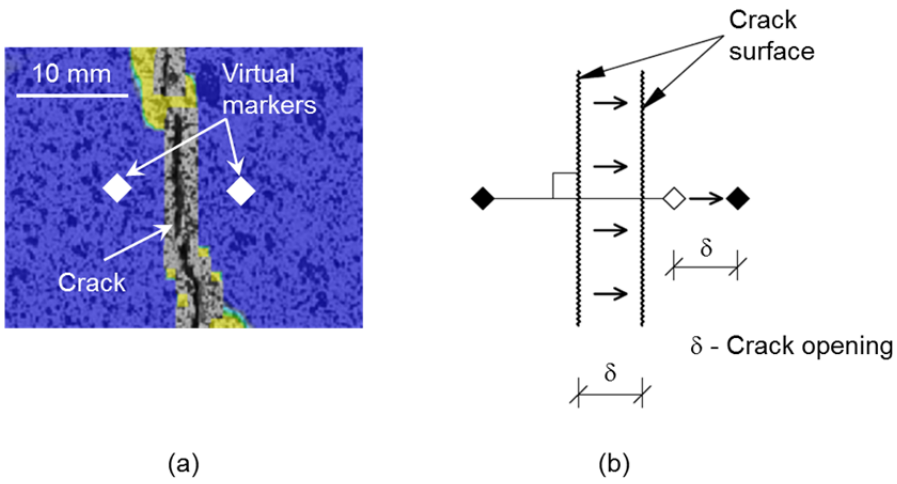


***Figure 2.14*** *Illustration of crack deformations: (a) illustration from DIC software; (b) schematic definition of opening*

## 2.5 Summary

This chapter provides details on the constituent materials, mixture proportions, and basic fresh and hardened properties for the steel fiber reinforced concrete (SFRC), polypropylene fiber reinforced concrete (PP-FRC) and Engineered Cementitious Composite (ECC) used in this thesis. Test procedures for the basic characterization of each material are described, obtained results are provided and the basic performance

of each material is compared. Basic details on the DIC technique, which is widely used throughout the Ph.D. work, are also provided.

Various tensile test methods have been performed on the FRC's to obtain cohesive relationships and tensile stress-strain responses. The results of the tensile tests show that the three types of FRC presented in this thesis have various tensile post-cracking responses. The maximum fiber bridging stress for ECC is higher than the first cracking strength, indicating a strain hardening post-cracking response is favored in direct tension. Tensile stress-strain results from ECC dogbone specimens verify the strain hardening post-cracking response. The first cracking strength of the PP-FRC and SFRC is higher than the maximum fiber bridging stress, indicating a tension softening post-cracking response is favored for the SFRC and PP-FRC.

Time-dependent deformations of ECC were measured through two series of creep studies and a shrinkage study. Although ECC-type materials have been investigated for the past couple of decades, relatively little information is available on these properties. As time-dependent deformation are important factors to consider in structural design, these studies were deemed to be within the scope of the thesis' objective to facilitate the development of structural applications of FRC's with hardening post-cracking responses. Depending on the specimen preparation, creep results for ECC compared well with calculated creep coefficients from Eurocode 2 (EN1992-1-1 2010). Shrinkage results indicate ECC has a significantly higher shrinkage than most concretes. A large portion of the shrinkage was found to occur rapidly after exposure to drying. During the first 15 days of drying over 1000 με of shrinkage occurred; however, with an additional 63 days of drying, only 364 με of additional shrinkage occurred. As the vast majority of shrinkage occurred in the first 15 days, the application of ECC for precast panels is optimal. Installation of the precast ECC elements would therefore be completed after the majority of the shrinkage has occurred.

# Chapter 3

# Overview and evaluation of standardized test methods to characterize FRC

There is a general need in structural engineering for standard methods to quickly, easily and reliably verify the material properties achieved in-situ comply with the parameters assumed in the design. The direct tensile measurement procedures, described in Section 2.3.2, may be difficult to implement in practice due to the relative difficulty of the specimen preparation and the sensitivity of the testing procedures. Several standard flexural test methods exist, based on beams and plates geometries, to indirectly assess the tensile properties of FRC. This chapter investigates the suitability of these standard methods for FRC materials with tension softening and hardening responses. Initially numerous currently available tests methods for FRC are summarized and critiqued. Selected test methods are used to assess the load-deformation and corresponding crack formation responses for the studied FRC materials. The usefulness of the obtained results, with respect to structural design, is evaluated and recommended alterations to current standard beam sizes and notch configuration are given.

## 3.1 Available performance evaluation methods for FRC

The descriptions of testing and mechanical characterization of fiber reinforced concrete (FRC) provided in *fib* Model Code 2010 (fib 2012) emphasizes the significance of defining suitable material parameters, including post-peak tensile behavior, for structural design. Dimensioning and verifying the load capacity of any structural element made with randomly distributed fibers, with or without additional

traditional reinforcement, requires the determination of equivalent elastic post-cracking strengths of the FRC material. Many of the available standard methods to derive the post-cracking response of FRC are summarized in Table 3.1. Three main categories of tests, characterized by different set-up and generated stress fields, are used to evaluate the post-cracking response:

- Uni-axial tension tests, with a prescribed single crack or possible multiple cracking;
- Flexural beam tests, performed on notched or un-notched prisms, under three or four-point loading;
- Flexural plate tests (square panel with continuous support or round panel with 3 point supports).

As presented in Table 3.1, uni-axial tension tests of FRC include the notched specimens (162-TDF 2001; Pereira et al. 2010) for measuring the tensile stress-crack opening properties of FRC and the un-notched dogbone specimens (JSCE 2008; Larusson et al. 2010; Paegle & Fischer 2013) that provides the tensile stress-strain properties for strain hardening FRC materials.

The most common tests to characterize FRC are three- and four-point bending beam tests, with and without notches. The notched three-point bending test is the standard suggested in the *fib* Model Code (fib 2012), the Swedish standard for FRC (SS812310 2014) and for various design methods described in a technical report by Concrete Society Working Group (TR63 2007). Various standards for notched three-point bending testing exist, including the European standard EN 14651 (EN14651 2007), RILEM Technical Committee guidelines (162-TDF 2002) as well as in the standard by the Japan Concrete Institute (JCI-S-002 2003). Similarly, several standards exist for four-point bending tests, including ASTM C1609 (ASTM-C1609/C1609M-12 2012), DAfStb (DAfStb 2010), DBV - Guide to Good Practice (DBV 2007) and the standard by the Japan Concrete Institute (JCI-S-003 2007).

ASTM C1609 and JCI-S-003-007 use beams where b=h=a (Figure 3.5), while DAfStb and DBV use specimens where a>b;h (b=h=150 mm, but a=L/3=200 mm). Some standards allow the use of various sized beams, which should be selected as a function of fiber length (ASTM C1609). Still other standards use a particular specimen geometry, but set limits to fiber type and properties used in the FRC (JCI-S-003-2007). Finally, a notched four-point bending test is described in the Italian guidelines for design, construction and production control of FRC structures (CNR-DT204 2007).

***Table 3.1*** *Overview of test methods to characterize FRC*

| Test method | Type and shape of specimen | Fiber and aggregate limitations | Test setup | Results |
|---|---|---|---|---|
| **Direct tension** | | | | |
| **RILEM TC 162-TDF**<br>**Uni-axial tension test for steel fiber reinforced concrete**<br>(162-TDF 2001) | Cylindrical specimen with nominal diameter and length of 150 mm, notched circumferentially with a depth of 15 ±1 mm and a width of 2-5 mm. | Maximum size aggregate: 32 mm<br><br>Maximum fiber length: 60 mm | 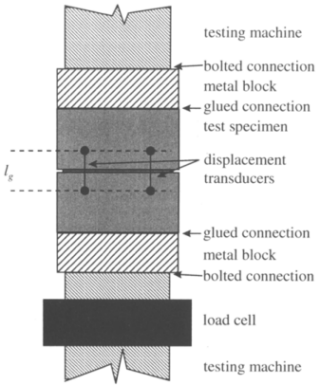 <br>Specimen glued to metal plates, connected to the testing machine using rigid connections.<br>Displacement rates are: 5 μm/min up to a displacement of 0.1 mm and 100 μm/min until the completion of the test (when a displacement of 2 mm is reached) | Stress-deformation curve<br> 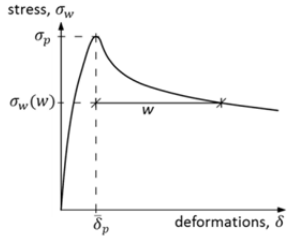 <br>Stress: $\sigma_w = \frac{P}{A_n}$<br>Crack opening: $w = \overline{\delta} - \overline{\delta}_p$<br>where: $\overline{\delta} = \frac{1}{n}\sum_{j=1}^{n} \delta_j$<br>$\delta_j$ - displacement of each LVDTs |

| Test method | Type and shape of specimen | Fiber and aggregate limitations | Test setup | Results |
|---|---|---|---|---|
| **Single crack notched coupon test*** Tensile test: stress-crack opening<br><br>(Pereira et al. 2012) | Specimens with 120 mm length, 50 mm width and 12-16 mm thickness. Notched on all sides with 0.5 mm thick notch. | Specimen designed for materials with small maximum aggregate size (0.18 mm) and fibers with a low flexural stiffness (PVA, PP and PAN) | 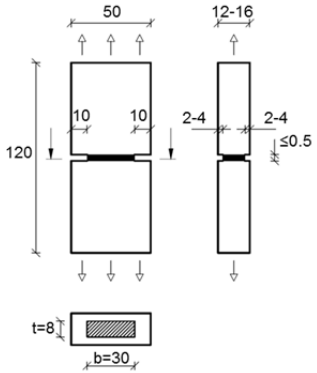 <br>Deformations are applied to the specimen through hydraulic grips, providing fixed support at both ends of the specimen. Loading rate - 0.3 mm/min | Load-crack opening curve (cohesive relationship)<br> 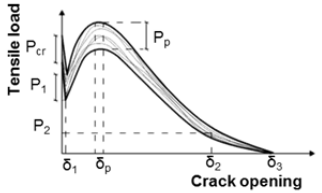 <br>Cracking, post-cracking and peak load (P), tensile stress (σ), and corresponding crack opening $\sigma_i = \frac{P_i}{bt}$ |
| **Single crack notched coupon test of SFRC*** Tensile test: stress-strain | Notched prism specimen with sizes of 150 mm x 150 mm x 150 mm. | Fiber length $l_f \leq 50$ mm Test method for SFRC | 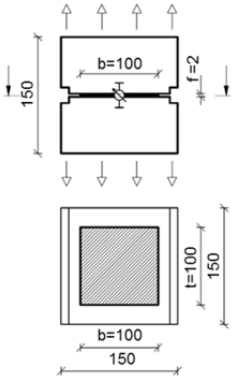 <br>Deformations applied to the specimen steel frame. Loading rate - Cross-head displacement controlled with 0.05 mm/min rate up to 2 mm crosshead displacement, then 0.5 mm/min | Load-crack opening curve (cohesive relationship)<br> 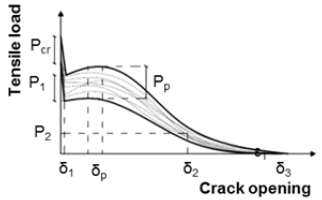 <br>Cracking, post-cracking and peak load (P), tensile stress (σ), and corresponding crack opening $\sigma_i = \frac{P_i}{bt}$ |

| Test method | Type and shape of specimen | Fiber and aggregate limitations | Test setup | Results |
|---|---|---|---|---|
| **JSCE Dogbone test** Tensile stress-strain (JSCE 2008) | Dogbone specimen with length of 330 mm and thickness of 13 or 30 mm. Representative cross section: *l*= 80 mm, *w*= 30 mm, *t*=13 or 30 mm | Minimum specimen thickness (t): t ≥ fiber length t ≥ 2 x maximum size aggregate. Intended for FRC with hardening post-cracking response | Vertical alignment between chucks. 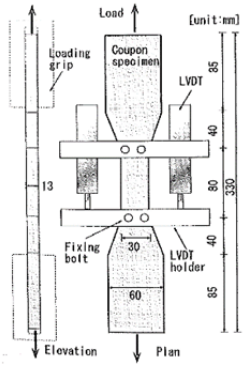  Fixed support on one end and pin support on the other. Constant deformation rate: 0.5 mm/min. LVDTs should have a precision of 1/1000 mm or higher. | Stress-strain curve 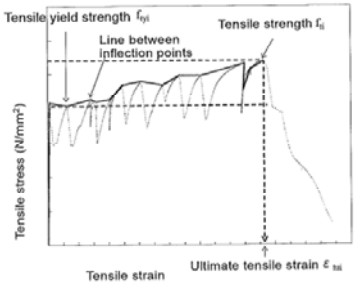  Tensile yield strength; maximum stress in the strain hardening region; tensile strength and ultimate tensile strain |
| **Tensile dogbone test*** Tensile test: stress-strain (Larusson et al. 2010; Paegle & Fischer 2013) | Representative cross section of 22 mm × 50 mm and with a representative length of 210 mm | Maximum size aggregate of 0.18 mm and fibers with a low flexural stiffness (PVA, PP and PAN) Intended for FRC with hardening post-cracking response | 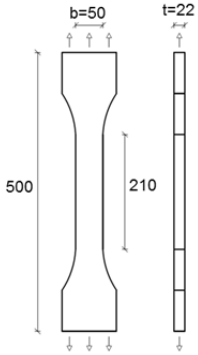  Deformations applied to the specimen through hydraulic grips providing fixed support at both ends of the specimen. Loading rate - 0.5 mm/min | Stress-strain curve 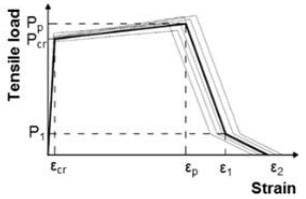  Cracking and peak load (P), tensile stress (σ), and corresponding tensile strain $\sigma_i = \frac{P_i}{bt}$ Ultimate strain |

| Test method | Type and shape of specimen | Fiber and aggregate limitations | Test setup | Results |
|---|---|---|---|---|
| **Wedge splitting test** | | | | |
| **Wedge splitting test** (NT-Build511 2005) | Cube specimens with size depending on the maximum fiber length or maximum size aggregate.<br><br>Notch ≤ 5mm wide | Dimensions of the specimen should be at least 3.5 times larger than the maximum fiber length | 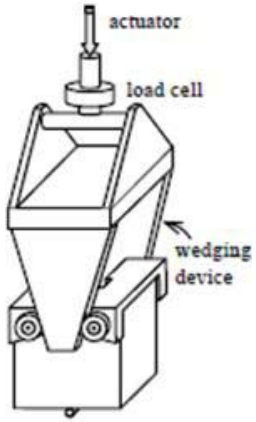 The specimen is placed on a linear support; two loading devices equipped with roller on each side are placed on the top and two wedges are pressed between the rollers. CMOD increases at a constant rate of 25 to 50 µm/min for CMOD between 0 to 0.2 mm and of 0.25 mm/min between 0.2 and 2 mm. When CMOD is larger than 2 mm, the rate may be increased to 0.5 mm/min. | Load-CMOD curve<br> 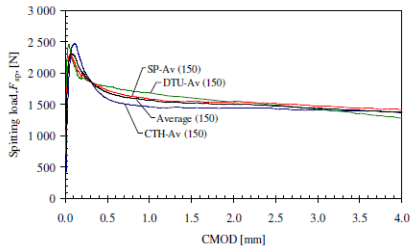 <br>Splitting force (approximation):<br>$F_{sp} = \frac{F_V}{2\tan(\alpha)}$<br>Specific fracture energy: $G_{f,CMOD} = \frac{W_{f,CMOD}}{A_{lig}}$<br>where:<br>$W_{f,CMOD}$ – area under load-CMOD curve<br>$A_{lig}$ – area of the ligament |

| Test method | Type and shape of specimen | Fiber and aggregate limitations | Test setup | Results |
|---|---|---|---|---|
| **Beam geometry: Three-point bending** | | | | |
| **EN 14651 – 2005*** (EN14651 2007) | Notched beam<br>w = d = 150 mm<br>550 mm ≤ s ≤ 700 mm,<br>$w_{notch}$ ≤ 5 mm,<br>$h_{sp}$ = 125 ±1 mm | Maximum size aggregate of 32 mm<br><br>Maximum fiber length of 60mm | 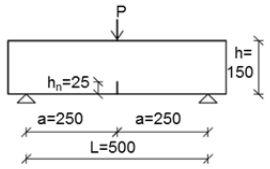 <br>Specimen rotated 90° from cast orientation before notching.<br>Test after 28 days | Load CMOD curve<br> 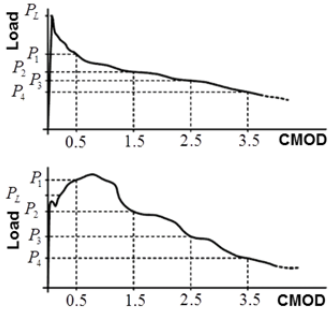 <br>Limit of proportionality (LOP):<br>$f_{ct,L}^{f} = \frac{3P_L L}{2bh_{sp}^2}$<br>*Where* $P_L$ *=max P wi*thin 0 ≤ *CMOD* ≤ 0.05 mm<br>Residual flexural tensile strength:<br>$f_{R,j} = \frac{3P_j L}{2b(h-h_n)^2}$ $j = 1,2,3,4$<br>at *CMOD* = {0.5, 1.5, 2.5, 3.5} |

| Test method | Type and shape of specimen | Fiber and aggregate limitations | Test setup | Results |
|---|---|---|---|---|
| **RILEM TC 162-TDF-2002** (162-TDF 2002) | Identical to EN 14651 | Identical to EN 14651 | Identical to EN 14651 | Load-CMOD curve 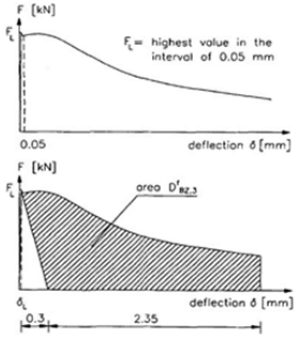  Limit of proportionality (LOP): $f_{ct,L} = \frac{3F_L L}{2bh_{sp}^2}$ Energy absorption capacity $D^f_{BZ,i}$ (area under the curve) Equivalent flexural tensile strengths: $f_{eq,2} = \frac{3}{2}\left(\frac{D^f_{BZ,2}}{0.50}\right)\frac{L}{bh_{sp}^2}$ $f_{eq,3} = \frac{3}{2}\left(\frac{D^f_{BZ,2}}{2.50}\right)\frac{L}{bh_{sp}^2}$ Residual flexural tensile strengths: $f_{R,j} = \frac{3F_j L}{2b(h-h_n)^2}$ $j = 1,2,3,4$ at $CMOD = \{0.5,\ 1.5,\ 2.5,\ 3.5\}$ |

| Test method | Type and shape of specimen | Fiber and aggregate limitations | Test setup | Results |
|---|---|---|---|---|
| ***fib* Model Code 2010** (fib 2012) | Identical to EN 14651 | Identical to EN 14651 | Identical to EN 14651 | Load-CMOD curve 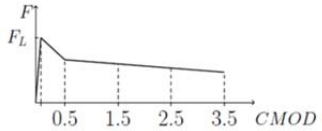  Limit of proportionality (LOP): $f_{ct,L} = \frac{3F_L L}{2bh_{sp}^2}$ Residual flexural tensile strengths: $f_{R,j} = \frac{3F_j L}{2b(h-h_n)^2} \qquad j = 1,2,3,4$ at $CMOD = \{0.5,\ 1.5,\ 2.5,\ 3.5\}$ Classification from ratio of characteristic residual strengths: $\frac{f_{R3k}}{f_{R1k}}$ $f_{R1k}$ - serviceability $f_{R3k}$ - ultimate |

| Test method | Type and shape of specimen | Fiber and aggregate limitations | Test setup | Results |
|---|---|---|---|---|
| **JCI-S-002-2003** (JCI-S-002 2003) | Notched beam, $w$ and $d \geq 4 \cdot d_a$, $s \geq 3.5d$, notch depth $a_0 = 0.3d$, notch width $n_0 \leq 5$ mm, $h_{sp} = 0.7 \cdot d$, according to JCI-SF2 | Minimum fiber content of 0.3% by volume<br><br>Maximum size aggregate $d_a \leq 0.5 l_{fiber}$ | 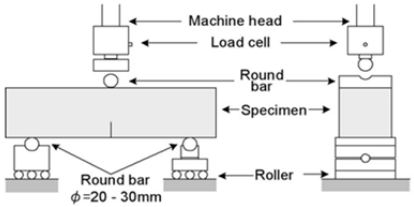 <br>Three-point bending test, span length min. $L = 3 \cdot d$, rotated 90° from cast orientation<br><br>Accuracy of min 1/500 or better, rate in terms of CMOD 0.0005$d$ to 0.004$d$/min or LPD 0.0004$d$ to 0.003$d$/min, loading until min CMOD= 0.02$d$ or LPD= 0.015$d$ | Load-CMOD curve<br> 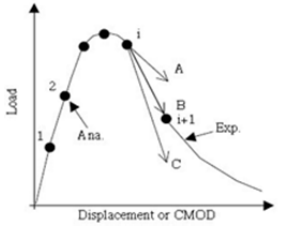 <br>Poly-linear inverse analysis<br>Cohesive stress-crack opening<br> 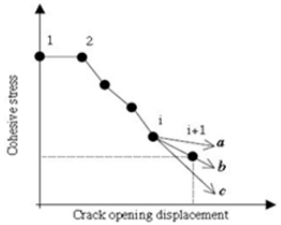 |

| Test method | Type and shape of specimen | Fiber and aggregate limitations | Test setup | Results |
|---|---|---|---|---|
| **Beam geometry: Four-point bending** | | | | |
| **CNR-DT 204/2006, Italian Recommendation** (CNR-DT204 2007) | Notched beam, 600 mm x 150 mm 150 mm, test as UNI 11039 | Minimum fiber content 0.3% by volume<br><br>Maximum size aggregate $d_a \leq 0.5 l_{fiber}$ | 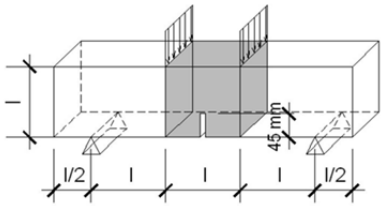 <br>Four-point bending test, span length $L$ = 450 mm,<br>$h_{sp}/L$ = 105 mm/450 mm = 0.233<br><br>Constant rate of 0.05 ±0.01 mm/min until 0.65 mm CMOD, after increase rate to 0.5 ±0.02 mm | Load- crack opening curve<br> 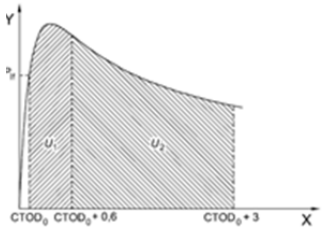 <br>Nominal strength-crack opening curve<br> 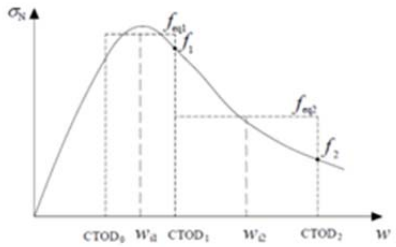 <br>Strengths at point values: $\sigma_N = \frac{6PL}{bh_{sp}^2}$<br><br>Or as mean values: $f_{eq1} = \frac{l}{b(h-a_0)^2} \cdot \frac{U_1}{0.6}$<br><br>$f_{eq2} = \frac{l}{b(h-a_0)^2} \cdot \frac{U_2}{2.4}$<br><br>where $U_1$ and $U_2$ are the areas under the load-CTOD curve |

| Test method | Type and shape of specimen | Fiber and aggregate limitations | Test setup | Results |
|---|---|---|---|---|
| **ASTM C1609/C1609M – 2010*** (ASTM-C1609 2012) | Beam specimen<br>No notch<br>$s \geq 3d + 50$ mm$\geq$ 350 mm,<br>$s \leq 2d + L$<br>$w = d \geq 3\ l_{fiber}$<br>$w = d = 150$ mm may be used if $l_{fiber}$ = 50 to 75 mm | Aggregate as C31/C31M or C42/C42M, $l_{fiber} \leq 1/3d$ | 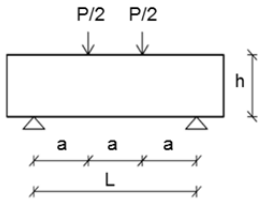 <br>Four-point bending test, span length $L = 3d \geq 300$ mm, rotated 90° from cast orientation, $h/L = d/3d = 0.33$ | 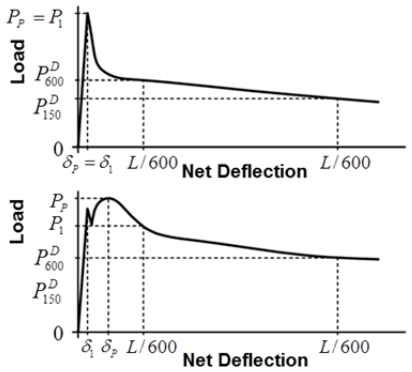 <br>First-peak and peak load (P), strength (f), and corresponding deflections<br>Residual load (P) and strength (f) at deflections of L/600 and L/150<br>$f_i = \frac{P_i L}{bd^2}$<br>Toughness (T) and equivalent flexural strength ratio (R) at deflection of L/150<br>$R^D_{T,150} = \frac{150 T^D_{150} L}{f_1 bd^2} \cdot 100\%$ |

| Test method | Type and shape of specimen | Fiber and aggregate limitations | Test setup | Results |
|---|---|---|---|---|
| **DAfStb-Richtlinie – 2010** (DAfStb 2010) | Beam specimen<br>No notch<br>$w = d = 150$ mm<br>$s = 700$ mm<br>Dimensions complying with DIN EN 12390-1, preparation with DIN EN 12390-2 | Maximum size aggregate - 16 mm for round aggregate, 22 mm for others,<br>fiber length, $l_{fiber} \geq 1.5 \cdot d_{aggregate}$ | 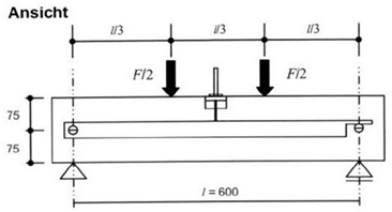 <br>Four-point bending test, span length $L$ = 600 mm, after 28 days,<br>$h/L$ = 150 mm/600 mm = 0.25<br><br>Controlled by central deflection, 0.10 mm/min until δ = 0.75 mm after a rate up to 0.30 mm/min is allowed. Deflection up to 3.5 mm, measuring points for each 0.01 mm | Load-deflection curve<br> 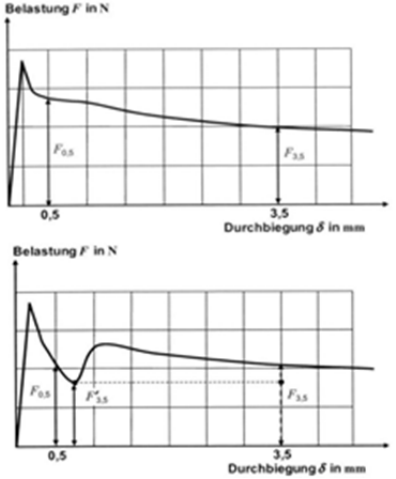 <br>Mean flexural tensile strength:<br>$f^f_{cflm,L1} = \frac{1}{n}\sum_{i=1}^{n}\frac{F_{0.5,i}l}{b_i h_i^2}$<br>$f^f_{cflm,L2} = \frac{1}{n}\sum_{i=1}^{n}\frac{F_{3.5,i}l}{b_i h_i^2}$<br>Characteristic flexural strength:<br>$f^f_{cflk,Li} = e^{\left(Lf^f_{cflm,L1} - k_s l_s\right)} \leq 0.51 f^f_{cflm,L1}$ |

| Test method | Type and shape of specimen | Fiber and aggregate limitations | Test setup | Results |
|---|---|---|---|---|
| **DBV - Guide to Good Practice - 2001** (DBV 2007) | Beam specimen No notch $w = d = 150$ mm, $s = 700$ mm, complying with DIN 1048 Part 1. | Aggregate after DIN 4226 [R10] Fibers approved by DIBt | 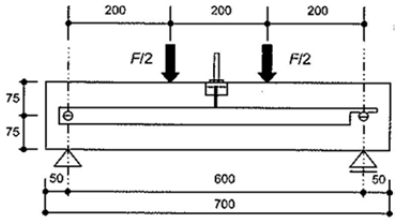 <br>Four-point bending test, span length $L = 600$ mm, rotated 90° from cast orientation, $h/L = 150$ mm/600 mm = 0.25<br><br>Piston travel should amount 0.2 mm/min, measuring deflection up to 3.5 mm | Load-deflection curve<br> 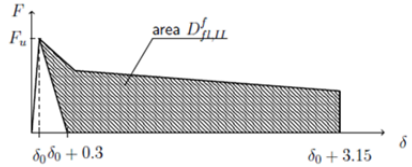 <br>Flexural tensile strength: $f^f_{ct,fl} = \frac{F_u L}{b h^2_{sp}}$<br>Equivalent flexural tensile strength:<br>$f_{eq,I} = \frac{D^f_{fl,I}}{0.5} \cdot \frac{L}{bh^2}$<br>where $D^f_{fl,i}$ is the contribution of fibers on energy absorbability<br>Mean flexural strength:<br>$f_{eqm,i} = f_{eqms,i} - \frac{s_{s,i} t_{10,(n-1)}}{\sqrt{n}}$<br>$s_{s,i} = \sqrt{\frac{\sum (f_{eqms,i} - f_{eq,i})^2}{(n-1)}}$<br>Equivalent tensile strength:<br>$f_{eq,ctm,I} = 0.45 f_{eqm,I}$<br>$f_{eq,ctm,II} = 0.37 f_{eqm,II}$ |

| Test method | Type and shape of specimen | Fiber and aggregate limitations | Test setup | Results |
|---|---|---|---|---|
| **JCI-S-003-2007** (JCI-S-003 2007) | Beam specimen<br>No notch<br>$w = d = 100$ mm, $s = 400$ mm<br>Made in accordance with JCI A 1132, tested in accordance with JIS A 1106 | Fiber length, $l_{fiber} \leq$ 40 mm | 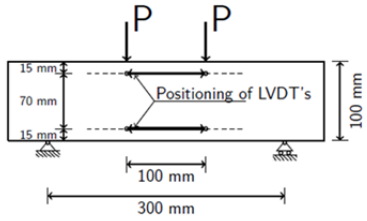 <br>Four-point bending test, span length $L$ = 300 mm, beam rotated 90° from cast orientation, $h/L$ = 100 mm/300 mm = 0.33<br>Controlled by deflection, LVDT's measuring at distance 15 mm and 85 mm from lower surface, constant rate of 0.3 ± 0.2 mm/min in terms of machine head speed, minimum 0.2 Hz | Stress-strain and moment-curvature<br> 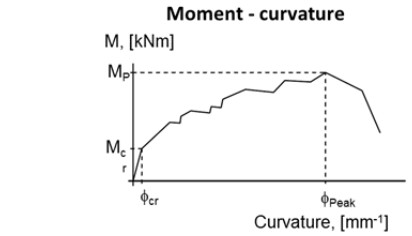 <br> 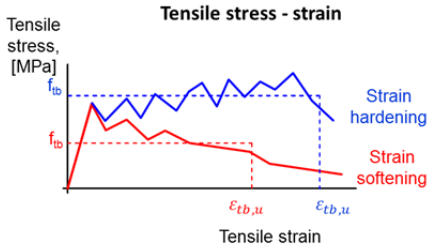 <br>Curvature:<br>Ultimate tensile strain:<br>$\varepsilon_{tu,b} = \phi_u \cdot D \cdot (1 - x_{n1})$<br>Ultimate compressive strain:<br>$\varepsilon_c = \phi_u \cdot D \cdot x_{n1}$<br>Tensile strength: $f_{t,b} = \frac{E \cdot \phi_u \cdot D \cdot x_{n1}^2}{2 \cdot (1 - x_{n1})}$ |

| Test method | Type and shape of specimen | Fiber and aggregate limitations | Test setup | Results |
|---|---|---|---|---|
| **Panel geometry** | | | | |
| **Dramix guidelines** | 600 mm square by 100 mm thick specimen, notch with depth of 10 mm and thickness of 2 mm. | Steel fiber reinforced shotcrete | 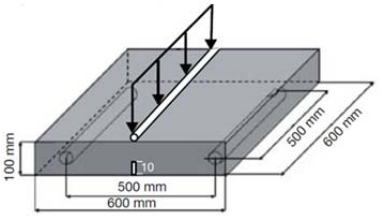 Three-point bending test, distance between the supports: 500 mm. The rough surface is the upper side.<br><br>A movement sensor bridges the notch in its centre. The test is carried out at an imposed crack opening rate. | Load-crack opening curve<br> 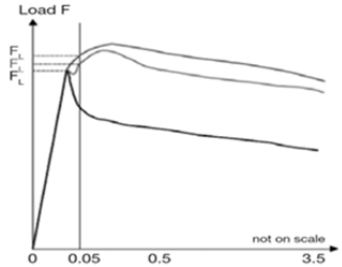 <br>Limit of proportionality (LOP):<br>$f_{ct,L}^{f} = \frac{3F_L L}{2bh_{sp}^2}$<br>*Where* $F_L$ *=max F wi*thin $0 \le CMOD \le$ 0.05 mm<br>Residual flexural tensile strength:<br>$f_{R,j} = \frac{3F_j L}{2b(h-h_n)^2}$ $j = 1,2,3,4$<br>at $CMOD = \{0.5; 1.5; 2.5; 3.5\}$ |
| **ASTM C1550 – 2010* Round Determinate Panel** (ASTM-C1550 2012) | Round Panel, $D$ = 800 mm, $d$ = 75 mm, prepared as mode of placement *in situ*, supported on 3 symmetrically placed pivots | Type of specimen: cast FRC or shotcrete<br>Aggregate for sprayed concrete approximately 10 mm, but no restrictions, have to take the effects into account. | 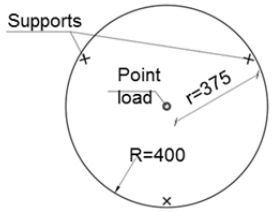 Measuring central deflection of panel, Increment < 0.05 mm, use at least 800 data points up to $\delta$ = 40 mm, hereafter 0.20 mm increments. | Load-deflection curve<br> 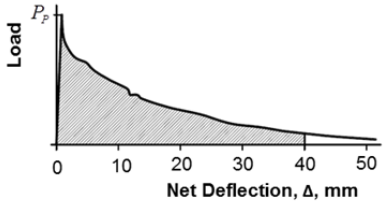 <br>Toughness ordinarily defined from net deflection of 5, 10, 20 or 40 mm. |

| Test method | Type and shape of specimen | Fiber and aggregate limitations | Test setup | Results |
|---|---|---|---|---|
| **EN 14488-5** (EN14488-5 2006) | Square specimen produced from a panel, sprayed and cured in a mold, with dimensions of 600 mm x 600 mm and trimmed to a thickness of 100 mm | Shotcrete | 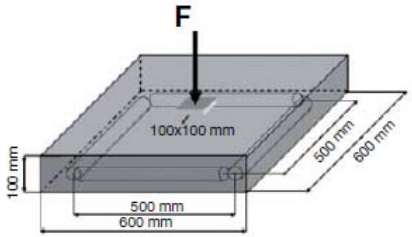 Rigid steel square loading block (100x100 mm, 20 mm thick) positioned at the centre of the upper face and a frame with a rigid square support (500 x 500 mm, 20 mm thick). Displacement controlled at a constant rate of (1 ± 0,1) mm/min at the centre of the slab, up to 30 mm of central deflection. | Load-deflection and energy-deflection curves 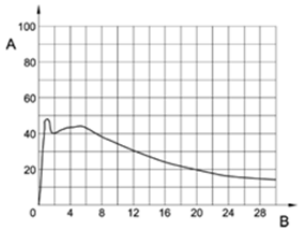 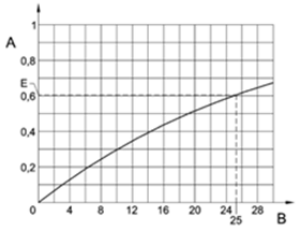 From the load-deflection curve the energy diagram Energy absorption capacity - area under the load-deflection curve between 0 and 25 mm deflection. |

* - Test methods used as part of the experimental program presented in this thesis

Flexural plate tests are also common test method, especially for sprayed FRC. The two most commonly used plate tests are ASTM C1550 (ASTM-C1550 2012) which is a round panel with 3 point supports and EN 14488-5 (EN14488-5 2006) which has a geometry of square panel with continuous support.

The objective of this chapter is to investigate the suitability of the main test categories described above to accurately characterize FRC materials in tension. The ability to characterize tension softening and hardening materials was considered. Furthermore, the usefulness, with respect to structural design, of the obtained results from the test categories is evaluated.

## 3.2 Selected test methods to characterize FRC

To evaluate advantages, disadvantages and specific features of each selected test method, experimental tests on three studied FRC materials were conducted. The selected test methods are marked with * in the first column in Table 3.1. Direct tensile testing methods and results are described in Section 2.3.2. From the flexural beam tests, two of the most common standard test methods are selected, the notched three point bending test according to EN 14651 and a four-point bending test according to ASTM C1609. In addition, the Round Determinate Panel (RDP) flexural plate test according to ASTM C1550 was performed. Variations of the ASTM C 1609 beam and ASTM C 1550 round panel geometries were also studied to assess the influence of specimen size and slenderness on the resulting material characterization.

The consistency and reliability of the test results were evaluated in terms of scatter of the test results, stress disturbance (compared to the classical stress filed according to beam theory) due to concentrated load and presence of the notch, influence of fiber orientation, fiber type, fiber properties and specimen size.

The materials used are described in detail in Chapter 2. The three types of materials used in this investigation were a steel fiber reinforced concrete (SFRC) and a polypropylene fiber reinforced concrete (PP-FRC) with a softening behavior in tension and a representative strain hardening material known as Engineered Cementitious Composite (ECC). In addition to the standard test methods, a DIC technique (See Section 2.4) was used in the experimental program to continuously measure specimen deformations and to detect and quantify the crack formation process. The test methods are divided into three categories, including 1) uniaxial tensile tests, 2) flexural beam tests, and 3) flexural plate tests. Table 3.2 shows an overview of flexural tests investigated in this thesis.

***Table 3.2*** *Overview of flexural tests investigated in this chapter*

| | ECC | PP-FRC | SFRC |
|---|---|---|---|
| ***Three-point bending beams*** | | | |
| According to EN-14651 | x | x | x |
| Reduced size | x | - | - |
| ***Four-point bending beams*** | | | |
| According to ASTM C1609 | x | x | x |
| Reduced size | x | - | - |
| ***Round determinate panel*** | | | |
| According to ASTM C1550 | x | - | x |
| Reduced size | x | - | - |

## 3.2.1 Direct tension

The material properties in uni-axial compression and tension are presented in Sections 2.3.1 and 2.3.2, respectively.

## 3.2.2 Flexural beam tests

Flexural beam tests are most commonly used standard test methods to determine residual post-cracking strength of FRC. However, standard test methods differ by loading configuration (three- and four-point bending), notch configuration and specimen geometry. Therefore, the suitability of two commonly used standard flexural beam test methods (ASTM 1609 and EN 14651) are compared and analyzed.

### 3.2.2.1 Notched three-point bending beam

For this study, three-point bending tests for ECC, PP-FRC and SFRC materials were conducted according to EN 14651. Moreover, for ECC, an additional geometry was selected to investigate any possible size effect. In doing so, the geometry for the standard bending test for mortar (EN196-1 2005) was adopted (40 x 40 x 160 mm). The geometry of the specimens is shown in Figure 3.1 and the size and the material of the beams are listed in Table 3.3.

Deformation controlled tests were performed with a loading rate of 0.05 mm/min up to a net deflection of 1.2 mm; beyond this point the loading rate was increased to 0.2 mm/min. The crack mouth opening displacement (CMOD) was measured using a clip gauge and mid-span deflections using LVDTs. The load and deflection measurements were captured with a frequency of 10 Hz. DIC measurements were taken from one surface of the specimen at 4 second intervals.

***Table 3.3*** *Properties of beam specimens*

| Name | Material | Test type | # | L mm | a mm | h mm | b mm | $h_n$ mm | Weight kg | a/h* |
|---|---|---|---|---|---|---|---|---|---|---|
| Three-point bending beams | | | | | | | | | | |
| 3P-ECC-40 | ECC | 3PB | 2 | 160 | 60 | 40 | 40 | 8 | 0.5 | 3/2 |
| 3P-ECC-150 | ECC | 3PB | 5 | 500 | 250 | 150 | 150 | 25 | 26.2 | 5/3 |
| 3P-PP-FRC-150 | PP-FRC | 3PB | 5 | 500 | 250 | 150 | 150 | 25 | 26.2 | 5/3 |
| 3P-SFRC-150 | SFRC | 3PB | 3 | 500 | 250 | 150 | 150 | 25 | 32.8 | 5/3 |
| Four-point bending beams | | | | | | | | | | |
| 4P-ECC-50 | ECC | 4PB | 3 | 450 | 150 | 50 | 150 | - | 8.7 | 3 |
| 4P-ECC-75 | ECC | 4PB | 3 | 450 | 150 | 75 | 150 | - | 10.5 | 2 |
| 4P-ECC-150 | ECC | 4PB | 5 | 450 | 150 | 150 | 150 | - | 26.2 | 1 |
| 4P-PP-FRC-150 | PP-FRC | 4PB | 4 | 450 | 150 | 150 | 150 | - | 26.2 | 1 |
| 4P-SFRC-150 | SFRC | 4PB | 6 | 450 | 150 | 150 | 150 | - | 32.8 | 1 |

* a/h - slenderness

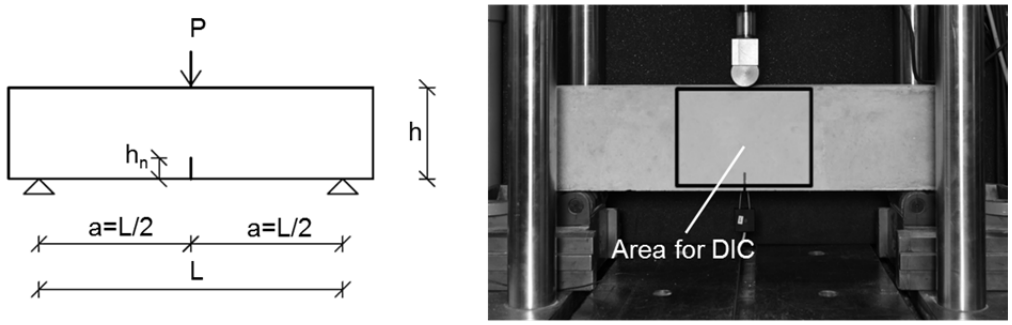


***Figure 3.1*** *Notched three-point bending beam setup: (a) specimen geometry; (b) test setup with measuring devices*

***Results – Notched three-point bending beams***

Figure 3.2(a-d) presents load versus CMOD curves for ECC, PP-FRC and SFRC beams with various dimensions. The secondary vertical axis of these diagrams provides the residual flexural stress calculated as material would be in elastic stage (called also as equivalent elastic flexural stress), $\sigma_{eq,el}$, which was derived using the following relationship:

$$\sigma_{eq,el} = \frac{3PL}{2b(h-h_n)^2} \tag{3.1}$$

where:

P – applied load;

L –beam span;

b – beam width;

h – beam height;

$h_n$ – notch depth.

Moreover, average residual flexural tensile strength values ($f_{R,j}$ $(j = 1 \dots 4)$), determined according to EN 14651 (EN14651 2007) at CMOD of 0.5 mm, 1.5 mm, 2.5 mm and 3.5 mm, respectively, and the residual flexural tensile strength at peak load ($f_{peak}$) are shown for all tested samples in Figure 3.2.

The residual tensile stresses are defined as follows:

$$f_{R,j} = \frac{3P_j l}{2bh_{sp}^2} \tag{3.2}$$

Where:

$f_{R,j}$ is the is the residual flexural tensile strength corresponding to CMOD=$CMOD_j$;

$P_j$ - load corresponding to $CMOD_j$ (see Figure 3.2);

$h_{sp}$ - distance between the notch tip and the top of the specimen ($h_{sp} = h - h_n = 125\ mm$).

Figure 3.2(a) and (b) illustrates results for ECC beams with 150 mm and 40 mm heights, respectively. Independent of the specimen dimension, the ECC material is found to have a deflection hardening response with average peak loads approximately 2 times larger than first cracking load. Comparing the results obtained from the standard beam height and the 40 mm beam height, the maximum residual strength measured in the 3P-ECC-40 beams is 12.2 MPa, or 1.5 times greater than the standard sized beam (3P-ECC-150, 8.0 MPa).

Figure 3.2(c) illustrates results for PP-FRC beams, all beams presented a deflection hardening response under three-point bending with average peak strength of 6.2 MPa. Figure 3.2(d) shows two of the three tested SFRC beams, which experienced a deflection softening behavior with a first cracking load slightly higher (~6%) than the second peak due to fiber bridging action. The remaining sample on the contrary showed a deflection hardening response with the second peak approximately 8% higher than the first peak. On average, the SFRC investigated had approximately a constant (approaching plastic) response, which was neither strictly hardening nor strictly softening in the observed range of CMOD.

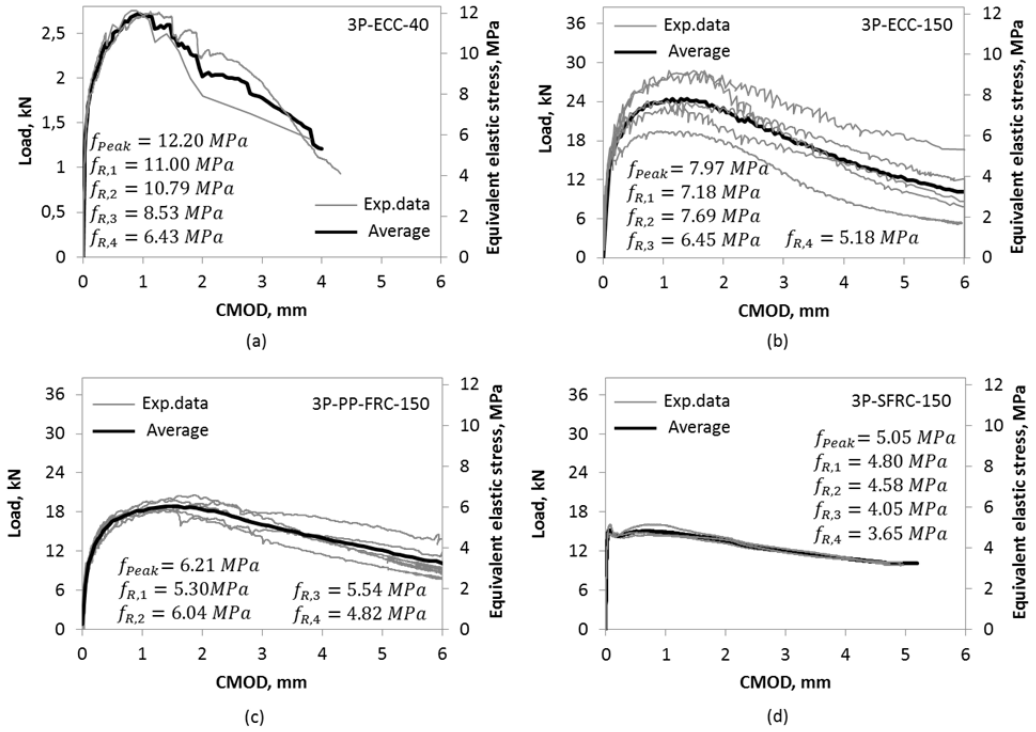


***Figure 3.2*** *Load-CMOD relationships of three-point bending beams: (a) 3P-ECC-40; (b) 3P-ECC-150; and (c) 3P-PP-FRC-150; and (d) 3P-SFRC-150*

Figure 3.3 reports the average equivalent elastic stresses versus normalized CMOD (normalized to the CMOD at peak load) for the ECC beams. The shapes of the curves for both ECC beams are similar, including the descending branch; however, the 3P-ECC-40 beams transferred higher equivalent elastic stress at all CMOD values. The higher stresses in smaller beams can be attributed to the following:

- Size effect in tension;
- An increased impact of the wall effect, causing preferential orientation of fibers in the smaller specimens; and
- The higher strain gradient experienced by shallower elements for the same top or bottom strain, which leads to a higher sectional redistribution of stresses.

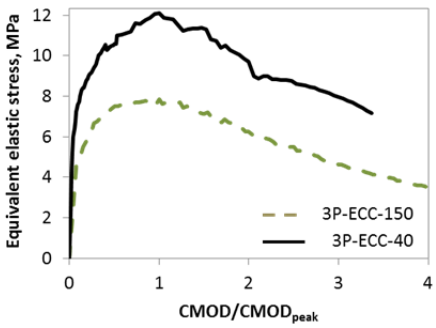


***Figure 3.3*** *Three-point bending beams: comparison between 3P-ECC-40 and 3P-ECC-150*

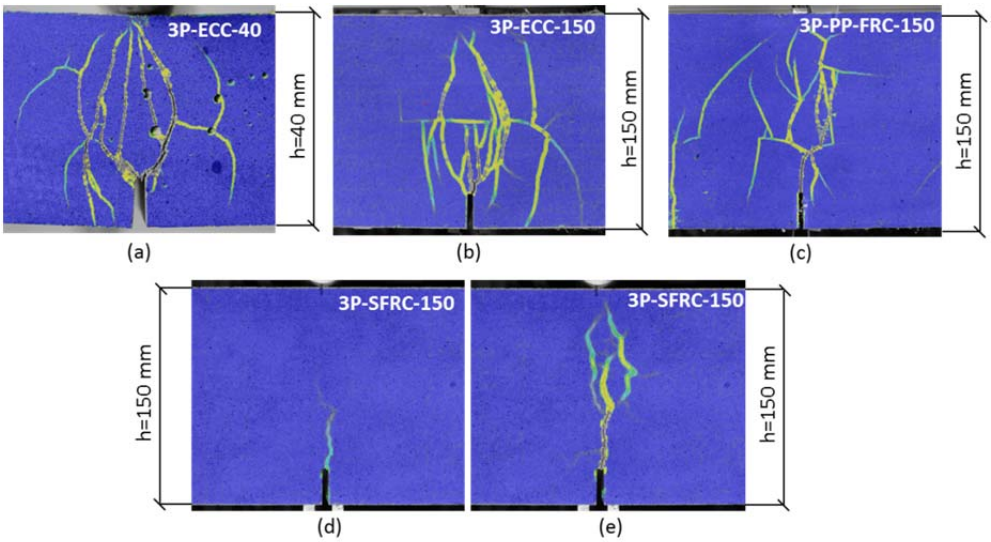


***Figure 3.4*** *Crack distribution of FRC beams under three-point bending: a) 3P-ECC-40 at peak, b) 3P-ECC-150 at peak, c) 3P-PP-FRC-150 at peak, d) 3P-SFRC-150 at peak and e) 3P-SFRC-150 at CMOD of 1 mm*

Figure 3.4(a) and (b) show typical crack patterns for the ECC beams at peak load from DIC measurements. The images indicate that multiple cracking occurs in ECC prior to reaching the peak load, regardless of beam dimension and cross-sectional reduction at the notch (i.e., point of maximum moment). Similar crack pattern at a peak load has been noticed also for PP-FRC beams (Figure 3.4(c)). Cracking can be observed on both sides of the notch, indicating that notch opening comprises only a portion of the beam deformations. Therefore, not all deformations are captured by a CMOD gauge located at the notch, which is the specified setup in the standard. Further, as multiple cracks form, CMOD measurements do not capture a true single crack opening response, which is important for service limit state design.

Peak load in the SFRC beams typically resulted in a single crack at the notch location (Figure 3.4(d)). Additional post-peak load crack mouth opening resulted in the development of additional cracks, as shown in Figure 3.4(e). While the load-CMOD response for SFRC (Figure 3.2(d)) indicated the investigated SFRC was not clearly a deflection hardening material, a multiple cracking response was observed right after the peak load was reached (Figure 3.4(e)). Therefore, for materials herein considered (ECC, PP-FRC and SFRC), three-point bending testing of a notched beam, where only load and CMOD are measured, does not provide a comprehensive representation of the material properties.

#### 3.2.2.2 Four-point bending

Several standards (ASTM C1609 (ASTM-C1609 2012), DAfStb (DAfStb 2010), DBV - Guide to Good Practice (DBV 2007), JCI-S-003-2007 (JCI-S-003 2007)) require four-point bending test to characterize FRC. While ASTM C1609 and JCI-S-

003-007 use beams where b=h=a (Figure 3.5), DAfStb and DBV use specimens where a>b;h (b=h=150 mm, but a=L/3=200 mm). Some standards allow the use of various sized beams, which should be selected as a function of fiber length (ASTM C1609). Other standards allow using a particular specimen geometry, but set limits to fiber type and properties used in the FRC (JCI-S-003-2007). In this study, tests according to ASTM C1609 (4P-ECC-150, 4P-PP-FRC-150 and 4P-SFRC-150 as in Figure 3.5 of ECC, PP-FRC and SFRC were conducted. Additional geometries of ECC beams were investigated with reduced heights of 50 and 75 mm. The specific geometries of the specimens used in this study are reported in Table 3.3.

The deformation controlled flexural test was performed with a loading rate of 0.05 mm/min up to a net mid-span deflection of 0.5 mm, and subsequently the loading rate was slowly ramped up to 0.25 mm/min. The load and LVDT measured deflections were captured with a frequency of 10 Hz, while DIC measurements were taken from one surface of the specimen at four second intervals.

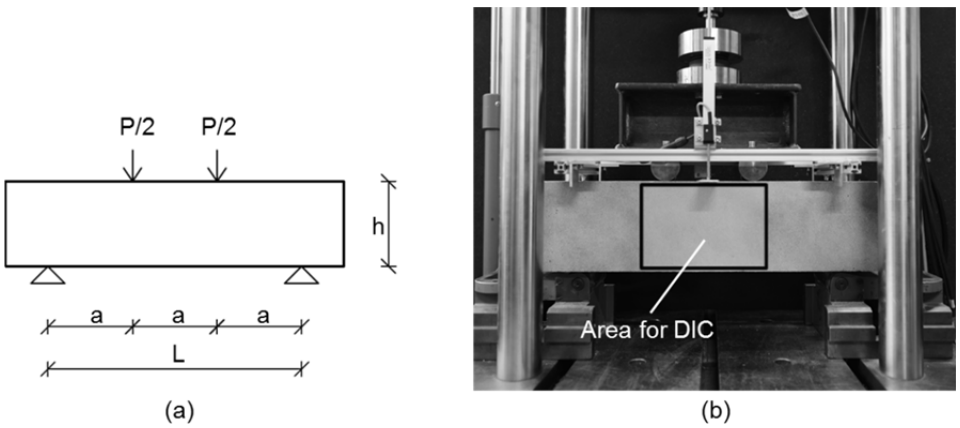


***Figure 3.5*** *Four-point bending beam: (a) specimen geometry; (b) test setup with measuring devices*

***Results – Four-point bending beams***

Figure 3.6 shows load-deflection curves of four-point bending tests for ECC beams of varying dimension, the results of PP-FRC and SFRC are presented in Figure 3.7. The secondary vertical axis provides the residual flexural stress ($\sigma_{eq,el}$), calculated by:

$$\sigma_{eq,el} = \frac{PL}{bh^2} \tag{3.3}$$

Where:

P – applied load;

L – beam span;

b – beam width;

h – beam height;

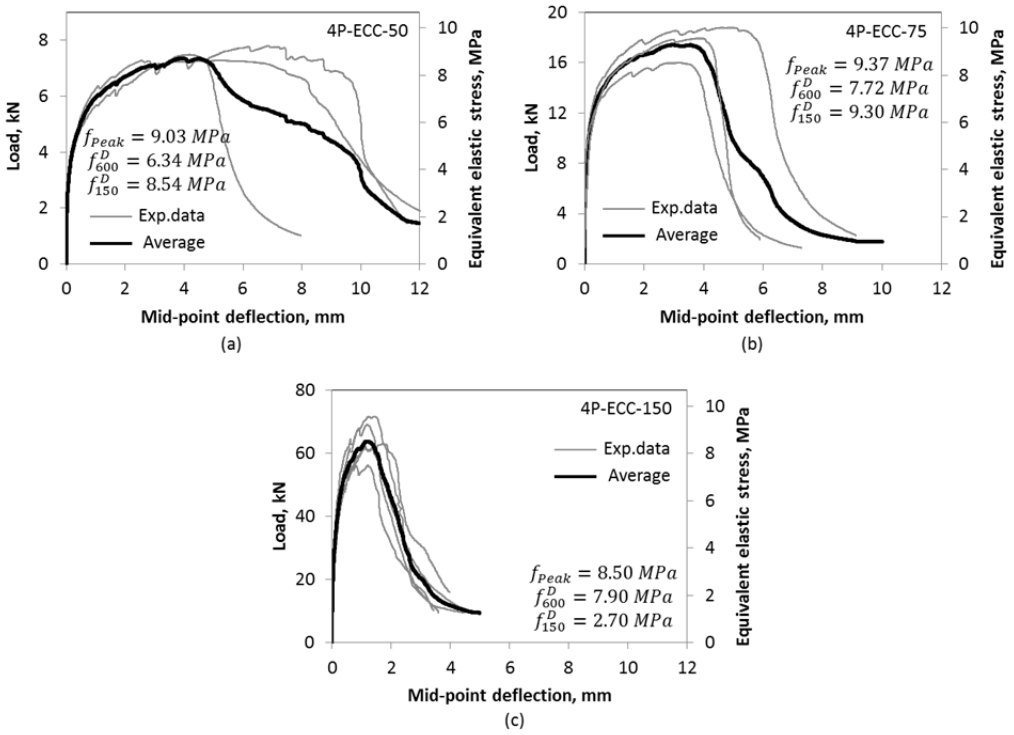


***Figure 3.6*** *Load-mid-span deflection relationships of ECC four-point bending beams (a) 4P-ECC-50; (b) 4P-ECC-75; and (c) 4P-ECC-150*

The plotted values shown in the diagram $f_{Peak,}$ $f_{600}^{D}$ and $f_{150}^{D}$ are average residual strength values determined according to ASTM C1609 (ASTM-C1609/C1609M-12 2012) at peak load, net deflection of L/600 (0.75 mm) and L/150 (3.0 mm) respectively.

Figure 3.6(a-c) presents the four-point bending test results of ECC beams with 50, 75 and 150 mm beam height, respectively. While all ECC beams had similar average peak strength (between 8.60 MPa and 9.35 MPa), beams with reduced height (4P-ECC-50/150 and 4P-ECC-75/150) had higher deflections at similar equivalent elastic flexural stress. The increased slenderness of the shallowest beams resulted in a decrease in stiffness and a significant enhancement in ductility.

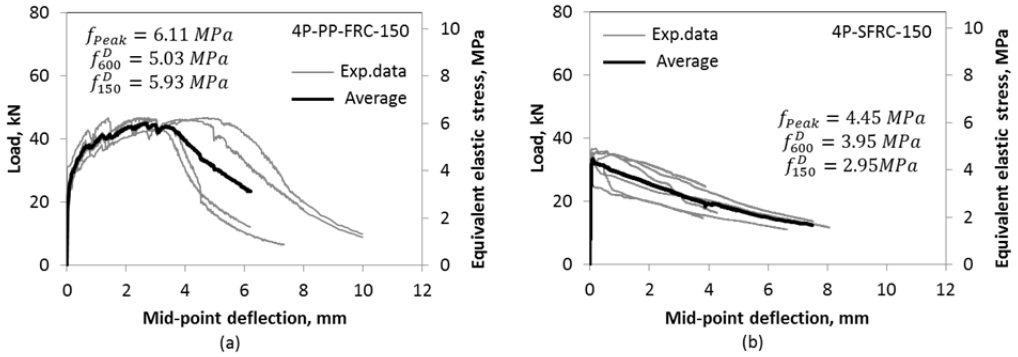


***Figure 3.7*** *Load-mid-span deflection relationships of (a) PP-FRC and (b) SFRC four-point bending beams*

Figure 3.7(a) and (b) show results of PP-FRC and SFRC beams respectively, with geometries according to ASTM C1609. The PP-FRC beams provided a deflection hardening response in four-point bending with a peak strength of 6.11 MPa, while the SFRC beams provided a deflection softening response with peak strength of 4.45 MPa. Comparing the behavior of standard sized ECC and SFRC beams, the peak strength of ECC (8.50 MPa) is almost twice as high as that of SFRC (4.45 MPa), whereas the residual strength at a mid-span deflection of L/150 (or 3 mm) is similar for both materials (2.70 MPa for ECC and 2.95 MPa for SFRC). This evidence indicates that even though ECC can resist a higher maximum load, the post-peak behavior of SFRC is more stable (i.e., with increasing deflection, the decay in flexural strength is more gradual in SFRC). This is likely due to a combination of factors, including differences in the interfacial properties of the fibers and cementitious matrices, the different maximum size aggregates and the fiber properties. In fact, the short 8 mm PVA fibers in ECC are able to resist and activate the bridging action for small values of crack opening. On the contrary, the 50 mm long steel fibers in the SFRC start working at larger crack widths, but are able to effectively bridge cracks with rather high widths (up to 3 mm). From a material design point of view, this suggests that the utilization of PVA fibers would provide high performance under service limit state (SLS) conditions, whereas a structure would more benefit from long steel fibers at the ultimate limit states (ULS). This also leads to a potential of a combined utilization of the two types of fibers, by suitably design a proper mix composition that could enhance this hybrid fiber system.

Figure 3.8(a) and (b) show typical peak load crack patterns in ECC beams with reduced height compared to traditional ASTM beams. The 50 mm high ECC beam (4P-ECC-50) in Figure 3.8(a) has a classical (i.e., Bernoulli) flexural behavior with well distributed flexural cracks with a regular crack spacing of approximately 13 mm over the constant moment region. The same evidence was found for the 4P-ECC-75 sample (Figure 3.8(b)), showing an average crack spacing of approximately 20 mm. In contrast, Figure 3.8(c) shows an irregular cracking for the 150 mm high ECC beam

with many cracks located outside the constant moment region, characterized by a typical mixed shear-flexure crack pattern. The varying slenderness of the beams likely causes the varying crack behaviors. Similar to ECC, the PP-FRC beams developed multiple cracks, as shown in Figure 3.8(d), both inside and outside the confines of the constant moment region, resulting in deflection hardening response.

Figure 3.8(e) shows a typical SFRC beam with a single main crack in the constant moment region at peak load. However, in the majority of the tested SFRC beams small secondary cracks were observed near peak loading. Figure 3.8(e) shows an example of a secondary crack outside of the constant moment region, with a maximum crack width of 0.03 mm.

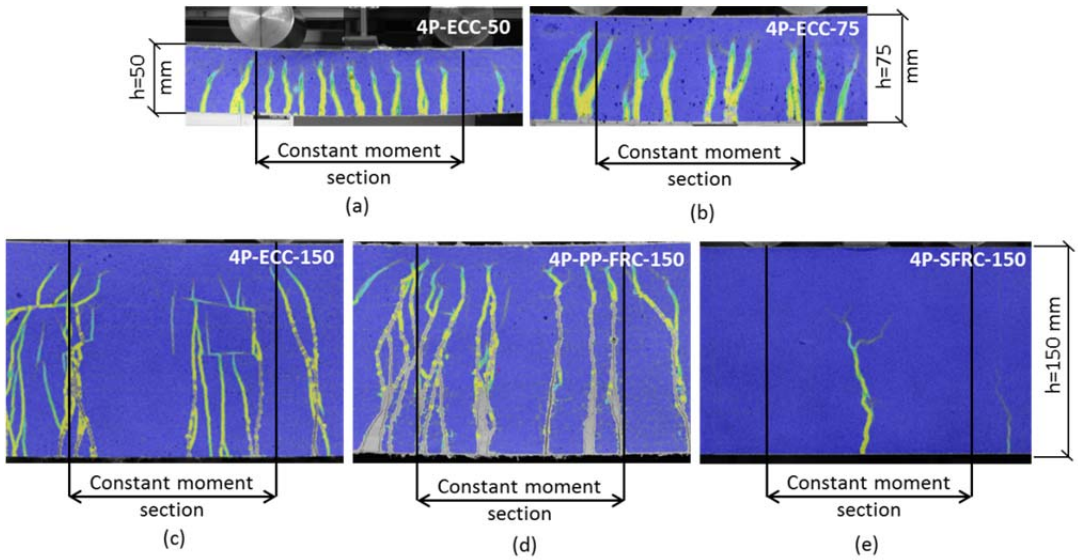


***Figure 3.8*** *Typical cracking at peak load for four-point bending beams: (a) 4P-ECC-50; (b) 4P-ECC -75; (c) 4P-ECC -150; (d) 4P-PP-FRC-150 and (d) 4P-SFRC-150*

## 3.2.3 Round determinate panel

The round determinate panel (RDP) test described in ASTM C1550-10 as a standard test method of FRC is an externally statically determinate system with a predictable and quantifiable crack pattern (i.e. using yield line theory a three-line crack pattern can be predicted (Johansen 1962; Tran et al. 2005)). The experimental program in this study included tests on specimens made according to ASTM C1550-10 as well as smaller panels recently proposed by Minelli and Plizzari (Minelli & Plizzari 2011). The RDP test setup is shown in Figure 3.9 with the geometry provided in Table 3.4.

***Table 3.4*** *Geometry and basic properties of RDP specimen*

| Name | Material | Test type | # | R mm | r mm | H mm | Weight kg | r/h |
|---|---|---|---|---|---|---|---|---|
| P-ECC-60 | ECC | Panel | 3 | 300 | 275 | 60 | 32.9 | ~4.6 |
| P-ECC-75 | ECC | Panel | 6 | 400 | 375 | 75 | 73.1 | 5 |
| P-SFRC-75 | SFRC | Panel | 6 | 400 | 375 | 75 | 91.6 | 5 |

* r/h – slenderness

RDP tests were conducted under a deformation controlled procedure with loading rates of 3.0 ±1.0 mm/min. The load and deformation measurements were captured at a frequency of 10 Hz, while DIC measurements were taken from the cracked surface of the panel (i.e., surface opposite of the load actuator in Figure 3.9(b)) at a ten second intervals. As the DIC system utilized only captured 2-dimensional deformations, only the formation of cracks were analyzed through DIC (i.e., vertical deformations and crack widths were not measured by DIC). Specimen deflections at the center point of the panel were measured by a LVDT. Moreover, to prevent damage to the camera, specimens were loaded from the bottom, with the camera positioned above the specimen. As the distance from the specimen surface to the DIC camera changes during testing, DIC measured crack widths would be distorted.

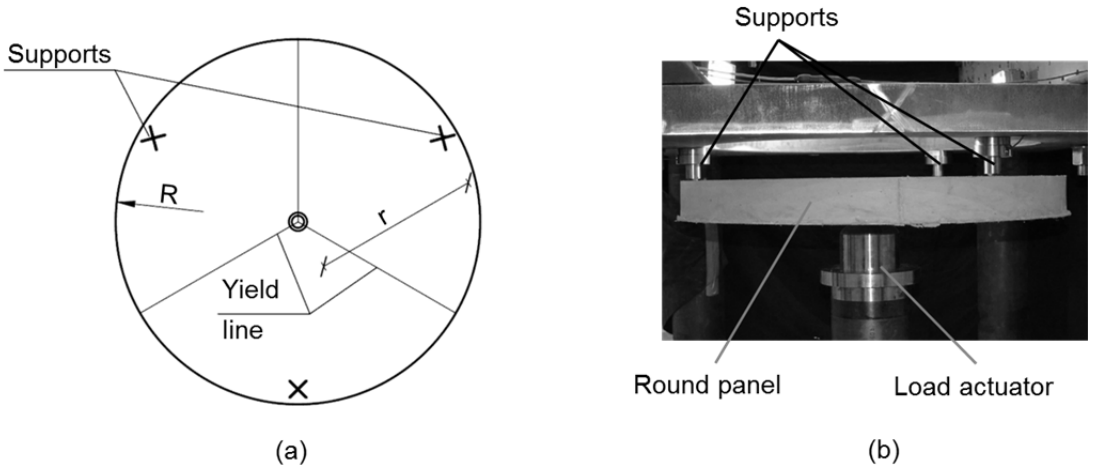


***Figure 3.9*** *Test setup of RDP: (a) specimen geometry (top view); (b) actual test setup (side view)*

***Results - RDP***

Figure 3.10(a,b) presents the load-center point deflection responses for the ECC RPD's P-ECC-75, with ASTM C1550 (ASTM-C1550 2012) dimensions, and P-ECC-60, with the smaller geometry suggested in (Minelli & Plizzari 2011), respectively. To determine the peak strengths of the RDP's, the corresponding moment for the centrally applied peak load should be determined. Previous studies show evidence that

the relation between the applied load at the center of the specimen and the moment along each radial yield can be found using Yield Line Theory (Bernard 2013; Johansen 1962). Thus, the flexural peak strength, $f_{Peak,}$ using elastic theory can be determined as follows:

$$f_{Peak} = \frac{2rP_p}{\sqrt{3}Rh^2} \tag{3.4}$$

Where:

$P_p$ – peak load;

r – distance between the loading point to supports;

R – radius of panel;

h – panel height

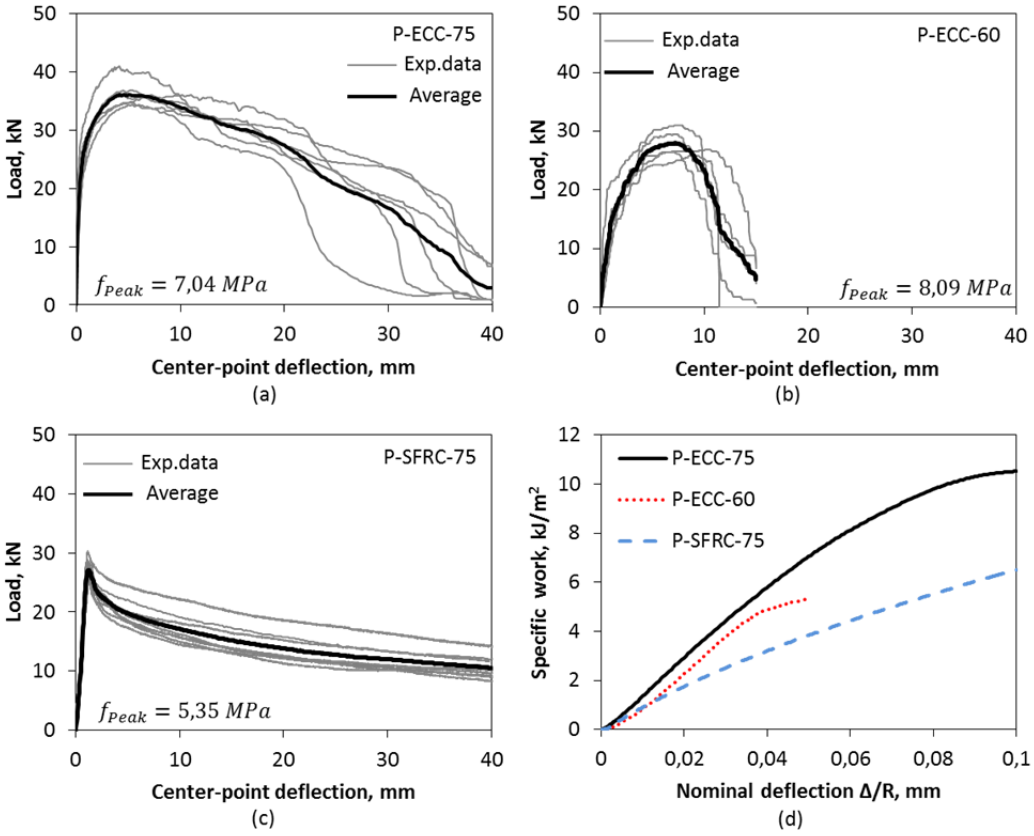


***Figure 3.10*** *Load-deflection curves of RDPs*

The calculated average peak strength of for ECC was 7.0 and 8.1 MPa for the standard and modified dimensions, respectively. Regardless of the RDP dimensions (standard or modified), similar deflection hardening responses of ECC were observed, with the modified RDP providing a higher peak strength.

Figure 3.10(c) presents the load-center point deflection responses of standard SFRC RDP's (ASTM-C1550 2012), showing a deflection softening response similar to that of four-point beam tests with SFRC (Figure 3.6). The peak strength of the SFRC panel was 5.4 MPa, which is 1.3 times lower than the peak strength of the corresponding ECC panel. However, as previously noticed in the other test methods, the decay in strength of SFRC is significantly more gradual than ECC under increasing deformation.

Figure 3.10(d) presents the specific work versus normalized deflection (with respect to the panel radius) for all RDPs. The specific work was calculated using the following relationship:

$$\overline{W} = \frac{1}{3Rh}\int_0^{\Delta} P d\Delta \tag{3.5}$$

Where:

$\overline{W}$ – specific work;

Δ – center-point deflection;

P – point load;

R – panel radius;

h – panel height.

From Figure 3.10(d), it emerges that the panel size does not influence the basic behavior of ECC as the shape of specific work versus normalized deflection curves is very similar. However, standard size ECC panels required more specific energy to reach the same normalized deflection and had a higher deflection capacity. As the studied ECC was able to carry higher loads than the SFRC, the energy absorbed to reach the same deflections is higher for ECC.

ASTM C1550 requires determination of energy absorption at the center point deflection values of 5, 10, 20 and 40 mm. Testing of the ECC panels was terminated when the post-peak load was <2 kN, at corresponding center-point deflections in the range of 36 to 50 mm. The average energy absorbed at 40 mm deflection of the standard ECC RDP (P-ECC-75) was 877 J (specific work, $\overline{W}$ = 10.5 kJ/m$^2$). While all SFRC panels collapsed at a deflection well beyond 40 mm, the average energy absorbed at 40 mm deflection of 585 J (specific work, $\overline{W}$ = 6.5 kJ/m$^2$) is 1.5 times lower than the maximum obtained values for ECC.

Four out of the six standard sized RDP of ECC failed before reaching 40 mm of deflection. Thus, the RDP tests provide further confirmation that ECC yields cracks with small width and improved distribution compared to SFRC. The results indicate the 40 mm deflection requirement of ASTM C1550 (ASTM-C1550 2012) is in contrast with the nature of ECC. The ECC was capable of significantly improved

energy absorption at lower displacements, but modifications are needed in the ASTM C1550 approach to accommodate ECC.

DIC measurements of ECC specimens tested according to ASTM C1550 (ASTM-C1550 2012) are presented in Figure 3.11(a-c). The occurrence of first crack in the specimen is difficult to capture as multiple cracks form at nearly the same time (Figure 3.11(a)). The initial cracks are located approximately along the three yield lines, starting from the load point and propagating towards the direction of the mid-span between neighboring supports (see Figure 3.9 and Figure 3.11(a)). As shown in Figure 3.11(b), additional deflections cause the formation of new cracks and the widening of existing cracks (note the yellow color in the DIC measurements is indicative of the widest cracks). At peak load, shown in Figure 3.11(b), almost all cracks have formed and a circular fan-shaped yield pattern can be observed. In the post-peak deformation regime (Figure 3.11(c)) typically three localized cracks develop from the load-point towards the direction of the mid-span between neighboring supports.

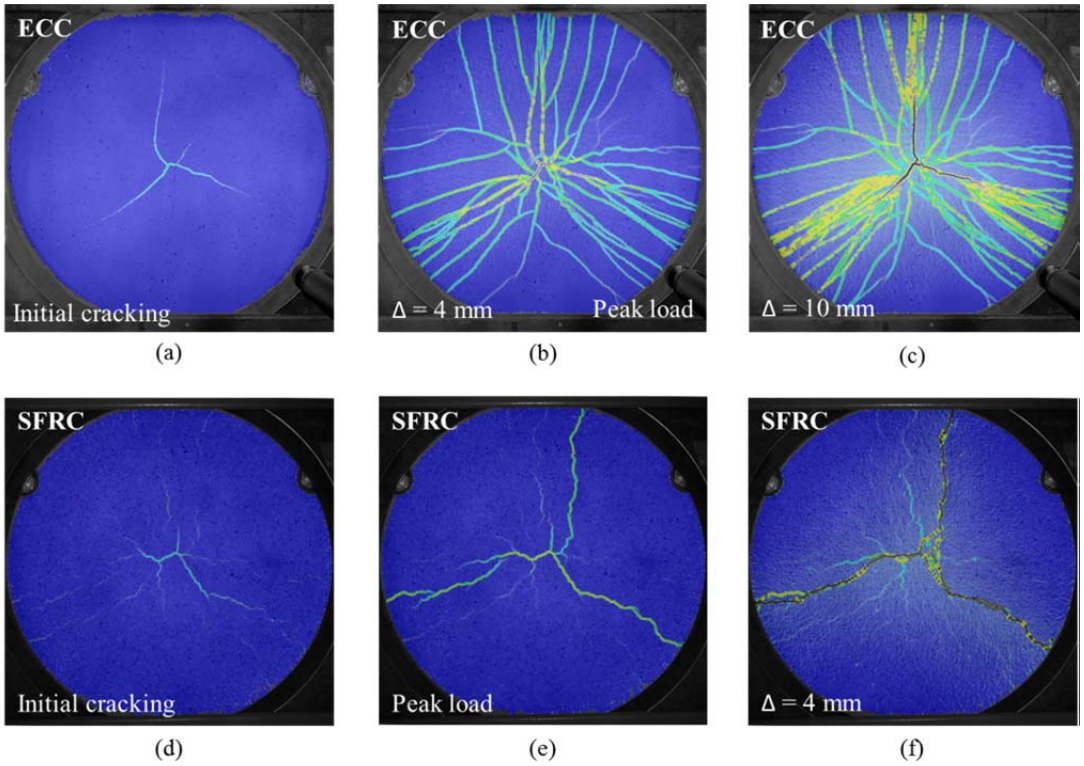


***Figure 3.11*** *Formation of cracks of typical RDP's by DIC: (a) P-ECC-75 initial cracking; (b) P-ECC-75 at a deflection of 4 mm; (c) P-ECC-75 at peak load; (d) P-SFRC-75 initial cracking; (e) P-SFRC-75 at peak load and (f) P-SFRC-75 at a deflection of 4 mm*

DIC results for SFRC RDP's are presented in Figure 3.11(d,e). Similar to ECC, the first crack in the specimen was not possible to unequivocally be captured as a number of small cracks formed nearly simultaneously (see Figure 3.11(d)). At peak load, three

main cracks can be observed in the locations of the anticipated yield lines; however, multiple smaller cracks are also present (Figure 3.11(e)). After the peak load, no new cracks form and existing cracks increased in width.

The formation of multiple cracking in SFRC panels investigated in this study differs from the experimental results on strictly tension softening materials obtained by Minelli and Plizzari (Minelli & Plizzari 2011). Minelli and Plizzari tested panels of SFRC containing 25-30 kg/m$^3$ of steel fibers ($V_f$ = 0.32-0.38%), which is approximately half the fiber volume fraction of the SFRC used in this study. The increased steel fiber volume fraction likely explains the differing material response as fewer fibers bridging a crack results in a reduced load transfer across a crack and, consequently, the possibility that multiple cracking can occur is strongly reduced.

## 3.3 Variability of individual test methods

As previously mentioned the most popular test methods to characterize FRC in flexure are three- and four-point bending test. However, there is an evidence that the results obtained from these tests has a high variability leading to low characteristic values obtained from beam tests (Bernard 2013; Minelli & Plizzari 2011). According to (Minelli & Plizzari 2011) the round determinate panel, with its larger sample size, multiple yield lines, and larger fracture area, reduces variability in test results compared to traditional beams, particularly for SFRC with low volumes of steel fibers.

Coefficients of variation, which describe the variability of test results, are presented in Table 3.5 for all tests of ECC and SFRC materials. For all test methods the coefficient of variation is relatively constant in the case of ECC.

The SFRC test results had similar variability as the ECC results, except for four-point bending tests. Three-point bending tests of SFRC provided very repeatable results with rather low scatter, which is in contrast some previous studies (Minelli & Plizzari 2011). The reduced scatter can be explained by the increased fiber content used in the SFRC used in this study ($V_f$=0.7%) compared to the relatively low fiber content ($V_f$=0.3%) in the previous work. The increased fiber content yielded a more uniform fiber distribution in both the RDP and beam specimens.

Therefore, no considerable reductions in variability were observed from RDP results and the beam tests for the materials investigated here. As a result, the RDP test, which was suggested to be effective for tension softening materials to significantly reduce the variability (Minelli & Plizzari 2011), is found less convenient and unnecessary for the materials considered in this study, as testing is significantly harder to perform with standard laboratory facilities and interpretation of results is less straight forward.

***Table 3.5*** *Overview of statistical evaluation of test results*

| **Coefficient of variation** (standard deviation/average value) | | | | | | | |
|---|---|---|---|---|---|---|---|
| **Three-point bending** | | | | | | | |
| | # | Peak load | Deflection at peak load | Load at $CMOD_1$ (0.5 mm) | Load at $CMOD_2$ (1.5 mm) | Load at $CMOD_3$ (2.5 mm) | Load at $CMOD_4$ (3.5 mm) |
| 3P-ECC-40 | 2 | 0.02 | 0.15 | 0.06 | 0.03 | 0.20 | 0.06 |
| 3P-ECC-150 | 5 | 0.16 | 0.24 | 0.14 | 0.16 | 0.20 | 0.29 |
| 3P-SFRC-150 | 3 | 0.05 | 0.02 | 0.04 | 0.03 | 0.02 | 0.03 |
| **Four-point bending** | | | | | | | |
| | # | Peak load | Deflection at peak load | Load at Δ=L/600 (0.75 mm) | Load at Δ=L/300 (1.5 mm) | Load at Δ=L/150 (3.0 mm) | Load at Δ=L/100 (4.5 mm) |
| 4P-ECC-50 | 3 | 0.04 | 0.24 | 0.05 | 0.05 | 0.01 | 0.01 |
| 4P-ECC-75 | 3 | 0.08 | 0.23 | 0.05 | 0.06 | 0.08 | 0.38* |
| 4P-ECC-150 | 5 | 0.10 | 0.18 | 0.07 | 0.10 | 0.33* | 0.10 |
| 4P-SFRC-150 | 6 | 0.04 | 0.28 | 0.20 | 0.20 | 0.21 | 0.19 |
| **Round determinate panel** | | | | | | | |
| | # | Peak load | Deflection at peak load | Energy absorbed at Δ=R/80 | Energy absorbed at Δ=R/40 | Energy absorbed at Δ=R/20 | Energy absorbed at Δ=R/10 |
| P-ECC-60 | 3 | 0.06 | 0.20 | 0.17 | 0.11 | 0.16 | - |
| P-ECC-75 | 6 | 0.07 | 0.22 | 0.08 | 0.07 | 0.05 | 0.15* |
| P-SFRC-75 | 6 | 0.05 | 0.11 | 0.08 | 0.09 | 0.11 | 0.14 |

*- after one of the specimens has failed

# - indicates the number of samples used to derive coefficients of variation

## 3.4 Discussion of selected test methods to characterize FRC

Various flexural test methods, initially developed for characterization of SFRC, that usually exhibits tension softening behavior (ASTM C1609, EN 14651, ASTM C1550), were investigated to determine reliable and readily implementable alternatives to the direct test methods presented in Chapter 2. In general, these can be divided into three categories, including the three-point bending test, four-point bending test and panel tests. Comparing the load versus displacement/deflection results of these test methods indicates the classification of certain FRC materials may depend on the selected test method. Table 3.6 shows that all test methods confirm that the investigated ECC and PP-FRC material had a deflection hardening response, whereas, various responses were found for the studied SFRC: deflection softening

according to ASTM C1609 and ASTM C1550 testing and almost a perfectly plastic response according to EN 14651.

***Table 3.6*** *Comparison of results from standard test methods*

| Test method | ECC | | PP-FRC | | SFRC | |
|---|---|---|---|---|---|---|
| | Classification | Peak strength MPa | Classification | Peak strength MPa | Classification | Peak strength MPa |
| Uni-axial tension | Strain hardening | 4.15 | Tension softening | 3.1 | Tension softening | 2.15 |
| Three-point bending EN 14651 | Deflection hardening | 7.8 | Deflection hardening | 6.21 | Almost perfectly plastic | 4.9 |
| Four-point bending ASTM C1609 | Deflection hardening | 8.5 | Deflection hardening | 6.11 | Deflection softening | 4.4 |
| RDP ASTM C1550 | Deflection hardening | 7.0 | - | - | Deflection softening | 5.4 |

Figure 3.12 illustrates both the anticipated crack patterns for three- and four-point bending beams according to bending beam theory and the actual observed crack patterns. For the notched three-point bending, the stress field according to bending beam theory (B-region) should result in a single crack extending from the notch, upward towards the loading point. The actual crack patterns obtained from three-point bending beams of the FRC materials studied, shown in Figure 3.4 and schematically in Figure 3.12 included multiple cracking. Multiple cracking indicates the notched mid-span section behaves as a disturbed region (D-region), with strain and stress fields that are much more complicated than those assumed in standards. The point load and the notch at the mid-span provide a stress concentration. The stress field at the weakened cross section (mid-span) is disturbed and far from being in accordance with traditional beam theory. In addition, high shear stresses develop in the beam, particularly for deflection hardening FRC materials. A number of four-point bending beams of the tested FRC materials failed due to shear rather than flexure. The accuracy of the prescribed analysis and evaluation procedure is weakened by these inconsistencies.

As a result, the material characteristics obtained by notched three-point bending tests are not fully representative of the FRC when multiple cracks develop from the notch, the vicinity of the notch, or elsewhere on the beam. The test method is based on the assumption that the notch will introduce a single flexural crack and the true crack opening and corresponding load capacity will be measured. When multiple cracks are formed from the notch, the measured CMOD is rather the sum of many smaller cracks

and does not represent true openings of these cracks. Thus the results would not represent the material correctly for SLS where limits are set by crack width. This fact entirely excludes strain hardening materials from being fully evaluated by the notched three-point bending test. It is noted that typically stress transfer across cracks will eventually reduce with increases in crack width, for example, see Figure 2.6. The near perfectly plastic SFRC also experienced unexpected disturbances due to the presence of the notch, with multiple cracks forming (see Figure 3.4).

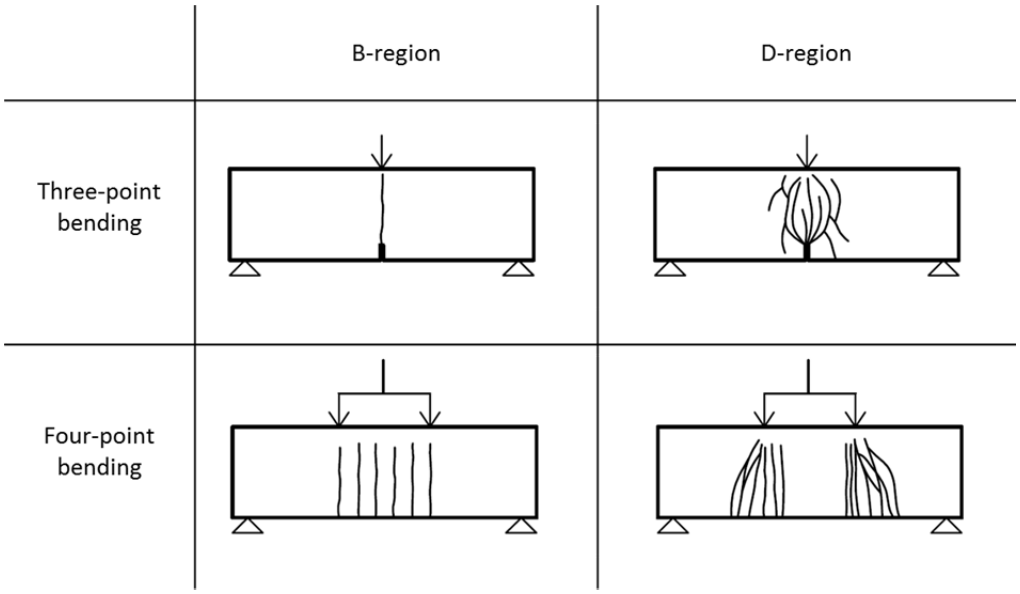


***Figure 3.12*** *Crack patterns in three- and four-point bending beams according to bending beam theory (B-region, assumption) and disturbed region (D-region, observed in this study)*

In conclusion, the notched three-point bending test does not characterize the pure flexural response of the material, as is suggested in the standards. The notched mid-span section behaves as a disturbed region (D-region), far from being subjected to a stress field according to bending beam theory (B-region). The extent and location of multiple cracking in the notched three-point bending beam, together with the impact of fiber distribution and orientation and the limited size of that fracture plane as discussed in Section 3.3, likely contributes to the experimental scatter typical of FRCs. In some cases, cracks may form outside the CMOD gage length and therefore be excluded from the measured CMOD, resulting in a reduction in the ultimate deformations. Additionally, the exact number of cracks forming from the notch may influence the measured CMOD at a given load and/or the load capacity.

Although the constant moment region of the four-point bending beam, illustrated in Figure 3.12, theoretically allows for the formation of multiple cracking of a deflection hardening material, cracks often occurred outside of the constant moment region for the ECC beams. Cracks forming outside of the constant moment region are influenced not only by bending but also by shear. The influence on shear stresses on flexural

performance was significant for the beams having a depth equal to 1/3 of the span (4P-ECC-150), as several cracks appeared outside the flexural span. Moreover, cracks were more concentrated in the region under the two loading points and were inclined (see Figure 3.8(c)) with a typical mixed shear-flexure crack pattern (Figure 3.12). In contrast, the ECC beams with reduced thickness (i.e. more slender) were found to have a regular multiple crack pattern in the constant moment region without additional cracks forming outside the constant moment region.

In case of failure occurring outside the constant moment region, the corresponding test results cannot be used according to the procedure described in ASTM C 1609. Based on the general experience at the Technical University of Denmark, failure cracks form outside the constant moment region in more than 25% of the ECC beams tested in accordance with ASTM C1609. To reduce the influence of shear stresses on the test results, a more slender beam geometry (i.e., reduced beam height, increased span length, or both) is recommended. As ECC is typically envisaged to be used in relatively slender structures with thicknesses of 50-75 mm, the ASTM beam test with reduced thickness would be preferable.

There is evidence the results of three- and four-point bending beams may vary significantly due to a number of reasons, including details of the specimen preparation and casting method (fiber distribution and orientation) and the amount of friction to rotation and translation in the supports (especially for high deformation values) (Wille & Parra-Montesinos 2012). If the supports cannot both rotate freely and accommodate a horizontal displacement, axial compressive stresses will be imposed on the cross-section of the beam. The axial load, similar to prestressing, affects the load-deformation response of the specimens and therefore also the measured flexural properties. Other studies have shown that even careful control of specimen preparation cannot prevent non-uniform fiber distribution in the critical section between different specimens especially in softening materials with low volume fraction of fibers (Minelli & Plizzari 2011), resulting in a high variability of results. However, this study with higher fiber contents, was able to obtain very consistent results for beam tests.

An RDP test, such as ASTM C1550, provides an alternative test method that accounts for both the material property of multiple cracking (if the material has a hardening characteristic) and the structural property of forming multiple (three) yield lines. In some cases, results obtained by the RDP test have lower variability due to its increased fracture area compared to beam tests (Minelli & Plizzari 2011). However, results of the RDP test are difficult to interpret. Recent research (Minelli & Plizzari 2015) has established a correlation between RDP and beam test results, allowing the results of RDP tests to be used in the structural design approach in the *fib* Model Code.

It should be emphasized that the ability of the material to form multiple cracking under tensile loading is a material property (related to the fiber bridging stress-crack opening behavior) that must not be confused for the formation of multiple cracks due to the structural configuration. The multiple cracking material property can be assessed by specific tensile tests as described in Chapter 2. Beam and plate tests of strain hardening FRC's will also show multiple crack formation in flexure. However, multiple cracks may also develop as a result of the structural configuration. For example, the structural load configuration of the RDP results in 3 yield lines, which can form three cracks with a tension softening FRC material or even conventional unreinforced concrete. The material property of multiple cracking must not be confused for multiple crack formation due to the structural configuration.

The comparison of the results of three-point bending test according to EN 14651 (EN14651 2007), four-point bending test according to ASTM C1609 (ASTM-C1609/C1609M-12 2012) and RDP tests according to ASTM C1550 (ASTM-C1550 2012) are presented in Table 3.6. For the strain hardening materials ECC, the lowest measured peak strength was determined by the RDP test (7.0 MPa) while the average peak strength of 7.8 and 8.5 MPa was measured of three- and four-point bending beams. For the tension softening SFRC, the highest peak strength was determined by the RDP test (5.4 MPa) while the peak strength obtained from the three-point and four-point bending tests were 4.9 MPa and 4.4 MPa, respectively.

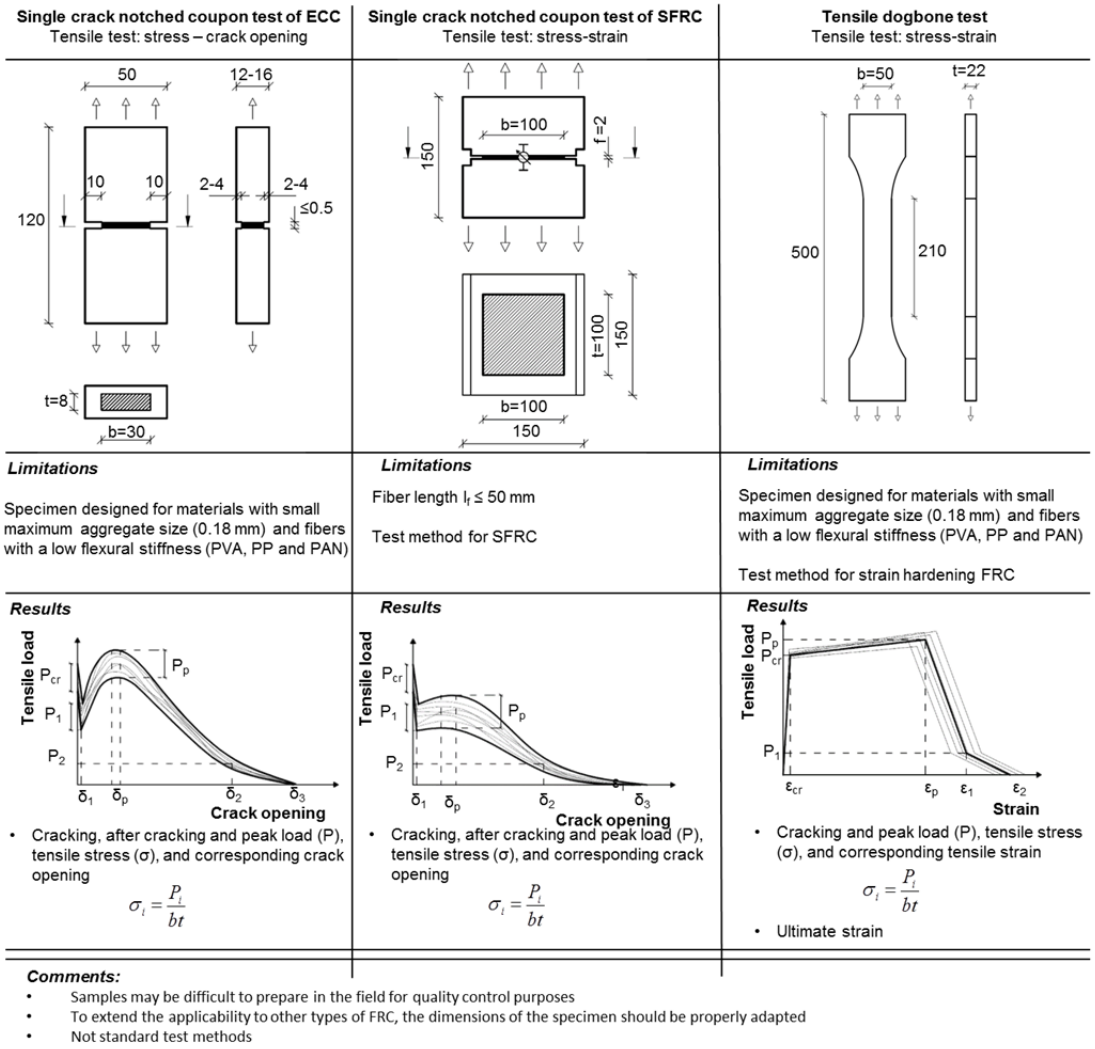


***Figure 3.13*** *Summary of tensile tests*

## 3.5 Conclusions

The test procedure and applicability of tensile test methods described in this chapter are summarized in Figure 3.13.The single crack notched coupon test and dogbone test most realistically describe the tensile properties and cohesive relationship of FRC. However, such samples may be difficult to prepare in the field and to test in a standard laboratory for quality control purposes. For this reason, alternative indirect test methods are needed to obtain tensile strength and load-deformation behaviors of FRC. Various test methods, based on beams and plates in flexure, were investigated in this study to assess their potential for determining the tensile properties of strain hardening and tension softening materials.

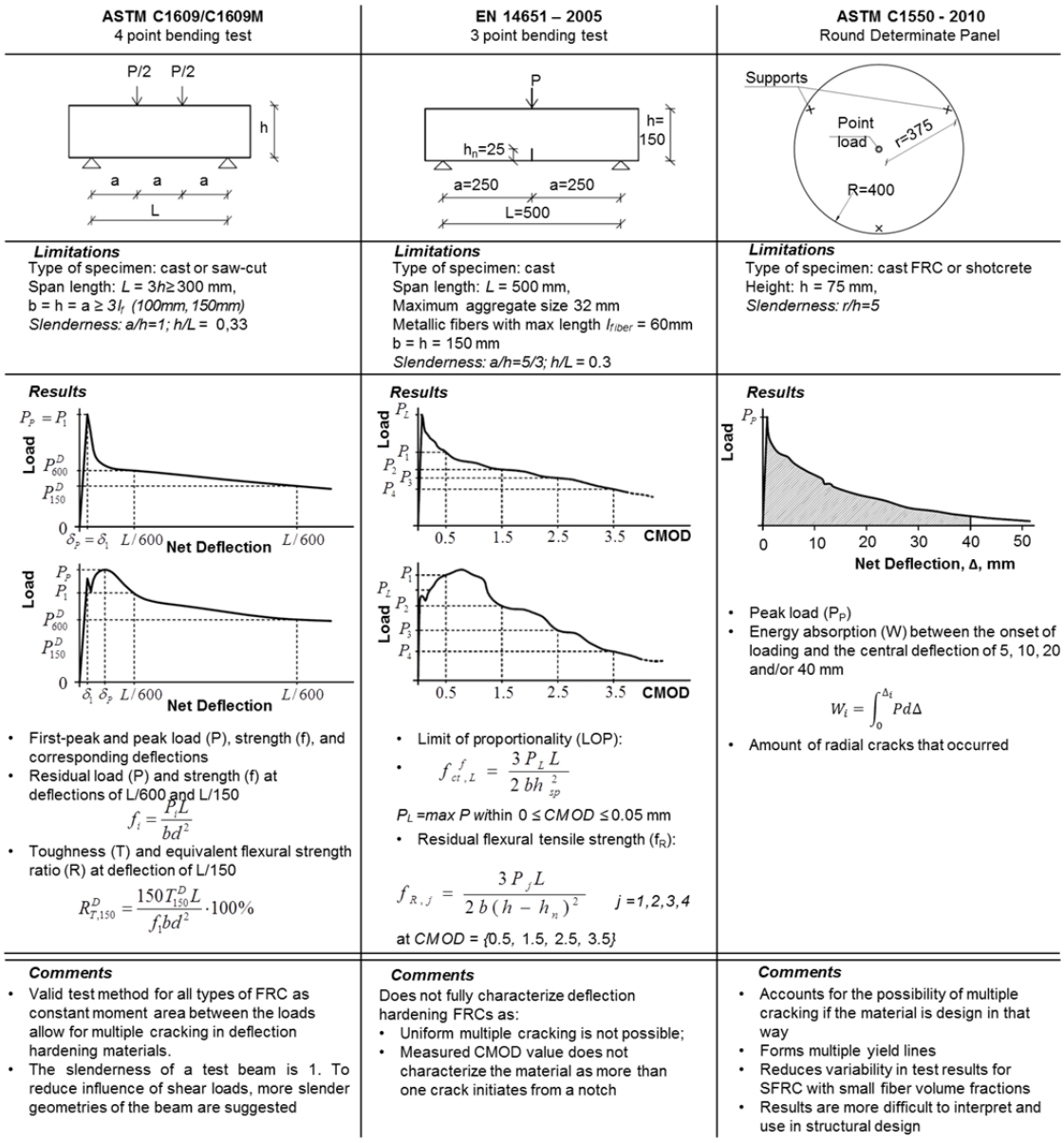


***Figure 3.14*** *Summary of standard test methods*

The test procedures and applicability of standard test methods described in this chapter are summarized in Figure 3.14. Certain test methods were found to be useful to characterize FRC in bending; however, for more accurate results modified test configurations are recommended, as follows:

- The notched three-point bending test is not suitable for strain hardening FRC materials and for some tension softening FRC materials. Crack formation around the notch (see Figure 3.4) does not follow bending beam theory as a result of a disturbed stress regions (flexure and shear) in the vicinity of the mid-span. Moreover, the stress field generating in the sample is significantly disturbed for the entire beam, particularly for deflection hardening FRC.

- The four-point bending tests characterize the material more realistically by accommodating multiple cracking, especially when using more slender beam geometries. In commonly used four-point bending tests the slenderness ratio a/h=1 (see Table 3.3) and the results are highly influenced by shear stresses. The authors recommend increasing the slenderness ratio a/h to 2 or higher to avoid this issue.
- The round determinate panel (RDP) test provides an alternative test to beams with a larger fracture area. The plate specimen as specified in ASTM C1550 can be considered a slender bending specimen, where cracking is induced predominantly by bending stresses and not by shear stresses. The load-deformation response is therefore governed by bending with additional effects induced by confining stresses in the radial direction of the plate.
- This study shows no significant reduction in the variability of test results when using the RDP test, compared to the three- and four-point bending tests. As the test RDP sample 1) is almost three times heavier than three- and four-point bending beams, 2) requires special equipment for testing, and 3) and results are currently more difficult to interpret and use in structural design, the four-point bending beam is the preferred test method to assess the FRC materials investigated in the study.
- When specifying the test method for characterization of a strain hardening FRC material, the specimen geometry shall be comparable to that of the actual structure. In particular, the thickness of the test specimen should be similar to that of the actual application to ensure similar fiber orientation and distribution. It is noted that, depending on fiber length, the element thickness will impact the potential for a preferential orientation of fibers, which should be considered in the geometry of test specimen. For materials designed to exhibit multiple cracking in the constant moment sections, this material performance property should be captured by the selected test method.
- To comply with the previously mentioned requirements for testing, to reduce the variability of test results for FRC materials with low fiber volume fraction, and to minimize the influence of shear on the test results, a modified four-point bending FRC beam test could be developed that uses slender and wider (to increase the fracture area) beams. Increasing the slenderness of the test specimen would generate a Bernoulli-like stress state. While this test setup would be suitable for any type of FRC material, the optimal dimensions of the beam should be assigned as a function of fiber dimensions and type, maximum aggregate size and the structural application for which the material will be used.

# Chapter 4

# Detailed analysis of strain, crack opening and stress profiles in flexural beams

This chapter provides a detailed analysis of DIC measurements from the four-point bending beams presented in Chapter 3. Using the DIC measurements, crack width profiles were measured below the neutral axis, while the compressive strain profile across the constant moment region is measured above the neutral axis. The DIC measured strain/crack width profiles are compared to the average tensile stress-crack opening response (see Section 2.3.2.2) and compressive properties (see Section 2.3.1) to derive the stress profile in the beam. Bending moments, calculated from these stress profiles, predict the applied flexural load and capacity reasonable well at given strain/crack width profiles. This result indicates a potential to predict the full flexural behavior of FRC materials based on the compressive and tensile single crack responses.

## 4.1 Connecting tensile and compressive properties to flexural behavior

Typical FRC flexural members are design based on the measured compressive strength and indirectly measured tensile properties, determined through analysis of a standard flexural test method. The tensile properties are determined based on various assumptions, which are inaccurate in some cases, see Section 3.4. Alternatively, using the direct tensile tests described in Section 2.3.2 and Table 3.1, the stress-crack opening properties (i.e., cohesive relationship) of FRC can be derived directly. The

direct tension test methods are difficult to implement as a standard test though as concluded in Section 3.5.

The formation of cracks, which is important to the underlying assumption in the evaluation of standard test procedures and to the established correlation models between flexural and tensile behavior, was assessed using the DIC system described in Section 2.4. Crack widths from the tensile region and strains from the compressive region, measured by the DIC system, were related to the corresponding stress levels using the experimentally measured load-deformation responses in compression and tension.

To evaluate the influence of the tensile properties on the flexural response, the crack opening profile has been measured over the heights of the beam. The measured flexural crack opening is compared to the crack opening from the direct tension tests and the stress transferred over the specific crack opening has been found. To determine the stress transferred in the compression part of the beam the strain over the constant moment region has been measured and compared to measured strain in direct compression and the corresponding stress value was found.

The motivation behind the study presented in this chapter was to investigate the effect of a tensile stress-crack opening response on the flexural behavior of FRC and to assess the prediction of flexural behavior using measured material properties, in particular the tensile stress-crack opening and compressive stress-strain relationships.

## 4.2 Strain and crack opening profiles in FRC flexural beams

The experimental program consisted of four-point bending beams according to ASTM C1609, compression cylinders and single crack notched coupon specimens of the ECC, PP-FRC and SFRC described in Chapter 2. The direct compression and tension tests procedures and results are described in Sections 2.3.1 and 2.3.2.2, respectively. The description and all results of four-point bending beams are given in Section 3.2.2.2.

The obtained average tensile stress-crack opening relationships for ECC, PP-FRC and SFRC are shown in Figure 4.1, with the complete data set presented in Section 2.3.2.2 and Figure 2.6. The average tensile strength was 4.8 MPa and 3.0 MPa for ECC and PP-FRC, respectively and the average compressive strength was 52.0 MPa and 38.6 MPa, respectively. The average tensile strength of SFRC was 2.15 MPa and compressive strength 57.1 MPa. The average elastic modulus in compression was 16.0 GPa for ECC, 14.6 GPa for PP-FRC and 34.5 GPa for SFRC.

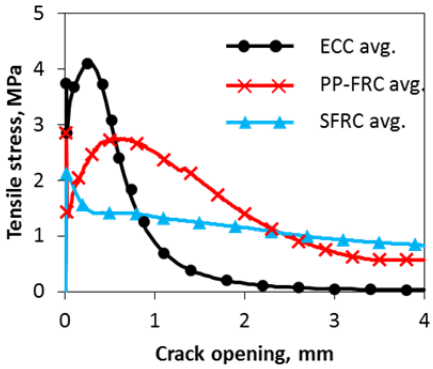


***Figure 4.1*** *Experimentally obtained tensile stress-crack opening relationships*

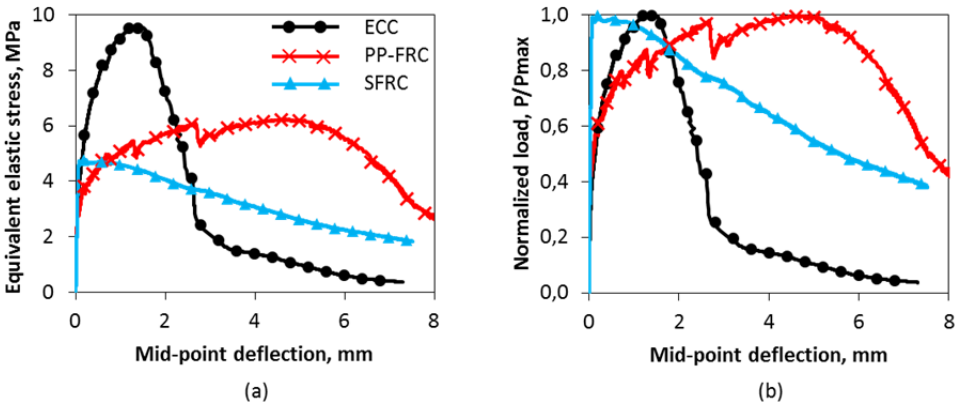


***Figure 4.2*** *Equivalent elastic flexural stress – mid-span deflection relationship*

Figure 4.2 shows the equivalent elastic stress flexural stress versus the mid-span deflection of representative beams for all three specimen types. The equivalent elastic stress is calculated as the bending moment (M) at the constant moment section of the beam divided by the section modulus. The normalized load ($P/P_{max}$) to normalized mid-span deflection (normalized over flexural span) diagram (Figure 4.2(b)) shows clearly that the PP-FRC is more ductile than the ECC beam. The presented ECC beam reaches its maximal load at deflections of approximately 1.3 mm while the PP-FRC beams reach the maximal load at deflections of 4.7 mm. The deflection hardening part of PP-FRC is significantly longer in terms of deflections than that of the ECC.

Figure 4.3 shows the flexural cracks of representative beams that formed at the ultimate stage. The crack width profile from each marked crack in Figure 4.3 was measured over the beam height, as shown in Figure 4.4(b,d,f). In each case, the measured crack was the ultimate plane of failure. As shown in Figure 4.4(a,c,e) the strain profile over the constant moment region was also measured for all beams. Strain profiles in Figure 4.4 show the average strain at varying mid-span deflections from a representative beam, while crack widths are taken from a single representative crack of the same beam. The strain profile is calculated as the measured deformation normalized by the length of the constant moment section.

As shown in Figure 4.4(a,c,e), the measured strain profile is linear over the beam heights in all cases. At the ultimate stage, the strain in the extreme tensile fiber reached 2.9% for the PP-FRC beam, 1.0% for the ECC beam reached, and only 0.2% for the SFRC beam. Figure 4.4(b,d,f) shows the measured flexural crack profile is linear, similar to the overall strain profile, with the highest crack openings at the tensile face of the beam. For the ECC used in this study, cracks rarely remained individual from top to bottom. In some instances, cracks branched for a portion of the beam height and subsequently reconnected at another location on the profile; see Figure 4.3(b). In such cases, the measured crack opening profile was not perfectly linear. In branched regions, the total crack opening was divided over two branches, reducing the measured crack opening. Once the crack remerged into a single crack, the measured opening increased again.

The maximum crack openings in the PP-FRC beam were significantly larger than those in the ECC and SFRC beams. The maximum crack openings at peak load in the ECC and SFRC beams were approximately 0.4 mm and 0.2 mm, respectively, while the maximum measured crack opening was 1.35 mm in the PP-FRC beam.

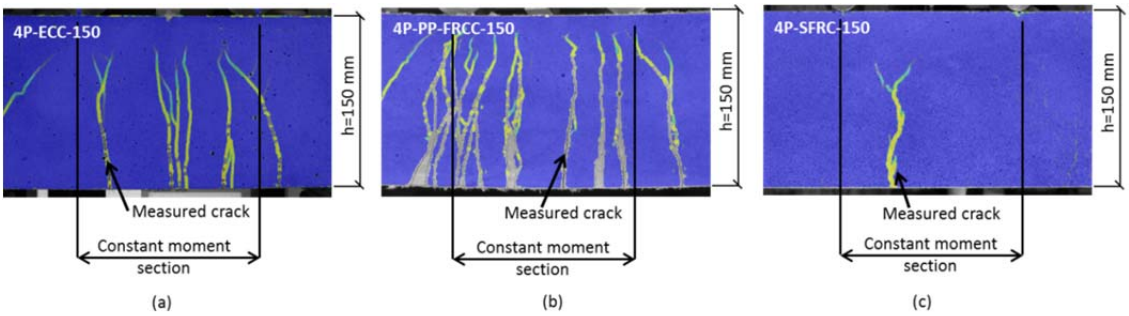


***Figure 4.3*** *Flexural cracks at ultimate load for (a) ECC, (b) PP-FRC, and (c) SFRC. Specimen names shown in the figure follow the naming convention in Table 3.3, where 4P means four-point bending beam.*

## 4.3 Stress profiles in FRC flexural beams

Figure 4.5 shows the derived flexural stress profile over the height of the ECC, PP-FRC and SFRC beams. The stress profile was computed using the DIC-measured flexural crack opening and strain profiles in Figure 4.4, and the material parameters extracted from single crack tensile in Figure 4.1 and compression tests in Figure 2.2. Tensile stresses were determined by comparing the crack width profile of the marked crack to the stress transferred across the corresponding crack openings from the cohesive relationship. Similarly, compressive stresses are determined through comparison of the measured strain in the compression zone of the beam to the measured behavior in compression. The stresses (both tensile and compressive) were directly extracted from material property tests (single crack tension and compression) at particular deformations.

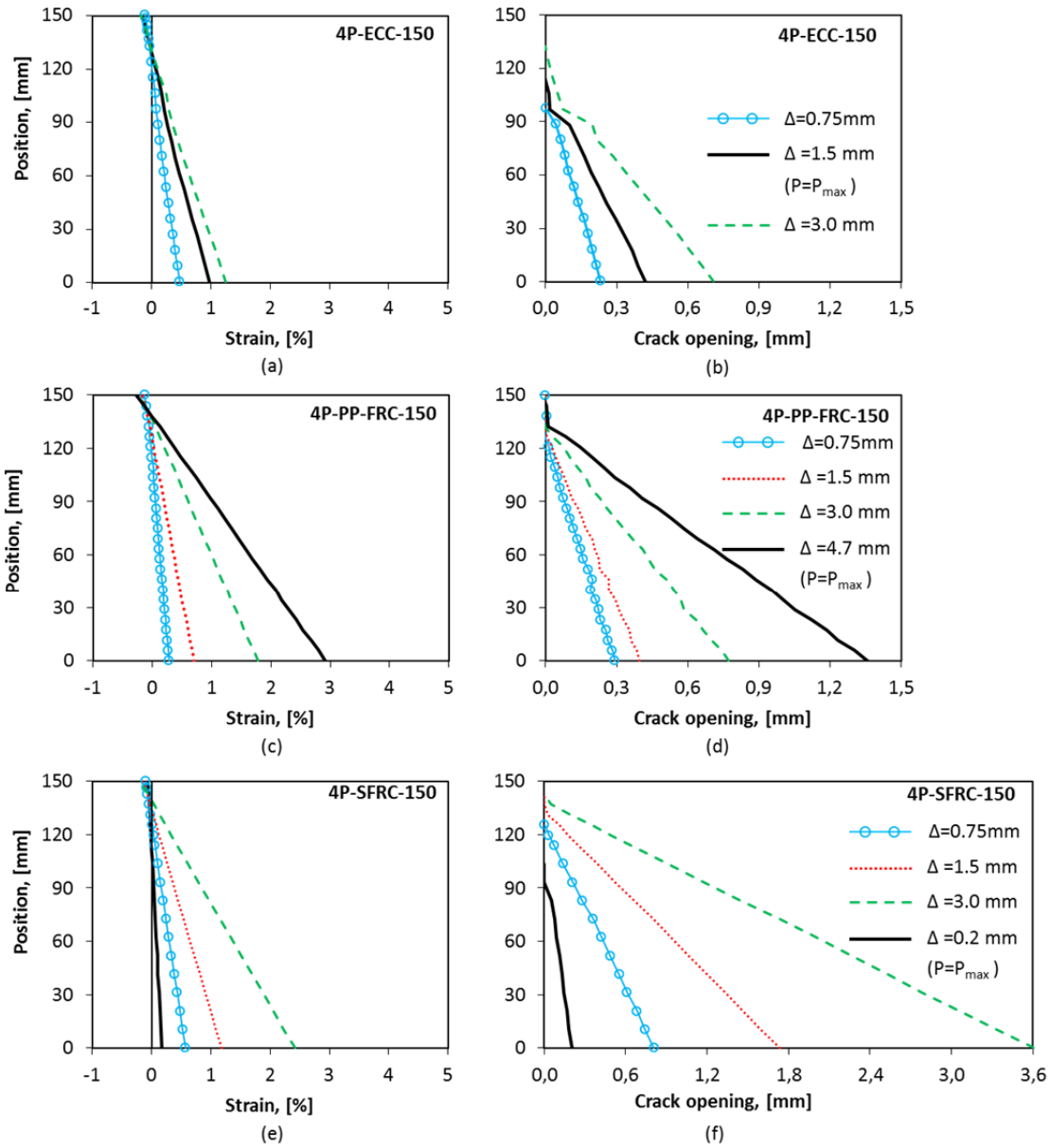


***Figure 4.4*** *Strain and crack opening profiles: Strain profiles in the constant moment region for (a) ECC, (c) PP-FRC and (e) SFRC and crack opening profiles for (b) ECC, (d) PP-FRC and (f) SFR representative crack. Specimen names shown in the figure follow the naming convention in Table 3.3, where 4P means four-point bending beam.*

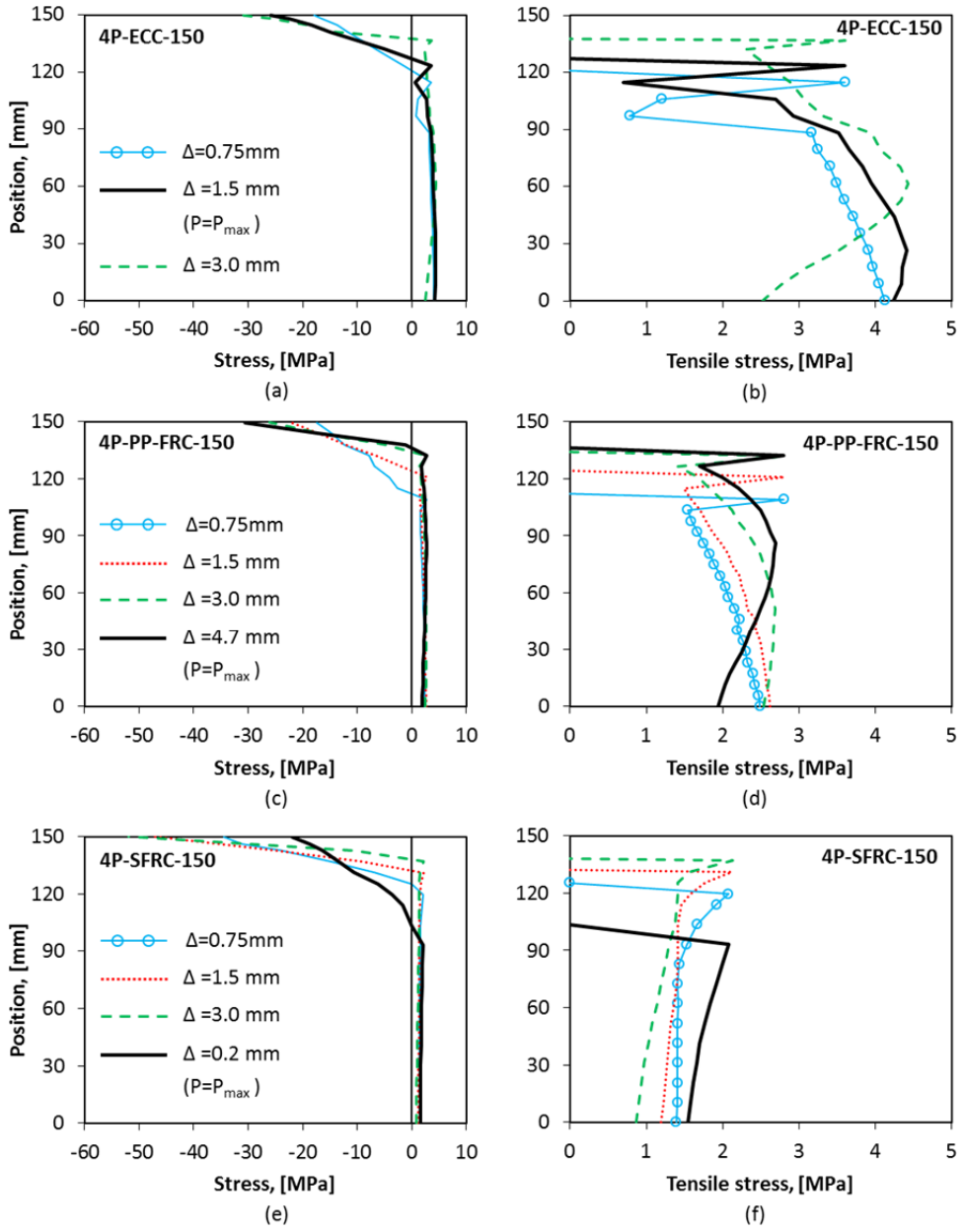


***Figure 4.5*** *Stress profiles in the cracked beams: Full stress profiles for (a) ECC, (c) PP-FRC and (e) SFRC representative crack and detailed tensile stress profiles for (b) ECC, (d) PP-FRC and (f) SFRC. Specimen names shown in the figure follow the naming convention in Table 3.3, where 4P means four-point bending beam.*

For the PP-FRC, the maximum tensile stress transfer across a crack occurs at a crack opening of approximately 0.6 mm (see Figure 4.1). As the maximum flexural crack opening found in the PP-FRC beam was approximately 1.35 mm, the stress transfer decreases for crack openings exceeding 0.6 mm. Nevertheless, as shown in Figure 4.5(d) the PP-FRC can resist additional load with crack mouth openings exceeding 0.6 mm due to the neutral axis changing its position.

***Table 4.1*** *Comparison of experimentally measured and estimated load*

| Mid-span deflection | 4P-ECC-150 | | 4P-PP-FRC-150 | | 4P-SFRC-150 | |
|---|---|---|---|---|---|---|
| | $P_{exp}$ | $P_{est}$ | $P_{exp}$ | $P_{est}$ | $P_{exp}$ | $P_{est}$ |
| mm | kN | kN | kN | kN | kN | kN |
| 0.75 | 60.4 | 63.3 | 36.6 | 40.3 | 34.9 | 29.4 |
| 1.50 | 71.7 | 75.8 | 40.4 | 47.5 | 33.0 | 27.6 |
| 3.00 | 11.4 | 11.6 | 42.4 | 51.8 | 27.2 | 23.9 |
| *$P_{exp}$=$P_{max}$ | 71.7 | 76.6 | 46.7 | 49.6 | 35.7 | 31.9 |

* for 4P-ECC-150 – 1.5 mm; for 4P-PP-FRC-150 – 4.6 mm; for 4P-SFRC-150 – 0.2 mm

The situation is similar for the ECC beams, as shown in in Figure 4.4(b). Again, as deflections increase, the position of the neutral axis approaches the compressive face, additional tensile stresses are transferred, and the moment capacity is increased. The maximum crack mouth opening at the ultimate stage in ECC beams of 0.4 mm was noticeably larger than the crack openings at the maximum load of single crack tensile specimens (0.25-0.3 mm).

For the SFRC, the peak load was reached almost immediately after cracking occurred. The maximum crack opening at the most tensile fiber of the beam was measured 0.2 mm at peak load.

Table 4.1 shows the experimentally measured load ($P_{exp}$) at various mid-span deflections and the estimated load ($P_{est}$) that should be applied to the beam to reach a specific crack opening. The resulting tensile force, calculated a s sum of tensile stresses in stress profile, shown in Figure 4.5, was multiplied by the moment arm, to calculate the estimated moment in the cross-section. $P_{est}$ is the corresponding applied load required to generate the calculated moment. Results in Table 4.1 indicate this simple model accurately predicted the actual applied loads within 5-10% for the ECC beams, 5-20% for the PP-FRC beams, and 5-15% for the SFRC. The results indicated potential in predicting flexural behavior based on compressive and tensile single crack behavior for the FRC materials studied. While this observation is perhaps not unexpected, the results also indicate the standard four-point bending beam test method accurately assesses the tensile characteristics of the studied FRC materials.

## 4.4 Conclusions

Results from flexural tests of the FRC materials studied (ECC, PP-FRC, and SFRC) were compared to information obtained from direct tension and compression tests. Based on the obtained experimental results from material properties tests and DIC measured strain and crack opening profiles, stress profiles for flexural beams were estimated. Bending moments, calculated from the stress profiles, predict the applied

loads and the loading capacities with reasonable accuracy, indicating the potential to predict the flexural behavior using compressive and tensile single crack behavior of the fiber reinforced concrete.

These results provided an early indication that modeling the flexural response of FRC based on the basic tensile and compressive responses is warranted, and that the four-point bending beam is a suitable means to assess tensile properties of the studied FRC materials. Chapter 5 describes a novel modeling approach for the prediction of the load-deformation response of flexural members constructed with FRC materials.

# Chapter 5

# Modeling the load-deformation response of FRC structural members

This chapter describes a modeling approach to predict the load-deformation response of FRC flexural elements. The model predicts the flexural behavior of FRC by assuming a loaded structure consisting of a multitude of interconnected cracked segments, called Representative Flexural Segments (RFS), combined with rigid segments representing uncracked regions. The behavior of the RFS is characterized by the energy needed to deform a segment by a given rotational angle which can be derived either from material properties in direct tension and compression or from flexural beam tests. The model, which can be applied to FRC materials with tension softening and strain hardening characteristics, predicts the load necessary to deform a structural element by a specific deflection. Experimentally obtained results from structural tests verify the model realistically predicts the load-deformation response of flexural elements.

The intent of the model developed in this chapter is to form a potential basis, including a general design approach, design equations, and design verification (i.e., quality control) test methods, for the codification of structural design with FRC's. The model presented here focuses on the flexural performance of FRC's. It is noted that should such a design code for FRC be developed and widely accepted, this would pave the way for significantly wider future structural applications of FRC.

## 5.1 Review of previous studies on structural design of FRC

In recent years, fiber reinforced concrete (FRC) with discrete, short, and randomly distributed fibers are being specified for structural applications with significant flexural loads, including ground- and pile-supported slabs, tunnel linings, various precast elements, raft foundations, and other applications (Oslejs 2008; Winkler et al. 2014). In certain cases, fibers provide the only reinforcement, while in other cases fibers are used in combination with a reduced amount of traditional reinforcement. Currently various design codes, guidelines and suggested methods of design procedure of FRC flexural member are available in the literature (DAfStb 2010; fib 2012; SS812310 2014). Typical FRC flexural members are design based on the measured compressive strength and tensile properties that are indirectly assessed through analysis of flexural test based on various, occasionally inaccurate, assumptions. Compressive properties of concrete and FRC are similar and can be determined from compressive cylinder or cube tests. For ordinary concrete, tensile strength is commonly assessed indirectly by the split cylinder test, various beam test methods, or through empirical relations to the measured compression strength. The split cylinder test (e.g., ASTM C 496, EN 12390-6) provides sufficient information for brittle materials in tension, where post-cracking tensile strength and deformations are negligible compared to cracking strength. However, materials with significant post-cracking strength and deformations, like FRC, require new test methods. Using the direct uni-axial tensile tests (162-TDF 2001; JSCE 2008; Paegle & Fischer 2013), the stress-crack opening or stress-strain properties of FRC can be derived directly and, together with the compressive properties, can be used in structural design. However, as previously discussed, the direct tension test methods samples are laborious and difficult to implement for field quality control purposes.

Alternatively, most design codes and recommendations for FRC (fib 2012; Ostergaard et al. 2005; JCI-S-003 2007; SS812310 2014; TR63 2007) proposed the use of three- or four-point bending tests to estimate tensile properties based on simplified assumption and analysis of the obtained load-deformation (strain), load-deflection, or load-CMOD curves. In most cases, simplified strain compatibility and stress block analysis of a layered cross section (i.e., an assumed stress profile) is required to compute the design ultimate moment capacity of a structural element. Therefore, two simplified assumptions are made, one for deriving the tensile properties from the flexural test, and a second in the design model for calculating the plastic moment capacity. Also, the flexural capacity of FRC members can be designed based on a moment curvature analysis (Soranakom & Mobasher 2009) using simplified and normalized moment-curvature properties of FRC derived from a three-point bending (162-TDF 2002). The model by Soranakom and Mobasher is developed mainly for slab applications where the internal moment is relatively low, compared to cracking moment, and shear is not critical. While this approach can be used to design both for

the ultimate strength and for serviceability, it is not intended for strain hardening FRC.

This chapter describes a novel modeling approach that links the energy required to induce rotational deformations in a representative flexural segment (RFS) to the load-deformation response of FRC structural members governed by flexure. Figure 5.1 illustrates the general modeling approach. The model develops the properties of the representative flexural segment through either direct tension, together with compression testing, or flexural testing. The properties assigned to the representative flexural segment describe the energy needed to deform the segment by a specific rotation angle. The properties of the RFS are assigned to deformable sections arranged between rigid sections to reflect the deformed shape of the structural element as predicted by yield line theory. The model can be applied to FRC materials with tension softening and strain hardening characteristics.

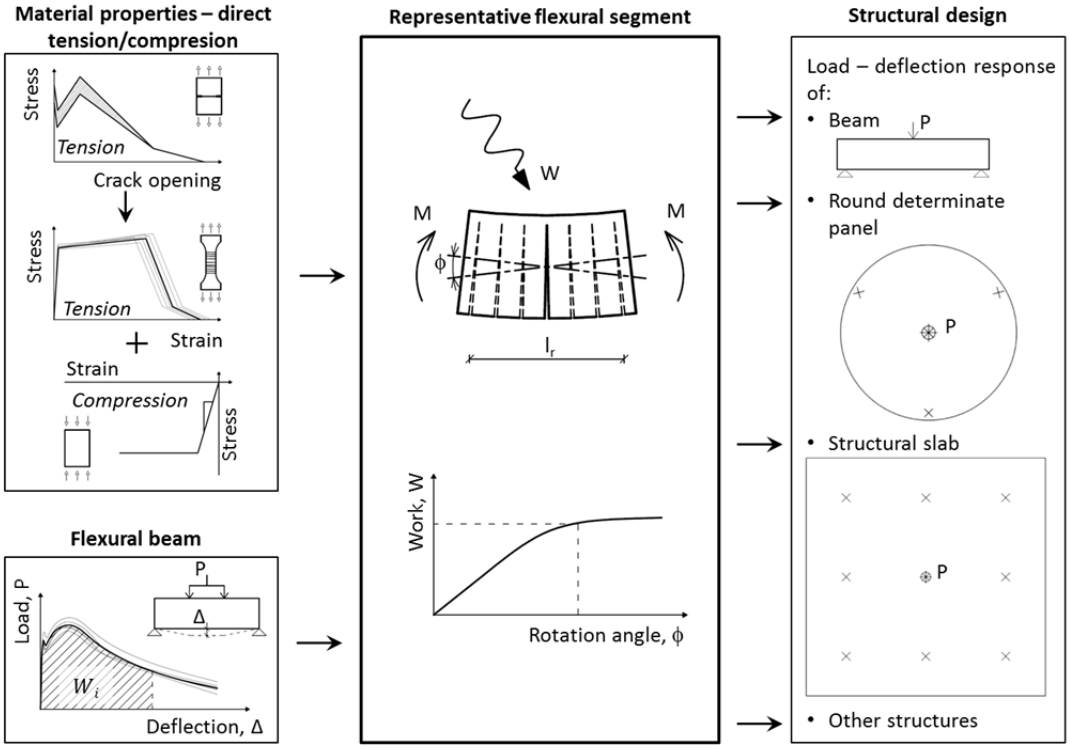


***Figure 5.1*** *Overview of connection between tensile and flexural elements*

## 5.2 Fundamental description of modeling approach

Figure 5.2 illustrates the RFS properties, which are derived from a moment-rotation angle relationship that is determined through testing and analysis procedures described in the folowing Sections 5.2.1 and 5.2.2. The area under the moment-rotation angle (M-ϕ) curve in Figure 5.2(a) is the work, $W_i$, needed to deform the RFS a given rotation angle, $\phi_i$, which can be expressed as:

$$W_i = \int_0^{\phi_i} M d\phi \tag{5.1}$$

As the work, $W_i$ and rotation angle, $\phi_i$, , are determined from a FRC segment with particular dimensions of width $b$, height $h$ and a representative length $l_r$, both parameters must be normalized to $\overline{W}$ [J/m$^2$] and angle $\overline{\phi}$ $[rad \cdot m]$ to characterize the material independent of the dimensions ($b$ and $h$):

$$\overline{W} = \frac{W}{h \cdot b} \quad and \quad \overline{\phi} = \phi \cdot h \tag{5.2}$$

Where $\overline{W}$ is normalized work and $\overline{\phi}$ is normalized rotation angle.

Figure 5.2(b) illustrates the derived normalized work-rotation angle relationship, which is applied to model the performance (i.e., load-deformation response) of a structural element. Section 5.5 provides case-studies on how the RFS is applied to various flexural elements and verifies the accuracy of the model through comparison with structural test results.

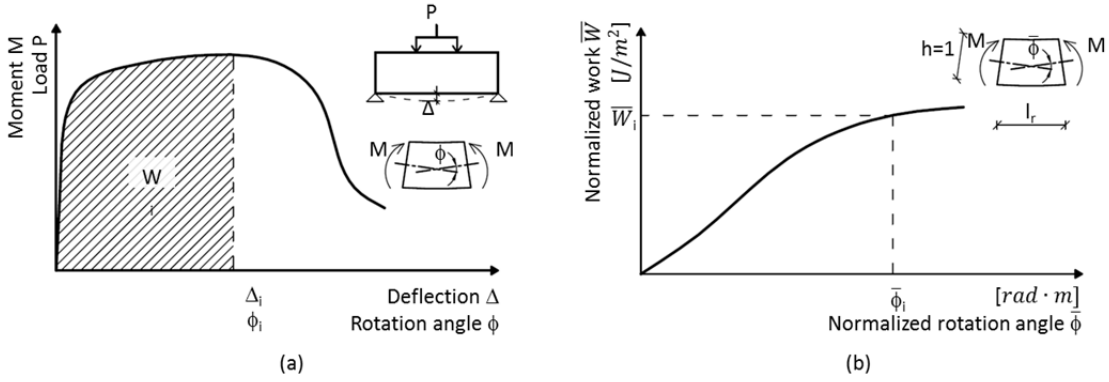


***Figure 5.2*** *(a) The moment-rotation angle relationship of the RFS and (b) the property of the RFS, which is the normalized work-rotation angle relationship*

As illustrated in Figure 5.1, the properties of the RFS may be derived through flexural or uniaxial tension/compression test methods. Section 5.2.1 describes the derivation of the RFS properties using flexural tests, while Section 5.2.2 describes the use of uniaxial tension and compression tests.

### 5.2.1 Derivation of RFS properties from flexural beams

Using standard beam test methods, the information in Figure 5.2(a) can be calculated from the measured load-deflection curve as a function of the beam geometry and loading configuration. Figure 5.3 illustrates the assumed simplified deformed shapes and corresponding curvature and rotation angle distributions over the length of three-

and four-point bending beams. As shown in Figure 5.3(a) and (b), the curvature and rotation angle distributions for four-point bending beams change depending on the post-peak response. For deflection hardening FRC (DH-FRC), the curvature is uniformly distributed across the middle third of the beam, while for deflection softening FRC (DS-FRC) the curvature is concentrated near the mid-span. Due to the concentrated loading in the three-point bending beam, the curvature and rotation angle distributions are assumed independent of deflection hardening/softening (Figure 5.3(c)).

The rotation angle can be determined as a function of the assumed deflected shape, the mid-span deflection and the beam length, as illustrated in Figure 5.3. For the four-point bending DH-FRC beam, the rotation angle can be expressed as follows:

$$\phi = \frac{6\Delta}{L} \tag{5.3}$$

For the four-point bending DS-FRC beam and three-point bending beams, the rotation angle can be expressed as follows:

$$\phi = \frac{4\Delta}{L} \tag{5.4}$$

Using Equations (5.2) through (5.4), the moment-rotation angle and corresponding normalized work-rotation angle relationship is established.

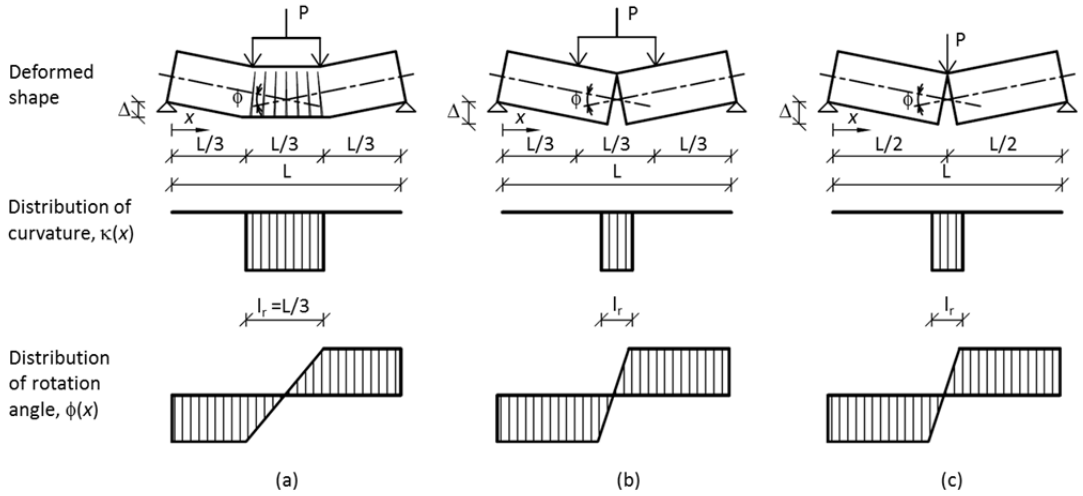


***Figure 5.3*** *Assumed deformed shapes and corresponding curvature and rotation angle distributions: (a) four-point bending DH-FRC beam, (b) four-point bending DS-FRC beam and (c) three-point bending beams*

## 5.2.2 Derivation of RFS properties from tension and compression

The properties of the RFS can also be established through uniaxial tension and compression responses, which are simplified in Figure 5.4(a) and (b) for tension

softening FRC and strain hardening FRC, respectively. The compressive response is represented as linear elastic, perfectly plastic, while the tensile response is represented by a multi-linear curve dependent on the post-cracking response (i.e., softening or hardening) of the material. This section presents the derivation of the RFS properties based on the compression and tension material parameters. The following subsections describe how material parameters are extracted from the two direct tension test methods considered in this study; the single crack notched coupon test (presented in Section 5.2.2.1) and the dogbone specimen (presented in Section 5.2.2.2).

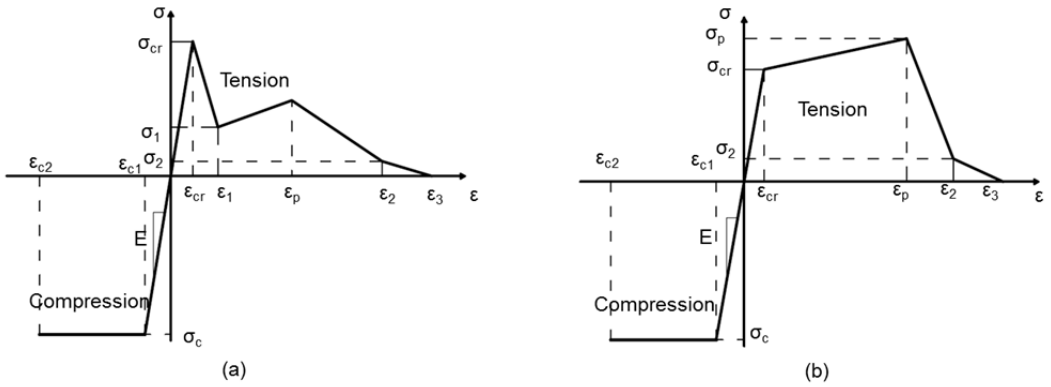


***Figure 5.4*** *Input data used to derive RFS properties for (a) a tension softening FRC, (b) a strain hardening FRC. Note: For strain hardening FRC, it is assumed that* $\boldsymbol{\sigma_{cr} = \sigma_1}$ *and* $\boldsymbol{\varepsilon_{cr} = \varepsilon_1}$

As shown in Figure 5.4, the compressive behavior of FRC is assumed bilinear with a linear elastic ($\sigma = E\varepsilon$) first stage and a perfectly plastic ($\sigma = \sigma_c$) second stage. The multi-linear tensile behavior of FRC is described by an initial linear elastic ($\sigma = E\varepsilon$) stage that terminates at the cracking strength, $\sigma_{cr}$. For tension softening FRC (Figure 5.4(a)) cracking results in an immediate and significant drop in stress. For a strain hardening FRC (Figure 5.4(b)), it is assumed that crack initiation results in an insignificant stress drop. The stress-strain relationships in Figure 5.4 can be expressed as:

$$\sigma(\varepsilon) = \begin{cases} \sigma_c & for\ \varepsilon_{c2} \le \varepsilon < \varepsilon_{c1} \\ E\varepsilon & for\ \varepsilon_{c1} \le \varepsilon < \varepsilon_{cr} \\ \sigma_{cr} + A'(\varepsilon - \varepsilon_{cr}) & for\ \varepsilon_{cr} \le \varepsilon < \varepsilon_1 \\ \sigma_1 + A\,(\varepsilon - \varepsilon_1) & for\ \varepsilon_1 \le \varepsilon < \varepsilon_p \\ \sigma_p + B\,(\varepsilon - \varepsilon_p) & for\ \varepsilon_p \le \varepsilon < \varepsilon_2 \\ \sigma_2 + C\,(\varepsilon - \varepsilon_2) & for\ \varepsilon_2 \le \varepsilon < \varepsilon_3 \end{cases} \tag{5.5}$$

Where:

$E = \dfrac{\sigma_c}{\varepsilon_{c1}}$ Modulus of elasticity

$$A' = \frac{\sigma_1 - \sigma_{cr}}{\varepsilon_1 - \varepsilon_{cr}}$$

$$A = \frac{\sigma_p - \sigma_1}{\varepsilon_p - \varepsilon_1}$$

$$B = \frac{\sigma_2 - \sigma_p}{\varepsilon_2 - \varepsilon_p}$$

$$C = \frac{-\sigma_2}{\varepsilon_3 - \varepsilon_2}$$

For strain hardening FRC $\sigma_{cr} = \sigma_1$ and $\varepsilon_{cr} = \varepsilon_1$ therefore the third line in Equation (5.5) is neglected.

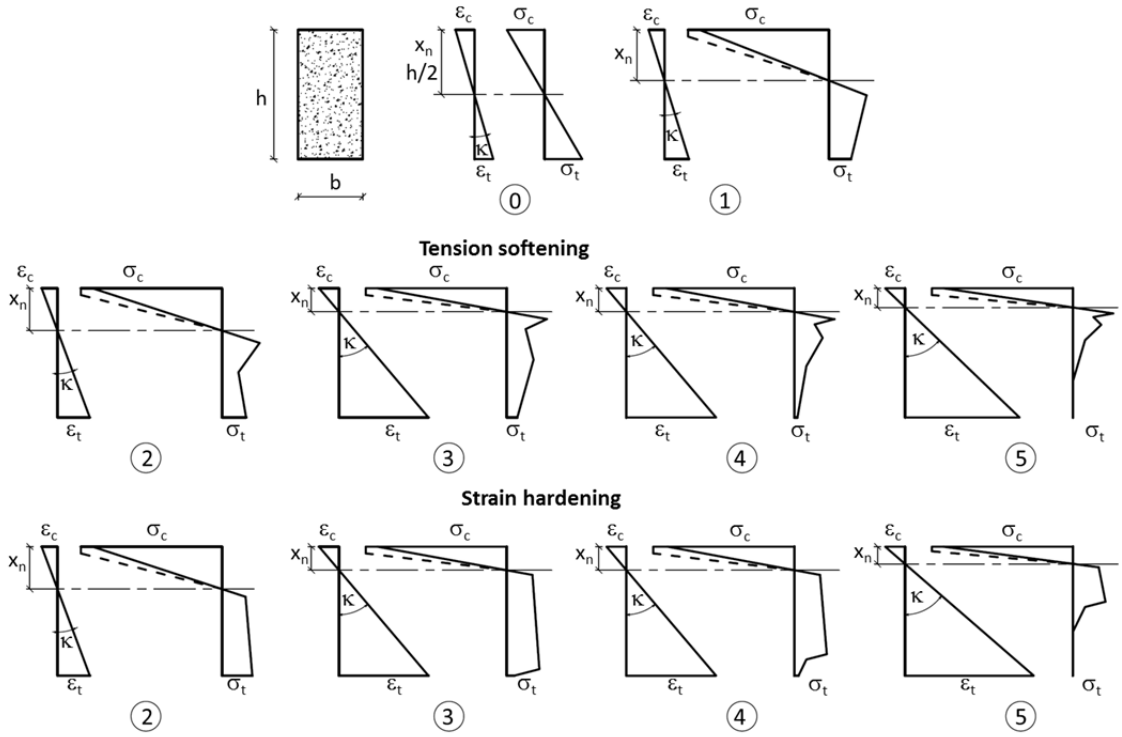


***Figure 5.5*** *Possible stress distribution stages over the cross section of the beam*

Figure 5.5 presents the possible stress distributions from Equation (5.5) applied to the RFS at various stages in the strain profile defined as:

- Stage 0 - $\varepsilon_t \leq \varepsilon_{cr}$
- Stage 1 - $\varepsilon_{cr} < \varepsilon_t \leq \varepsilon_1$
- Stage 2 - $\varepsilon_1 < \varepsilon_t \leq \varepsilon_p$;
- Stage 3 - $\varepsilon_p < \varepsilon_t \leq \varepsilon_2$;
- Stage 4 - $\varepsilon_2 < \varepsilon_t \leq \varepsilon_3$; and
- Stage 5 - $\varepsilon_t > \varepsilon_3$.

where $\varepsilon_t$ is strain in tension at bottom fiber of the beam. Stage 0 represents the cross section of beam before cracking, while stage 1 represents the immediate stress drop after cracking. As mentioned above, for strain hardening FRC, this drop is assumed negligible. After stage 1, Figure 5.5 provides distinct stress profiles for tension softening and strain hardening FRC. These profiles are based on measured stress profiles presented in Figure 4.5.

According to (Elsaigh 2007), with the assumptions that 1) the internal force are in equilibrium with external load, 2) plane section perpendicular to the center plane remain plane through bending, and 3) internal axial force is zero; the moment-curvature relation can be found by the following four steps:

1. Choose the tensile strain values of bottom fiber of the beam;
2. For a given bottom fiber tensile strain value calculate the corresponding compressive strain and the heights of compressive zone, $x_n$:

$$\frac{x_n b}{\varepsilon_c}\int_{\varepsilon_c}^{\varepsilon_t}\sigma(\varepsilon)\,d\varepsilon = 0\ (Internal\ axial\ force\ is\ zero) \tag{5.6}$$

$$\frac{x_n}{h} = \frac{\varepsilon_c}{(\varepsilon_c - \varepsilon_t)} \tag{5.7}$$

3. Calculate corresponding moment, M:

$$M = \frac{x_n^2 b}{\varepsilon_c^2}\int_{\varepsilon_c}^{\varepsilon_t}\sigma(\varepsilon)\varepsilon\,d\varepsilon \tag{5.8}$$

4. Calculate corresponding curvature, κ:

$$\kappa = \frac{\varepsilon_t}{(h - x_n)} \tag{5.9}$$

According to classical beam theory, integrating curvature over the length of the beam provides the change in rotation angle:

$$\phi_x = \int_0^{x\ (0\le x\le L)} \kappa\,dx + C_1 \tag{5.10}$$

Where

$$C_1 = -\int_0^{L/2} \kappa\,dx \tag{5.11}$$

Assuming curvature is uniform and concentrated in a representative flexural segment that has a representative length, $l_r$, while the rest of the beam is rigid with $\kappa = 0$, the rotation angle ($\phi$, as shown in Figure 5.3) at increment, *i* (as shown in Figure 5.2) can then be calculated as:

$$\phi_i = \kappa_i \, l_r - \frac{1}{2}\kappa_i \, l_r = \frac{1}{2}\kappa_i \, l_r \tag{5.12}$$

Representative length is determined empirically, based on the geometry of the element, or the expected spacing between failure cracks. *fib* Model code 2010 (fib 2012) and Swedish standard SS 812310 (SS812310 2014) refers to representative length as characteristic length $l_{cs} = h$ in case of FRC without traditional reinforcement.

The representative length $l_r$ is assumed equal to the RFS height for DS-FRC and for standard three-point DH-FRC beams (Figure 5.3(b) and (c)). For standard four-point DH-FRC beams, the representative length is equal to the length where multiple cracking is expected to occur, or the length of the constant moment region (Figure 5.3(a)).

#### 5.2.2.1 Single crack notched coupon test

This section describes the general analytical method used to determine the tensile stress-strain (σ-ε) relationship of FRC using the single crack notched coupon test procedure described in Section 2.3.2. The described concept was previously used in (Yang & Fischer 2006); however, the existing model is extended in this section by adding a bi-linear softening branch.

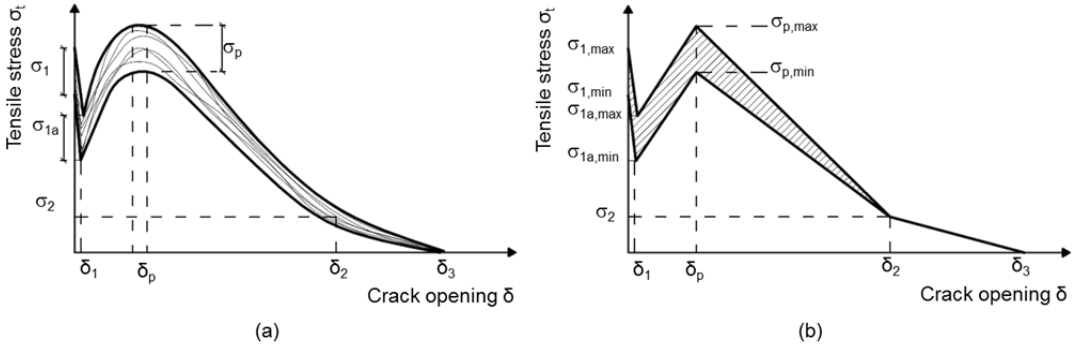


***Figure 5.6*** *Single crack tension: (a) example of experimentally obtained tensile stress-crack opening relationships; (b) Tensile stress-crack opening relationship used for model*

Figure 5.6(a) illustrates experimentally obtained stress-crack opening curves from the single crack FRC samples, which are used to develop the simplified tensile stress-crack opening relationship shown in Figure 5.6(b). The tensile stress-crack opening relationship in Figure 5.6(b) can simulate strain hardening, and the accompanying multiple cracking, or tension softening responses of FRC under uniaxial tension. The tensile stress-crack opening relationship shown in Figure 5.6(b) consists of the upper and lower limits of the following parameters:

- The cracking strength ($\sigma_{1,min}$ and $\sigma_{1,max}$) with a corresponding crack opening of 0;
- The strength immediately after cracking ($\sigma_{1a,min}$ and $\sigma_{1a,max}$) with an assumed corresponding crack opening of 0 (shown in Figure 5.6(b) as $\delta_1$, which is slightly offset from 0 for illustrative purposes only);
- The peak fiber bridging strength ($\sigma_{p,min}$ and $\sigma_{p,max}$) with corresponding crack opening ($\delta_p$) which is defined as the average corresponding crack opening from experimental observations;
- The post-peak fiber bridging behavior is assumed bi-linear, with a stress ($\sigma_2$) and corresponding crack opening ($\delta_2$) marking the slope change in the post-peak (softening) branch;
- The critical crack opening ($\delta_3$) at which the stress transferred across the crack reaches approximately 0.

As shown in Figure 5.4, the RFS requires the tensile response of the FRC to be characterized as a stress-strain relationship. To convert the stress-crack opening relationship in Figure 5.6(b) to stress-strain the modeling approach in (Yang & Fischer 2006) is used. Figure 5.7 illustrates the model and provides an example of its application. The model predicts the stress-strain behavior of a virtual specimen with length, L, which is randomly divided into segments with width equal to the minimum crack spacing, $s_i$, (Figure 5.7(a)). The minimum crack spacing, $s_i$, is dependent on sizes and distribution of flaws in cementitious matrix and the mixture design of the FRC (Wang 2004). Each segment is assigned an un-cracked stiffness, EA, while the interfaces between segments are assigned tensile stress-crack opening relationships. As shown in Figure 5.7(b), each tensile stress-crack opening relationship is determined randomly (uniform probability distribution) by selecting parameters from within the constraints of the upper and lower limits determined from experimental data. By applying step-wise deformations to the virtual specimen, the follow occurs:

- The virtual specimen deforms elastically up to the lowest assigned cracking strength ($\sigma_{1,min}$). When this stress value is reached, the interface with the lowest cracking strength opens, resulting in a drop in the average stress to the $\sigma_{1a}$ value assigned to the 'cracked' interface.
- With continued deformation, the 'cracked' interface continues to open and the tensile stress in the virtual specimen increases according to the crack stiffness, ($K_{f,i}$) assigned to the 'cracked' interface.
- Subsequent cracking occurs as the tensile stress in the virtual specimen reaches the next lowest cracking strength ($\sigma_{1,i=2}$) assigned. The preset interfaces continue to crack until the lowest assigned cracking strength ($\sigma_{1,i}$) remaining exceeds the assigned fiber bridging strength ($\sigma_p$) of the previously

'cracked' interfaces, or until all preset interfaces have 'cracked' (i.e., crack saturation).

- With continued deformation, the lowest assigned peak fiber bridging strength ($\sigma_p$) of the 'cracked' interfaces is reached, resulting in a decreased tensile stress in the virtual specimen, leading to the failure. The model assumes that only the interface with the lowest assigned peak fiber bridging strength continues to open after this point is reach.

If the material is tension softening, the maximum peak fiber bridging strength is lower than the minimum matrix cracking strength (i.e., $\sigma_{p,max} < \sigma_{1,min}$) and a single crack is formed. To determine the uniaxial tension stress-strain curve for tension softening FRC, the crack opening is normalized by the representative length of the RFS shown in Figure 5.3(b) and (c).

For a virtual specimen with multiple cracking, the deformation of each 'cracked' interface is summed and the strain in the virtual specimen is calculated by normalizing by the initial specimen length. As the tensile stress-crack opening relationships of each interface are selected randomly (uniform probability distribution), the modeled uniaxial tension stress-strain curves differ each time the model is run. To ascertain an average uniaxial tension stress-strain curve, the model is simply run numerous times and the averaged curve is used in the RFS.

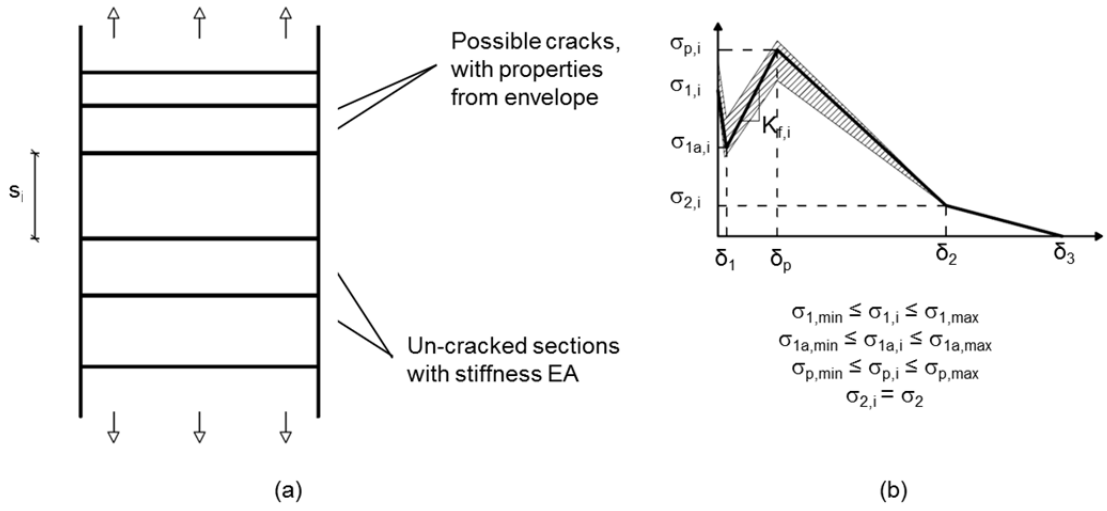


***Figure 5.7*** *Principle of model to predict uni-axial tensile stress-strain behavior from stress-single crack opening properties*

### 5.2.2.2 Dogbone specimen

For strain hardening FRC, the uniaxial tension stress-strain relationship in Figure 5.4(b) is directly measured using the dogbone specimen discussed in Section 2.3.2.3.

## 5.3 Modeling structural responses using the RFS

Structures subjected primarily to flexural loading can be assumed to consist of individual rigid segments, connected by deformable segments that require energy to induce rotational deformations. The amount of energy required to induce rotations is dependent on the properties of the RFS and the extent to which the segment is deformed. The RFS properties include the normalized work-rotation angle relationship shown in Figure 5.2(b) and the geometry of the segment.

To model the load-deflection response of a FRC structural element using the RFS, the first step is to assess the possible deformed shapes of the structure. Plastic analysis was used to determine the favored deformed shape of the FRC structural element and to assign the locations of rigid and deformable segments. The rotation angle of the yield lines, which are assumed equal to the rotation angle of the deformable segments, can be calculated from the geometry of the deformed shape. By knowing the normalized work-rotation angle relationship (Figure 5.2(b)) of an RFS, with a unit height and unit width, the work-rotation angle relation can be derived for a segment with a height of $h_s$ as:

$$W_{s,i} = \overline{W}_i \cdot h_s \quad and \quad \phi_{s,i} = \frac{\overline{\phi}_i}{h_s} \tag{5.13}$$

where $W_{s,i}$ is the work done to deform a segment with a height of $h_s$ and unit width ($b=1$) by a rotation angle $\phi_{s,i}$, and $\overline{W}_i$ is the normalized work needed to deform a segment with a unit height ($h=1$) and unit width ($b=1$) for a normalized rotation angle $\overline{\phi}_i$.

The work done to deform a structure for a deflection $\Delta_i$ is a sum of work done by all segments for a corresponding rotation angle:

$$W_{st,i} = \sum W_{s,i} \tag{5.14}$$

Also the external work done to deform a structure for a deflection can be calculated as:

$$W_{st,i} = \int_0^{\Delta_i} P_{st}\, d\Delta \tag{5.15}$$

Thus, the load applied to the structure can be derived as:

$$P_{st} = \frac{dW_{st}}{d\Delta} \tag{5.16}$$

Thus the full load-deflection behavior of a structure is determined.

## 5.4 Determination of input parameters

Two series of experimental studies were performed: i) material testing for determination of input parameters and ii) structural testing for the application and verification of the model. Two distinct FRC's were tested, the ECC and the SFRC described in Chapter 2. Section 2.1 provides details on the materials and specimen preparations, while Sections 2.3 and 3.2 provide details on the material characterization methods.

### 5.4.1 Determination of material properties

#### 5.4.1.1 Compression

Detailed information of compressive properties of ECC and SFRC are provided in Section 2.3.1. The average measured compressive strength was 52.0 MPa, and 57.1 MPa for ECC and SFRC, respectively. The average secant elastic modulus in compression was 16.0 GPa in ECC and 34.5 GPa in SFRC. The bilinear compressive curve given in Figure 3.4 of Eurocode 2 (EN1992-1-1 2010) was used, with ultimate strains of 0.45% and 0.35% of ECC and SRFC, respectively.

#### 5.4.1.2 Tensile stress-crack opening

The tensile stress-crack opening properties from Section 2.3.2 have been averaged in Figure 5.8(a) and (b) and are used as input data for the model here. For strain hardening FRC these test results have been used to predict the overall uni-axial tension properties in terms of tensile stress-strain. To predict the multiple cracking in uni-axial tension, the variation of test results were taken account. Therefore, the minimum and maximum cracking strengths, immediate post-cracking strengths, and fiber bridging strengths has been determinate in Figure 5.8(c). The post-peak fiber bridging strength has been assumed bilinear.

The SFRC used in this study had a clear tension softening behavior, with a matrix cracking strength considerably higher than the maximum fiber bridging strength. As no multiple cracking was expected in this material, the average tensile stress crack opening properties of SFRC were directly used in modeling the flexural behavior, as shown in Figure 5.8(b) and (c).

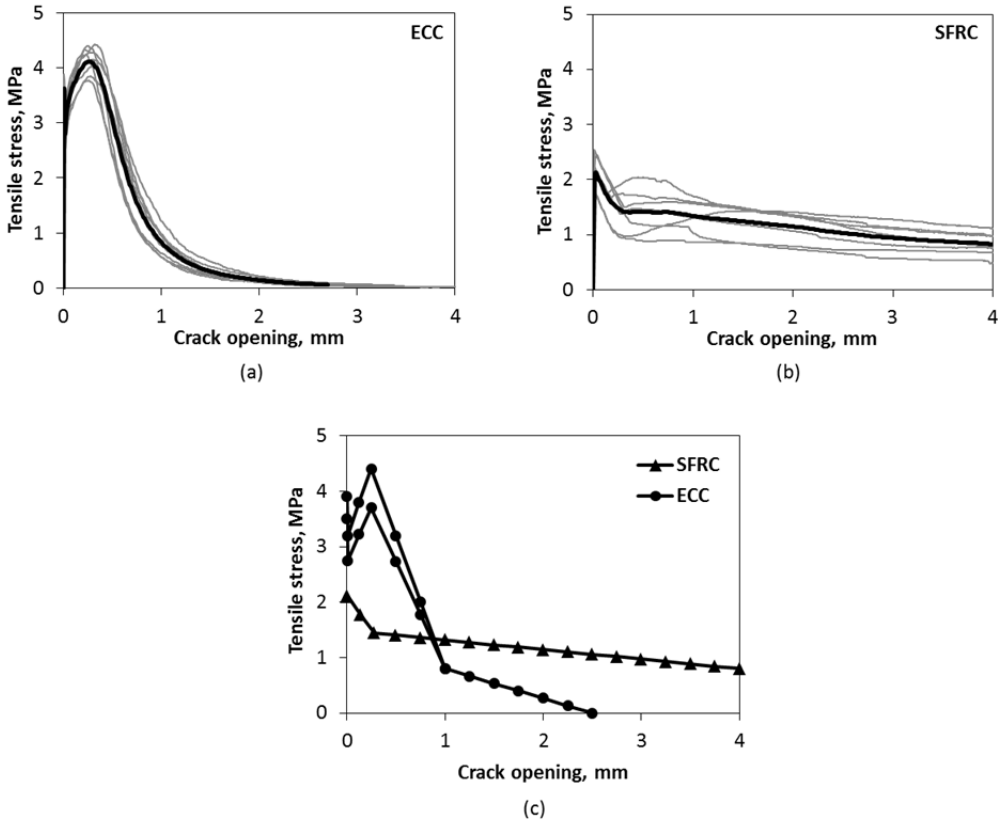


***Figure 5.8*** *Tensile stress – crack opening of single crack notched coupon tests: (a) experimentally obtained of ECC; (b) experimentally obtained of SFRC; (c) input for model*

#### 5.4.1.3 Tensile stress-strain

Dogbone testing, which allows for the formation of multiple cracks, was performed and modelled for the strain hardening ECC only. As discussed in Section 5.2.2.1 and illustrated in Figure 5.7, the model for predicting the tensile stress-strain behavior of the dogbone specimen selects random values from within the envelope of measured tensile stress-crack opening response in Figure 5.8(c). As shown in Figure 5.9(a), which provides model results from 20 runs, each iteration of the model provides a unique result. This variation in model results is similar to the behavior observed in experimental results shown in Figure 5.9(b). The average model result, plotted both in Figure 5.9(a) and (b), indicates the model accurately estimates the dogbone (stress-strain) response based on the single crack results.

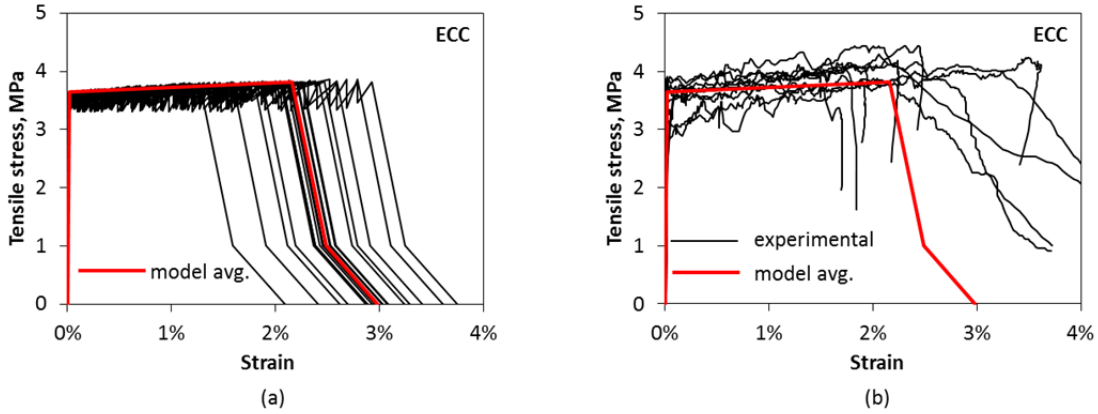


***Figure 5.9*** *Tensile stress-strain: (a) Results of model and (b) experimental results with average curve from model*

#### 5.4.1.4 Flexural beam

Figure 5.10 shows the average of the experimentally obtained load-deflection responses from ECC and SFRC four-point bending beams, which are presented in Section 3.2.2.2.

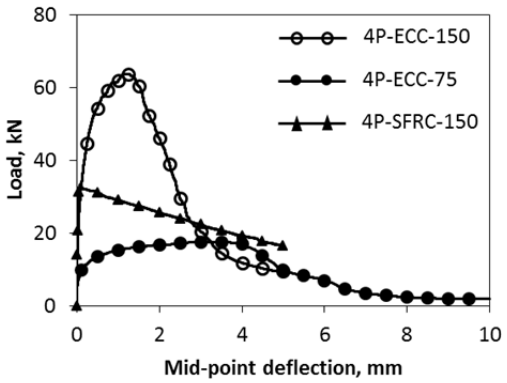


***Figure 5.10*** *Experimentally obtained results of four-point bending beams*

### 5.4.2 Determination of RFS properties

Sections 5.2.1 and 5.2.2 explain that the normalized work-rotation angle relationship of the RFS can be derived directly from flexural beams or modeled from tension and compression properties. Figure 5.11 shows the properties of the RFS determined for a strain hardening FRC (ECC) and a tension softening FRC (SFRC). In both cases, the RFS properties were determined from the analysis process outlined in Section 5.2 on direct tension/compression test results (shown in red in Figure 5.11) and from four-point bending beams (shown in black in Figure 5.11). The properties of the RFS determined for the SFRC were nearly identical regardless of the derivation procedure, while properties for the ECC varied depending on the analysis method. Properties for ECC obtained from four-point bending beams with a height of 75 mm and from the uniaxial tension/compression compared well, while properties obtained a 150 mm

high beam indicate less energy needed to deform the RFS at given rotational deformations. Differences in the properties of the RFS obtained from beams with varying heights and from analysis of direct tension/compression test data is likely attributable to variations in preferential fiber orientation. The tensile notched coupon test, with thicknesses ranging from 12 to 16 mm, may cause an aligned orientation of the fibers. By increasing the specimen dimensions (e.g., 4P-ECC-75 and -150), the fiber orientation is more random causing a change in the material response. The model currently does not directly account for varying fiber orientation.

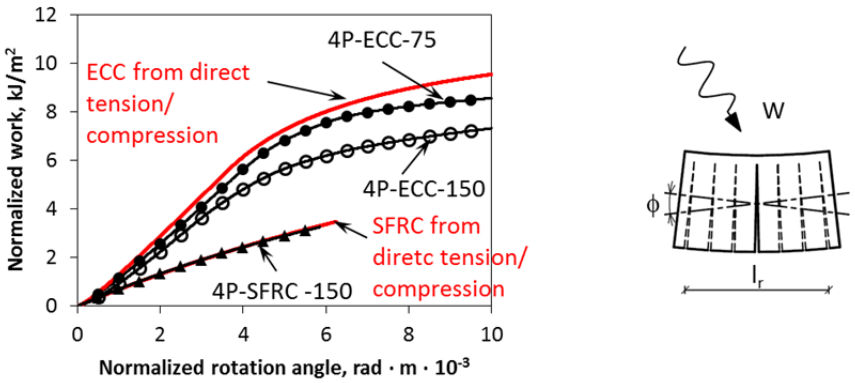


***Figure 5.11*** *RFS properties observed by direct tension/compression method and from four-point bending beams*

## 5.5 Model verification

To assess the accuracy of the modeling approach, four-point bending beams and structural round determinate panels (RDP) were tested as presented in the following sections.

### 5.5.1 Beams modeled from RFS properties determined through direct tension and compression

Figure 5.12(a) and (b) show experimentally obtained and modeled load-deflection curves for ECC four-point bending beams with heights of 150 mm and 75 mm, respectively. Results in Figure 5.12(b) show the model quite precisely predicts the behavior of the 75 mm high four-point bending beam, although slightly (<1.1 times) overestimates both the peak strength and the corresponding deformation capacity compared to the average experimentally observed curve. Figure 5.12(a) shows the experimentally obtained and modeled load and deformation capacity for the 150 mm high four-point bending beam are not predicted as accurately by the model. The experimentally obtained peak strength averaged from five beams was approximately 1.2 times lower that the modeled strength and the deflection at peak load approximately two times smaller than the modelled. These differences may be a result of size effect of the larger beams, as was observed in (Zi et al. 2014), and due to the

orientation of the fibers. The single crack tensile coupon test sample and the dogbone test samples are cast with a thickness of 12 to 25 mm, which results in a beneficial preferential orientation of the fibers. For the beams, with larger cross-sections, the fiber orientation is more random and therefore less beneficial to the section properties and the structural performance. The model, in its current state, does not account for size effect or the orientation of fibers.

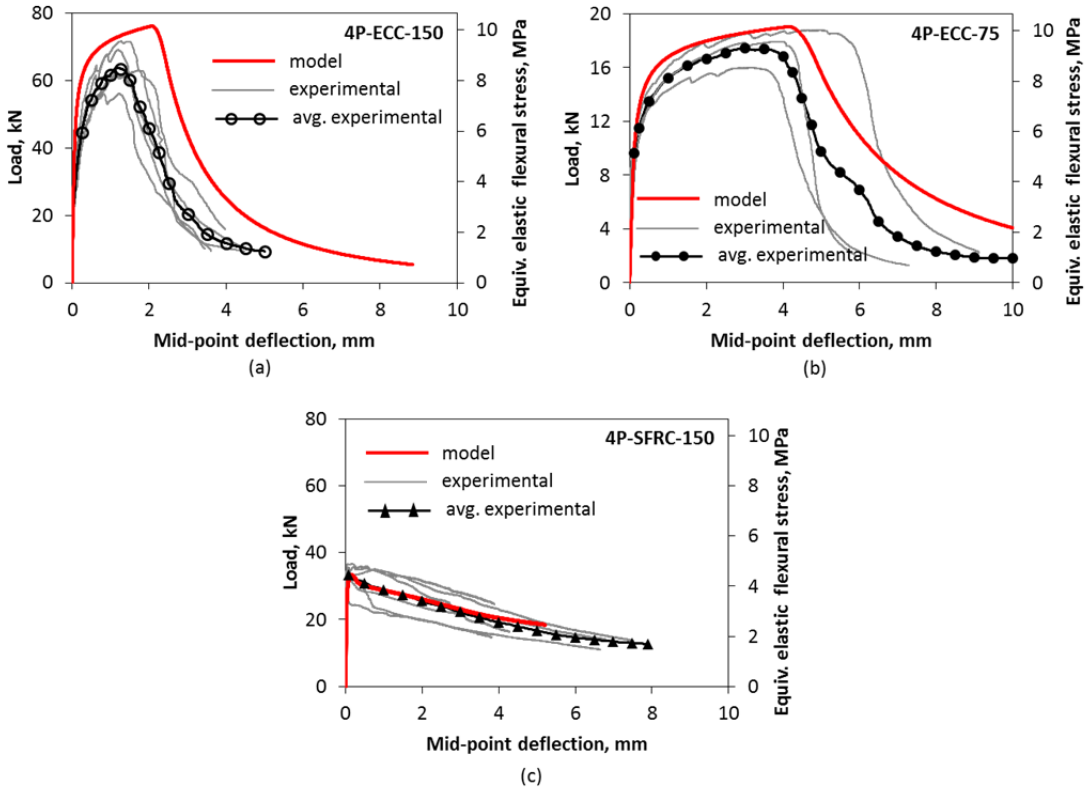


***Figure 5.12*** *Experimentally obtained and model results of four-point bending beams: (a) ECC with a height of 150 mm (ASTM beam), (b) ECC with a height of 75 mm and (c) SFRC with a height of 150 mm (ASTM beam)*

Figure 5.12(c) shows experimentally obtained and modeled load-deflection curves for the SFRC four-point bending beam. The modeled behavior provides a nearly perfectly match of the average experimental result. It should be noted that the SFRC tensile and beam samples were casted with identical cross-sections and using the same procedures; therefore, it is expected that the fiber distribution and orientation in the SFRC samples were more similar than the ECC samples.

### 5.5.2 Round determinate panel from RFS properties determined through both direct tension/compression and flexure

Experimental results from the round determinate panel tests are shown in Figure 5.15 compared to load-deflection curves from the model determined using the RFS properties in Figure 5.11.

Round panels with dimensions in accordance with ASTM C 1550 were supported at three points, as shown in Figure 5.13, with load applied to the center point. The details on experimental program of RDP are presented in Section 3.2.3. According to yield line theory, three yield lines will form in the panel, with height $h_p$, running from the loading point to the mid-spans between the individual supports, as shown in Figure 5.13. The behavior of the yield lines is represented by the RFS, while rigid segments are assumed to form between the separate yield lines.

Figure 5.14 provides the assumed deformed shape and cracking and the DIC measured cracking of the RDP's. Figure 5.14(a) and (b) shows single cracks form at each yield lines in the deflection softening SFRC, while Figure 5.14(c) and (d) shows multiple cracks formed at each yield line in the deflection hardening ECC. The representative length, $l_r$ is equal to the length where multiple cracking is expected. In this case, the maximum representative length for ECC (the representative length at the edge of the sample) was determined based on experimental results. As indicated in Figure 5.14(c), the assumed crack distribution initiates at the point load, fanning out at a 60° angle centered around the yield line, until the maximum representative length is reached. The representative length, $l_r$ influences the energy required to induce deformations and is therefore an important model parameter.

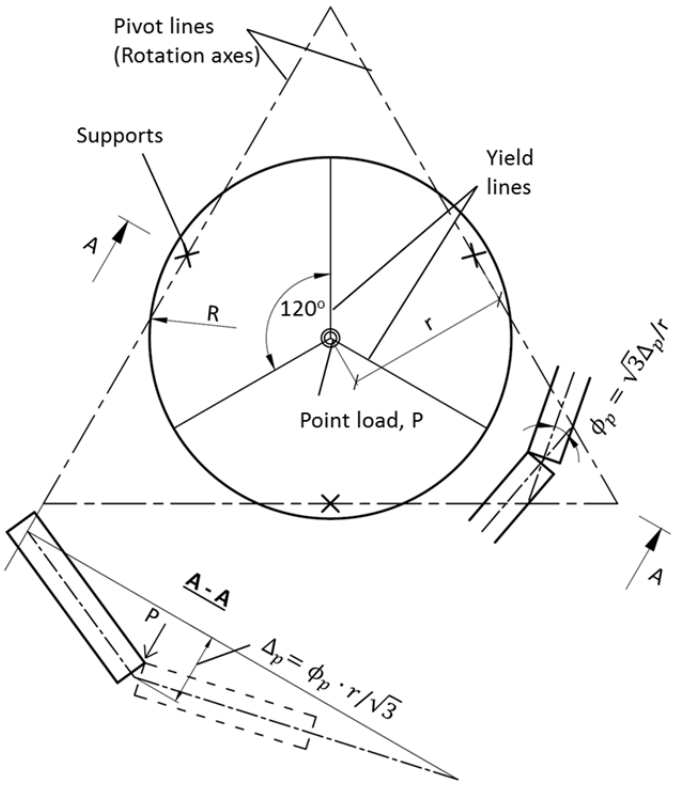


***Figure 5.13*** *Deformed shape of RDP*

To model the structural response of the round panels, the normalized properties of the RFS in Figure 5.11 must be scaled to the geometry of the element (i.e., panel height, $h_s = h_p = 75\ mm$) using Equation (5.13). Using the scaled rotation angle of the RFS, $\phi_{s,i}$, the center point deflection of the round panel can be calculated as:

$$\Delta_{p,i} = \frac{\phi_{p,i} \cdot r}{\sqrt{3}} \tag{5.17}$$

Additionally, scaling of the normalized work in Figure 5.11 allows for the calculation of the corresponding work required to deform the entire panel, $W_{p,i}$, by a center point deflection of $\Delta_{p,i}$ as:

$$W_{p,i} = W_{s,i} \cdot 3R \tag{5.18}$$

where R is the radius of the panel (400 mm). Finally, the corresponding center point load applied, $P_{st,i}$, to reach the mid-point deflection of $\Delta_{p,i}$ using Equation (5.16) can be written as:

$$P_{p,i} = \frac{2(W_{p,i} - W_{p,i-1})}{\Delta_{p,i} - \Delta_{p,i-1}} - P_{p,i-1} \tag{5.19}$$

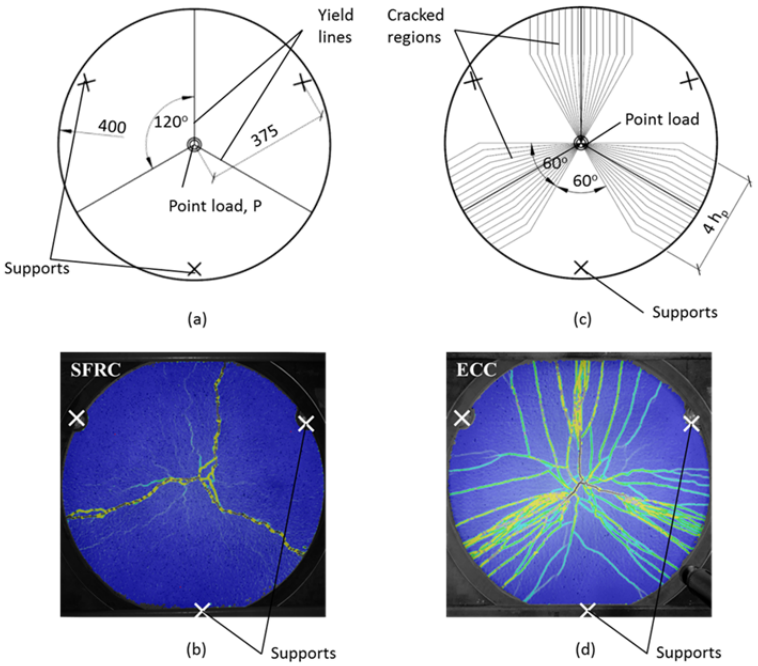


***Figure 5.14*** *Round panel for model verification: (a) Assumed deformed shape and other details of the round panel, (b) Post-peak load cracking of SFRC round panel, (c) Assumed crack distribution of ECC round panel, and (d) Post-peak load cracking of ECC round panel*

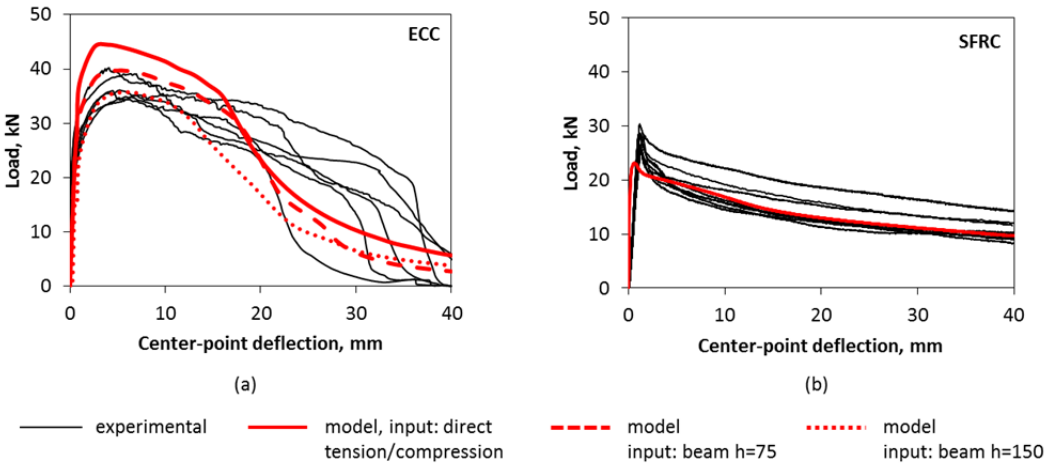


***Figure 5.15*** *Experimentally obtained and model results of RDP (ASTM C1550): (a) of ECC; (b) of SFRC*

Figure 5.15(a) provides the experimentally observed and modeled load center-point deflection curves of deflection hardening ECC. The modeled response using the behavior of RFS obtained by direct tension/compression properties slightly overestimates the strength of the round panel by approximately 20%, while behavior of RFS obtained from the 75 mm high four-point bending beam highly accurately predict the experimental response. The RFS properties obtained from the 150 mm high four-point bending beams underestimates the load carrying capacity compared to

experimental results. Figure 5.15(b) provides the experimentally observed and modeled load center-point deflection curves of deflection softening FRC (SFRC). The modeled curve accurately predicts the post peak behavior of SFRC round panels while the peak strength is underestimated by approximately 25%. Possible explanations for the differences between experimental and modeled responses may be attributed to size effects and differences in the fiber orientation in the specimens used for RFS property determination and the round panels.

## 5.6 Conclusions

A model to predict the load-deformation response of FRC flexural elements is presented in this chapter. The model assumes a loaded structure consists of cracked rotationally deformable segments, called representative flexural segments (RFS), connected by rigid segments. The model considers the balance between work done on the deformed structure and the energy required to induce the corresponding rotational deformations in the RFS. The properties of the RFS are the energy needed to deform a segment by a given rotational angle. These properties can be derived either from material properties in direct tension and compression or from flexural beam tests.

The flexural response in terms of load-deflection of a structural element can be accurately predicted using the model described before. The model verification has been done in two steps:

- The flexural behavior of ECC and SRFC beams has been predicted using RFS properties obtained from direct tension and compression. The modeled load-deflection curves have been compared to experimentally observed results. The model predicted the behavior of four-point bending beams well.
- The flexural behavior of SFRC and ECC round panels has been predicted using RFS properties obtained either from direct tension and compression, or four-point bending beams. The modeled results either form direct tension and compression or flexural beams were found to be realistic.

However, the predictions are more precise if the cross-section dimensions of tensile specimens (especially thickness of the specimen) are similar to that of beam or panel.

For deflection hardening materials, an additional model was developed which accurately predicts the tensile stress-strain (dogbone) behavior based on the tensile stress-crack opening (single crack notched coupon test) behavior.

An additional verification of the model is presented in Chapter 6 on large-scale slabs of SFRC and ECC.

# Chapter 6

# Structural slab: Model verification and application

This chapter presents large-scale testing of FRC structural slabs. The slabs provide both a means for verification of the model presented in Chapter 5 and to highlight a potential application of FRC, which is an objective of the Ph.D. work (see Section 1.2).

The practical and technological benefits achieved by using FRC for the structural examples in this chapter, which include a tunnel lining and a pile-supported slab, include the following:

- In both structural cases, the FRC requires significant energy to induce deflections and has a high deflection capacity. The lack of a brittle failure provides an inherent safety in the structure.
- The use of traditional reinforcement and the corresponding practical considerations of bending schedules, reinforcement placement, aggressivity of the prevailing exposure conditions toward the steel, etc. are eliminated.

## 6.1 Selected structural applications of FRC and loading conditions

Two permanent structural applications for which the use of concrete reinforced exclusively with fiber is increasingly common are industrial flooring slabs and tunnel linings (Chiaia et al. 2009; Oslejs 2008; Winkler et al. 2014). Additionally, sprayed

FRC (or fiber reinforced shotcrete) is commonly used in subsurface mining operations and as temporary support for tunnel and shaft linings to support the soil/rock surface in the multicomponent ground control system (Clark et al. 2010; Martin et al. 2011), as illustrated in Figure 6.1. These ground control systems, with the intention of protecting against potential collapse during excavation, are comprised of an arrangement of rock bolts that are anchored into presumably stable rock masses, a wire mesh, and the sprayed FRC (shotcrete).

For pile-supported slabs and rock bolt-supported sprayed FRC, there is a potential for a support to either fail or undergo excessive deformations due to worse than anticipated soil conditions. This case is illustrated in Figure 6.2 for the failure of a rock bolt in a tunnel or mine lining wall. In both cases, to prevent a more significant failure of the slab or lining, the FRC must support a larger span than was designed for in the ideal conditions (see Figure 6.2).

The beneficial use of FRC in these applications is the significant energy required to induce deflections. It was shown in Figure 3.10(d), from RDP testing, and Figure 5.11, the RFS properties that the energy required to induce deformation of ECC is greater than for SFRC. This underlines the potential application for FRC materials with particular properties (e.g., high energy absorption capacity) in pile-supported slabs and tunnel linings.

The following section describes mock-up testing to investigate the situation of a failed support for slabs of both the tension softening SFRC and the strain hardening ECC.

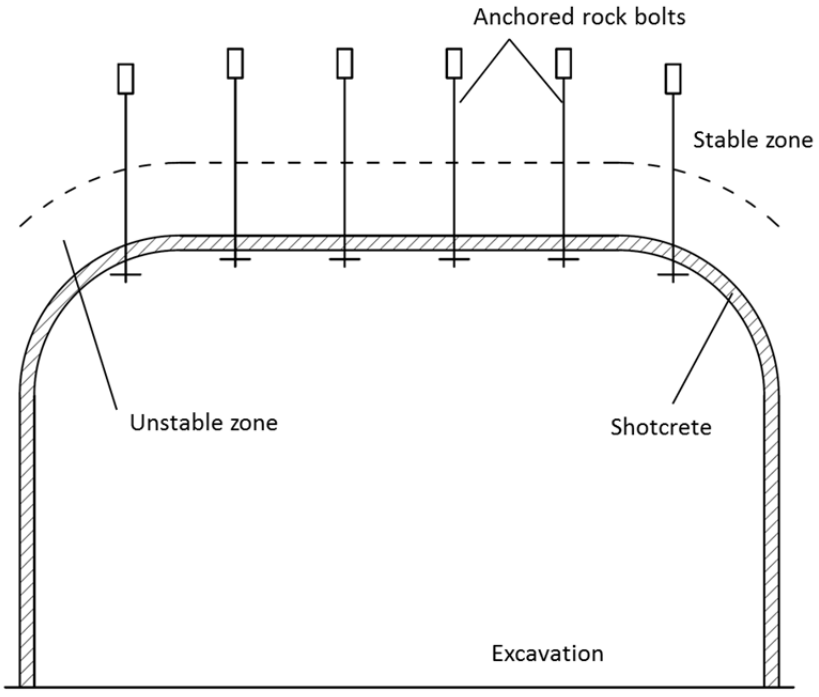


***Figure 6.1*** *Rock bolt arrangement in tunnel*

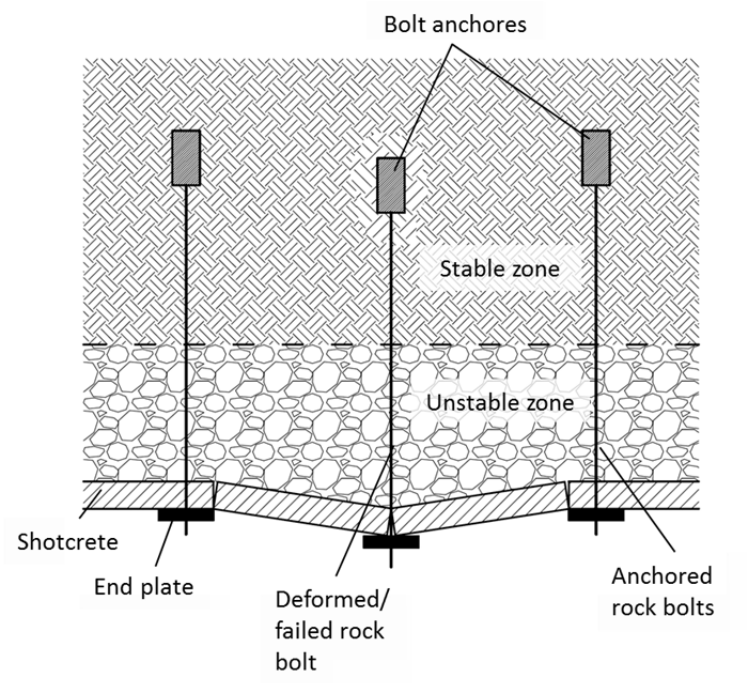


***Figure 6.2*** *Assumed deformations in rock mass and supporting shotcrete due to extensive deformations/failure of one rock bolt*

## 6.2 Mock-up testing of FRC structural slabs

The slab test is intended to represent a pile-supported slab with a faulty pile or a tunnel/mine lining with a local failure of a rock bolt. Two structural slabs, with a size of 5 m x 5 m, were tested as shown in Figure 6.3. The slabs were cast on a reaction floor, with a membrane placed between the test slab and the reaction floor to avoid bonding, and tested by a vertical deformation applied by pushing the test slab upwards. The slab was divided in four testing areas (Figure 6.3) from which area I and II was used for continuous testing. The slab was supported with point supports with a step of 1 m x 1 m with a 110 mm diameter transfer plate located on top of the test slab. The transfer plates were connected to strong floor by a 30 mm diameter steel threaded rods. The center point of each testing area was supported so that deformations could be applied to that support by piston pushing the support up.

The ECC slab had an average thickness of 70 mm, while the SFRC slab had an average thickness of 125 mm. The deformations of the loading point of the slab were measured with LVDTs with a frequency of 2 Hz, while DIC measurements were taken from the cracked surface of the panel facing away from the load at ten second intervals. As the DIC measurements utilized are only capturing 2-dimensional deformations, only in-plane crack formation and crack widths were detected and measured by DIC.

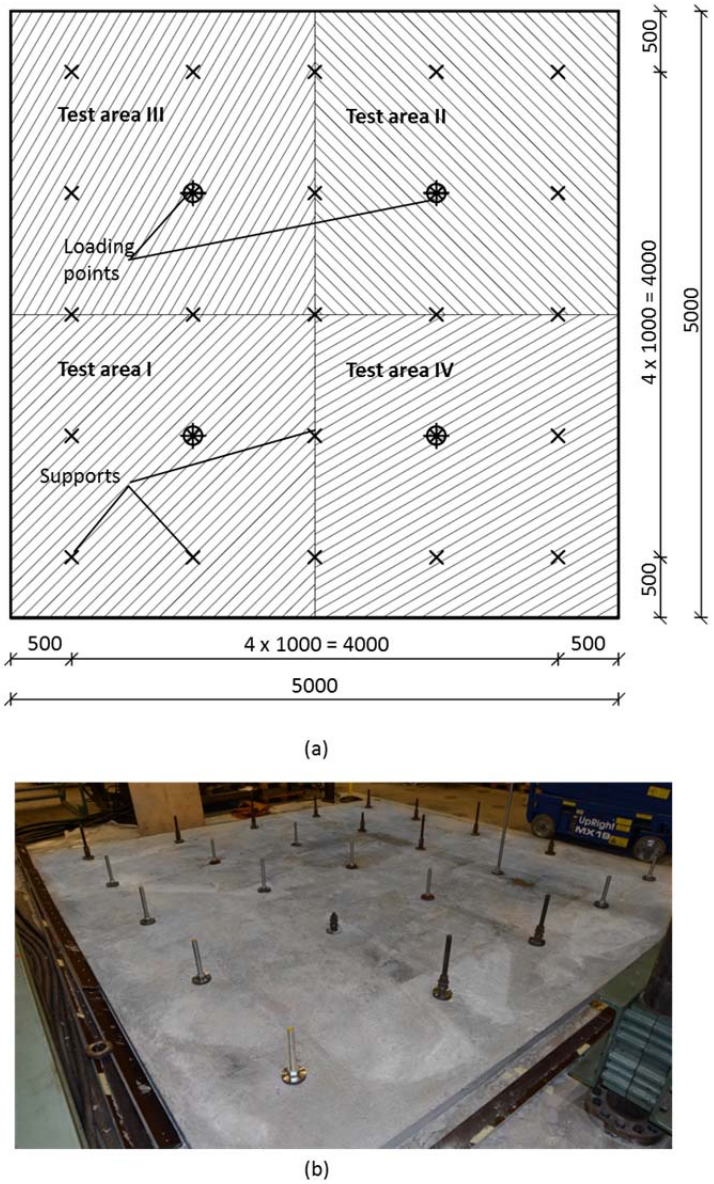


***Figure 6.3*** *Test setup of structural slab: (a) specimen geometry (top view); (b) actual test setup*

## 6.3 Structural analysis of a FRC structural slab

To predict the load-deflection response of a structural slab with extensive deformations at a point support, the model described in Chapter 5 was applied. The modeling approach links the energy required to induce rotational deformations in a representative flexural segment (RFS) to the load-deformation response of FRC structural members governed by flexure. The model determines the properties of the RFS through materials characterization to describe the energy needed to deform the segment to a specific rotation angle. In an actual structural element, the properties of the RFS are assigned to deformed sections located between rigid sections to reflect the deformed shape as determined by yield line theory. The model predicts the load

necessary to deform a structural element by a specific deflection. The properties of the RFS are derived from standard flexural beam test data or from direct tension/compression material properties. The details on model are described in Chapter 5 and the observed RFS properties are presented in Figure 5.10.

The geometry of one testing area of structural slab is shown in Figure 6.4(a) with predicted yield lines. To model the structural response of the structural slab with the height $h_{sl}$, the normalized properties of the RFS in Figure 5.11 must be scaled to the geometry of the element (i.e., structural slab, $h_{s,ECC} = h_{sl,ECC} = 70\,mm$ and $h_{s,SFRC} = h_{sl,SFRC} = 125\,mm$) using Equation (5.13). The behavior of the yield lines is represented by the RFS, while rigid segments are assumed to form between the separate yield lines. For a deflection softening FRC, single cracks form at each yield lines, while multiple cracks form at each yield line in a deflection hardening FRC. During testing, digital image correlation was used to assess the cracking pattern of positive moment side of the SFRC and ECC specimens. Figure 6.4(c) and (d) show the post-peak load cracking response of the structural slab.

Eight radial yield lines (Figure 6.4(a)) are predicted to form from a loading point in the direction of middle between the supports where cracks will form caused by positive bending moment. Each of these yield lines under the applied deflection of $\Delta_{sl,i}$ will have a rotation angle $\phi_{sl1,i}$:

$$\phi_{sl1,i} = \frac{\Delta\sqrt{5}}{3 \cdot a} \tag{6.1}$$

The negative moment forms the yield lines in opposite side of the slab forming an octagon around the perimeter of the testing area (Figure 6.4) with rotation angles perpendicular to the yield lines under the applied deflection of $\Delta_{sl,i}$ :

$$\phi_{sl2,i} = \frac{4 \cdot \Delta \cdot \sin(\pi/4)}{3 \cdot a} \tag{6.2}$$

$$\phi_{sl3,i} = \frac{\Delta}{a} \tag{6.3}$$

The work done by each type of the yield line to deform the slab to deflection$\Delta_{sl,i}$:

$$\begin{aligned} W_{sl1,i} &= W_s(\phi_{sl1,i}) \cdot 8 \cdot c \\ W_{sl2,i} &= W_s(\phi_{sl2,i}) \cdot 4 \cdot b \\ W_{sl3,i} &= W_s(\phi_{sl3,i}) \cdot 4 \cdot a \end{aligned} \tag{6.4}$$

Where a, b and c are presented in Figure 6.4(a), a= 1000 mm, b=707 mm and c=1118 mm. The work done on the entire slab to induce deformation of the center point, $\Delta_{sl,i}$ is computed as:

$$W_{sl,i} = W_{sl1,i} + W_{sl2,i} + W_{sl3,i} \tag{6.5}$$

The corresponding center point load applied, $P_{st,i}$, to reach the mid-point deflection of $\Delta_{p,i}$ using Equation (5.16) can be written as:

$$P_{sl,i} = \frac{2(W_{sl,i} - W_{sl,i-1})}{\Delta_{sl,i} - \Delta_{sl,i-1}} - P_{sl,i-1} \tag{6.6}$$

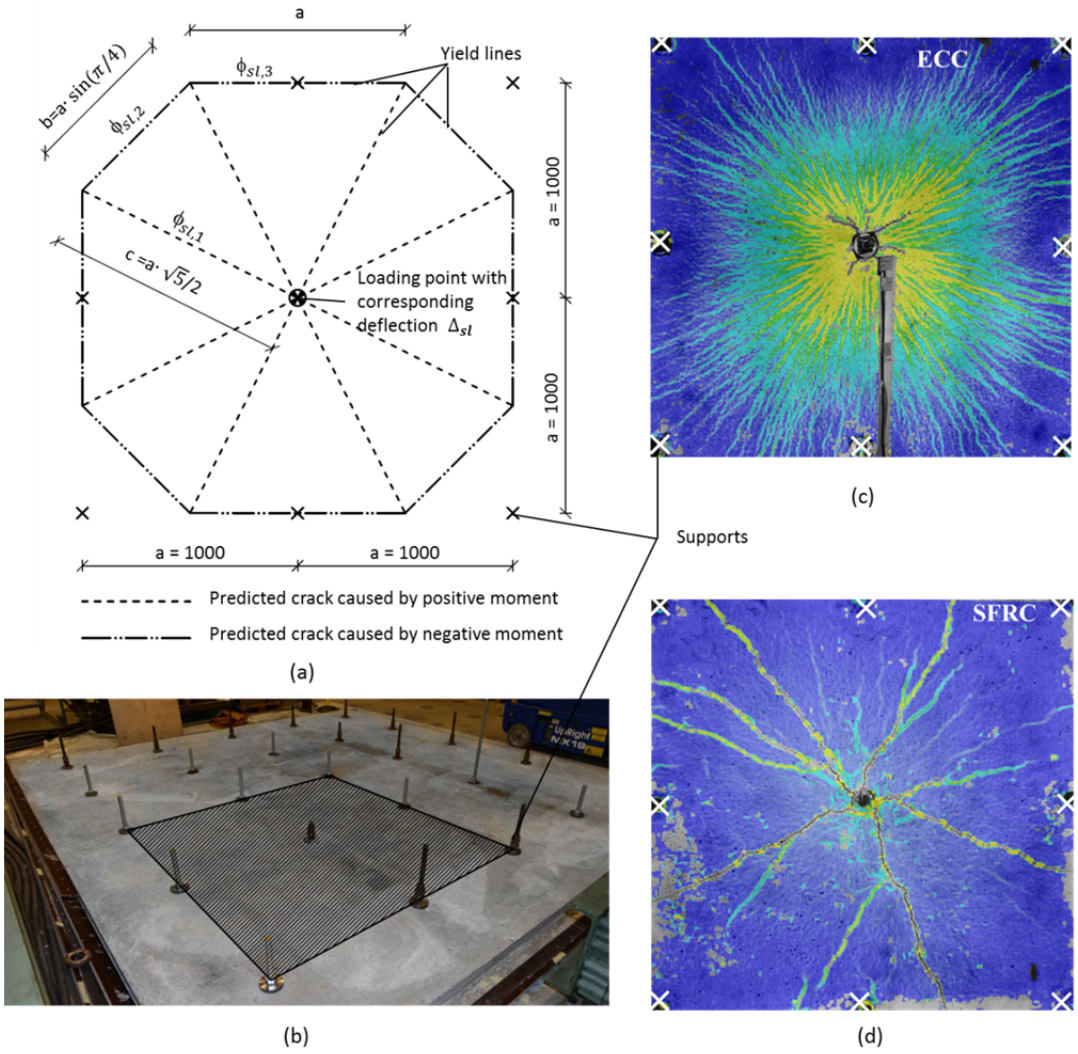


***Figure 6.4*** *Structural slab: (a)deformed shape of one test area of structural slab; (b) position of selected testing area in test setup; (c) measured crack distribution of top surface of testing area of ECC; and (d) measured crack distribution of top surface of testing area of SFRC*

## 6.4 Comparisons of model and experimental results

The experimental and model results of the load-deflection of structural slab are presented in Figure 6.5. The modeled and experimental results match very well for ECC, as shown in Figure 6.5(a). The modeled curve fitting between two experimentally obtained results are predicted using RFS properties that are obtained

from four point bending beam with a structural depth of 75 mm. The structural depth of the ECC slab tested was 70 mm, which is similar to the beam heights from what properties of FRS are obtained. Unfortunately the continuously tested ECC slabs failed under punching shear after 40-80 mm of center point deflection, thus the full load-deflection response could not be detected.

The model predicted the behavior of SFRC slab quite well; however, the model underestimated the strength of the slab for approximately 10 kN at peak load. The experimental results are therefore slightly higher than the predicted results, which may be due to a difference in the casting approaches used for the beams and the slab. The model is based on results in direct tension and flexural beams, both casted in beam molds with dimensions of 150 mm x 150 mm x 600 mm. The slab was casted by pouring concrete in the center of the slab and manually spreading the concrete around to ensure slab area. This placement approach was though to preferentially orientate the fibers horizontally in a 2-dimensional orientation. Previous design codes (fib 2012; SS812310 2014) have also recognized the impact of the fiber orientation and provide a fiber orientation fiber to scale the design load capacity of FRC members.

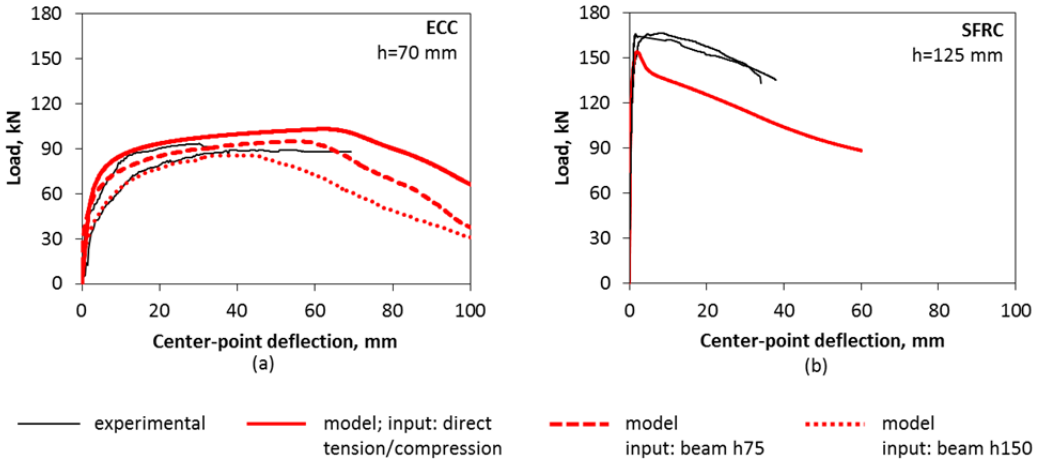


***Figure 6.5*** *Experimentally obtained and model results of structural slab: (a) of ECC with an average height of 70 mm and (b) of SFRC with an average height of 125 mm*

## 6.5 Conclusions

This chapter presents results from large-scale testing of structural slabs of ECC and SFRC, which were used to demonstrate a potential application of FRC materials and to provide a dataset for verification of the model presented in Chapter 5.

For both FRC materials tested, multiple cracks were observed. While the SFRC formed cracks mostly in the predicted locations of yield lines, ECC showed an extensive multiple cracking in the vicinity of each yield line. The deflection hardening ECC carried increased load with the formation of new cracks, until an ultimate

punching shear failure around the load plate. The load carrying capacity of SFRC was gradually reducing with additional deformation once cracks formed in the location of yield lines.

The behavior of the ECC and SFRC structural slabs was modeled using the representative flexural segments (RFS) as described in Chapter 5, applied to geometry of the slab as described in Section 6.3.

The model predicts the behavior of ECC slab in a realistic way; however, the more precise modeled results are obtained from a beam with similar structural heights.

The model predicted the behavior of SFRC slab quite well; however, the model underestimated the strength of the slab for approximately 15% at peak load. The difference may be due to a difference in the casting approaches used for the beams and the slab.

# Chapter 7

# Shear behavior of reinforced Engineered Cementitious Composites (ECC) beams

This chapter presents an example application of ECC, as an alternative to traditional shear reinforcement (i.e., stirrups). This use of FRC is not without precedent in current structural design codes. From 2008, ACI 318 introduced prescriptive requirements whereby under particular situations the minimum shear reinforcement can be substituted by steel fibers. This chapter investigates the influence ECC has on the shear behavior of a reinforced ECC (RECC) system.

The study investigates and quantifies the effect of ECC's strain hardening and multiple cracking behaviors on the shear capacity of reinforced beams with varying stirrup spacing. The shear cracking and failure mechanisms of RECC and reinforced concrete (RC) are described in detail. Detailed analyses of the crack formation and development indicated that for RC, shear stresses transfer across cracks through stirrups, aggregate interlock and dowel effect of longitudinal reinforcement. For RECC, shear stresses are transferred by an additional mechanism, fiber bridging, which induced multiple cracking and increased ultimate shear stress compared to the RC beams.

## 7.1 Review of previous studies of the shear behavior of FRC

Particular structural members such as coupling beams, beam ends, short cantilevers, etc. have to resist primarily shear loading. Traditionally in reinforced concrete structures, these members are reinforced with steel shear reinforcement as vertical or

inclined discrete stirrups. As shear failure is typically brittle, large safety factors are prescribed for such Reinforced Concrete (RC) structures. If a more ductile shear failure was possible in RC structures, lower safety factors could be introduced, reducing the amount of shear reinforcement required for an element. The shear capacity of beams, as predicted by various design codes, vary by a factor of more than 2 (Bentz et al. 2006). This disparity is due to the lack of a rational, widely accepted theory for calculating the shear strength of RC beams as well as different load and resistance factors. Another common problem associated with shear resistance is related to reinforcement congestion, which may lead to voids and insufficiently compacted concrete resulting in low compressive strength (Majdzadeh et al. 2006). Therefore, if the shear strength and ductility of concrete as a material could be altered from a brittle to more ductile failure, the demand of traditional stirrups in these elements could be decreased, or potentially eliminated, as safety factors for shear capacity of structure could be reduced. ECC and other Fiber Reinforced Concretes (FRC) may provide such an increased ductility, and for the past decades, the shear behavior of FRC flexural members has been extensively investigated. The addition of fibers has been found to improve the shear resistance and to enhance the shear crack distribution in Reinforced FRC (R/FRC) structures with and without traditional stirrups (Altoubat et al. 2009; Choi et al. 2007; Imam et al. 1997; Kanda et al. 1998; Li et al. 1992; Majdzadeh et al. 2006; Narayanan & Darwish 1987; Parra-Montesinos 2006).

The influence of fibers on concrete shear strength is typically attributed to two main factors: 1) directly by improved stress transfer across the inclined shear crack; and 2) indirectly by controlling crack widths and distribution, allowing increased aggregate interlock and dowel action of longitudinal reinforcement (Altoubat et al. 2009; Parra-Montesinos 2006).

Recently, work has been initiated to include FRC in standard reinforced concrete codes. However, there is currently no broadly used international consensus on addressing these improvements in design codes. For example, the use of deformed steel fibers in place of minimum shear reinforcement was investigated by ACI Subcommittee 318-F, “New Materials, Products, and Ideas” (Parra-Montesinos 2006). The study focused on structural beams, where the nominal shear strength attributed to the concrete was not exceeded and therefore minimum transverse reinforcement was required. Based on data from an extensive literature review, the use of deformed steel fibers as an alternative to minimum transverse shear reinforcement was proposed (Parra-Montesinos 2006) and included initially in ACI 318-08 (ACI-318 2008) and has continue in the latest versions of ACI 318 (ACI-318 2014). To ensure adequate material properties of the fiber reinforced concrete, several statements were included in ACI 318-08, including: a) the minimum content of deformed steel fibers should be greater than or equal to 0.75% by volume; the residual strength obtained from flexural

tests in accordance with ASTM C1609 should be b) greater than or equal to 90% of the measured first-peak strength at mid-span deflection of 1/300 of the span length; c) greater than or equal to 75% of the measured first-peak strength at mid-span deflection of 1/150 of the span length. By point "b" and "c" ACI-318 suggests using flexural tests to indirectly evaluate the shear behavior of Steel Fiber Reinforced Concrete (SFRC). However, this approach has been questioned. Dinh et. al. (Dinh et al. 2011; Dinh et al. 2010) favor an approach where the residual flexural strength of FRC in beam specimens is assessed at mid span deflections as a function of fiber length and assumes that a single crack forms in FRC beam under four point bending. For materials such as ECC or other FRC with multiple cracking under flexural load this approach is overly conservative.

The Russian design code SP 52-104-2009 (SP52-104 2010) provides an alternative where the tensile and compressive strength of FRC are a function of the amount and properties of the fibers and the strength class of the concrete matrix. In this approach an analytical model predicts the shear capacity of beams using empirical formulas. The shear strength of an R/FRC beam is provided by the concrete contribution in the compressive zone and a sum of contributions from stirrups and fibers in the tensile zone. The code allows the use of SFRC without traditional shear reinforcement for beams with a height less 150 mm; however, minimum traditional shear reinforcement is needed for beams with a height more than 150 mm even if SFRC can resist all shear stresses. This approach applies only to particular types of steel fibers.

Similar to ACI 318, the *fib* Model Code (fib 2012) and RILEM TC 162-TDF recommendations (162-TDF 2003) specify the use of the residual flexural strength at specific crack openings from flexural beam tests to predict the shear capacity of FRC.

Japan Society of Civil Engineering (JSCE) provides recommendations for design and construction of high performance fiber reinforced cementitious composites (JSCE 2008) with material properties including multiple fine crack (<0.2 mm) formation and pseudo-strain hardening response (ultimate tensile strain >0.5 %) under uni-axial tensile loading. The results are highly dependent on tensile strength of the FRC, however, a test method to measure the tensile strength is not provided. Researchers have used factored values of the ultimate strength (Kanakubo et al. 2010; Kanda et al. 1998; Shimizu et al. 2006) or first cracking strength in direct tension (Nagai et al. 2002), or the flexural strength of FRC (Kabele 2005). A more precise measure of the tensile strength of FRC should be formulated.

Numerous other approaches have been suggested to predict shear capacity (Ashour et al. 1992; Choi et al. 2007; Dinh et al. 2011; Imam et al. 1997; Kwak et al. 2002; Majdzadeh et al. 2006; Mansur et al. 1986; Narayanan & Darwish 1987; Sharma 1986; Shimizu et al. 2006), however, the precision of the results are highly dependent on a specific geometry of the specimen, the fiber type and composite properties of

FRC. Although each proposed method predicted the shear strength of a specific beam precisely, the estimate of beams with different geometry, material composition or fiber type are underestimated or overestimated by two to three times (Dinh et al. 2011; Kwak et al. 2002).

## 7.2 Shear testing of reinforced ECC

For this study, experimental tests were conducted to examine the shear behavior of ECC beams in terms of the shear capacity and cracking behavior. For comparison, typical concrete specimens with and without transverse reinforcement were also investigated.

### 7.2.1 Materials

The experimental program consists of reinforced ECC (RECC) beams with 8 mm long, randomly distributed polyvinyl alcohol (PVA) fibers and reinforced concrete (RC) beams. For all RECC beams, the same mortar composition was used, consisting of fly ash, cement, water, sand, quartz powder and 2% by volume of PVA fibers. The concrete mixture used for the reference beams was made with standard components using cement, water and graded aggregates with a maximum size of 16 mm. The concrete was intended to have the similar compressive strength as the ECC used in the companion beam specimens. The mixture proportions of ECC and concrete are listed in Table 2.3 and Table 7.1

***Table 7.1*** *Mixture proportions of concrete*

| | $kg/m^3$ |
|---|---|
| Cement | 372 |
| Sand 0-4 mm | 758 |
| Aggregate 4-8 mm | 374 |
| Aggregate 8-16mm | 756 |
| Water | 156 |

### 7.2.2 Shear test configuration

In previous studies, various test setups have been used to determine the behavior of concrete materials in shear. Most often used are three and four-point bending tests, shear panel tests (Vecchio & Collins 1986), various modifications of notched specimen tests (Majdzadeh et al. 2006; Shang & Van Zijl 2007) and modifications of the Ohno shear test (Kanda et al. 1998; Li et al. 1994). In this study, the load configuration was designed similarly to the Ohno shear beam test to investigate the

shear behavior in a realistic situation, while reducing the influence of the moment on inclined crack formation.

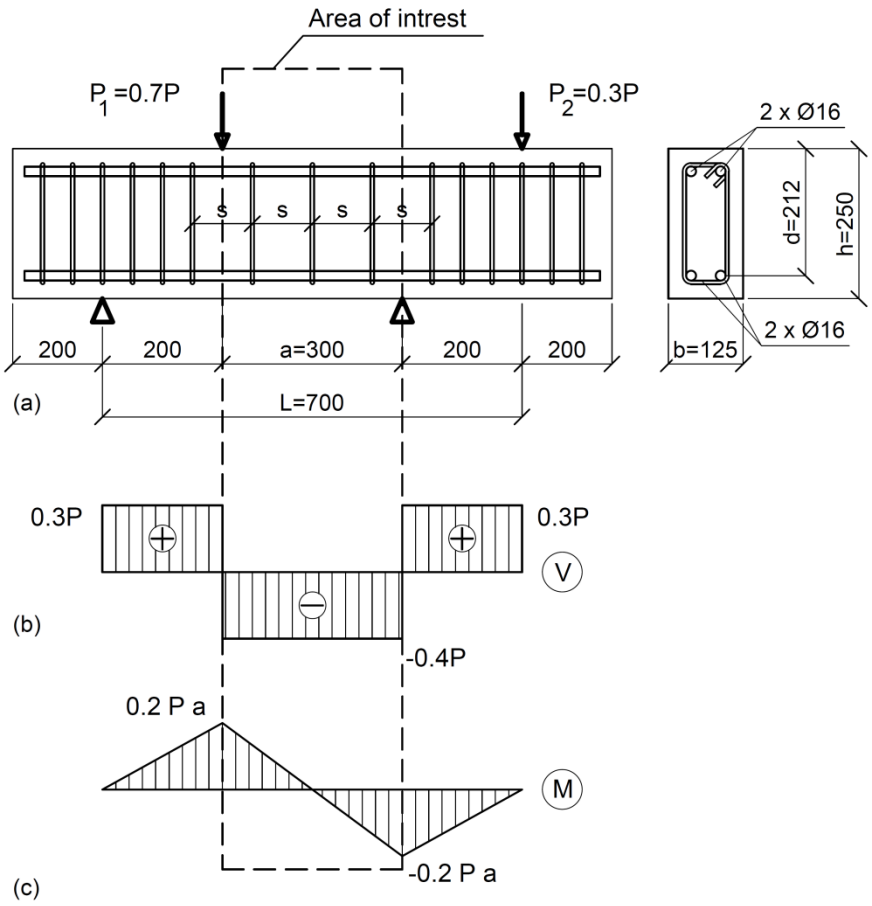


***Figure 7.1*** *Shear beam test setup configuration (a), shear force distribution (b), moment distribution (c)*

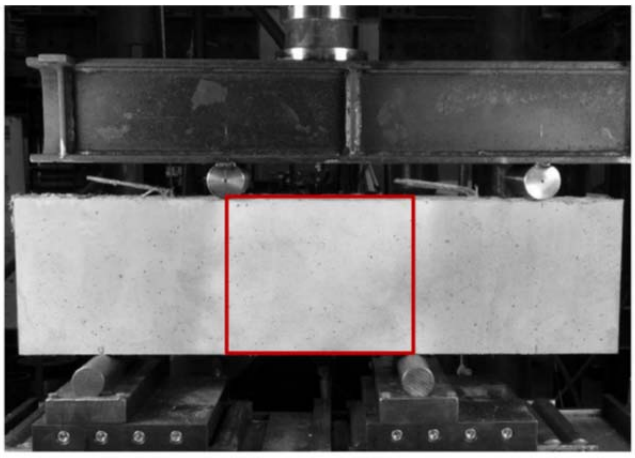

***Figure 7.2*** *Test set-up and area of interest*

The test set-up for the shear beam tests is shown in Figure 7.1 and Figure 7.2. The load was applied through a secondary load beam and rollers with a diameter 60 mm. The beams were loaded in a displacement controlled procedure with a loading rate of 0.02 mm/s cross-head displacement. The beams were 1100 mm long, 250 mm high and with a width of 125 mm. The shear span that was investigated was situated in the middle part of the beam with a length of 300 mm resulting in a ratio a/d=212/300=1.4. To eliminate the influence of changing shear crack angle, the geometry of the beams and the test setup was chosen to force shear cracks to form at a 40°-45° angle.

All beams were reinforced with four ∅16 mm longitudinal reinforcement bars, placed in the corners with 25 mm cover from adjacent surfaces. Selected beams were reinforced with ∅6 mm transverse reinforcement. The spacing of the ∅6 mm transverse reinforcement varied as an approximate function of the effective height, d (d, ½d, and ¼d) of the beam as summarized in Table 7.2 and Figure 7.1. Additionally, specimens without transverse reinforcement were tested for both RC and RECC. Yield strength, $f_y$, of the longitudinal and transverse reinforcement was 550 MPa.

***Table 7.2*** *Reinforcement detailing in the test specimens*

| Beam | Material | Transverse reinforcement | | | Tensile and compressive reinforcement | | |
|---|---|---|---|---|---|---|---|
| | | ∅ | spacing | ratio | ∅ | amount | ratio |
| | | mm | mm | % | mm | # | % |
| RECC-0 | ECC | - | - | 0 | 16 | 2 | 1.52 |
| RC-0 | RC | | | | | | |
| RECC-d | ECC | 6 | 200 | 0.23 | | | |
| RC-d | RC | | | | | | |
| RECC-½ d | ECC | 6 | 100 | 0.45 | | | |
| RC-½ d | RC | | | | | | |
| RECC-¼ d | ECC | 6 | 50 | 0.90 | | | |
| RC-¼ d | RC | | | | | | |

## 7.2.3 Deformation measurements

A commercial digital image correlation (DIC) system (Aramis, GOM) was used to capture deformations of the front surface of the specimens in the region of interest (Figure 7.2). The system consists of two black and white 4 mega pixel charged couple device (CCD) cameras and a data acquisition system which captures and processes the images. The two CCD cameras were positioned at the same height and were focused on the same surface, but from different angles, allowing 3D deformation measurements. The images were recorded once per second. In order to facilitate the

DIC measurements, adequate contrast in the greyscale of individual objects is required. This was achieved by using black and white spray paint to apply a stochastic speckle pattern as shown in Figure 7.9. A calibration was preformed prior to testing, using a calibration plate provided by the manufacturer of the DIC system. The DIC system tracks movements of small areas (called facets) of the specimen surface corresponding to 15 by 15 pixel square areas. The system also collects input of loading data from the testing machines such that specific images are easily associated with a recorded load. Additional details on the DIC technique and equipment are available in the literature (Pease et al. 2006; GOM 2005) Deformations of selected beams were verified by an arrangement of LVDT's positioned on the back of the specimens.

## 7.3 Shear performance of reinforced ECC

The typical tensile stress-strain response of ECC is shown in Figure 2.8. The average first cracking strength in tension for the ECC used in this study was 4.0 MPa and the average ultimate tensile strength was 4.5 MPa, while the splitting tensile strength, according to EN 12390-6 (EN12390-6 2002), was 4.1 MPa for conventional concrete. The average compressive strength of ECC and concrete was 53.6 and 52.0 MPa, respectively. Detailed descriptions on compressive and tensile testing are provided in Sections 2.3.1 and 2.3.2.

### 7.3.1 Shear stress-strain relationship

Figure 7.3 and Table 7.3 provide experimental values on the shear behavior of RC and RECC beams. The experimentally determined ultimate shear load $V_u$, ultimate shear stress $\tau_u$, and the crack angle $\varphi$ are shown in Table 7.3. Experimental results are averaged from two identical beam specimens. The equation for calculated shear stress (MPa) was:

$$\tau_u = V_u/(b \cdot d),$$

where $V_u$ is the ultimate shear force (kN), $b$ is the width of the beam (mm) and $d$ is the effective depth (mm). As shown in Table 7.3, RECC provides modest improvements in the shear capacity over RC beams (maximum 34% increase) with equivalent amounts of shear reinforcement. For a stirrup spacing of d, the shear capacity is 35% higher than in RC, however, for other stirrup spacing ECC improves the capacity by 20% on average. As previously noted, similar compressive and tensile strengths were observed in ECC and concrete. However, the elastic modulus of concrete (31.4 GPa) measured from compressive cylinders was almost 2 times bigger than that of ECC (16.0 GPa) resulting in similar variation in shear stiffness. As a result of the high difference in stiffness between ECC and concrete, the initial shear deformations under constant load level were smaller for RC than RECC (initial slope in curves in Figure

7.3). However, initiation of a shear cracking in RC resulted in a rapid increase in shear deformations. Shear crack formation in the RECC caused a gradual increase in deformations. The shear deformations at ultimate load were similar for both the RECC and the RC beams without transverse reinforcement and with transverse reinforcement with d/2 and d/4 spacing (Table 7.3). For the transverse reinforcement with spacing of d, the shear deformations at ultimate load were 1.25 times higher for the RECC beams. The RECC beams resisted approximately 1.2 to 1.35 times the shear loads compared to RC beams (Table 7.3).

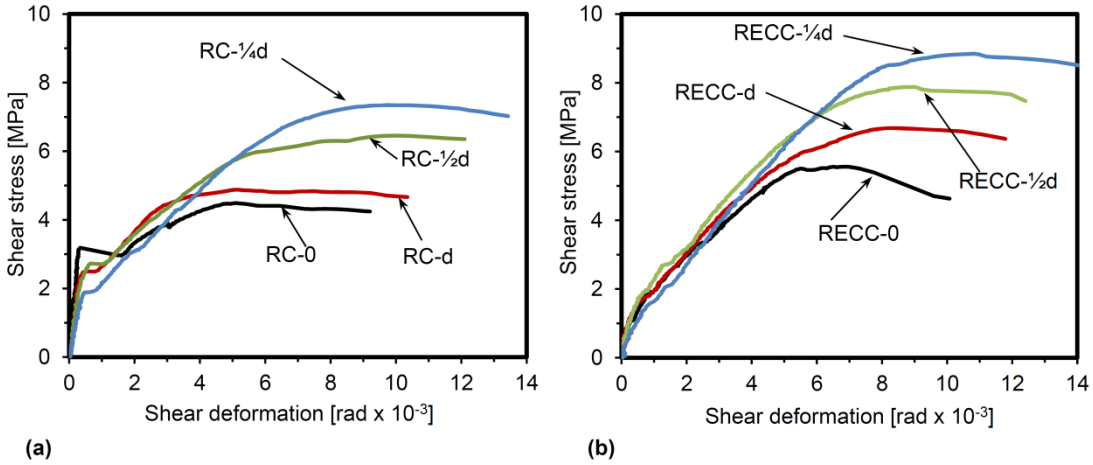


***Figure 7.3*** *Shear stress - strain relationship for (a) RC and (b) RECC. Deformations captured using DIC.*

***Table 7.3*** *Test results from shear beam tests*

| | Ultimate shear force, $V_u$ | Ultimate shear stress, $\tau_u$ | Shear strain at ultimate, $\varepsilon_u$ | Shear crack angle, $\varphi$ | $\tau_{u\,ECC} / \tau_{u\,RC}$ | $\varepsilon_{u\,ECC} / \varepsilon_{u\,RC}$ |
|---|---|---|---|---|---|---|
| | kN | MPa | rad x $10^{-3}$ | deg | | |
| RECC-0 | 150 | 5.7 | 6.65 | 42.5 | 1.19 | 1.07 |
| RC-0 | 129 | 4.8 | 6.20 | 42.5 | | |
| RECC-d | 179 | 6.7 | 7.77 | 42.5 | 1.34 | 1.24 |
| RC-d | 134 | 5.0 | 6.26 | 44.0 | | |
| RECC-½d | 200 | 7.5 | 8.36 | 43.5 | 1.21 | 0.98 |
| RC-½d | 164 | 6.2 | 8.51 | 43.0 | | |
| RECC-¼d | 234 | 8.8 | 10.84 | 42.5 | 1.20 | 1.07 |
| RC-¼d | 193 | 7.3 | 10.05 | 43.5 | | |

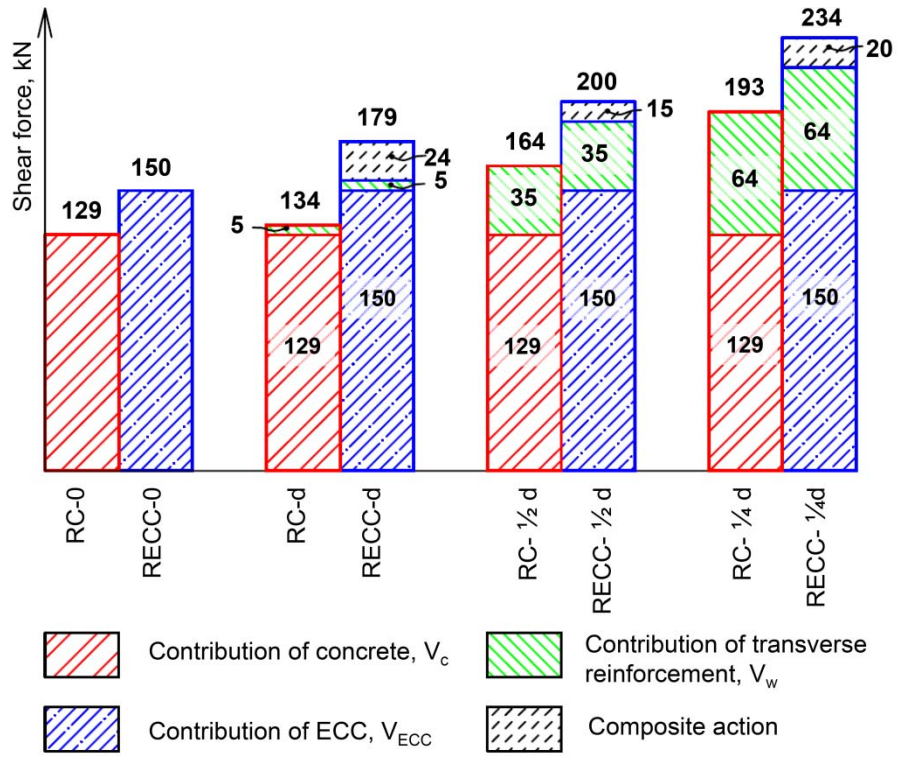


***Figure 7.4*** *Contribution of concrete and ECC, transverse reinforcement and composite action on shear capacity*

The shear carrying capacity of the reinforced concrete beams without additional transverse reinforcement was determinate experimentally to be129 kN ($V_c$) (Figure 7.4). The additional shear carrying capacity of stirrups ($V_w$) can be determinate as the difference between ultimate shear force ($V_u$) in the beams with transverse reinforcement and the contribution from the concrete ($V_c$).

$$V_w = V_u - V_c$$

The additional contribution of transverse reinforcement in shear carrying capacity is presented in Figure 7.4. The shear carrying capacity of RECC without transverse reinforcement was measured 150 kN.

For FRC, the shear capacity of a member can be considered to be the sum of the contributions from fibers ($V_f$), the concrete matrix ($V_c$) and the transverse reinforcement ($V_w$) (Dinh et al. 2011; JSCE 2008; Majdzadeh et al. 2006). In some cases the contribution of the fibers and the concrete matrix are treated as a combined value (Imam et al. 1997; Narayanan & Darwish 1987; Sharma 1986). It can be assumed that the contribution from transverse reinforcement is constant for the RECC and the RC beams with the same transverse reinforcement spacing. Thus, the ultimate shear force in the RECC beam should be a sum of contribution of shear carrying capacity by ECC ($V_{ECC}$) and the additional contribution of transverse reinforcement

($V_w$). However, Figure 7.4 illustrates that there is an additional contribution in ultimate shear load by RECC between 15 kN and 24 kN. This additional contribution may be due to improved composite action of RECC.

### 7.3.2 Shear crack deformations

Previous investigations on the shear behavior of RECC beams have not reported details on the crack formation process, which can be described as a combined crack opening and sliding. As shown in Figure 7.5, the total crack deformation, *u*, consists of crack opening, or perpendicular separation between crack surfaces, and crack sliding, or parallel translation of crack surfaces. Using DIC, deformations are measured by selecting two virtual markers on the images of the specimen with marker on each side of the crack (Figure 7.5). Subsequently, the relative displacements between the two markers were obtained using standard DIC techniques. Initially the line between these two markers is set to be perpendicular to the predicted crack surface as illustrated in Figure 7.5. The crack opening and sliding values (for RECC values taken as the average value of at least six visible cracks) at *4.5* MPa and ultimate load are shown in Table 7.4. Additional measurements are presented in Figure 7.6, as discussed in a later section.

The comparison of measured crack deformations (opening and sliding) at a shear stress of 4.5 MPa and ultimate show that individual crack widths measured in RECC are significantly smaller than those in RC under similar applied shear stresses, regardless of transverse reinforcement configuration.

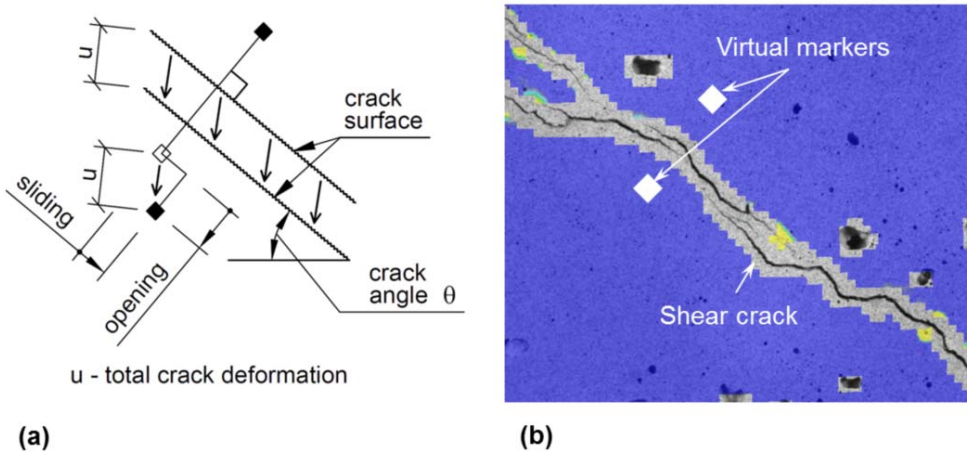


***Figure 7.5*** *Illustration of crack deformations: (a) schematic definition of crack opening and sliding; (b) illustration from DIC software*

Shear reinforcement in RC increases the shear resistance directly through the tensile capacity of stirrups and indirectly by improved aggregate interlock as shear

reinforcement controls crack widths. For the same shear stress level, an addition of 0.9% of traditional shear reinforcement (no stirrups vs stirrups with spacing s=¼d) reduced crack sizes by 20% to 25% (see Table 7.4). In RECC, the use of transverse reinforcement reduced the crack sizes by approximately 50% at a stirrup spacing of s=¼d.

***Table 7.4*** *Values of crack opening and sliding*

Shear stress – 4.5 MPa

| | Values of individual shear cracks | | Values of all shear cracks | | |
|---|---|---|---|---|---|
| | Opening | Sliding | # of | Opening | Sliding |
| | mm | mm | cracks | mm | mm |
| RC-0 | 1.00 | 0.30 | 1 | 1.00 | 0.30 |
| RC-d | 0.75 | 0.20 | 1-2 | 0.78 | 0.20 |
| RC-½d | 0.50 | 0.15 | 3 | 0.64 | 0.15 |
| RC-¼d | 0.20-0.30 | 0.05 | 4 | 0.55 | 0.14 |
| RECC-0 | 0.15 | 0.05 | 5-9 | 0.61 | 0.11 |
| RECC-d | 0.10 | <0.05 | 6-10 | 0.60 | 0.17 |
| RECC-½d | 0.10 | <0.05 | 8-9 | 0.50 | 0.14 |
| RECC-¼d | <0.10 | 0 | 9-10 | 0.50 | 0.14 |

Ultimate shear stress

| | Values of individual shear cracks | | Values of all shear cracks | | |
|---|---|---|---|---|---|
| | Opening | Sliding | # of | Opening | Sliding |
| | mm | mm | cracks | mm | mm |
| RC-0 | 1.10-1.40 | 0.40-0.90 | 1 | 1.36 | 0.46 |
| RC-d | | | 1-2 | 1.59 | 0.66 |
| RC-½d | | | 4 | 1.70 | 0.58 |
| RC-¼d | | | 4-5 | 1.95 | 0.70 |
| RECC-0 | 0.25-0.35 | 0.05-0.20 | 8-10 | 1.39 | 0.48 |
| RECC-d | | | 9-12 | 1.49 | 0.38 |
| RECC-½d | | | 11-14 | 1.61 | 0.30 |
| RECC-¼d | | | 15-16 | 2.06 | 0.24 |

The total number of shear cracks detected by the DIC system and the combined sliding and opening (i.e., measured across all cracks) in the RC and the RECC beams are presented in Table 7.4. Experimental results indicate that ECC's contribution to

the shear capacity is similar to that of steel shear reinforcement. Fibers in the cementitious matrix control shear crack widths and improve crack distribution. For example, only one shear crack was detected for the RC beam without transverse reinforcement while eight to nine cracks were detected in the corresponding RECC beams. The RC beams with transverse reinforcement with d/4 spacing had 4-5 cracks at ultimate load, while the similarly reinforced RECC beams had 15-16 cracks. Additionally, fibers in ECC improved shear resistance by bridging cracks and transferring stresses over the crack. Individual crack deformations at ultimate load for the individual materials are similar regardless of the amount of transverse reinforcement; however, for RECC the crack deformations (opening and sliding) at failure were 20% to 25% of the crack size in RC (Table 7.4). This indicates the potential benefits of RECC in structures exposed to moisture and other aggressive substances.

The sum of all crack openings at the ultimate loads increase by adding more transverse reinforcement. This is due to the fact that the individual crack openings are similar at ultimate stage independent of the amount of transverse reinforcement. Therefore, as the number of cracks in beams with more reinforcement increases, the total deformations increase. The experimental results indicate that additional shear reinforcement reduces the sliding of shear region for both materials at a stress level of 4.5 MPa. The sliding of shear cracks is highly dependent on opening of a single crack for RC as aggregate interlock restricts sliding. The contributions from fibers and traditional reinforcement reduce the sliding of shear crack until ultimate loading.

### 7.3.3 Formation of shear cracks

Figure 7.6 and Figure 7.7 show the calculated strain spectrum from DIC measurements overlaid on an image of the specimen surface. The DIC system provides a useful illustration of the cracking behavior by overlaying a color-contour of facet strains on an image of the deformed specimen. Light colors indicate high facet strains (indicating cracking has occurred in either concrete or ECC), while the dark color indicates low facet strains. Although strain does not accurately represent crack formation, the images indicate cracks with regions of very high strains. The blank areas in the color contour overlay are caused by unrecognizable facets either by excessive deformations or by entrapped air pores on the specimen surface (Pease et al. 2006).

Figure 7.6 illustrates the development of cracks at varying load levels in RC (left column) and RECC (right column) beam specimens with stirrup distance s=d (RC-d and RECC-d). As can be seen, the main shear cracks develop directly along the diagonal between load and support and in some cases a shear-compression failure was clearly noticed. Additional cracks parallel to this diagonal form in RECC. For RC the first visible cracks appear at a shear stress of approximately $\tau$=2 MPa, which

corresponds to 40% of ultimate shear stress. Before the shear stress reaches τ=3 MPa, the shear crack is visible between load and support points. The majority of cracks forms before the loading reaches τ=3 MPa. Additional load causes crack openings to increase, but additional cracks are typically not introduced in RC.

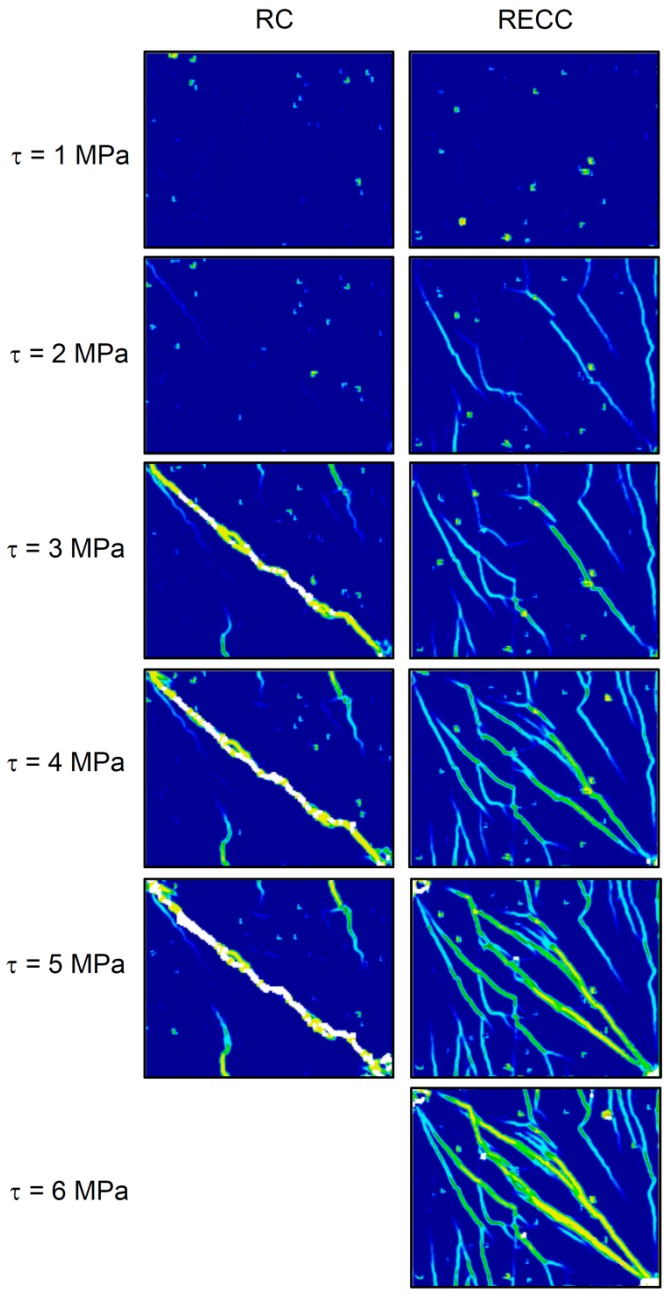


***Figure 7.6*** *Crack formation in a) RC and b) RECC beam specimens at different load stages (The area illustrated in the figure is marked as "area of interest" in Figure 7.2)*

In the RECC-d beam (Figure 7.6, right column) a different cracking behavior was observed. The first diagonal shear cracks appear in the RECC-d beam at a shear stress of approximately τ=1.5 MPa with secondary parallel cracks initiating in close

proximity and short sequence. At τ=2 MPa the first flexural cracks appear in the regions where the flexural moment in the shear span is the largest. Flexural cracks, which initially form vertically, propagate at an inclination due to shear forces in the beam. Shear cracks continue to develop further into the beam at shear stress of τ=3 MPa which corresponds to 45% of the ultimate shear strength. The cracks propagate at an angle of approximately 43° between the load points. Some of the cracks (indicated in light color) seen in the images are several micro cracks, which cannot be differentiated due to limited resolutions of the images. Increased micro cracking occurs parallel to the first developed shear crack band in image which corresponds to shear stress of τ=5 MPa. More flexural cracks develop further into the beam and the widths of all cracks increase. The subsequent ultimate failure occurred in a localized fracture plane parallel to the first developed shear crack as the two beam parts are separated perpendicular to the fracture plane.

Figure 7.7 shows the crack patterns at ultimate load for RC and RECC beams with varying amounts of stirrups. All beams demonstrated failure due to shear loading. Similar to the behavior in uni-axial tension, RECC beams exhibited multiple cracking under shear loading prior to localization and failure. Results clearly show that increasing traditional shear reinforcement in RC and RECC beams led to formation of more cracking prior to failure. Figure 7.8 and Figure 7.9 illustrate a significant difference in crack distributions from RC and RECC beams. Cracking in RECC beams consisted of a large number of fine cracks, while RC beams tended to have a small number of wider cracks. The total deformations induced by cracking were similar in RC and RECC beams; however individual crack openings were minimized in RECC beams.

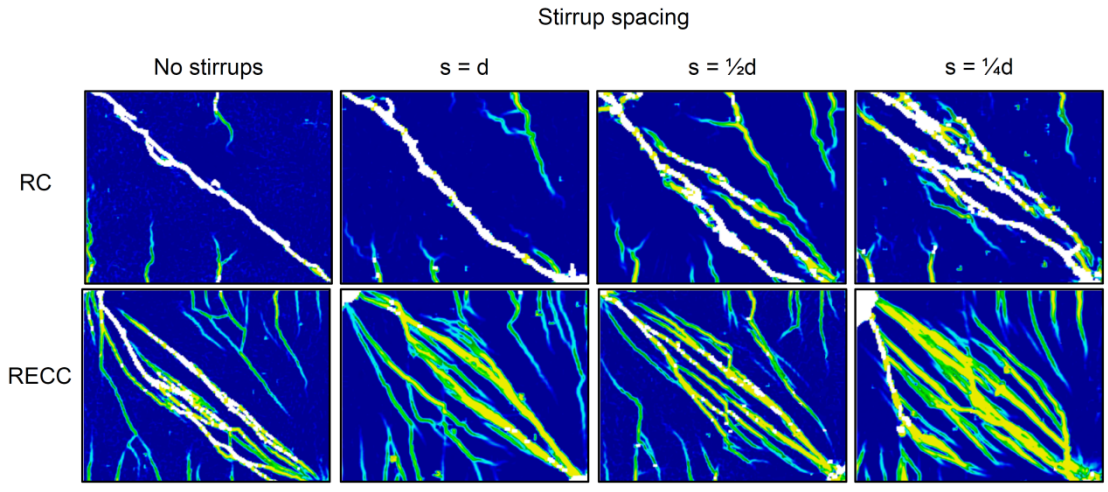


***Figure 7.7*** *Crack distribution of a) RC and b) RECC beams at 100% of ultimate strength for increasing amounts of shear reinforcement (The area illustrated in the figure is marked as "area of interest" in Figure 7.2)*

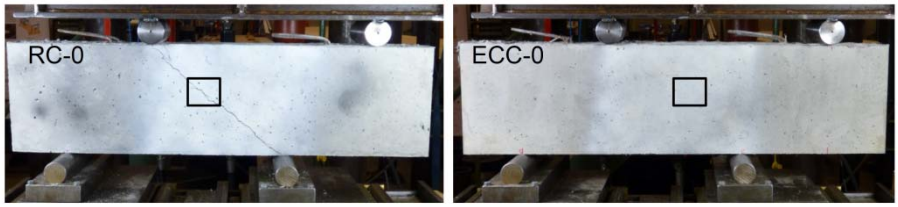


***Figure 7.8*** *Shear cracks in beam at ultimate load: a) RC and b) RECC*

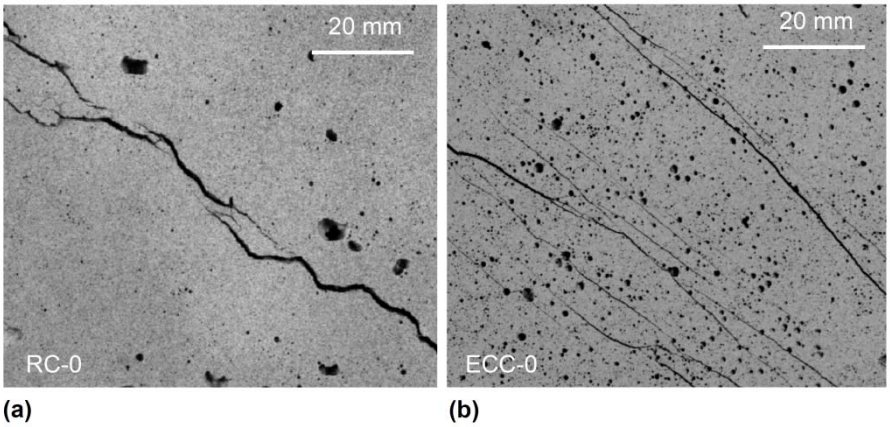


***Figure 7.9*** *Zoom in highlighted region in Figure 7.8: a) RC and b) RECC*

### 7.3.4 Shear crack development

The investigation of shear crack formation and propagation is important to improve the current understanding of the shear behavior of structures. The intention is to develop more precise predictions of the shear capacity and to increase understanding of shear cracking behavior, which may lead to the development and design of materials with increased shear resistance and deformation capacity.

Figure 7.10 shows the observed crack opening and sliding responses for RC and RECC specimens with and without conventional transverse reinforcement obtained by DIC. First cracking strengths were similar for RC and RECC, although in most cases it was ~10-30% higher for RC. However, the initial (immediate) crack opening was on average 10 times larger for RC beams. The initial crack opening for RC reduced by addition of stirrups, while stirrups had only minimal impact on initial crack opening for RECC. Crack opening occurs prior to crack sliding in RECC, while crack sliding occurs simultaneously with crack opening in RC. Crack sliding initiated in RECC after crack openings of roughly 0.1 mm, which is approximately ½ the maximum particle size contained in the RECC material. Crack sliding and opening in the RECC beams occurred at an increased rate once crack widths exceeded approximately 0.20 - 0.25 mm. With additional crack opening, the majority of PVA fibers in the ECC

ruptured, leading to shear failure. Optimization of the composite action between fibers and cementitious matrix could lead to a fiber pullout failure which would provide further increase in ductility prior the ultimate failure.

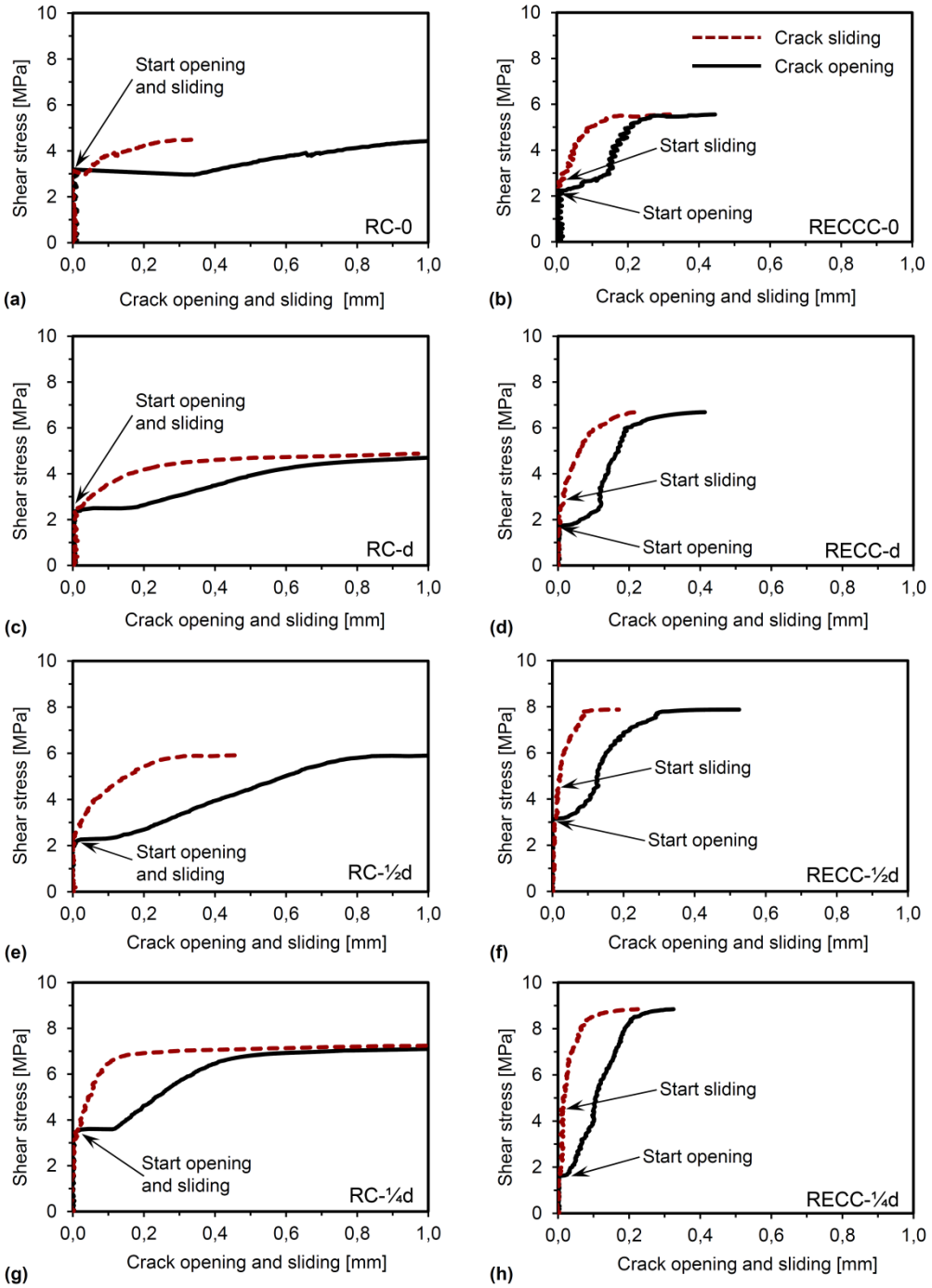


***Figure 7.10*** *Characteristic shear stress - crack opening and sliding deformation relationship for: (a) RC-0; (b) RECC-0; (c) RC-d; (d) RECC-d; (e) RC-½d; (f) RECC-½d; (g) RC-¼d and (h) RECC-¼d beams*

## 7.4 Phenomenological model of shear crack development

To explain the mechanisms controlling shear cracking and failure in both RC and RECC, a phenomenological model has been developed and is illustrated in Figure 7.11 based on the results shown in Figure 7.10. In RC before cracking, stirrup and concrete strains are equal. As concrete cracks at small strains, significant loading of shear reinforcement only occurs after inclined shear cracks form in the concrete. Thus, stirrup spacing does not influence the initial cracking strength. Figure 7.11 (b) and (c) illustrate the shear crack development mechanism for reinforced concrete (RC) consisting of four stages:

1. Crack formation – brittle fracture occurs, resulting in crack opening and relatively small crack sliding without increasing load. For concrete without transverse reinforcement, approximately 30% of the ultimate crack opening occurs in stage 1; by adding transverse reinforcement, the immediate crack opening at first shear crack formation is reduced.
2. Crack opening and sliding increase with additional load resisted by activation of aggregate interlock and stirrups bridging the crack. The amount of crack sliding is highly dependent on aggregate interlock which is highly dependent on aggregate size. The effect of aggregate interlock is reduced with additional crack deformations as fewer aggregates participate, thus, the stress in the stirrups increases. Specimens without transverse reinforcement transfer shear stresses across the crack by aggregate interlock additionally to the dowel effect of the longitudinal reinforcement. Due to reduced aggregate interlock and lack of stirrups, the crack opens and slides more rapidly. Reduced aggregate interlock results in significant crack sliding. For smaller transverse reinforcement spacing, multiple cracking can occur at this stage.
3. Stage 3 starts when the transverse reinforcement starts to yield and aggregate interlock becomes insignificant due to increased crack openings. This stage is delayed through the addition of larger amounts of traditional reinforcement in the element, due to improved control of crack sizes. Shear stresses are mainly transferred across the crack by stirrups. Crack opening and sliding occurs very rapidly and without significantly increased applied load.
4. Failure – specimen failure is caused by rupture of the stirrups.

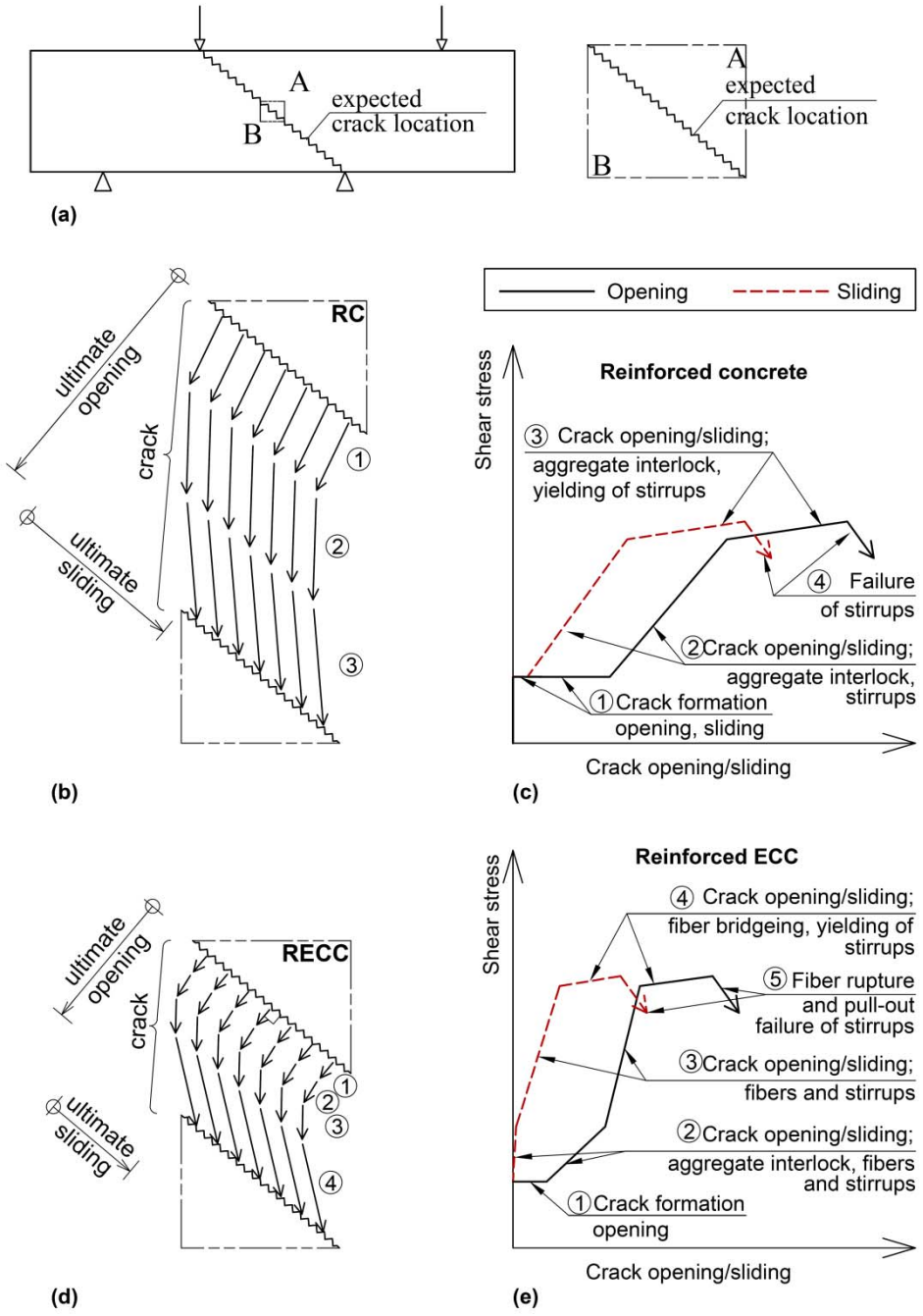


***Figure 7.11*** *Shear crack development mechanism of RC and RECC: (a) expected shear crack location; (b) and (c) crack development in RC; (d) and (e) crack development in RECC*

For RECC, shear load is transferred across the cracks by fiber bridging. The shear crack behavior of RECC can be characterized by the following stages as illustrated in Figure 7.11 (d) and (e):

1. Initiation of crack opening – brittle crack opening without noticeable sliding. Sliding is resisted by an immediate activation of aggregate interlock, provided by fibers transferring stresses across the crack.

2. Initiation of crack sliding – crack opening slowly increases with relatively small sliding (<0.03mm). Crack opening and sliding are restrained mainly by fiber bridging, aggregate interlock and stirrups. Due to the small aggregate size (the largest particle size in the ECC is quartz sand with a maximum particle size of 0.18 mm) and fibers ($\varnothing_f$=0.040 mm), the shear resistance from stirrups and aggregate interlock occurs at a smaller crack opening compared to RC. Evidence shows that crack deformations increase with shear load more rapidly in this stage than in following stage. The increased deformation rate may indicate that the traditional reinforcement requires additional deformations to be fully activated on transferring stresses over the crack.
3. Reduced rate of combined crack opening and sliding – crack opening and sliding develop slowly mainly due to fibers and stirrups bridging cracks. The effect of aggregate interlock is reduced due to crack opening exceeding half of the maximum aggregate size (roughly 0.1mm). For RECC beams without transverse reinforcement, crack opening and sliding increase more rapidly. Additional transverse reinforcement inhibits crack opening and sliding due to the increased cross-sectional area of materials bridging the crack. At this stage the stirrups and longitudinal reinforcement (dowel effect) are fully activated.
4. Increased rate of combined crack opening and sliding – crack opening and sliding is resisted mainly by stirrups. Shear stress carried by the stirrups increases and ultimately yielding is reached in the stirrups. At this stage, fibers reach maximum bridging stress and cracking localizes, leading to failure. At the end of this stage additional load causes pullout and/or rupture of the fibers at the weakest crack.
5. Failure – the failure of the specimen is caused by rupture of stirrups in RECC and pull-out and failure of fibers in ECC.

Furthermore, during stages 2 and 3 for RECC, additional shear cracks may form due to the multiple cracking feature of ECC, temporarily reducing the crack opening rate of the existing shear cracks.

The dowel effect by longitudinal reinforcement takes place in the shear stress transfer zone over the crack throughout all stages, but the influence of this mechanism is not included in the schematic description in Figure 7.11.

## 7.5 Conclusions and remarks

The benefits of RECC, regards to resisting shear, include improved shear resistance and cracking control. Similar to uni-axial tension, multiple cracking of ECC occurs in shear. The first cracking strength was slightly higher for the RC used in this study;

however, the initial crack opening of the RC was 10 times larger than that in the RECC.

Crack deformations for the RECC were between 3 and 5 times smaller than for RC at similar load levels. The addition of stirrups in RC controls cracks widths as more stirrups resulted in reduced initial crack opening and total crack deformations (opening and sliding). Initial crack opening was independent of stirrup spacing in the RECC beams. The contributions of ECC on shear behavior of RECC include:

- Fiber bridging of shear crack, thus increasing the shear capacity;
- Traditional shear reinforcement is activated at smaller individual crack deformations (opening and sliding);
- Crack deformations are limited by fiber bridging mechanism and by activating traditional shear reinforcement at smaller crack deformations.

Based on the shear stress-strain responses and DIC measurements of the specimen deformations, a phenomenological descriptions of the shear crack opening, crack sliding and subsequent failure of RC and RECC are proposed. For the RC the shear loads over the shear crack can be transferred only by stirrups, aggregate interlock and fiber dowel effect of longitudinal reinforcement. The crack development mechanism for RECC is more complex due to the fiber bridging mechanisms, which induces multiple cracking resulting in smaller crack openings at a given shear stress as well as higher ultimate shear stress. As the ECC matrix used in this study had a maximum aggregate size of 0.18 mm, aggregate interlock in RECC was not as significant as in RC.

The use of RECC provides improved shear resistance, controlled crack sizes and a more ductile shear failure. However, additional increases in the ductility at shear failure are possible by engineering the composite such that fiber bridging and resistance against shear sliding can be maintained remaining fibers active by fiber pullout rather than rupture.

# Chapter 8

# Lightweight composite floor and roof panels

This chapter reports on experimental investigation of the structural behavior of a prefabricated modular roof and floor system, developed as part of this Ph.D. study as an example application of ECC. The lightweight prefabricated modular system consists of thin ECC plates connected to lightweight steel joists. This work is a continuation of previous studies completed in DTU on prefabricated floor and roof panels where a composite panel was made with steel joists integrally cast in the ECC slab and a semi-modular assembly of a thin-walled ECC slab and steel truss girders. The modular concept introduced in this chapter aims at ease of manufacturing and storage processes of the panels by casting the ECC slab in relatively small elements and subsequently joining them with the lightweight steel profiles. The focus of this chapter is on the development of a modular panel and experimental investigation of the structural behavior of the system under service conditions and at ultimate.

## 8.1 Potential application of ECC

The globally increasing need for economic, durable, attractive and high quality housing requires innovative technologies to meet this demand with particular consideration of their environmental impact, sustainability, and life-cycle performance. Current trends in the construction sector are towards prefabricated modular structures and intrinsically reinforced structural elements that can be

automatically manufactured in a factory setting with mass-customized design and a multitude of assembly configurations.

Recent innovative advances in fiber reinforcement technology and the introduction of ECC have provided the prerequisites to achieve a high performance and economically viable alternative to traditional reinforced concrete materials for specific applications, such as thin-walled precast concrete elements without additional steel reinforcement. Examples of these applications are prefabricated panels for wall, floor, and roof elements.

An increasing number of structural roof and floor panels, both prefabricated and cast-in place, exist and are commonly used in the construction industry. The most commonly used prefabricated structural panels are presented in Figure 8.1, including double-T panel (Figure 8.1(a)) and hollow core panel (Figure 8.1(b)). Also, a composite concrete-steel floor panel that consists of a relatively thin reinforced concrete slab and a steel truss integrally cast into the slab (Figure 8.1(c)) is currently used and can be either with poured in place or precast concrete (Hambro 2009).


***Figure 8.1*** *Commonly used prefabricated structural panels: (a) double-T panel (www.stubbes.org); (b) hollow core panel (www.oberbeton.com.ua) and (c) Hambro panel* (Hambro 2009)

The most popular semi-prefabricated panels include biaxial hollow core panels known as Bubbledeck (Figure 8.2(a)), filigree panels (Figure 8.2(b)), reinforced concrete on a corrugated steel deck, also known as pan deck (Figure 8.2(c)) all of which are requiring casting of a concrete overlay at the construction site (in-situ). Timber-concrete composite panels are also used in practice. They utilize the tension properties of timber combined with the compression strength of concrete to create relatively light and thin structural panel (Crocetti et al. 2014; Kuhlmann 2008). Recent publication on timber-concrete panels (Crocetti et al. 2014) suggests to use a

prefabricated timber-concrete panel with SFRC. More details on comparison between available composite panels can be found elsewhere (Larusson et al. 2013).

Although these existing concrete composite panels are widely used, the building industry develops further with the increasing demand on new structural elements. The development of newer precast structural elements includes the request for lightweight, implementation versatility, reduced construction time and cost and higher durability performance. All of these requirements interact and affect each other and need to be addressed during the design process.

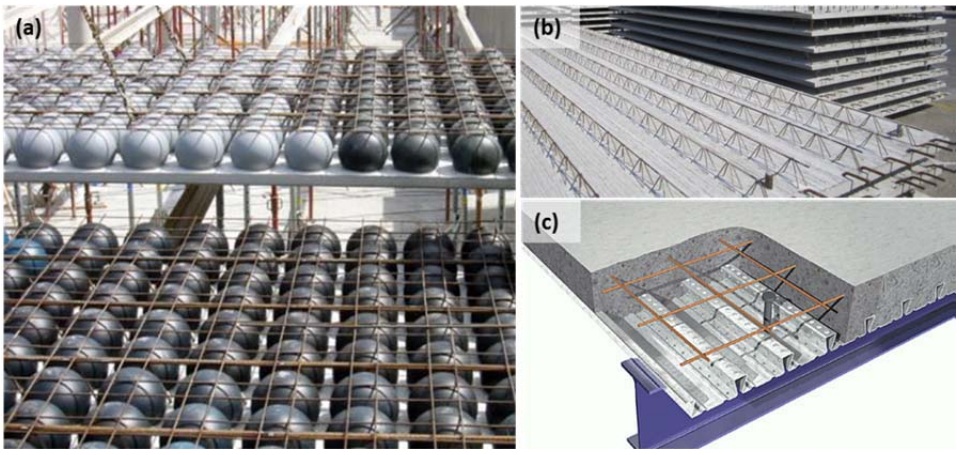


***Figure 8.2*** *Semi prefabricated structural panels: (a) biaxial hollow core panel known as Bubbledeck (www.archello.com); (b) filigree panel (www.vollert.de); and (c) reinforced concrete on a corrugated steel deck, also known as pan deck (www.swuk.net)*

In this context, by utilizing the properties of ECC in structural elements such as prefabricated floor and roof panels allows for a more efficient construction process. As described in Section 1.1.6, ECC has the ability to exhibit strain hardening due to a specifically designed interaction between the cementitious matrix, the fibers and their interfacial bond. As a result of the ductile tensile load-deformation behavior of ECC, structural members can be designed with reduced sectional dimensions compared to those of traditional reinforced concrete. More specifically, unreinforced ECC in combination with light gage steel joists can be utilized in the development of prefabricated modular floor and roof panels.

## 8.2 Development of modular lightweight composite floor and roof panels

The objective of the panel systems presented in this chapter was to develop a lightweight, easy to install alternative to traditional and heavier prefabricated floor and roof panels by implementing ECC. The following sections describe the developments stages of the modular lightweight composite floor and roof panels,

including prior work by others and new developments and findings from this PhD study.

### 8.2.1 Initial developments at DTU – Integrally cast panels (ICP)

The first attempt to develop a composite panel of ECC and a steel substructure was integrally cast panels (ICP) shown in Figure 8.3(a) (Fischer 2010; Larusson et al. 2013). The ECC floor panel was designed as a composite member with lightweight steel joists integrally cast in a 50 mm thick ECC slab. The steel joists used were galvanized light-gage steel channels with punch-outs along the embedded web and flange to ensure composite action. The steel joists were 300 mm high, 70 mm wide and with a wall thickness of 2.66 mm and a yield strength of 350 MPa. The thin walled profiles were embedded 25 mm into the 50 mm thick ECC slab, resulting in an overall structural height of 325 mm. The panel was cast inverted, with the top slab surface facing downward during fabrication. Prior to ECC placement, the steel joists were positioned at the slab mid-height and held in place by means of precast ECC chairs. The ECC was self-consolidating to ensure proper consolidation around the steel joists without additional vibration needed during the casting process. The ICP was developed to reach the necessary criteria for floor and roof panels according to codes of practice, such as loading capacity, deflection limits and dynamic response.

The shortcoming of the ICP design was the shrinkage deformations of the ECC. As described in Section 2.3.3, ECC undergoes significant shrinkage deformations during curing and the first month of drying. As the steel joists were integrally cast in the ECC, the steel joists restricted the possibility of ECC to deform freely resulting in significant shrinkage-induced cracking and downward deflections.

### 8.2.2 Developments by Larusson – Semi-modular panels (SMP)

In continuation of development of lightweight composite panel with ECC slab involved precast ECC slab and a subsequently mounted steel truss substructure introducing a semi-modular concept (later in this chapter referred as SMP) shown in Figure 8.3(b).

The unique feature of the proposed semi-modular design were individual anchor points integrally cast with the ECC slab, which were subsequently used to attach a steel truss substructure. By casting individual anchor points into the ECC, the slab was allowed to shrink and deform independent of the substructure prior to assembly of the composite panel without causing shrinkage-induced stresses and cracking and undesirable deflections of the lightweight composite panel during curing.

The SMP consisted of a 50 mm thick ECC slab and steel substructure (steel truss) with a height of 275 mm, resulting in a total height of 325 mm. Due to the small thickness of the ECC slab, no suitable commercially produced cast-in place anchor

plates were available. Custom made anchor plates were fabricated to fit within the shallow depth of the ECC slab. Four SMPs were tested to measure the structural behavior. Three of four SMPs had a bolted steel truss substructure and one SMP had a welded truss substructure.

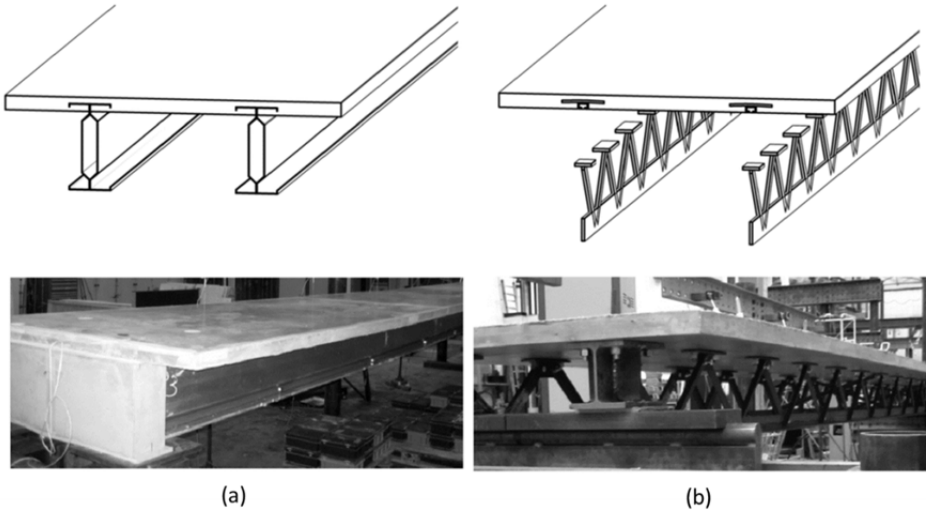


***Figure 8.3*** *Development of lightweight composite floor and roof panels: (a) integrally cast panel (ICP) and (b) semi-modular panel (SMP)* (Larusson et al. 2013)

The development and properties of ICP and SMP are described by Larusson (Larusson et al. 2013). The paper concludes that the deflections and natural frequencies of both types of panels were found to be within acceptable limits. The dynamic properties of the tested specimens were shown to meet typical structural performance requirements; however, additional research was needed to further improve the dynamic behavior towards higher natural frequencies and improved damping. Both the ICP and SMP offered the flexibility of adapting to a multitude of different performance requirements by selection of a specific combination of ECC slab and steel substructure, thereby controlling the strength and stiffness properties of the panel. However, the SMP involved casting a full size ECC slab (50 mm thin, 1.2 m wide and 8.4 m long) with cast-in anchor points in the bottom of the slab. Subsequently, the slab had to be turned around to mount the steel substructure. The handling of a thin ECC slab is a complicated procedure as the slab is very flexible and could be easily damaged during handling.

### 8.2.3 Developments in this study – Modular panels (MP)

Based on these previous experiments, a new modular system for the lightweight composite floor and roof panels with ECC slab was developed in this study, as shown in Figure 8.4. The details on the modular panel (MP) are illustrated in Figure 8.5. The

biggest benefit of the MP is the modular concept of casting ECC slab. The full ECC slab consists of smaller precast plates, which are more robust during handling. Custom-made cast-in elements shown in Figure 8.6 are placed in ECC for connecting the plates to the steel joists. The ECC plates were cast in a size of 1.0 m x 1.2 m with four cast-in elements. ECC plates that were designed to be located at the end of the composite panel, where shear forces are maximized, included six cast-in elements. The precast ECC plates had no protrusions, which otherwise would complicate storage, and had a total weight of approximate 130 kg each. Thus, the ECC plates were easy to cast and to handle and required limited space for storage during curing.

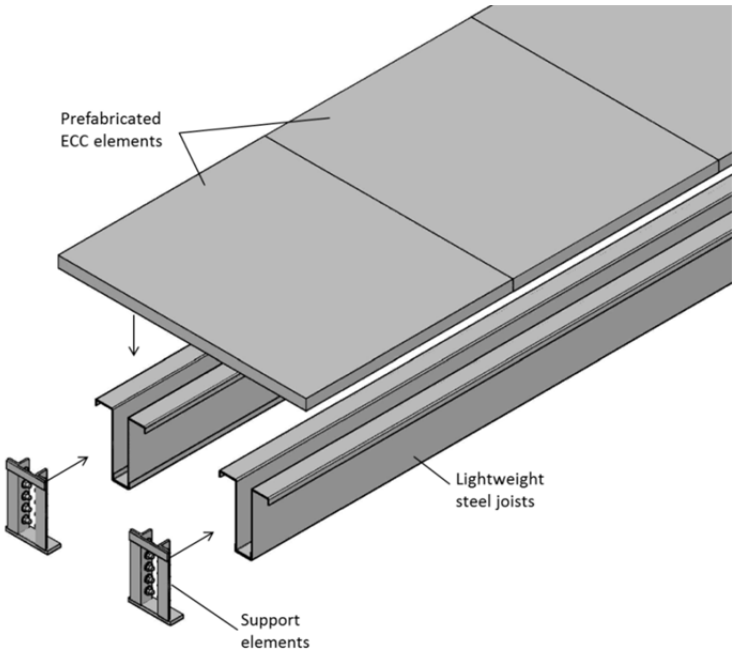


***Figure 8.4*** *Prefabricated modular lightweight floor and roof panel MP*

The ECC slab and the steel joists develop a composite action in the direction of the larger span of the panel. In between the joists, ECC acts as a continuous one-way slab. For the design of the composite panel, the following assumptions were made: a linear elastic strain distribution through the depth of the sections and plane sections remain plane after deformations. Furthermore, the panel is assumed to behave as an ideal composite without any movements in connections. That is, the connections between the ECC slab and cast-in element, and the connection between the lightweight steel joists and the cast-in elements are rigid. Keeping that in mind, also, the connections have been designed. Assuming a linear elastic behavior of the materials, the resisting bending moment of the deck sections is estimated based on two failure criteria: the compression capacity of ECC is reached or yielding of the steel substructure.

The present Eurocode (EN1994 2007) for composite steel and concrete structures does not give precise values for serviceability limits. Limits may be included in National Annexes or may be specified for each project and agreed with the client. For

the design of the panels, the serviceability limit state (SLS) was set as a maximum (mid-span) deflections of L/400 under uniformly distributed load of 4 kN/m$^2$, or 20 mm.

For the design, the deflections, Δ, of the composite panel with span, *L*, are determined using equations for a simply supported beam with uniformly distributed load, $q$. The mid-span deflection (Δ) can be found:

$$\Delta = \frac{5\ q\ L^4}{384\ E\ I_{Eq}} \tag{8.1}$$

Where $E\ I_{Eq}$ is the equivalent stiffness with *E* being the Elastic modulus of ECC and $I_{Eq}$ is the equivalent moment of inertia of composite cross-section.

The natural frequency and damping ratio are important parameters in the serviceability design of floors under human activities. If the proper values for dynamic response of a floor have not been reached, the level of the dynamic effects could induce excessive vibrations, causing user discomfort conditions and even compromising the structural system (Gandomkar et al. 2011; Mello et al. 2008). From the equation of motion, the natural frequency, *f,* of the system with a constant stiffness ($E\ I_{Eq}$), mode shape, *n*, and mass, *m*, is determined as:

$$f = \frac{n^2\ \pi}{2\ L^2}\sqrt{\frac{E\ I_{Eq}}{m}} \quad with\ n = 1, 2, 3 \ldots and\ m = w/g \tag{8.2}$$

where w is weight per unit length and g is the gravity acceleration ($g = 9{,}8\ m/s^2$). To evaluate the damping ratio, (ζ) of the structure, low damping is assumed, i.e. $\sqrt{1-\zeta^2} \approx 1$, thus the damping ratio can be written as:

$$\zeta = \frac{\ln\left(\frac{u_t}{u_{t+T}}\right)}{2\ \pi} \tag{8.3}$$

where $u_t$ is the peak amplitude at time t and $u_{t+T}$ is the amplitude at time, *t*, plus one period, *T*.

### 8.2.4 Construction approach

For full-scale testing, the MP was designed to have length of an 8.0 m and the width of 1.2 m. As illustrated in Figure 8.5, each MP consisted of 8 ECC plates and 4 lightweight steel profiles (Figure 8.7(a)) connected in 2 joists. Two types of ECC plates were made – with 4 and with 6 cast-in elements to provide connection points to steel joists. Each MP had 2 ECC plates with 6 cast-in elements that were positioned at the ends of the panel where the highest shear forces were expected.

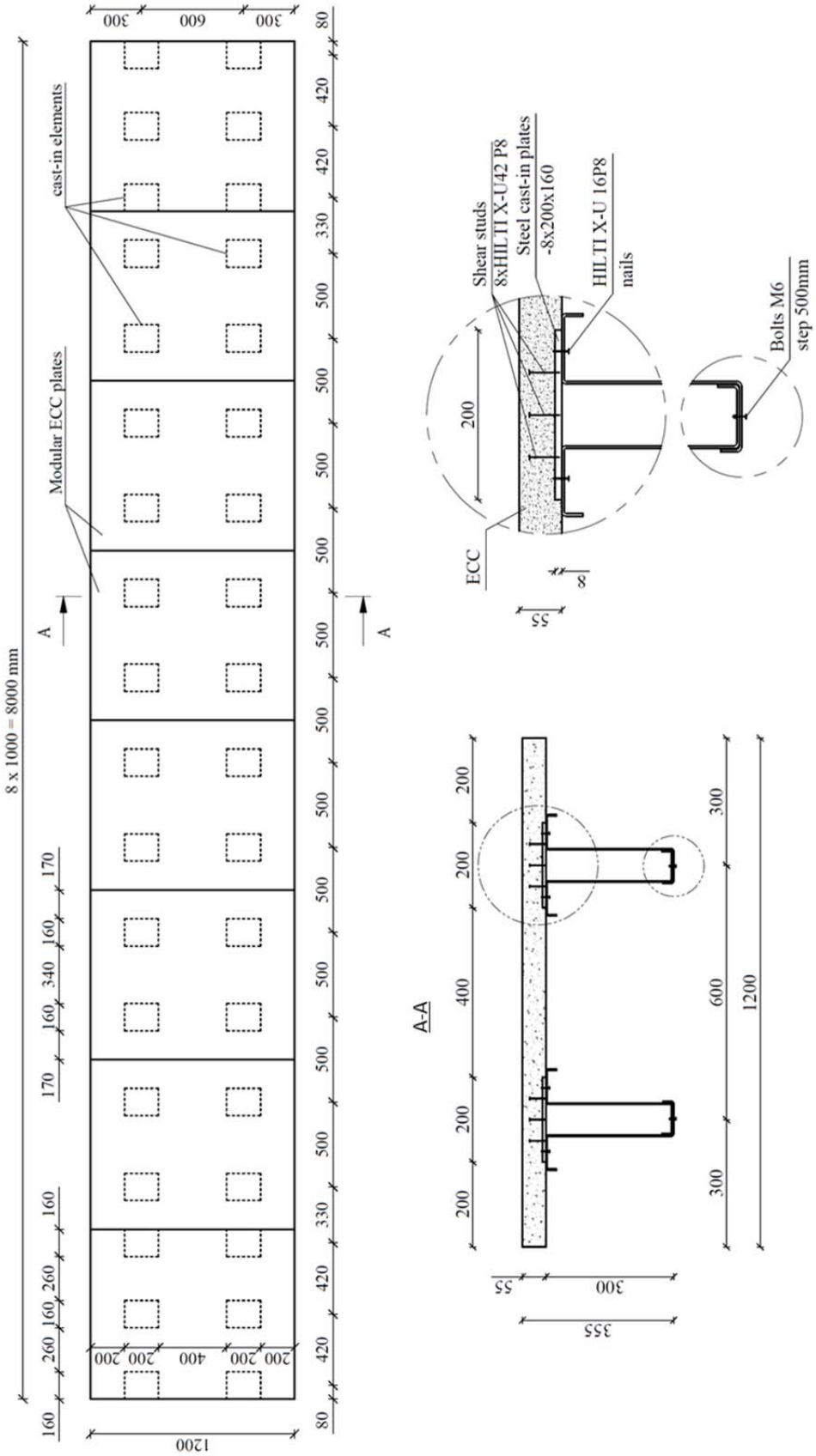


***Figure 8.5*** *Design details of modular lightweight floor and roof panel MP2*

Each cast-in element (Figure 8.6) consisted of 8 mm thick steel plate (200 mm x 160 mm) with 8 steel nails with a length of 45 mm that provided the shear connection between the cast-in elements and the ECC plate. The nails were shot in the steel plate with HILTI DX 460 powder actuated tool. The cast-in elements were symmetrically positioned in the bottom of the ECC plate mold (smooth surface down) and ECC was cast on top of that. The fresh and hardened properties of the ECC are described in Chapter 2. The plates were cured for at least 28 days before the composite deck was assembled.

The steel substructure of each MP consisted of 2 steel joists, each of these joist consisted of two lightweight steel Z-profiles. The details of each profile are illustrated in Figure 8.7(a). To achieve the composite action in the modular panel, the steel joists were connected with ECC through the cast-in elements. The connection was provided through 16 mm long steel nails that were shot through lightweight steel profile in cast-in element in the steel plate with HILTI DX 460 powder actuated tool. Details of the connection are provided in Figure 8.5. For the first panel in total 4 nails were connecting each cast-in element with the steel joists (16 nails per each ECC plate), the connection was strengthened for the second and third element by having 6 nails in each connection (24 nails per ECC plate). The height of the steel joist was 300 mm, thus the total height of the MP was 355mm.

To prevent a local failure in steel joists at the supports, special support elements were designed to transfer the shear loads from supports to the web of the steel joists. The details of the support elements are illustrated in Figure 8.7(b).

***Construction for real applications***

The intended construction of the MP for actual applications involves pre-casting of the ECC plates and assembly of the composite panel on construction site. Construction of the MP will consist of:

- Prefabrication of the cast-in elements and casting of ECC plates. The ECC plates should be cured and stored for a total of 28 days before assembling the composite panel, to undergo the majority of drying shrinkage deformations.
- Selection of the steel joists for the composite panel based on the specific application. The steel joists should be chosen taking into account the intended span length and performance requirements of the panel. The geometry of the steel joists shall be selected to allow connection between the steel substructure and the cast-in elements in the ECC plates.
- The assembly of the composite panel. The ECC plates shall be located on a flat surface with cast-in elements facing upwards. The ECC plates shall be butted against each other such that no gaps are present between individual plates or gap-cast. The steel joists are then placed on top of the ECC plates and the connection is made with steel nails, shot into the steel plate with a powder

actuated tool. The support elements are finally connected to the ends of the steel joists and the composite panel can be placed in the needed position in the building.

***Figure 8.6*** *Cast-in element with powder actuated nails*

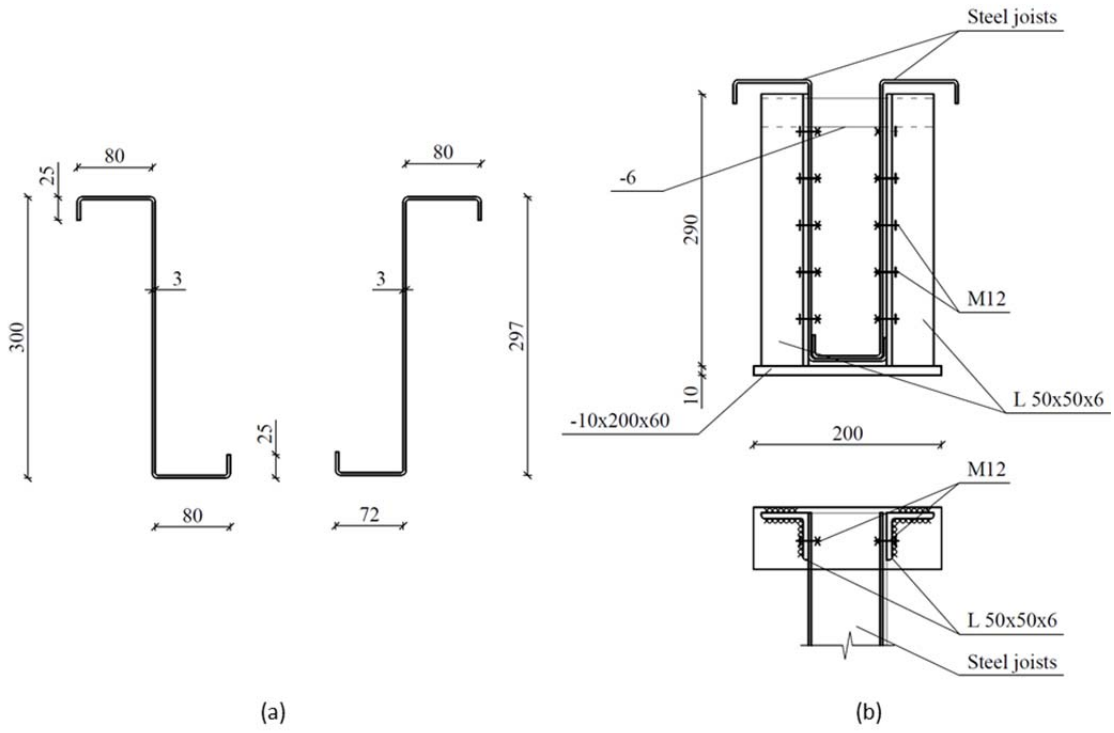


***Figure 8.7*** *Modular lightweight floor and roof panel MP2: (a) details of steel joists and (b) details of supports*

## 8.3 Experimental investigation of panels

The testing of lightweight composite panels with ECC slab was carried out for serviceability limit state (SLS) and ultimate limit state (ULS). The test setup is shown in Figure 8.8, the composite panel was simply supported at both ends with a span of

8.00 m. At each end the panel was supported at two points with a 0.60 m distance between them. The same types of tests with similar dimensions were carried out on previously tested ICPs and SMPs, thus the results can be compared.

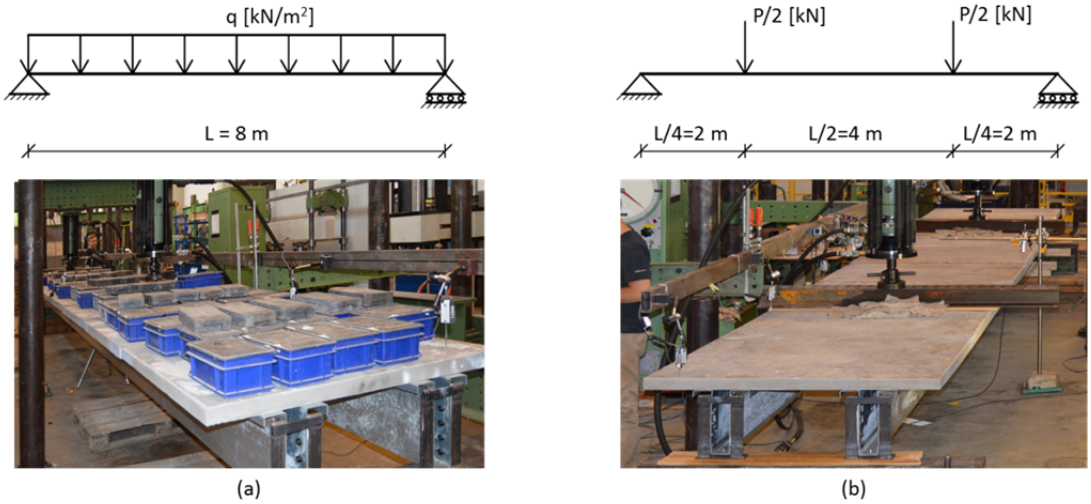


***Figure 8.8*** *Test setup of (a) serviceability and (b) ultimate limit state testing*

## 8.3.1 Serviceability testing

Loading at the SLS was applied to the specimens by a uniformly distributed load of 50 kN evenly over the 8 m long span resulting in a surface load of 4.0 kN/m$^2$ (Figure 8.8(a)). The distributed loading was applied in four steps with increments of 12.5 kN, or 1.0 kN/m$^2$ at each step. Also, natural frequency and damping were measured during SLS testing. Throughout SLS testing, the deflections were measured at 8 points of the panel at each load step. The deflections were measured with LVDTs at locations as illustrated in Figure 8.9, three measurements were taken at every load step and the average values are used for results. The locations of LVDTs are presented in Figure 8.9; two LVDTs were located in the mid-span in both sides of the panel (LVDTs 4 and 8) to measure the maximum deflection. Two LVDTs were positioned to measure deformations on top of the support (LVDTs 1 and 7); this was done to measure the settlement of the supports, thus allowing to calculate the real deflections of the panel. Four other LVDTs were symmetrically positioned in the region between support and mid-span (LVDTs 2, 3, 5 and 6).

During SLS loading, the dynamic response of the panels was measured by inducing a vibration in the composite elements and measuring its decay. From the obtained data the natural frequency and damping ratio were determined for each load increment (0, 1, 2, 3 and 4 kN/m$^2$). The vibrations were measured using a laser measuring device with a frequency of two thousand points per second. The laser had a measuring distance between 30 and 70 mm, thus the laser was situated approximately 40 mm under the ECC plate in the middle of the composite panel.

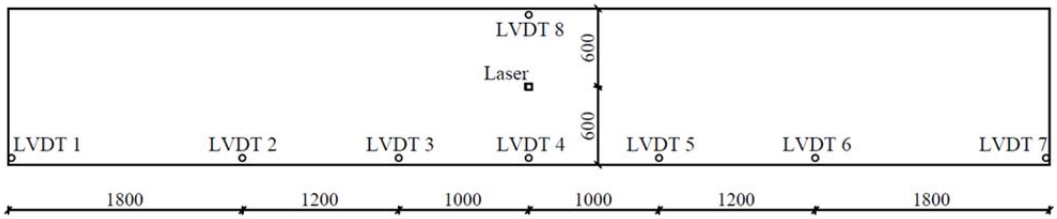


***Figure 8.9*** *Locations of deformation measuring devices*

### *Results*

The results in terms of measured deflection at uniformly distributed load up to 4 $kN/m^2$ are presented in Figure 8.10. All three types of lightweight composite panels with ECC slab on top of the steel substructure, i.e., ICP, SMP and MP were subjected to the same type of loading, thus the results of modular panels developed in this chapter are compared to results of ICP and SMP.

The ICP specimens deflected 2.9 mm at mid-span for each 1.0 kN/m$^2$ applied, SMP with steel truss substructure with bolted connections deflected ~4.9, 4.3 and 2.9 mm, while the SMP with a welded steel truss substructure 2.5 mm. The modular panels had the smallest deflection in average 2.0 mm per 1 kN/m$^2$ of applied surface load. Most of the specimens showed a linear load-deflection response during SLS loading with a maximum deflection at 4 kN/m$^2$ of less than L/400 = 20mm.

The results of dynamic response of the composite panels are presented in Figure 8.11. The vibrations of the panel were measured and the natural frequency and the damping data were obtained. For all composite panels tested, the natural frequency at self-weight only was between 8.1 and 10.2 Hz; the ICP and two of SMP with the bolted substructure had a natural frequency around 8.2 Hz while other panels around 10 Hz. At load of 4 kN/m$^2$ the natural frequency lowered to between 3.8 and 5.6 Hz (Figure 8.11(a)).

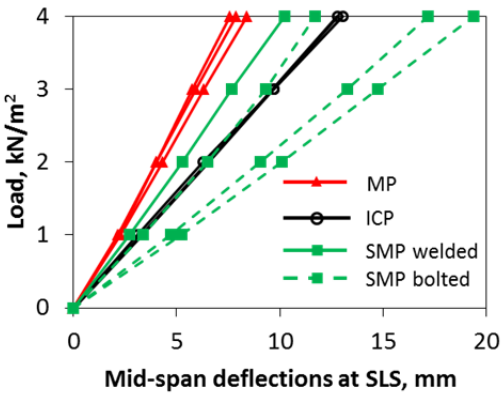


***Figure 8.10*** *Mid-span deflections under uniformly distributed surface load at SLS testing*

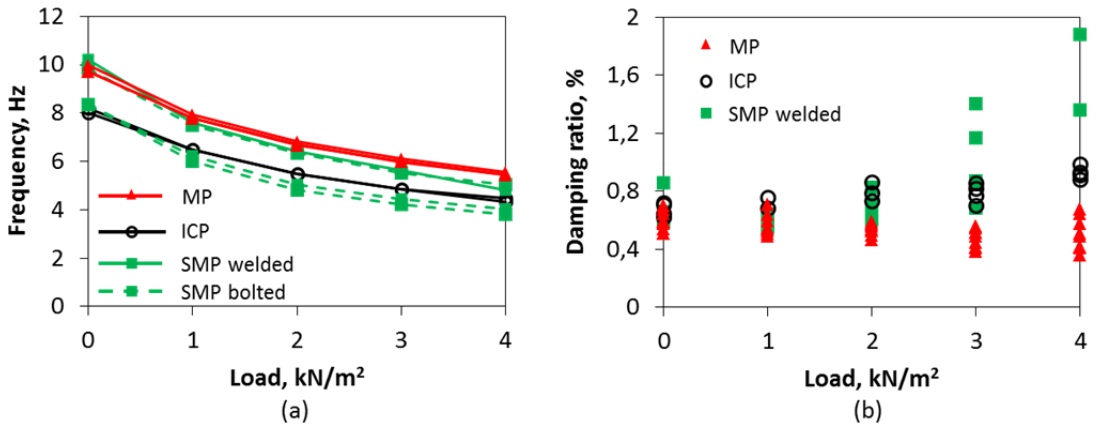


***Figure 8.11*** *SLS testing: (a) measured natural frequency and (b) damping*

The derived damping results are presented in Figure 8.11(b). The results indicate that the damping ratio of the welded SMP and ICP was increasing by applying more load to the specimen. However, the results from the MP show almost constant average damping ratio with increased loading. The damping measurements of SMP with bolted truss connections were not usable due to unexpected slip in the bolted connections.

## 8.3.2 Ultimate limit state

To evaluate the behavior of the composite panel at ULS, a four-point bending test at a loading configuration as shown in Figure 8.8(b) was used. The load was gradually applied to the panel through two pistons gradually at a rate of 2±1 mm/min. All panels tested were instrumented with two LVDTs with a maximum measuring distance of 100 mm at the mid-span of the panel (Figure 8.9 LVDT's 4 and 8). Because the first panel was subjected to a much higher deflection than 100 mm, lasers also were used to measure the deflections at mid-span for second and third panel. The laser used had a measuring range between 100 – 600 mm. The lasers were positioned approximately 110 mm above the panel. The deflections were measured with a frequency of 2 Hz. All deformations are measured after self-weight was applied.

***Results***

The results of ULS testing in terms of load versus mid-span deflection are presented in Figure 8.12. The lowest load resistance was for SMP with the bolted truss substructure. These panels had an ultimate load 90 -140 kN which is equivalent to 9.4-14.5 kN/m$^2$ uniformly distributed surface load. The ICP, MP and SMP with a welded substructure had an ultimate load of 272-310 kN equivalent to 28.3-32k kN/m$^2$ surface load.

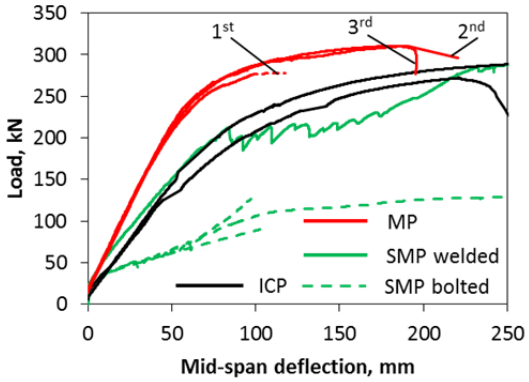


***Figure 8.12*** *Load – mid-span deflection relationships of composite panels at ULS testing*

## 8.4 Structural performance of composite panels

The full set of experimental data and details of the design of the ICP and SMP are presented elsewhere (Blond & Pedersen 2008) (Larusson 2008). The main analytically calculated and experimentally observed results of the lightweight composite panels with ECC slab are presented in Table 8.1. In the comparison, SMP only with the welded steel truss substructure has been used.

All three lightweight composite panels with ECC slab were with significantly reduced (2-3 times) self-weight compared to traditional hollow-core panel for similar span length. The self-weight of ICP and SMP was practically identical at ~155 kg/m, while the MP was slightly heavier 182 kg/m.

### 8.4.1 Performance at SLS

The analytically calculated deflections and natural frequencies at SLS of SMP and MP very well predicts the experimentally observed values with a maximum difference less than 5% (Table 8.1). The difference between analytically calculated and experimentally observed deflections and frequencies was higher for ICP with a difference up to 20%. For the analytical calculation the structural behavior of the composite panel in SLS is supposed to be in the elastic stage, also all connections in the composite panel are assumed to be rigid. These assumptions were correct for SMP and MP panels. The ECC slab of ICP was cracked before testing as a result of shrinkage in ECC that was restricted by integrally cast steel joist resulting in cracking of cementitious material. This cracking resulted in reduced bending stiffness of the panel.

However, the mid-span deflections at 4 kN/m$^2$ load was 13.0 mm for one of the ICP panels, 10.2 mm for welded SMP and 8.4 mm for one of the MP (Figure 8.10). These values comply with the assumed requirement of having deflections lower than L/400 = 20 mm. Furthermore, in some cases ACI 318 states more conservative values of allowed deflection of concrete construction supporting or attached to nonstructural

elements likely to be damaged by large deflections being L/480 that is 16.7 mm. All measured deflections under SLS loading of 4 kN/m$^2$ were also smaller than this requirement.

The natural frequency and damping ratio are important values to reveal floors serviceability under human activities. According to Bachmann (Bachmann 1995) the targeted value of natural frequency for the floors with walking should be higher than 5 Hz for highly damped floors (damping, $\zeta \geq 5$ %) and higher than 7.5 Hz for floors with low damping ($\zeta \leq 5$ %). As the modular panel is a lightweight composite structure with low damping, the comfortable natural frequency would be higher than 7.5 Hz. The value is set to shift the natural frequency away from the offending harmonic of walking forces. Bachmann also states that these limits of natural frequencies are calculated in a simple and effective way but sometimes may be unnecessarily conservative. Thus, if necessary, more accurate calculations should be made.

The measured natural frequency of all three types of panels at a self-weight only (q=0kN/m$^2$) complies with the requirement of frequency f≥7.5 Hz (Table 8.1). However, at the uniformly distributed load of 4.0 kN/m$^2$, the natural frequencies vary between 4.7 and 5.5 Hz that is below the conservative requirement of 7.5 Hz. The increase in the natural frequency between the different specimens is directly related to the increase in stiffness of the composite panels and inversely related to its mass and applied load. Due to the low weight of the ICP, SMP and MP, any superimposed loading is significant considering the low self-weight of the specimens. Therefore, any additional weight will decrease the natural frequency of lightweight composite panel with ECC slab proportionally more than for heavier, conventional panels.

***Table 8.1*** *Comparison of analytically calculated (theor.) and experimental measurements (exp.) of properties of lightweight composite panels with ECC plates*

| | **ICP**** | | **SMP***** | | **MP**** | |
|---|---|---|---|---|---|---|
| | theor. | exp. | theor. | exp. | theor. | exp. |
| Self-weight, *kg/m* | 157 | - | 154 | - | 182 | - |
| Bending stiffness EI, $kN \cdot m^2$ | $2.38 \cdot 10^4$ | - | $2.58 \cdot 10^4$ | - | $3.36 \cdot 10^4$ | - |
| Deflections, *mm* | | | | | | |
| at q=4 $kN/m^2$* | 10.74 | 12.92 | 9.93 | 10.21 | 7.62 | 7.96 |
| Frequency, *Hz* | | | | | | |
| at q=0 $kN/m^2$* | 9.4 | 8.1 | 9.8 | 9.8 | 10.4 | 9.8 |
| at q=4 $kN/m^2$* | 4.7 | 4.4 | 4.9 | 5.0 | 5.5 | 5.5 |
| Damping ratio, % | | | | | | |
| at q=0 $kN/m^2$* | - | 0.59-0.86 | - | 0.63-0.72 | - | 0.51-0.7 |
| at q=4 $kN/m^2$* | - | 1.36-1.88 | - | 0.88-0.99 | - | 0.36-0.68 |
| ULS | | | | | | |
| Peak load, kN | 226 | 284 | 287 | 291 | 287 | 300 |
| at deflection, mm | - | 218-500 | - | 282 | - | 120-190 |
| Failure mode | Fracture of steel substructure<br>Compression failure of ECC | | Combination of yielding of steel sub-structure and compression of ECC | | Buckling of steel substructure<br>Compression of ECC<br>Combination of buckling of steel substructure and failure of connection between ECC and steel substructure | |

*- additional to self-weight

** - average results of panels tested (average of two for ICP and average of three of MP)

*** - Results of semi-modular panel with welded connections

The measured decay of the free vibrations of the panels and damping ratios were found to be 0.6-1.8% for ICP , 0.6-1.0% for SMP and 0.5-0.7 for MP depending on the applied load (Figure 8.11 and Table 8.1). The lowest values of damping were noticed for MP. Although the self-weight and the bending stiffness of the panel is higher than that of ICP or SMP, the decay of the vibrations are less effective due to discontinuous ECC slab on top of the steel substructure. The vibrations of the panel induce a positive (the same direction as the deflections from self-weight) and negative deflection in the panel. When the positive deflections are induced to MP, the ECC slab undergoes the compression and a MP has a stiffness of full composite. However, when negative deflections are imposed to the MP, the ECC slab does not transfer any tensile stresses over the connection parts of ECC plates and thus the

bending stiffness of the MP is equal to bending stiffness of the steel substructure (half of bending stiffness of composite). In case of ICP and SMP, the experimentally observed damping ratios increased with increased loading. Most likely this is a result of additional decay mechanisms in vibrations due to friction between the loading blocks. Additional research is needed into the dynamic response of the lightweight composite panel system to confirm the design is serviceable when used as a floor panel. No specific dynamic requirements in terms of natural frequency and damping ratio are set for roof panels.

### 8.4.2 Performance at ULS

Experimentally observed ultimate loads with corresponding deflections and the analytically predicted ultimate loads are presented in Table 8.1. All of the composite panels resisted a slightly higher ultimate load than analytically predicted. The analytical calculations and experimentally observed ultimate loads varied by less than 5% in case of welded SMP and MP. Higher differences were observed in the ICP, where the panels resisted 25% more load that was expected.

Two ICP specimens were tested; the first reached a total load of 276 kN at mid-span deflection of 218 mm before one pair of the thin walled steel profiles fractured leading to failure of the panel. The second ICP specimen reached a total load of 292 kN with a mid-span deflection of 300-500 mm before compression failure of the ECC slab occurred.

Three SMP panels with a bolted substructure were tested. All three specimens failed due to failure of the steel substructure with an ultimate load of 90-140 kN at a mid-span deflection of 100-500mm. During the ULS testing of bolted SMP, slip in the bolted connections was observed and was visible as small drops in load-deflection graphs in Figure 8.12. SMP with welded steel truss substructure reached a total load of 291 kN at 282 mm of mid-span deflection before the failure of the panel. The element failed from a combination of compression failure in ECC and yielding of steel substructure directly below the loading points.

The MPs tested had a very similar composition thus the load carrying capacity was similar for all three panels varying between 278 and 310 kN at a mid-span deflection between 120 and 190 mm (Figure 8.12). Although the load carrying capacity of three panels tested varied only by 10%, each panel had a different failure mode. First of the panels tested failed as a result of buckling of the steel substructure under one of the loading-points as illustrated in Figure 8.13(a). Extensive local deformations in the substructure, especially in the flange part of the steel joists resulted in an increasing gap between the ECC slab and the steel joists, thus reducing the strength of the connection (Figure 8.13(b)). By applying more load a sudden failure occurred when two ECC plates located at the end of the MP lost the shear connection with steel joists.


***Figure 8.13*** *Failure of MP (first panel); (a) buckling of steel joists under one of the loading point and (b) subsequently failure of the connection between steel joists and the cast-in elements (first panel)*

As a result of the sudden failure mode of the first panel, the connection between the steel joists and ECC plates were strengthened by adding two HILTI X-U 16P8 nails per cast-in element for the second and third panel. The second MP tested failed due to compression failure (Figure 8.14) in ECC with an ultimate load of 310 kN at mid-span deflections of 190mm. After the ultimate load was reached, extensive deformations in the compression zone of the composite panels led to buckling of the steel substructure.

The third MP tested failed due to a combination of buckling (Figure 8.15(a)) of the steel substructure under one loading point and shear failure in connection between ECC and steel joists at an ultimate load of 310 kN at a mid-span deflection of 182 mm. Two types of shear connection failure were noticed: failure in the connection between the steel substructure and cast-in elements (Figure 8.15(b)) and failure of the cast-in element (Figure 8.15(c)). The failure in cast-in elements occurred by pullout of the cast-in nails from the steel plates. The failure of the MP was sudden and it was not possible to notice which one of the three types of failure modes occurred first.

After ULS testing of MP, extensive cracking of ECC was observed. The ECC plates that were subjected to higher shear loads (two plates from each end of the panel) had a crack pattern similar to that shown in Figure 8.16 around the cast in elements.

***Figure 8.14*** *Compression failure of MP panel (second panel) at mid-span*

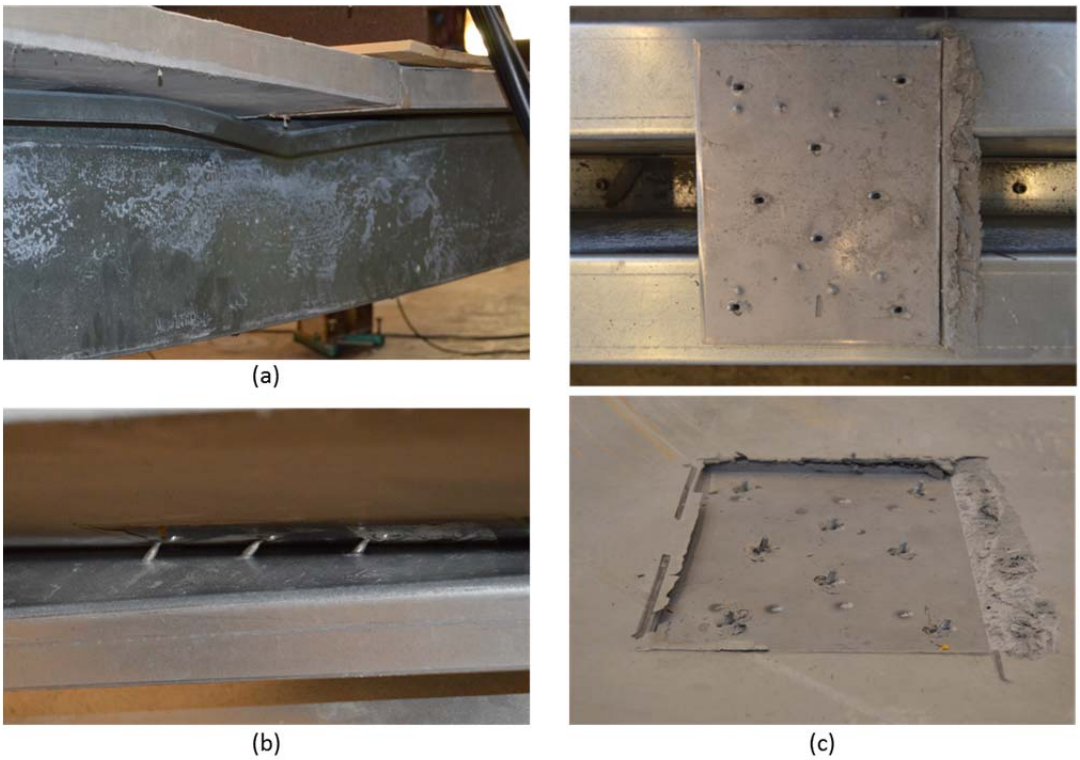


***Figure 8.15*** *Failure of MP (third panel): (a) buckling of flange of steel joists under one of the loading point, (b) failure of shear connection between cast-in elements and steel substructure and (c) failure of cast-in element*

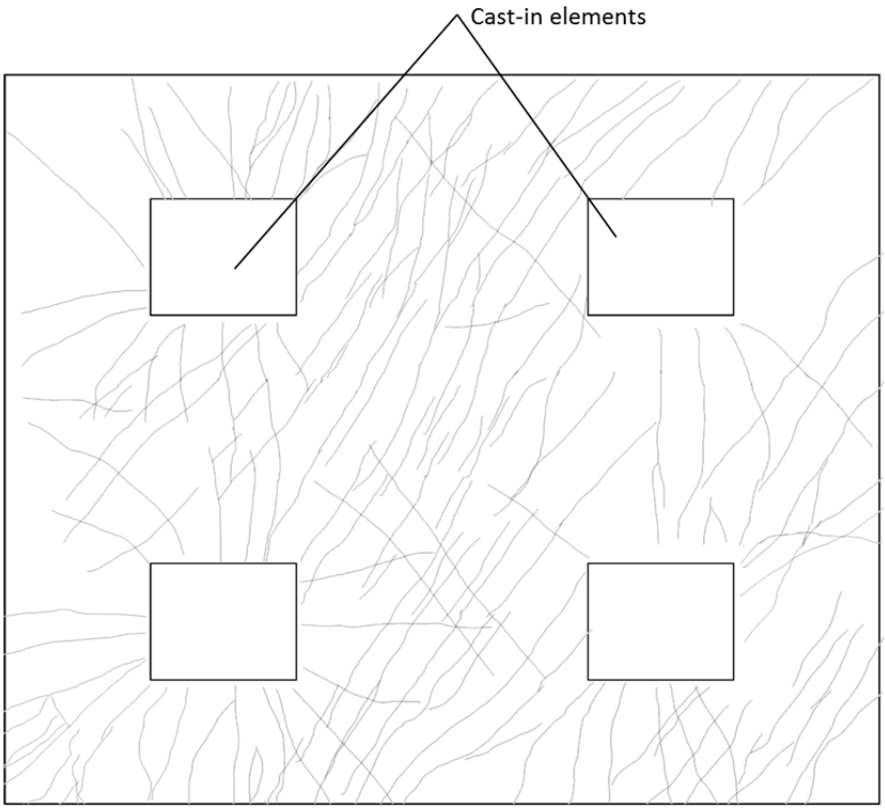


***Figure 8.16*** *Crack map of ECC plate located in the maximum shear region after ULS testing*

## 8.5 Conclusions

A new prefabricated lightweight composite panel with ECC slab was developed and the structural performance was investigated. The composite panel had a modular configuration and consisted of precast ECC plates and a lightweight steel substructure. The structural behavior of the developed modular panel (MP) was compared to the performance of previously developed lightweight composite panels with ECC slabs – integrally cast panel (ICP) and semi modular panel (SMP) developed by Larusson et.al. (Blond & Pedersen 2008; Larusson et al. 2013).

The ICP was manufactured as a composite member; lightweight steel joists were integrally cast with a 50 mm thick ECC slab. Although the ICP showed good structural performance, large shrinkage deformations of the ECC were restricted by the integrally cast lightweight steel joist resulting in considerable cracking in ECC. The proposed semi-modular panel introduced individual anchor points cast-in with the ECC slab, which were subsequently used to attach a steel truss substructure. By casting individual anchor points into the deck, the slab was allowed to shrink and deform independently of the substructure prior to the assembly of the composite panel without causing shrinkage induced stresses and cracking and undesirable deflections of the deck panel during curing. Although the shrinkage induced cracking was solved by SMP, handling a thin ECC slab before assembly with the steel substructure was a

complicated procedure as the slab is very flexible and any inattentive movement can result in cracking or collapse of the ECC slab.

Thus, a new prefabricated lightweight composite panel with ECC slab was developed and its structural performance investigated. The composite panel had a modular configuration, consisting of precast ECC plates and lightweight a steel substructure. The precast ECC plates were cast in sizes of 1.0 m x 1.2 m with a thickness of 55 mm, the plate had four or six cast-in elements for connection to the steel joists. The precast ECC plates had no protrusions, easing storage and handling, with a total weight of approximately 130 kg each. Thus, the ECC plates were easy to cast and handle and required limited space for storage. The features of the composite panel included:

- Lightweight design due to the small thickness of the ECC plates and use of the lightweight steel joists;
- Modular components that are easy to store and prefabricate on the jobsite immediately prior to placement;
- The configuration and bending stiffness of steel substructure can be tailored to the required performance and span length;
- The use of the precast ECC plates eliminates the need for steel reinforcing bars or welded wire mesh;
- The precast ECC element can undergo the majority of drying shrinkage deformations without external restraint.

The structural behavior in terms of deflection and vibration testing under SLS and load-deflection response under ULS has been performed. The ultimate load caring capacity of panels tested was consistent with predicted results. The deflection capacity of the MP was significant (L/60-L/42) before the ultimate load was reached. At SLS testing the deflection were within the targeted limits. While the MP concept was found to be a suitable lightweight composite panel for applications in roofs, more research is needed to make sure that requirements of natural frequency and damping ratio are met for application in floors with pedestrian traffic.

# Chapter 9

# Summary and conclusions

## 9.1 Summary

The central aim of the work presented in this Ph.D. thesis was to develop an approach, one that could be easily implemented by most structural engineers, to facilitate the wider use of FRC materials for structural applications. To accomplish this, commonly used test methods to characterize FRC were investigated in detail using digital image correlation (DIC) to assess their usefulness in verifying design assumptions are fulfilled during construction. A new design approach for FRC materials with softening or hardening post-cracking responses was developed to predict flexural behavior of a structural element. Example structural applications of FRC were conceived and tested. The model was applied to specific applications to provide design examples and to verify the accuracy of the developed model.

## 9.2 Overview of findings and conclusions

The following sections connect findings and conclusions from various chapters of the thesis in final remarks on the following themes:

- Test methods to characterize FRC materials,
- Development of a model to predict flexural behavior of FRC, and
- Testing of potential applications of FRC materials.

### 9.2.1 Investigation of test methods to characterize FRC

Two types of tensile test methods are used to characterize FRC: single crack notched coupon test (tensile stress-crack opening) and dogbone test (tensile stress-strain). Both test methods provide significant insight for the characterization of ECC. The single crack notched coupon test provides quantitative and fundamental information on the cohesive relationship of FRC materials and provides an indication of whether an FRC material is strain hardening or softening in tension. If the first cracking strength is lower than the maximum fiber bridging stress, the material is likely to have a strain hardening behavior in uni-axial tension, while materials with maximum fiber bridging stress less than the first cracking strength are likely to have a softening response. The dogbone test characterizes the overall strain capacity, crack distribution and ductility of FRC materials. For tension softening materials, the single crack coupon and dogbone tests show similar information as failure in tension softening materials by definition occurs at a single crack location.

Results from tensile testing show that the three FRC materials presented in this thesis had varying post-cracking responses. The maximum fiber bridging stress for the ECC was higher than the first cracking strength, indicating a strain hardening post-cracking response is favored in direct tension. Tensile stress-strain results from ECC dogbone specimens verify a strain hardening post-cracking response. The first cracking strength of the PP-FRC and SFRC was higher than the maximum fiber bridging stress, indicating a tension softening post-cracking response is favored for the SFRC and PP-FRC.

The single crack notched coupon test and dogbone test most realistically describe the tensile properties and cohesive relationship of FRC. However, such samples may be difficult to prepare in the field and to test in a standard laboratory for quality control purposes. For this reason, it was concluded that alternative test methods are needed to obtain mechanical behavior of FRC. Various test methods, based on beams and plates in flexure, were investigated in this study to assess their potential as a test method to verify structural design assumptions are maintained during construction.

As presented in Chapter 3, certain test methods were found to be useful to characterize FRC. To improve the accuracy of the provided results, certain recommendations on the applied test method and configurations were provided, as follows:

- The notched three-point bending test is not suitable for strain hardening FRC materials and for some tension softening FRC materials. Crack formation around the notch does not follow bending beam theory as a result of a disturbed stress regions (flexure and shear) in the vicinity of the mid-span. Moreover, the stress field generating in the sample is significantly disturbed for the entire beam, particularly for deflection hardening FRC.

- The four-point bending tests characterize the material more realistically by accommodating multiple cracking, especially when using more slender beam geometries. In commonly used four-point bending tests the slenderness ratio a/h=1 and the results are highly influenced by shear stresses. Therefore, to avoid this issue, the increased slenderness ratio a/h to 2 or higher is recommended.
- The round determinate panel (RDP) test provides an alternative test to beams with a larger fracture area. The plate specimen as specified in ASTM C1550 can be considered a slender bending specimen, where cracking is induced predominantly by bending stresses and not by shear stresses. The load-deformation response is therefore governed by bending with additional effects induced by confining stresses in the radial direction of the plate.
- When specifying the test method for characterization of a FRC material, the specimen geometry shall be comparable to that of the actual structure. In particular, the thickness of the test specimen should be similar to that of the actual application to ensure similar fiber orientation and distribution. For materials designed to exhibit multiple cracking in the constant moment sections, this material performance property should be captured by the selected test method.

### 9.2.2 Development of a model to predict flexural behavior of FRC

The results presented in Chapter 4 provided an indication that modeling the flexural response of FRC based on the basic tensile and compressive responses is warranted for FRC materials for both softening and hardening post-cracking responses. Chapter 5 describes a new design approach for FRC materials with softening or hardening post-cracking responses that was developed to predict flexural behavior of a structural element.

The model predicts the flexural behavior of FRC by assuming a loaded structure consists of cracked rotationally deformable segments, called representative flexural segments (RFS), connected with rigid segments. The model considers the balance between work done on the deformed structure and the energy required to induce the corresponding rotational deformations in the RFS. The properties of the RFS are the energy needed to deform a segment by a given rotational angle. These properties can be derived either from material properties in direct tension and compression or from flexural beam tests.

The flexural response in terms of load-deflection of a structural element can be accurately predicted using the model described before. The model was verified through the following comparisons with experimental results:

- The flexural behavior of ECC and SRFC beams has been predicted using RFS properties obtained from direct tension and compression. The modeled load-

deflection curves have been compared to experimentally observed results. The model predicted the behavior of four-point bending beams well.

- The flexural behavior of SFRC and ECC RDP's was predicted using RFS properties obtained either from direct tension and compression, or four-point bending beams. The modeled results either from direct tension and compression or flexural beams were found to realistically and accurately predict both the load and deformation of the RDP's.
- Structural slabs of ECC and SFRC were constructed and tested under flexural loading. Comparisons of the model predicted capacities and deformations indicated the model accurately predicts the flexural response of the slabs.

It was noted in all cases that the predictions were more precise if the cross-section of the test specimens (especially thickness) were similar to the actual structure.

The developed model is relatively simple, compared to fracture mechanics or finite element based models. Nevertheless, the model accurately predicts the load-deflection behavior of the structure. Therefore, the model has a great potential to be applied by most structural engineers for the design of FRC members under flexural loading.

### 9.2.3 Example applications

Chapter 6, 7 and 8 describe the following potential applications of FRC materials:

- A pile-supported slab or tunnel/mine lining,
- Full or partial replacement of traditional shear reinforcement with fibers,
- Prefabricated lightweight composite roof and floor panels with an ECC slab.

As steel fibers are allowed to be used as an alternative to minimum transverse shear reinforcement in ACI 318-08 (ACI-318 2008), the impact of ECC on shear behavior was investigated in Chapter 7. The benefits of using RECC with regards to resisting shear loads include improved shear resistance and cracking control.

The contributions of ECC on shear behavior of RECC include:

- Fiber bridging across shear cracks increase the shear capacity with or without traditional shear reinforcement (i.e., stirrups);
- Stirrups are activated with smaller crack deformation (opening and sliding), as measured at the surface of the beam;
- Crack deformations are limited by fiber bridging mechanism and by activating traditional shear reinforcement at smaller crack deformations.

Based on the shear stress-strain responses and DIC measurements of the specimen deformations, a conceptual descriptions of the shear crack opening, crack sliding and subsequent failure of RC and RECC was proposed. For RC, shear load is transferred across cracks by stirrups, aggregate interlock and the dowel effect of the longitudinal

reinforcement. The crack development mechanism for RECC is more complex due to the fiber bridging mechanisms. Multiple cracking is induced, resulting in smaller individual crack openings at a given overall shear deformation and a higher ultimate shear stress.

In Chapter 8, a prefabricated lightweight composite panel with ECC slab was developed and its structural performance investigated. The composite panel had a modular concept, consisting of precast ECC plates and lightweight a steel substructure. The precast ECC plates were cast in sizes of 1.0 m x 1.2 m with a thickness of 55 mm, the regular plate had four cast-in elements for connection to the steel joists. The precast ECC plates had no protrusions, easing storage and handling, and had a total weight of approximately 130 kg each. Thus, the ECC plates were easy to cast and handle and required limited space for storage. The features of the composite panel included:

- Lightweight design due to the thickness of the ECC plates and use of the lightweight steel joists;
- Modular components that are easy to store and prefabricate on the jobsite immediately prior to placement;
- The configuration and bending stiffness of steel substructure can be tailored to the required performance and span length;
- The use of the precast ECC plates eliminates the need for steel reinforcing bars or welded wire mesh;
- The precast ECC element can undergo the majority of drying shrinkage deformations without external restraint.

# Bibliography


162-TDF, R.T.C., 2002. RILEM T.C. 162-TDF: Test and design methods for steel fibre reinforced concrete - Bending test - Final recommendations. *Materials and Structures*, 35(9), pp.579–582. Available at: http://dx.doi.org/10.1007/BF02483127.

162-TDF, R.T.C., 2003. RILEM T.C. 162-TDF: Test and design methods for steel fibre reinforced concrete - sigma-epsilon-design method - Final recommendations. *Materials and Structures*, 36(262), pp.560–567.

162-TDF, R.T.C., 2001. RILEM T.C. 162-TDF: Test and design methods for steel fibre reinforced concrete. Uni-axial tension test for steel fibre reinforced concrete. Recommendations. *Materials and Structures*, 34(235), p.3.

ACI-318, 2008. *ACI 318-08 building code requirements for structural concrete and commentary*, ACI Committee 318.

ACI-318, 2014. *ACI 318-08 building code requirements for structural concrete and commentary*, ACI Committee 318.

Altoubat, S., Yazdanbakhsh, A. & Rieder, K.-A., 2009. Shear behavior of macro-synthetic fiber-reinforced concrete beams without stirrups. *ACI Materials Journal*, 106(4), pp.381–389.

Ashour, S.A., Hasanain, G.S. & Wafa, F.F., 1992. Shear behavior of high-strength fiber reinforced concrete beams. *ACI Structural Journal*, 89(2), pp.176–184.

ASTM-C1437, 2013. *Standard Test Method for Flow of Hydraulic Cement Mortar*, ASTM.

ASTM-C1550, 2012. *Standard Test Method for Flexural Toughness of Fiber Reinforced Concrete (Using Centrally Loaded Round Panel)*,

ASTM-C157, 2008. *Standard Test Method for Length Change of Hardened Hydraulic-Cement Mortar and Concrete*, ASTM.

ASTM-C1609, 2012. *ASTM-C1609/C1609M-12 Standard Test Method for Flexural Performance of Fiber-Reinforced Concrete (Using Beam With Third-Point Loading)*, ASTM.

ASTM-C1609/C1609M-12, 2012. *Standard Test Method for Flexural Performance of Fiber-Reinforced Concrete (Using Beam With Third-Point Loading)*,

Aveston, J. & Kelly, A., 1973. Theory of multiple fracture of fibrous composites. *Journal of Materials Science*, 8(3), pp.352–362.

Azizinamini, A. et al., 2013. *SHRP 2 report Design guide for bridges for service life*, Transportation Research Board.

Bachmann, H., 1995. *Vibration problems in structures : practical guidelines*, Basel, Switz. ; Boston, Mass. : Birkäuser Verlag.

Balaguru, P. & Ramakrishnan, V., 1988. Properties of fiber reinforced concrete: workability, behavior under long-term loading, and air-void characteristics. *ACI Materials Journal (American Concrete Institute)*, 85(3), pp.189–196.

Bentz, E.C., Vecchio, F.J. & Collins, M.R., 2006. Simplified modified compression field theory for calculating shear strength of reinforced concrete elements. *ACI Structural Journal*, 103(4), pp.614–624.

Berard, A., 1874. Improvement in artificial stone. Available at: https://www.google.com/patents/US157903.

Bernard, E.S., 2013. Development of a 1200-mm-Diameter Round Panel Test for Post-Crack Assessment of Fiber-Reinforced Concrete. *Advances in Civil Engineering Materials*, 2(1), pp.457–471.

Blond, M. & Pedersen, M.., 2008. *Structural Improvements of Composite Deck System*. Denmark: DTU.

Broek, D., 1991. *Elementary engineering fracture mechanics* Fourth revised edition., Kluwer Academic Publishers.

Bywalski, C. & Kaminski, M., 2013. Rheological strains in concrete modified with steel fibre reinforcement. *Journal of Civil Engineering and Management*, 19(5), pp.656–664.

Chern, J.-C. & Young, C.-H., 1989. Compressive creep and shrinkage of steel fibre reinforced concrete. *International Journal of Cement Composites and Lightweight Concrete*, 11(4), pp.205–214.

Chiaia, B., Fantilli, A.P. & Vallini, P., 2009. Evaluation of crack width in FRC structures and application to tunnel linings. *Materials and Structures*, 42(3), pp.339–351.

Choi, K.K., Wight, J.K. & Park, H.G., 2007. Shear strength of steel fiber-reinforced concrete beams without web reinforcement. *ACI Structural Journal*, 104(1), pp.12–21.

Clark, C.C. et al., 2010. Report on early strength performance of modern day weak rock mass shotcrete mixes. *Sme Annual Meeting and Exhibit 2010, Sme Annu. Meet. Exhib*, pp.662–667.

CNR-DT204, 2007. *Guidelines for design, construction and production control of fiber reinforced concrete structures. Italy*, National Research Council of Italy,.

Crocetti, R. et al., 2014. An Innovative Prefabricated Timber-Concrete Composite System. *Materials and joints in timber structures: recent developments of technology*, 9, pp.507–516.

DAfStb, 2010. *Deutscher Ausschuss fur Stahlbeton, DAfStb-Richtlinie Stahlfaserbeton (Guidelines for Steel Fiber Reinforced concrete)*,

DBV, 2007. *Guide to Good Practice. Steel Fibre Concrete* G. S. for Concrete & C. Technology, eds., DBV.

Dinh, H.H. et al., 2011. Shear strength model for steel fiber reinforced concrete beams without stirrup reinforcement. *Journal of Structural Engineering*, 137(10), pp.1039–1051.

Dinh, H.H., Parra-Montesinos, G.J. & Wight, J.K., 2010. Shear behavior of steel fiber-reinforced concrete beams without stirrup reinforcement. *ACI Structural Journal*, 107(5), pp.597–606.

Elgaard Jensen, H., 1992. *Creep and shrinkage of high-strength concrete : A test report*, Bærende Konstruktioner, Danmarks Tekniske Højskole. Afdelingen and ABK.

Elsaigh, W.A., 2007. *Mdelling the behaviour of steel fiber reinforced concrete pavements*. University of Pretoria.

EN12390-6, 2002. *DS/EN 12390-6:2009 Testing hardened concrete - Part 6: Tensile splitting strength of test specimens* D.-328 Betonteknologi, ed., Danish Standard.

EN14488-5, 2006. *Testing sprayed concrete - Part 5: Determination of energy absorption capacity of fibre reinforced slab specimens*,

EN14651, 2007. *DS/EN 14651 Test method for metallic fibre concrete. Measuring the flexural tensile strength (limit of proportionality (LOP), residual)*, Danish Standard.

EN196-1, 2005. *Methods of testing cement. Determination of strength*,

EN1992-1-1, 2010. *Eurocode 2: Design of concrete structures – Part 1 - 1:General rules and rules for buildings*, CEN.

EN1994, 2007. *Eurocode 4: Design of composite steel and concrete structures,*, CEN.

fib, 2012. *Model Code for Concrete Structures 2010 - Final draft, fib Bulletin No. 65 and 66*, Ernst & Sohn.

Fischer, G., 2010. Application of Engineered Cementitious Composites (ECC) in prefabricated modular housing. *American Concrete Institute, ACI Special Publication*, (268 SP), pp.17–27.

Fischer, G. & Li, V.C., 2002. Influence of matrix ductility on tension-stiffening behavior of steel reinforced engineered cementitious composites (ECC). *ACI Structural Journal*, 99(1), pp.104–111.

Fischer, G., Stang, H. & Dick-Nielsen, L., 2007. Initiation and development of cracking in ECC materials: Experimental observations and modeling. *Proceedings of the 6th International Conference on Fracture Mechanics of Concrete and Concrete Structures*, 3, pp.1517–1522.

Gandomkar, F.A., Wan Badaruzzaman, W.H. & Osman, S.A., 2011. The natural frequencies of composite profiled steel sheet dry board with concrete infill (PSSDBC)

system. *Latin American Journal of Solids and Structures, Lat. Am. J. Solids Struct*, 8(3), pp.351–372.

GOM, 2005. GOM Optical Measuring Techniques, "Aramis v5.4 User Manual", GOM mbH. Available at: www.gom.com.

Hambro, 2009. *Hambro Technical Manual (Canada): Composite Floor Systems.*, Available at: http://www.hambro-floors.ws.

Hannant, D.J., 1978. *Fibre cements and fibre concretes*,

Hiraishi, Y. et al., 2003. Steel Corrosion at Bending Cracks in Ductile Fiber Reinforced Cementitious Composites. In *28th Conference on Our World in Concrete & Structures*. pp. 333–340.

Imam, M. et al., 1997. Shear domain of fibre-reinforced high-strength concrete beams. *Engineering Structures*, 19(9), pp.738–747.

JCI-S-002, 2003. *JCI-S-002-2003 Method of test for load-displacement curve of fiber reinforced concrete by use of notched beam*, Japan Concrete Institute Standard.

JCI-S-003, 2007. *JCI-S-003-2007 Method of test for bending moment–curvature curve of fiber-reinforced cementitious composites*, Japan Concrete Institute Standard.

Johansen, K.W., 1962. *Yield line theory*, London: Cement and concrete association.

JSCE, 2008. *Recommendations for design and construction of High Performance Fiber Reinforced Cement Composites with fine multiple cracks*,

Kabele, P., 2005. Fracture Behavior of Shear-Critical Reinforced HFRCC Members. In *Proceedings on the International RILEM Workshop on High Performance Fiber Reinforced Cementitious Composites (HPFRCC) in Structural Applications*. Honolulu, Hawaii, USA, pp. 383–392.

Kanakubo, T. et al., 2010. Shear transmission on crack surface of ECC. In et al. B. H. Oh, ed. *Proceedings of FraMCos-7, Jeju (Korea)*. pp. 1623–1630.

Kanda, T., Watanabe, S. & Li, V.C., 1998. Application of pseudo strain hardening cementitious composites to shear resistant structural elements. In *Fracture Mechanics of Concrete Structures Proceedings FRAMCOS-3 AEDIFICATIO Publishers, D-79104 Freiburg, Germany*.

Katzer, J., 2006. Steel Fibers and Steel Fiber Reinforced Concrete in Civil Engineering. *The Pacific Journal of Science and Technology*, 7(1), pp.53–58.

Kuhlmann, J. U. Schanzlig, 2008. A timber-concrete composite slab system for use in tall buildings. *Structural Engineering International: Journal of the International Association for Bridge and Structural Engineering (iabse), Struct Eng Int J Int Assoc Bridge Struct Eng*, 18(2), pp.174–178.

Kunieda, M. & Rokugo, K., 2006. Recent Progress on HPFRCC in Japan Required Performance and Applications. *Journal of Advanced Concrete Technology*, 4(1), pp.19–33.

Kwak, Y.-K. et al., 2002. Shear strength of steel fiber-reinforced concrete beams without stirrups. *ACI Structural Journal*, 99(4), pp.530–538.

Larusson, L., 2008. *Detailed Design of a Composite Floor Deck Element*. Denmark: DTU.

Larusson, L.H., Fischer, G. & Jonsson, J., 2010. Mechanical interaction of Engineered Cementitious Composite (ECC) reinforced with Fiber Reinforced Polymer (FRP) rebar in tensile loading. In *Advances in Cement-Based Materials - Proceedings of the International Conference on Advanced Concrete Materials*. CRC Press, pp. 83–90.

Larusson, L.H., Fischer, G. & Jonsson, J., 2013. Prefabricated floor panels composed of fiber reinforced concrete and a steel substructure. *Engineering Structures*, 46, pp.104–115.

Lárusson, L.H., Fischer, G. & Jönsson, J., 2011. Mechanical interaction between concrete and structural reinforcement in the tension stiffening process. In *High Performance Fiber Reinforced Cement Composites 6*. Springer.

Lepech, M., 2009. This concrete thinks it's metal. *Seattle Daily Journal of Commerce*.

Lepech, M.D. & Li, V.C., 2009. Application of ECC for bridge deck link slabs. *Materials and structures*, 42(9), pp.1185–1195.

Li, C.V. & Fischer, G., 2002. Reinforced ecc - an evolution from materials to structures. In *FIB Proceedings of the 1st fib Congress*.

Li, V.C., 1998. Engineered Cementitious Composites - Tailored Composites Through Micromechanical Modeling. In A. Bentur A. A. Mufti N. Banthia, ed. *Fiber Reinforced Concrete: Present and the Future*. anadian Society for Civil Engineering, pp. 64–97. Available at: http://hdl.handle.net/2027.42/84667.

Li, V.C. et al., 1994. On the shear behavior of engineered cementitious composites. *Advanced Cement Based Materials*, 1, pp.142–149.

Li, V.C. & Kanda, T., 1998. Engineered Cementitious Composites for structural applications. *Journal of Materials in Civil Engineering*, 10, pp.66–69.

Li, V.C., Ward, R. & Hamza, A.M., 1992. Steel and synthetic fibers as shear reinforcement. *ACI Materials Journal*, 89(5), pp.499–508.

Maidl, B.R., 1995. *Steel fibre reinforced concrete*, Ernst.

Majdzadeh, F., Soleimani, S.M. & Banthia, N., 2006. Shear strength of reinforced concrete beams with a fiber concrete matrix. *Canadian Journal of Civil Engineering*, 33(6), pp.726–734.

Mangat, P. & Azari, M., 1985. A theory for the creep of steel fiber reinforced cement matrices under compression. *Journal of Materials Science*, 20(3), pp.1119–1133.

Mansur, M., Ong, K. & Paramasivam, P., 1986. Shear Strength of Fibrous Concrete Beams Without Stirrups. *Journal of Structural Engineering*, 112(9), pp.2066–2079. Available at: http://dx.doi.org/10.1061/(ASCE)0733-9445(1986)112:9(2066).

Martin, L. et al., 2011. An Analysis of Flexural Strength and Crack Width for Fiber-Reinforced Shotcrete Used in Weak Rock Mines. *Trans Soc Min Metal Explor TP-09-062*, (328), pp.542–549.

Mello, A.V.A. et al., 2008. Dynamic analysis of composite systems made of concrete slabs and steel beams. *Journal of Constructional Steel Research*, 64(10), pp.1142–1151.

Minelli, F. & Plizzari, G., 2011. A New Round Panel Test for the Characterization of Fiber Reinforced Concrete: A Broad Experimental Study. *Journal of testing and evaluation*, 39(5), pp.889–897.

Minelli, F. & Plizzari, G., 2015. Derivation of a simplified stress-crack width law for Fiber Reinforced Concrete through a revised round panel test. *Cement and Concrete Composites*, 58, pp.95–104.

Miyazato, S. & Hiraishi, Y., 2005. Transport properties and steel corrosion in Ductile Fiber Reinforced Cement Composites. *11th International Conference on Fracture 2005, ICF11*, 2, pp.1500–1505.

Nagai, S. et al., 2002. Shear capacity of ductile wall with high performance fiber reinforced cement composite. In *Proceedings of the 1st fib Congress*.

Narayanan, R. & Darwish, I.Y.S., 1987. Use of steel fibers as shear reinforcement. *ACI Structural Journal (American Concrete Institute)*, 84(3), pp.216–227.

NT-Build511, 2005. *Wedge splitting test method (WST): fracture testing of fibre-reinforced concrete (mode I)*, Nordtest.

Naaman, A., 2008. High-Performance Construction Materials: Science and Applications. In Y. L. C.J. Mo Shi, ed. pp. 91–153.

Naaman, A. & Shah, S., 1979. Fracture and Multiple Cracking of Cementitious Composites. *Fracture Mechanics Applied To Brittle Materials*, 1979(678), pp.183–201.

Naaman, A.E., 2007. Tensile strain-hardening FRC composites: Historical evolution since the 1960's. *Advances in construction materials*, pp.181–202.

Oslejs, J., 2008. New Frontiers for Steel Fiber-Reinforced Concrete: Experience from the Baltics and Scandinavia. *Concrete international -Detroit-*, 30(5), pp.45–50.

Ostergaard, L., Walter, R. & Olesen, J.F., 2005. Method for determination of tensile properties of engineered cementitious composites (ECC),. *Construction Materials : Proceedings of ConMat'05 and Mindess Symposium*, pp.74–74.

Paegle, I. & Fischer, G., 2013. Evaluation of test methods used to characterize fiber reinforced cementitious composites. In J. Kaminskis, ed. *Proceedings of the International Conference: Innovative Materials, Structures and Technologies*. Riga: RTU Press, pp. 122–128.

Paegle, I. & Fischer, G., 2011. Shear crack formation and propagation in reinforced Engineered Cementitious Composites. In *International Rilem Conference on Advances in Construction Materials Through Science and Engineering*.

Parra-Montesinos, G.J., 2006. Shear Strength of Beams with Deformed Steel Fibers - Evaluating an alternative to minimum transverse reinforcement. *Concrete International - the Magazine of the American Concrete Institute*, 28(11), p.57.

Pease, B.J., Geiker, H. M.R. Stang & Weiss, W.J., 2006. Photogrammetric Assessment of Flexure Induced Cracking of Reinforced Concrete Beams under Service Loads. In *Proceedings of the 2nd International RILEM Symposium, Advances in Concrete through Science and Engineering, Québec City, Canada*.

Pereira, E. et al., 2010. Crack formation and tensile stress-crack opening behavior of Fiber Reinforced Cementitious Composites (FRCC). *7th International Conference on Fracture Mechanics of Concrete and Concrete Structures (FraMCoS 7)*.

Pereira, E.B., Fischer, G. & Barros, J.A.O., 2012. Direct assessment of tensile stress-crack opening behavior of Strain Hardening Cementitious Composites (SHCC). *Cement and concrete research*, 42(6), pp.834–846.

Piascik, R.S. & Newman, J. J. C., 1996. An extended compact tension specimen for fatigue crack growth and fracture testing. *International Journal of Fracture*, 76(3), pp.43–8.

Romualdi, J.P. & Mandel, J.A., 1964. Tensile strength of concrete affected by uniformly distributed and closely spaced short lengths of wire reinforcement. *American Concrete Institute – Journal*, 61(6), pp.657–671.

Shah, B.V. S.P. Rangan, 1971. Fiber reinforced concrete properties. *J Amer Concrete Inst*, 68(2), pp.126–35.

Shang, Q. & Van Zijl, G.P.A.G., 2007. Characterising the shear behaviour of strainhardening fibre-reinforced cement-based composites. *Journal of the South African Institution of Civil Engineering*, 49(2), pp.16–23.

Sharma, A., 1986. Shear-strength of steel fiber reinforced-concrete beams. *Journal of The American Concrete Institute*, 83(4), pp.624–628.

Shimizu, K. et al., 2006. Shear Behavior of PVA-ECC Beams. In *International RILEM Workshop on High Performance Fiber Reinforced Cementitious Composites in Structural Applications*.

Soranakom, C. & Mobasher, B., 2009. Flexural Design of Fiber-Reinforced Concrete. *ACI Materials Journal*, 106(5), pp.461–469.

SP52-104, 2010. *Building Norms and Rules SP 52-104-2009. Steel fiber reinforced structures*, Moscow.

Sprince, A. et al., 2014. Crack propagation in concrete with silica particles. *Advanced Materials Research*, 842, pp.470–476.

Sprince, A., Korjakins, A. & Pakrastinsh, L., 2013. Time-dependent behavior of high performance fiber-reinforced concrete. *Advanced Materials Research, Adv. Mater. Res*, 705(705), pp.75–80.

SS812310, 2014. *SS 812310:2014 Fibre Concrete – Design of Fibre Concrete Structures*, Swedish Standard Institute.

Swamy, R.N., Mangat, P.S. & Rao, C.V.S.K., 1974. The Mechanics of Fiber Reinforcement of Cement Matrices. *ACI Special Publication*, 44, pp.1–28.

TR63, 2007. *Guidance for the design of steel-fibre-reinforced concrete* C. Society, ed.,

Tran, V., Bernard, E. & Beasley, A., 2005. Constitutive modeling of fiber reinforced shotcrete panels. *Journal of Engineering Mechanics-ASCE*, 131(5), pp.512–521.

Vecchio, F.J. & Collins, M.P., 1986. Modified compression-field theory for reinforced concrete elements subjected to shear. *Journal of The American Concrete Institute*, 83(2), pp.219–231.

Velasco, R.V. et al., 2009. Basic creep of steel fibers reinforced composites. *Proceedings of the 8th Int. Conference on Creep, Shrinkage and Durability Mechanics of Concrete and Concrete Structures*, pp.735–739.

Wang, V.C. S.; Li, 2004. Tailoring of Pre-existing Flaws in ECC Matrix for Saturated Strain Hardening. In *Proceedings of FRAMCOS-5*. Vail, Colorado, U S A, pp. 1005–1012. Available at: http://hdl.handle.net/2027.42/84774.

Wille, K. & Parra-Montesinos, G.J., 2012. Effect of Beam Size, Casting Method, and Support Conditions on Flexural Behavior of Ultra-High-Performance Fiber-Reinforced Concrete. *ACI Materials Journal*, 109(3), pp.379–388.

Winkler, A., Edvardsen, C. & Kasper, T., 2014. Examples of bridge, tunnel lining and foundation design with steel fibre reinforced concrete. In *Proceedings of FRC 2014 Joint ACI-fib International Workshop Fibre Reinforced Concrete: from Design to Structural Applications*.

Yang, J. & Fischer, G., 2006. Simulation of the tensile stress-strain behavior of strain hardening cementitious composites. *Measuring, monitoring and modeling concrete properties*, pp.25–31.

Zi, G., Kim, J. & Bazant, Z.P., 2014. Size Effect on Biaxial Flexural Strength of Concrete. *ACI Materials Journal*, 111(3), pp.319–326.

# Publication list (not included in the thesis)


Paegle, I., Minelli, F., Fischer, G. "Influence of testing method on the derivation of the constitutive law of fiber reinforced concrete", Cement and Concrete Composites, submitted manuscript

Paegle, I., Fischer G. "Shear behavior of reinforced Engineered Cementitious Composites (ECC) beams", Cement and Concrete Composites, submitted manuscript

Paegle, I., Fischer G. "Modeling the load-deformation response of FRC structural members", International conference "High Performance Fiber Reinforced Cement Composites 6", 2015.

Finazzi S., Paegle I., Fischer G., Minelli F. "Influence of bending test configuration on cracking behavior of FRC" Proceedings of the "3rd All-Russian International Conference on Concrete and Reinforced Concrete", 2014

Paegle, I., Fischer G. "Evaluation of test methods used to characterize fiber reinforced cementitious composites" Proceedings of the "International Conference: Innovative Materials, Structures and Technologies", editor: Janis Kaminskis, 2013, pp 122-128.

Paegle, I., Fischer G. "Shear crack formation and propagation in fiber reinforced cementitious composites (FRCC)" Proceedings of the "High Performance Fiber Reinforced Cement Composites 6",RILEM State of the Art Reports, editors: Gustavo J. Parra-Montesinos, Hans W. Reinhardt, A. E. Naaman, Volume 2, 2012, pp 231-238

Paegle, I., Fischer G. "Evaluation of standardized test methods to characterize fiber reinforced cement composites" Proceedings of the "Second RILEM international conference on Strain Hardening Cement Composites", 2011

Paegle, I., Fischer G. "Shear crack formation and propagation in reinforced Engineered Cementitious Composites" Proceedings of the "International RILEM Conference on Advances in Construction Materials Through Science and Engineering", ISBN: 978-2-35158-116-2, 2011

Paegle, I., Fischer, G. "Shear behavior of reinforced Engineered Cementitious Composites (ECC) beams" Proceedings of Advances in cement-based materials / Editor: van Zijl, Gideon Pieter Adriaan Greeff; Boshoff, William Peter - Leiden: CRC Press, 2010 (75-82 p.)

The work presented in this thesis offers new insights into application of Fiber Reinforced Concrete (FRC) in structural elements and presents findings on experimental characterization and quantification of material properties in tension, bending, shear and creep. A new design model for FRC materials with softening and hardening post-cracking responses was developed to predict the flexural behavior of structural elements. The model was applied in specific cases to provide design examples and to verify its accuracy.

**DTU Civil Engineering**
Technical University of Denmark

Brovej, Bygning 118
2800 Kongens Lyngby

www.byg.dtu.dk

ISBN 9788778774170
ISSN 1601-2917